THE UNIVERSITY OF OKLAHOMA

GRADUATE COLLEGE

NUMERICAL SIMULATION OF NONLINEAR BUOYANCY WAVES IN THE LOWER ATMOSPHERE

A Dissertation

SUBMITTED TO THE GRADUATE FACULTY

in partial fulfillment of the requirements for the

degree of

Doctor of Philosophy

By

PENGFEI ZHANG
Norman, Oklahoma
1997

UMI Number: 9726712

NUMERICAL SIMULATION OF NONLINEAR BUOYANCY WAVES IN THE LOWER ATMOSPHERE

A DISSERTATION APPROVED FOR
THE SCHOOL OF METEOROLOGY

BY

Brian Fiedler

R J Doviak

William H. Beasley

ACKNOWLEDGMENTS

First of all, I would like to thank Dr. Richard Doviak, my major advisor, for his insightful and patient guidance during the last 7 years and for reviewing and editing this thesis. Without his help, this research would not have been possible. I would also like to thank Dr. Brian Fiedler for his help in developing the model used in this research and his advice during the course of this research. Thanks also go to my other committee members, Drs. Kelvin Droegemeier, Douglas Lilly, William Beasley, and Joao Cruz, for their helpful suggestions to my research.

Discussions with Dr. Yu-Chieng Liou have been very helpful to my research. I gratefully acknowledge the professors, the staff members and my fellow graduate students in the School of Meteorology, University of Oklahoma for their friendship and help during my years as a graduate student.

This research has been supported by the National Science Foundation, through Grant ATM-9111541 to the Cooperative Institute for Mesoscale Meteorological Studies. Facilities, equipment, and personnel support for portions of this work have been provided by the Center for Analysis and Prediction of Storms, the University of Oklahoma School of Meteorology. I appreciate the contributions made by all these institutions.

Finally, I would like to express my deep appreciation to my wife, Jian Zhang, for her love and many beneficial suggestions for my research. I also thank my parents for their support and encouragement.

ABSTRACT

A 2D dry incompressible vorticity-stream function model is developed and used to investigate nonlinear buoyancy waves, especially internal solitary waves and related phenomena in the lower atmosphere. Using this model some essential properties of internal solitary waves have been successfully simulated. For the first time reversed recirculation within large amplitude solitary waves has been found in the simulations. The existence of recirculation enables large amplitude solitary waves to trap air and transport it. Meanwhile, due to viscosity the trapped air continuously leaks out during the transport. The influences of surface friction and ambient vertical wind shear on solitary waves are also studied.

On the basis of the preceding studies, an internal solitary wave generated by a thunderstorm outflow, observed by NSSL's Doppler weather radar, a 444m tall tower and a surface network, is modeled. The simulation results show a quite good agreement with the observation in several aspects. The simulation also gives us a further understanding of the origin, propagation, and decay of the solitary wave, as well as its detailed kinematic and thermodynamic structure.

TABLE OF CONTENTS

Page

Acknowledgments iv

Abstract v

Table of contents vi

List of figures viii

List of tables xi

Chapter

1. Introduction 1

1.1 Nonlinear buoyancy waves in the atmosphere 2

1.2 The developments of solitary wave theory 4

1.3 Laboratory experiments 9

1.4 Numerical modeling 10

1.5 Our research objectives 11

2. Numerical Model 14

2.1 Model equations and operation procedure 14

2.2 Boundary conditions 18

2.3 Finite difference scheme for time integration 20

2.4 Finite difference scheme for spatial derivatives 22

2.5 Stretched vertical coordinate 26

2.6 Initial conditions 27

3. The results of weakly-nonlinear solitary wave theory 28

4. Numerical simulations of solitary waves 32

4.1 Propagation of solitary waves 32

4.2 Collisions of two solitary waves 43
4.3 Generation of solitary waves by thunderstorm outflow 47
4.4 Trajectories of air parcels 55
5. Structures and properties of large amplitude solitary waves 64
5.1 Generation of pure large amplitude solitary waves 64
5.2 Configurations of reversed recirculation within large amplitude solitary waves 66
5.3 Configurations of normal recirculation within large amplitude solitary waves 82
5.4 Trapping and leaking effects of large amplitude solitary waves 83
5.5 The relations among amplitude, wavelength, and wave speed of solitary waves 93
6. The effects of turbulent eddy diffusivity and wind shear on solitary waves in the atmospheric boundary layer 97
6.1 K theory 97
6.2 Effects of turbulent eddy diffusivity 98
6.3 Effects of wind shear 118
7. A solitary wave related case study by using the model 128
7.1 Brief introduction of the case 128
7.2 The set up of the model for the case study 133
7.3 Evolution of the solitary wave in the simulation 137
7.4 Comparison between observation and simulation results 151
8. Summary and conclusion 173
REFERENCES 178
APPENDIX A 182
APPENDIX B 185

LIST OF FIGURES

Figure Page

2.1 Buoyancy fields of a large amplitude solitary wave..25

4.1 Schematic diagram of a solitary wave 35

4.2 Schematic diagram of the distribution of grid points in the domain.....................36

4.3 The time-dependent horizontal velocity on the surface 38

4.4 Horizontal velocity u, vertical velocity w fields, and streamlines y.....................40

4.5 As in Fig.4.4 except for t=40000sec 41

4.6 As in Fig.4.3 except for a 300m amplitude solitary wave...............................42

4.7 Time-dependent horizontal velocity on the surface z=0 45

4.8 As in Fig.4.7 except for 30m and 300m amplitude solitary waves 46

4.9 Sketch map of functions...48

4.10 Potential temperature profiles 50

4.11 Time series of buoyancy b fields 51

4.12 Trajectory of a air parcel...56

4.13 Trajectories of four air parcels 59

4.14 Time-dependent horizontal velocities of four air parcels...............................61

5.1 Buoyancy b, horizontal velocity u and vertical velocity w fields........................65

5.2 Magnified horizontal velocity u, vertical velocity w, buoyancy b fields................67

5.3 Schematic diagram of (a) normal and (b) reversed recirculation.........................69

5.4 Schematic diagram of reversed recirculation...71

5.5 Time series of buoyancy b and horizontal velocity u fields 74

5.6 Vertical profiles of (a) horizontal velocity u and (b) potential temperature θ 81

5.7 As in Fig.5.4 but for normal recirculation 82

5.8 Time series of ink field 85

5.9 Ink profiles..91

5.10 The relations between amplitude and speed of solitary waves 93

5.11 Potential temperature profiles 94

5.12 As in Fig.5.10 except for the relations between amplitude and wavelength..........96

6.1 Time series of buoyancy b field 100

6.2 Magnified buoyancy b, horizontal velocity u, and vertical velocity w fields...........102

6.3 Time series of buoyancy b field 104

6.4 Magnified buoyancy b, horizontal velocity u, and vertical velocity w fields..........106

6.5 Magnified buoyancy b, horizontal velocity u, and vertical velocity w fields...........109

6.6 Profiles for different eddy diffusivities 110

6.7 Magnified buoyancy b, horizontal velocity u, and vertical velocity w fields...........111

6.8 Wavelength l vs wave amplitude a 112

6.9 Wavespeed c vs wave amplitude a..113

6.10 Magnified buoyancy b, horizontal velocity u, and vertical velocity w fields 117

6.11 Buoyancy fields at t=8000sec with same shear but two wind directions 120

6.12 As in Fig.6.12 but for the vertical velocity fields...122

6.13 Magnified Richardson number Ri and buoyancy b fields at t=8000sec................123

6.14 Magnified Richardson number Ri and buoyancy b fields at t=14000sec 124

6.15 Ink field for downstream wave at t=8000sec...125

6.16 Ink and buoyancy fields for upstream wave at t=14000sec 127

7.1 Isochrones of leading solitary wave position and location of the tower................130

7.2 Vertical profiles of temperature observed by rawinsonde and tower....................131

7.3 Ambient wind profiles measured by tower and Doppler radar............................132

7.4 Vertical profiles of potential temperature and horizontal wind...........................134

7.5 A time series of magnified horizontal velocity, 'ink' and buoyancy fields.............139

7.6 The evaluation of wave and density current speeds..153
7.7 Vertical profiles of horizontal velocity relative to the ground of observation 157
7.8 Horizontal velocity of observation and simulation vs time at four levels...............159
7.9 Vertical velocity of observation and simulationvs time at two levels...................162
7.10 Temperature field of (a) observation and (b) simulation.................................164
7.11 Magnified vertical velocity field of leading solitary wave at 3000sec 166
7.12 Magnified vertical velocity field of leading solitary wave at 4500sec 166
7.13 A scenario for the evolution of thunderstorm-generated solitary waves 169
7.14 The evolution of the solitary wave and density current in the simulation.............170

LIST OF TABLES

Page

4.1 Parameters in the solitary wave simulations 34

6.1 The properties of the first waves at t=12000 sec 114

6.2 The properties of the second waves at t=12000 sec..114

Chapter

1

Introduction

When studying weather phenomena in the atmosphere, we should include ubiquitous buoyancy waves. Buoyancy waves are believed to be an important mechanism for the transportation of energy and momentum, the formation of turbulence, and the initiation of severe mesoscale weather phenomena. Hence understanding the origin, propagation, and decay of these buoyancy waves in the atmosphere is a significant task for meteorologists.

Based on their properties, internal buoyancy waves can be divided into two types: 1) linear periodic waves; 2) nonlinear waves. The first type has been extensively investigated and applied to explain many atmospheric phenomena. But it has been increasingly observed that internal buoyancy waves propagating in the atmosphere have large amplitudes and are non-periodic and highly nonlinear. If these large amplitude waves interact with a proper environments, they can initiate or enhance deep conviction

(Zhang, and Fritsch 1988; Carbone et al. 1990). They also are able to produce strong wind shear at low altitudes which can jeopardize aircraft flying near the ground (Christie and Muirhead 1983; Doviak and Christie 1989). So more and more attention in recent years is being paid to the second type of buoyancy waves. A good example of nonlinear internal buoyancy wave observed in the atmosphere is the solitary wave which has a remarkably large amplitude with a single isolated crest.

1.1 Nonlinear buoyancy waves in the atmosphere

In the late 1940's and early 1950's several authors suggested nonlinear waves may exist in the atmosphere. Abdullah (1955) first reported a large amplitude wave of single elevation (i.e. a solitary wave) which moved eastward over Kansas and produced a pressure increase of 3.4 mb on the surface during the morning hours of June 29, 1951.

The first definitive observation of atmospheric solitary waves was made by Christie et al. (1978) in Australia. Unlike the most common linear periodic horizontally propagating buoyancy waves in the troposphere, they found a large number of unusual isolated waves in over two years of continuous observation. These waves with relative large amplitude are interpreted as internal solitary waves propagating along a nocturnal inversion.

Another well-known phenomena related to nonlinear wave activity in the lower atmosphere in northeastern Australia is called "morning glory". It is a strong wind squall or a series of wind squalls, usually in company with one or more roll-cloud formations, occurring commonly near dawn during the spring months over the south margin of the Gulf of Carpentaria and the adjacent Cape York Peninsula (Clarke 1972; Neal et al. 1977a, b). Morning glory roll-clouds with considerable regularity retain their forms for several hours and extend in length for several hundreds kilometers parallel to the wave crests. These roll-cloud formations are found to be associated with a sequence of evolving solitary waves. They also found that similar large amplitude propagating wave phenomena without cloud occur frequently over much of Australia. In a recent paper, Christie (1992) reviews some new observations of morning glory waves and related nonlinear wave disturbances in Australia's Gulf of Carpentaria, and further clarifies the interpretation and propagation characteristic of morning glories.

The atmospheric phenomena associated with nonlinear large amplitude waves are not only frequently observed in Australia, but also elsewhere (Shreffler and Binkowski 1981; Goncharov and Matveyev 1982; Hasse and Smith 1984). Doviak and Ge (1984) observed an atmospheric solitary wave with a Doppler radar, a tall tower and surface network over central Oklahoma. This observation gave the first detailed and Stereoscopic X-ray view of an atmospheric solitary wave. Using more complementary sensors including two Doppler radars, satellite, rawisonde and a 500m tall instrumented tower, Mahapatra, Doviak and Zrnic (1991) observed an atmospheric undular bore which is interpreted as a sequence of solitary waves. The undular bore originated in western Oklahoma and the Texas Panhandle and propagated southeasterly to central Oklahoma through a ground-based stable layer created by the outflows of thunderstorm and strengthened by nocturnal cooling during the night and early morning. These waves then dissipated before reaching eastern Oklahoma. The leading wave of the wavetrain was the strongest among the waves and propagated at the fastest speed, 12.3m/s. This wave produced a pressure rise about 2.4 mb above the ambient value and a perturbation velocity with peak value 13m/s on the surface. The speeds of the succeeding waves decreased progressively as the amplitudes of these waves diminish progressively. The well-organized oscillatory structure of the first several waves were clearly observed by all the sensors.

With the aid of a 50 MHz wind profiler, a 10 cm wavelength Doppler radar and a balloon-borne sounding system, Ramamurthy et al. (1990) made observations of exceptionally large amplitude waves which further confirmed the importance of understanding the morphology and behavior of the atmospheric solitary wave. They reported two separate solitary waves with vertical displacements on order of 4 km which is comparable to the scale height of lower troposphere. These waves propagated over 1000 km from Missouri to Ohio with no obvious change in their structure. The waves significantly acted on the organization of a band of precipitation and other weather phenomena.

1.2 The development of solitary wave theory

The beginning of theoretical studies of solitary waves dates from the discovery by Korteweg and de Vries in 1895 of a solvable nonlinear equation which has a solitary wave solution. This nonlinear equation

$$\frac{\partial f}{\partial t}+c_0\frac{\partial f}{\partial x}+\alpha f\frac{\partial f}{\partial x}+\beta\frac{\partial^3 f}{\partial x^3}=0 \tag{1.1}$$

is called KdV equation for shallow water. Where f is the profile (e.g. vertical displacement) of the wave, and c_0 is the linear phase speed of an extremely long wave having infinitesimal amplitude. The coefficients of the nonlinear and dispersive terms, α and β, are determined by the nature of wave propagation medium. A solitary wave solution of the KdV equation is

$$f(x) = a * \sec h^2[(x - ct)/\gamma] \tag{1.2}$$

where a is the amplitude of solitary wave, c is the phase speed of solitary wave and γ is the wavelength determined both by the amplitude *a* and the depth of medium *h*. The solution is strictly correct only if a/h<<1.

Zabusky and Kruskal (1965) raised the curtain on the modern development of KdV theory. Using a computer to solve a particular version of the KdV equation to study the interaction of two solitary waves, they discovered the particle-like behavior of solitary waves. They coined the term "soliton" for a solitary wave which retains its identity even if it collides with other waves. Since then the solitary wave theory has widely appeared in many fields like meteorology, fluid dynamics, and electronic engineering.

Benjamin (1967) and Davis and Acrivos (1967) independently found a whole new class of solitary waves for deep water. Later Ono (1975) developed the theory for this case and derived an evolution equation which has been named the Benjamin-Davis-Ono (BDO) equation.

$$\frac{\partial f}{\partial t} + c_o \frac{\partial f}{\partial x} + \alpha f \frac{\partial f}{\partial x} + \beta \frac{\partial^2}{\partial x^2} H(f) = 0 \tag{1.3}$$

where H(f) denotes the Hilbert transformation of f, and α and β reflect the structure of waveguide (For details see Chapter 3).

The basic properties of the KdV and BDO equations have been widely studied since the discovery of the solitary wave solution. Both KdV and BDO equations have not only one solitary wave solution, but also multiple-solitary wave solutions which have been proved by Hirota (1971), Matsuno (1979) and Chen et al.(1979). Miura et al. (1968) and Nakamura (1979) have separately showed the KdV and BDO equations are completely integrative with infinitely many conservation laws and indicated both solitary wave solutions of these two equations have the soliton nature.

The original KdV and BDO equations only provide a simplified model for the internal atmospheric solitary wave propagating with finite amplitude on a horizontally homogeneous inversion layer (i.e. the waveguide). Considering the stratified fluid with wind shear, and with a slow temporal and spatial variation which is common in the atmosphere, Grimshaw (1981a) and Maslowe and Redekopp (1979,1980) generalized the equations which caused the coefficients α, β be functions of time and space. The turbulence dissipation, and radiation damping due to waves propagating away from the waveguide have been also considered by Grimshaw (1980, 1981a, b). These two factors are included into two extra terms, one for dissipation and the other for radiation. The possibility of the existence of a critical layer where the phase speed of the wave is equal to the ambient flow speed have been examined by Maslowe and Redekopp (1980). The critical layer can prevent energy radiation through the upper non-neutral stable layer.

Generally speaking, the KdV equation is applicable to shallow fluids. Nevertheless, the solution of the KdV equation is a good first-order approximation for large scale atmospheric solitary waves with horizontal wavelengths comparable to the height of troposphere (Christie et al. 1978). On the other hand, the BDO equation is suitable for waves in deep fluids. For example, surface-based stable layer of depth h much smaller than the depth of a deep neutral or weakly stable layer satisfies the deep fluid condition. Thus, long buoyancy waves with finite amplitude propagating in a shallow stable layer, overlain by deep neutral air, are governed by BDO equation.

When the internal solitary wave has a very large amplitude (i.e. $a/h \geq 1$) and there is recirculation within it, the weakly-nonlinear solitary wave theory described above is no longer applicable. The fully-nonlinear wave theory is required, but the theoretical studies on this field are relatively limited. Davis and Acrivos (1967) numerically and experimentally investigated the internal solitary wave propagating in a fluid of infinite depth and found a region of closed streamlines near the center of the solitary wave when the dimensionless amplitude (a/h) is greater than 1.2. Tung et al. (1982) extended the weakly nonlinear theory of long internal buoyancy wave to the fully nonlinear case in which the restriction of small amplitude and long wavelength is removed. They showed theoretically and numerically the existence of a large amplitude solitary wave with permanent form, and found when the amplitude of wave increases to a certain value the phase speed ceases to be linearly proportional to the amplitude. The closed streamline region, called the recirculation region, also appeared within the large amplitude wave in the results of Tung et al. (1982). The other result which Tung et al. (1982) emphasized is that " slight changes in the ambient density stratification can produce quite different solutions at large amplitude". It reminds us that the accuracy of measured temperature profiles is actually important for studying atmospheric internal solitary waves of large amplitude.

Pullin and Grimshaw (1988) has given an answer about the limitation of the amplitude of solitary wave. The amplitude of internal solitary wave is unbounded and the profiles of different amplitude waves have similar shapes and differ only by a scale factor as the density difference vanishes.

Almost all these developments in studies of KdV and BDO equations are used to extend investigation to all sorts of observations of nonlinear buoyancy waves in the atmosphere. Actually the KdV and BDO equations provide only the basic tools for studying the weakly nonlinear buoyancy wave phenomena, thus other methods like laboratory and numerical experiments are needed.

It is worth pointing out that the derivations of KdV and BDO equations, and the solution of fully-nonlinear internal wave theory developed by Tung et al. (1982), are all based on the assumption that the variables such as density and potential temperature, are constant on the same streamline and the value of a variable is determined from the upstream unperturbed flow where the value is known. When the closed streamlines appear in the flow, this assumption is violated and the value on the closed streamlines can not be obtained from the upstream flow. So present theories leave a blank area in the region of closed streamlines. However the circulating fluid within the large amplitude internal solitary wave plays an important role in the propagation of the wave and in trapping and transporting fluid.

1.3 Laboratory experiments

The laboratory experiment is an important approach in the study of buoyancy waves. Most experiments are carried out in a water tank which gives a direct view of the behavior of buoyancy waves under different circumstances. Maxworthy (1980) showed that an evolving sequence of highly nonlinear internal solitary waves, ordered by their amplitudes, can be created when a region of mixed fluid, with an excess of potential energy over the ambient, collapses into a stratified fluid. The inner-circulation inside the solitary waves, and the trapped mixed fluid which initiated the waves, are found within the leading solitary wave. He also found that the trapped fluid slowly leaks rearward as the wave amplitude decreases. The experiment of interaction of two solitary waves proved the soliton property of the internal solitary wave. He concluded the solitary wave can be easily generated under many circumstances if a waveguide is present.

The experimental results of the formation of an internal undular bore by a moving obstacle on the bottom or top boundary of a uniform fluid, or a static obstacle in a flowing fluid, or movement of a gravity current through a two-layer fluid, have been reported by several authors (Baines 1984; Wood and Simpson 1984; Rottman and Simpson 1989). They showed the relation between the strength and speed of the bore and the shape of obstacle or the speed and the depth of gravity current.

The temporal and spatial variation of the waveguide can affect the propagation of solitary waves, and even cause the breaking of waves like ocean waves crashing onto a sloping sea shore. Kao et al. (1985) provided a complete scenario of the breaking of an internal solitary wave of depression in a fluid with hyperbolic tangent density profile.

The wave breaking occurred when the wave encountered a sloping bottom which changes the depth of fluid in the direction of wave travel. Through quantitative measurements, he found " the onset of wave-breaking was governed by shear instability".

1.4 Numerical Modeling

The rapid development of high-speed computers and computational fluid dynamics has had a great impact on the way of studying wave motions in the atmosphere. In recent years, instead of solving the KdV and BDO equations analytically or numerically, the primitive equation model is adopted to simulate the atmospheric phenomena of buoyancy waves. The numerical model is able to solve the analytically intractable problem, and at very little cost compared to laboratory experiments. Most observations of nonlinear buoyancy waves in the atmosphere provide a complicated background fields of temperature and wind under different initial and boundary conditions, which is difficult, and sometimes impossible, to handle using an analytical method or laboratory experiments; but a numerical model can simulate the evolution of buoyancy waves under these conditions.

By using a two-dimensional numerical model, Crook and Miller (1985) and Hasse and Smith (1989) found if a density current moved into a shallow stable layer, an undular bore was generated and propagated ahead of the density current. Hasse and Smith have made a further study and used the ratio of the phase speed of an infinitesimal amplitude long wave to the speed of the equivalent gravity current in absence of the stable layer to characterize the evolution of the density current and the generation of the undular bore. Hasse (1991) also reported that large amplitude waves gradually decay due to energy radiation into an upper weakly stable layer. The effects of a critical layer on properties of an internal solitary wave have been studied by Skyllingstad (1991). The numerical model results indicates that wave absorption at the critical level increases as the ambient stability increases; whereas as the ambient stability becomes weak, the absorption reduces, and then the reflection of the critical level increases, even wave instability might happen if the Richardson number of the ambient flow is smaller than 1/4.

1.5 Our Research Objectives

Our key objective is to develop a numerical model to study the properties of large amplitude solitary waves in the atmosphere and to compare these numerical results with an observation of a family of evolving solitary waves. Although the basic structure and behavior of atmospheric internal buoyancy waves are reasonably understood using weakly nonlinear wave theory, laboratory and numerical simulations, questions remain about the characteristics of the wave under complicated environments. I intend to focus primarily on the following topics:

1) In an ideal waveguide, like a horizontal homogeneous stable layer overlaid by a deep neutral layer without any friction, solitary waves can propagate with their identity for all time. The atmosphere is considered as an ideal waveguide when we simplify the problem, but strictly speaking, the realistic properties of atmosphere, such as turbulence viscosity, surface friction, no neutral layer above the waveguide (to prevent the leakage of wave energy to the upper atmosphere), and degradation of waveguide caused by solar

radiation or other reasons, are not negligible most of time. These factors lead to the decay of nonlinear internal buoyancy waves via the dissipation and radiation of the wave energy. The vertical wind shear in the ambient is another factor which influences the properties of the wave. Due to the limitations of the theory, laboratory, and numerical experiments, the effects of these factors on the nonlinear buoyancy waves, especially the waves with large amplitude, are not completely understood. I intend to examine the influences of these factors on the properties of large amplitude waves.

2) Nonlinear buoyancy waves with large amplitude and accompanying phenomena like recirculation within the wave and trapped ambient fluid, are found in the theoretical studies, laboratory experiments, and observations. Previous studies have given some preliminary results, but the structures of temperature and velocity inside the recirculation region, and the mechanism of trapping and leaking are still unknown.

3) A multisensor observation reported by Doviak and Ge (1984) provided a detailed view of a solitary wave. The previous analysis (Doviak et al., 1991) indicates this observation presented a quite complete picture of a solitary wave phenomenon. Thus it gives us an unique opportunity to probe deeply into the essence of nonlinear atmospheric buoyancy waves by comparing the observations with our numerical simulations.

Toward our objectives, a two-dimensional, vorticity-stream function, incompressible model has been constructed and operated. The model equations and operation procedure are presented in detail in Chapter 2. The numerical scheme, initial and boundary conditions, and stretched coordinate which are adopted in the model are described in the rest of Chapter 2. For testing the model performance, the results of weakly nonlinear wave theory is used and thus it is briefly reviewed in Chapter 3. Using the model, the propagation and collisions of solitary waves of small amplitude are simulated and the numerical results are compared with the weakly nonlinear wave theory in Chapter 4. Because the simulation of the solitary wave in the atmosphere and understanding of their behavior are our ultimate objectives, the preliminary results of generation and propagation of solitary waves are examined with the aid of an air parcel tracer technique described in Chapter 4. In Chapter 5 the properties and structures of large amplitude solitary waves are closely investigated. Chapter 6 presents the study of the effects of turbulent eddy diffusivity and wind shear on solitary waves in the lower atmospheric boundary layer. The results of numerical simulation of a solitary wave related case are provided in Chapter 7. The main achievements in the thesis are summarized in Chapter 8.

Chapter

2

Numerical Model

2.1 Model equations and operation procedure

Our major goal of developing the numerical model is to study the propagation and evolution of large amplitude waves in the atmosphere and to compare results with observations. Although wave phenomena in the real atmosphere is always three-dimensional, in some cases it can be treated as a two-dimensional phenomena to simplify the problem. Meanwhile, some two-dimensional properties of large amplitude waves, which we intend to study in this dissertation, are still unknown. Under the guide of these desires, a two-dimensional (2D) incompressible vorticity-stream function model is developed because the vorticity-stream function method is one of the most popular methods for solving the 2D incompressible Navier-Stokes equations. The model equations can be derived from the following 2D Navier-Stokes momentum equations in a Cartesian coordinate system,

$$\frac{\partial u}{\partial t}+u\frac{\partial u}{\partial x}+w\frac{\partial u}{\partial z}=-\Theta\frac{\partial \pi}{\partial x}+\upsilon_h\frac{\partial^2 u}{\partial x^2}+\upsilon_v\frac{\partial^2 u}{\partial z^2} \qquad (2.1)$$

$$\frac{\partial w}{\partial t}+u\frac{\partial w}{\partial x}+w\frac{\partial w}{\partial z}=-\Theta\frac{\partial \pi}{\partial z}-g+\upsilon_h\frac{\partial^2 w}{\partial x^2}+\upsilon_v\frac{\partial^2 w}{\partial z^2} \qquad (2.2)$$

and the adiabatic equation

$$\frac{\partial \Theta}{\partial t}+u\frac{\partial \Theta}{\partial x}+w\frac{\partial \Theta}{\partial z}=\kappa_h\frac{\partial^2 \Theta}{\partial x^2}+\kappa_v\frac{\partial^2 \Theta}{\partial z^2} \qquad (2.3)$$

where u, w, Θ are horizontal , vertical velocities and potential temperature, g is the gravitational acceleration, $\Pi \equiv C_p(\frac{p}{p_0})^{\frac{R_d}{C_p}}$ in term of Exner function, where C_p is the specific heat of dry air at constant pressure, p_o is a reference pressure at 1000 mb and R_d is the gas constant for dry air. υ and κ are kinematic and thermal viscosity, subscript h and v represent horizontal and vertical.

We assume there exists a basic state in which potential temperature Θ_0 is constant and pressure field is in hydrostatic balance (i.e., $\Theta_0\frac{\partial \Pi_0(z)}{\partial z}=-g$) where $\Pi_0(z)$ is only a function of height z. Subtracting this state from Eq.(2.1) and (2.2), and writing $\Theta=\Theta_0+\theta(x,z,t)$ and $\Pi=\Pi_0(z)+\pi(x,z,t)$, we get

$$\frac{\partial u}{\partial t}+u\frac{\partial u}{\partial x}+w\frac{\partial u}{\partial z}=-(\Theta_0+\theta)\frac{\partial \pi}{\partial x}+\upsilon_h\frac{\partial^2 u}{\partial x^2}+\upsilon_v\frac{\partial^2 u}{\partial z^2} \qquad (2.4)$$

$$\frac{\partial w}{\partial t}+u\frac{\partial w}{\partial x}+w\frac{\partial w}{\partial z}=-\theta\frac{\partial \Pi_0}{\partial z}-(\Theta_0+\theta)\frac{\partial \pi}{\partial z}+\upsilon_h\frac{\partial^2 w}{\partial x^2}+\upsilon_v\frac{\partial^2 w}{\partial z^2} \qquad (2.5)$$

We also assume $\theta << \Theta_0$, so term $\Theta_0 + \theta$ can be replaced by Θ_0. Now the momentum equations are simplified as

$$\frac{\partial u}{\partial t} + u\frac{\partial u}{\partial x} + w\frac{\partial u}{\partial z} = -\Theta_0\frac{\partial \pi}{\partial x} + \upsilon_h\frac{\partial^2 u}{\partial x^2} + \upsilon_v\frac{\partial^2 u}{\partial z^2} \tag{2.6}$$

$$\frac{\partial w}{\partial t} + u\frac{\partial w}{\partial x} + w\frac{\partial w}{\partial z} = -\Theta_0\frac{\partial \pi}{\partial z} + g\frac{\theta}{\Theta_0} + \upsilon_h\frac{\partial^2 w}{\partial x^2} + \upsilon_v\frac{\partial^2 w}{\partial z^2} \tag{2.7}$$

The adiabatic equation becomes

$$\frac{\partial \theta}{\partial t} + u\frac{\partial \theta}{\partial x} + w\frac{\partial \theta}{\partial z} = \kappa_h\frac{\partial^2 \theta}{\partial x^2} + \kappa_v\frac{\partial^2 \theta}{\partial z^2} \tag{2.8}$$

We differentiate Eq.(2.7) with respect to x and Eq.(2.6) with respect to z and subtract one from the other; the vorticity equation is thus obtained.

$$\frac{\partial \zeta}{\partial t} + u\frac{\partial \zeta}{\partial x} + w\frac{\partial \zeta}{\partial z} + \zeta\left(\frac{\partial u}{\partial x} + \frac{\partial w}{\partial z}\right) = \frac{g}{\Theta_0}\frac{\partial \theta}{\partial x} + \nu_h\frac{\partial^2 \zeta}{\partial x^2} + \nu_v\frac{\partial^2 \zeta}{\partial z^2} \tag{2.9}$$

where $\zeta = \frac{\partial w}{\partial x} - \frac{\partial u}{\partial z}$.

For a two dimensional incompressible flow the continuity equation in Cartesian coordinates is

$$\frac{\partial u}{\partial x} + \frac{\partial w}{\partial z} = 0 \tag{2.10}$$

and stream function can be defined by

$$u=-\frac{\partial\psi}{\partial z},\qquad w=\frac{\partial\psi}{\partial x}\tag{2.11}$$

By substituting Eq.(2.10) and (2.11) into Eq.(2.8), (2.9), and using the definition vorticity, the 2D incompressible vorticity-stream function model equations can be derived.

Vorticity equation

$$\frac{\partial\zeta}{\partial t}-\frac{\partial\psi}{\partial z}\frac{\partial\zeta}{\partial x}+\frac{\partial\psi}{\partial x}\frac{\partial\zeta}{\partial z}=\frac{\partial b}{\partial x}+\upsilon_h\frac{\partial^2\zeta}{\partial x^2}+\upsilon_v\frac{\partial^2\zeta}{\partial z^2}\tag{2.12}$$

Poisson equation

$$\frac{\partial^2\psi}{\partial x^2}+\frac{\partial^2\psi}{\partial z^2}=\zeta\tag{2.13}$$

Adiabatic equation

$$\frac{\partial b}{\partial t}-\frac{\partial\psi}{\partial z}\frac{\partial b}{\partial x}+\frac{\partial\psi}{\partial x}\frac{\partial b}{\partial z}=\kappa_h\frac{\partial^2 b}{\partial x^2}+\kappa_v\frac{\partial^2 b}{\partial z^2}\tag{2.14}$$

where $b=g\dfrac{\theta}{\Theta_0}$.

These equations can be solved numerically by using a time-marching procedure described by the following steps:

1) Give initial conditions for ζ, ψ and b at time t=0.

2) Solve the vorticity and adiabatic equations for ζ and b at each interior grid point at time $t = t + \Delta t$ by using time -marching method.

3) Solve the Poisson equation for new ψ at all points by using new ζ at interior grid points.

4) Find the velocity components from $u = -\frac{\partial \psi}{\partial z}$ and $w = \frac{\partial \psi}{\partial x}$.

5) Determine the values of ζ and b on the boundaries by using the values of ζ, ψ and b inside the boundary, and boundary conditions.

6) Return to step 2 for next time step.

After completing above steps at the desired time, the velocity components u, w and buoyancy b are determined in the whole computational domain.

2.2 Boundary conditions

In the model, the lateral boundaries are radiation boundaries in order to allow internally generated waves to pass out of the model domain freely. To construct the open boundaries, the following equations are used instead of the model equations at right side boundary,

$$\frac{\partial f}{\partial t} = -(u + c)\frac{\partial f}{\partial x}, \tag{2.15}$$

and at left side boundary,

$$\frac{\partial f}{\partial t} = -(u - c)\frac{\partial f}{\partial x}, \tag{2.16}$$

where f represents variables ζ and b, and c is an estimate of the phase speed of the dominant internal waves propagating in the model domain.

Because this simple open boundary condition can not allow internal waves of all wavelength with different phase speeds to propagate out of the domain without reflections, the "sponge" boundary conditions are applied at and near the lateral and top boundaries to minimize the false reflections of waves at the boundaries. The following equation is used

$$\frac{\partial f}{\partial t} = -\gamma(x,z) * f \tag{2.17}$$

The damping rate $\gamma(x,z)$ is a spatial function. In our simulations, it is a linear function of x with a maximum on the boundaries and gradually decreasing to the zero within a certain distance (about 10% of the domain width and height) in the model domain

In some numerical experiments, an inflow which originates from the right side boundary is imposed to simulate the ambient wind field or to keep the waves of interest in the domain.

The bottom and top boundaries in the model are rigid (i.e. w=0 at z=0 and z=H). Consequently, from Eq.(2.11) the boundary conditions for the stream function ψ can be found as constants. In this case, ψ is set equal to zero on the bottom; the value on the top is derived from the integral of Eq.(2.11)

$$\psi_{top} = \int_0^H \overline{u}_r(z)dz \tag{2.18}$$

where $\overline{u}_r(z)$ is the wind profile of inflow at right side boundary.

For vorticity ζ, the reflection scheme is applied on the top and bottom boundaries for the inviscid rigid boundary condition. In implementing reflection, three rows of fictitious grid points are defined above the top and below the bottom of the domain respectively. Values of ζ at the fictitious points are assigned using the reflection process. The vorticity ζ is odd with respect to the top and bottom boundaries. This means that the values at fictitious points is set equal to the respective values at their mirror image points in the domain.

There is no heat flux at the top and bottom boundaries which implies that

$$\frac{\partial b}{\partial z} = 0 \qquad \text{at } z=0 \text{ and } z=H. \tag{2.19}$$

Hence the values of buoyancy b at the fictitious points are set equal to the values at the bottom and top boundaries respectively.

2.3. Finite difference scheme for integration

For appropriate and satisfactory accuracy, the third-order Adams-Bashforth scheme is applied for time integration in our numerical model.

$$f(t+\Delta t) \approx f(t)+\Delta t\,[23F(t)-16F(t-\Delta t)+5F(t-2\Delta t)]/12 \tag{2.20}$$

At the initial time, $F(t-\Delta t)$ and $F(t-2\Delta t)$ are not available, so the Euler scheme is used:

$$f(t+\Delta t) \approx f(t)+\Delta t\,F(t) \tag{2.21}$$

At the second time-step , the second-order Adams-Bashforth scheme

$$f(t+\Delta t) \approx f(t)+\Delta t\,[3F(t)-F(t-\Delta t)]/2 \tag{2.22}$$

is used.

The truncation error is the difference between the partial derivative and its finite-difference representation. Durran (1991) noticed that the relative importance of temporal and spatial differencing error in the numerical simulation of a propagating sinusoidal wave is largely determined by the absolute value of the Courant number,

$$\mu = \frac{c\Delta t}{\Delta x}$$

where c is the wave speed. In our numerical experiments, the speeds of gravity wave are around 10m/s, the Δt is 1 sec (even smaller in some experiments) and Δx is 200m. So the Courant number is 0.05, which is much smaller than 1. It makes the truncation errors significantly small to satisfy the accuracy we need.

2.4. Finite difference schemes for spatial derivative

The fifth-order, upstream advection schemes are applied to calculate the advective term in the model equations.

$$\frac{\partial f}{\partial x} \approx \frac{1}{60\Delta x}[-3f(x+2\Delta x)+30f(x+\Delta x)+20f(x)-60f(x-\Delta x)+15f(x-2\Delta x)-2f(x-3\Delta x)] \tag{2.23}$$

and

$$\frac{\partial f}{\partial x} \approx \frac{1}{60\Delta x}[2f(x+3\Delta x)-15f(x+2\Delta x)+60f(x+\Delta x)-20f(x)-30f(x-\Delta x)+3f(x-2\Delta x)] \tag{2.24}$$

The first equation is preferable for $u>0$ and the second for $u<0$ when the advective term $u\frac{\partial f}{\partial x}$ is calculated in the model. Near the lateral boundaries it is impossible to use the fifth-order scheme, so third-order and second-order schemes are applied. The numerical schemes are as follow:

The third-order scheme

$$\frac{\partial f}{\partial x} \approx \frac{1}{6\Delta x}[f(x-2\Delta x)-6f(x-\Delta x)+3f(x)+2f(x+\Delta x)] \qquad \text{for } u>0 \tag{2.25}$$

$$\frac{\partial f}{\partial x} \approx \frac{1}{6\Delta x}[-2f(x-\Delta x)-3f(x)+6f(x+\Delta x)-f(x+2\Delta x)] \qquad \text{for } u<0 \tag{2.26}$$

The second-order scheme

$$\frac{\partial f}{\partial x} \approx \frac{1}{2\Delta x}[f(x+\Delta x) - f(x-\Delta x)] \tag{2.27}$$

The numerical schemes used in z direction in the model is similar to the schemes in x direction except the function $\frac{\partial \eta}{\partial z}$ in the schemes are in a stretched vertical coordinate (see next section for detail).

The truncation errors for the third-order schemes (Eq.(2.25) and (2.26)) and the fifth-order schemes (Eq.(2.23) and (2.24)) can be calculated by expressing each term on the right-hand side of these equations as a Taylor series. The lowest-order terms of the truncation error are $\pm\frac{1}{12}(\Delta x)^3\frac{\partial^4 f}{\partial x^4}$ and $\pm\frac{1}{720}(\Delta x)^5\frac{\partial^6 f}{\partial x^6}$ respectively. The order of lowest truncated spatial term in fifth-order scheme is two larger than the order of third-order scheme. Because Δx is a finite quantity, the fifth-order scheme has smaller truncation error than the third-order. In particular, the fifth-order scheme produce less damping on the solution than third-order scheme. Hence high-order spatial differences ensure a higher degree of accuracy.

It is appropriate at this point to comment on our use of odd-order advective scheme in the model. The use of odd-order schemes avoids the need to introduce artificial viscosity terms in the model to keep it numerically stable, because odd-order schemes have more damping on the solution than even-order scheme. In the odd-order scheme, the lowest-order term of the truncation error contains even-order partial derivatives $\frac{\partial^{2n}}{\partial x^{2n}}$ which plays a role similar to the viscosity terms (Anderson 1984).

Generally, this is called implicit viscosity as opposed to explicit viscosity, like terms $\upsilon_h \frac{\partial^2 \zeta}{\partial x^2}$, and $\upsilon_v \frac{\partial^2 \zeta}{\partial z^2}$ in Eq.(2.12), which are purposely added to a model equation.

In order to find the differences of 3rd and 5th order advection schemes in the buoyancy wave modeling, two numerical simulations of solitary wave propagation with the same conditions except for the advection schemes in the model are conducted. A large amplitude solitary wave is given at initial time. A low level stable layer with constant Brunt- Väisälä frequency N covered by a deep neutral layer provides a wave guide for the propagation of the wave.

For the sake of comparison, the solitary waves displayed in buoyancy fields at the initial time, and after 25000 seconds with different numerical schemes are shown in the same figure (Fig.2.1). Comparing these three pictures, we found that the shapes (amplitude and wavelength) of the waves almost unchanged after 25000 seconds of propagation, if either the 3rd or 5th order schemes are applied. Theoretically, solitary wave should propagate with constant speed and same shape in the background condition employed in our model. The model results indicate that the model handles it quite well. More simulations for the test of the model will be shown and discussed in the succeeding sections.

By comparing the locations of these two waves at t=25000 sec, we also find that the solitary wave (3rd order wave) obtained using a 3rd order advection scheme lags slightly behind the wave (5th order wave) derived using a 5th order advection scheme (see Fig.2.1). It means the speed of 5th order wave is slightly faster than the speed of 3rd

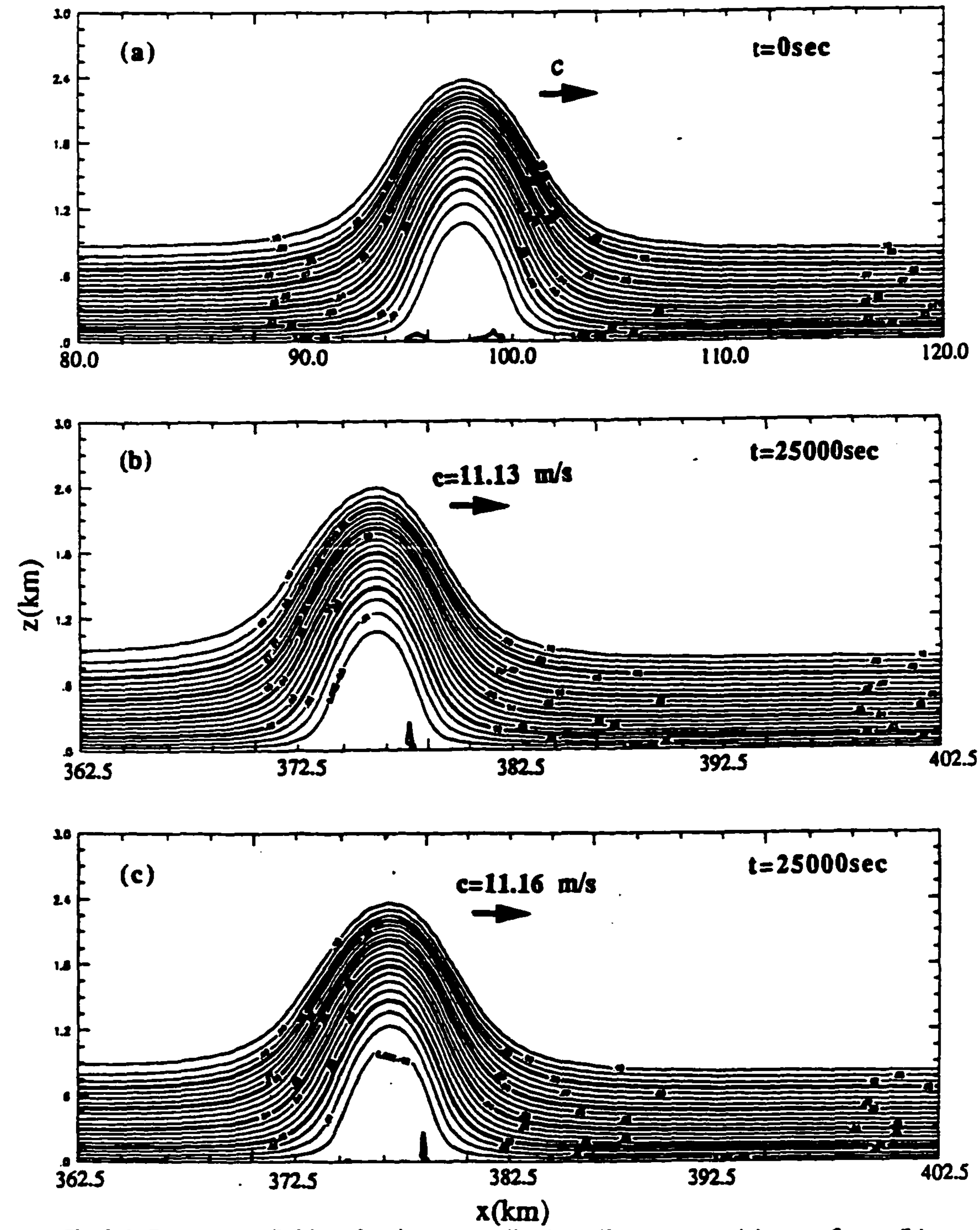

Fig.2.1 Buoyancy fields of a large amplitude solitary wave (a) at t=0sec; (b) at t=25000sec by using 3rd order advection scheme; (c) at t=25000sec by using 5th order advection scheme. The wave propagates rightward.

order wave. Through simple calculations, we obtained the speed of 3rd order and 5th order waves are 11.13m/s and 11.16m/s respectively. The difference is 0.03m/s. The results are consistent with the previous theoretical discussions about truncation errors of different schemes. Because 5th order scheme provides less dissipation in the truncation term than 3rd order scheme, the speed of 5th order wave should be faster and more accurate than the speed of 3rd order wave. On the other hand, the unlikeness of these two schemes is not obviously displayed in the shapes of the waves. Perhaps longer period simulation will help to tell the difference.

Theoretically, 3rd order advection scheme costs less computer time than 5th order scheme. We found the difference of computer time in the above simulations is quite small. So a 5th order advection scheme is applied in the our model for more accuracy.

2.5. Stretched vertical coordinate

Because the region, in which we are interested, is within 10-20% of height of the domain, the stretched grid is very effective to be used in the model. The transformation relation between the constant grid and the stretched grid in this model is given by

$$z = [\frac{\tanh(b\eta - b)}{\tanh(b)} + 1] * H, \qquad 0 \le \eta \le 1 \qquad (2.28)$$

where b is a stretching scale factor and η is the new vertical coordinate. The value of η is between 0 and 1. With this transformation, the chain rule is used to replaced the vertical derivatives.

$$\frac{\partial}{\partial z}=\frac{\partial\eta}{\partial z}\frac{\partial}{\partial\eta} \tag{2.29}$$

$$\frac{\partial^2}{\partial z^2}=(\frac{\partial\eta}{\partial z})^2\frac{\partial^2}{\partial\eta^2}+\frac{\partial^2\eta}{\partial z^2}\frac{\partial}{\partial\eta} \tag{2.30}$$

In the stretched system, the vertical grid intervals are no longer constant and increase with height. Comparing with the constant grid coordinate, the higher spatial resolution is achieved in the region of interest with same total grid points.

2.6. Initial condition

The initial data of stream function ψ, vorticity ζ and buoyancy b are required as the input of the model. The initial background fields are horizontally uniform in the whole domain, and vertical wind profile $\bar{u}(z)$ and potential temperature profile $\theta(z)$ is z dependent. The basic state stream function $\bar{\psi}$ and vorticity $\bar{\zeta}$ can be derived by

$$\bar{\psi}(z)=-\int_0^z\bar{u}(s)ds \tag{2.31}$$

$$\bar{\zeta}=-\frac{\partial\bar{u}(z)}{\partial z} \tag{2.32}$$

The specified initial fields of stream function, vorticity and buoyancy vary with the different numerical experiments. These will be detailed in the following sections.

Chapter

3

The Results of Weakly Nonlinear Solitary Wave Theory

Christie (1989) gives a good review of the theory of first-order weakly-nonlinear waves in the lower atmosphere. Following Christie, we assume the vertical displacement of a streamline in the stable layer is the product of two separated functions.

$$\eta(x,z,t) = A(x,t)\phi(z) \tag{3.1}$$

where $\phi(z)$ is the normalized dimensionless vertical modal function and $A(x,t)$, with the dimension of displacement, is governed by the BDO equation,

$$\frac{\partial A}{\partial t} + c_o \frac{\partial A}{\partial x} + \alpha A \frac{\partial A}{\partial x} + \beta \frac{\partial^2}{\partial x^2} H(A) = 0 \tag{3.2}$$

where $H(A)$ is defined by the Hilbert transform,

$$H(A(x)) = \frac{1}{\pi}\int_{-\infty}^{+\infty}\frac{A(s)}{s-x}ds \tag{3.3}$$

Here, x is the horizontal coordinate in the direction of propagation, and z is the original height of streamline in the undisturbed flow far away from the disturbance. The linear long wave speed c_o, the coefficients of the nonlinear and dispersive terms, α and β, and vertical modal function $\phi(z)$ are determined by the characteristics of the background flow.

The time-dependent solitary wave solution of the BDO equation is given by Ono (1975) in the form

$$A(x,t) = \frac{a\lambda^2}{(x-ct)^2+\lambda^2} \tag{3.4}$$

where the phase speed of solitary wave is

$$c = c_o + \frac{\alpha a}{4} \tag{3.5}$$

and the relation between wave amplitude a and wavelength λ is

$$\lambda = \frac{4\beta}{\alpha a} \tag{3.6}$$

The vertical displacement of the solitary wave streamline in the neutral layer is given by

$$\eta(x,z,t) = \frac{a\lambda(\lambda+z-h)}{(x-ct)^2+(\lambda+z-h)^2} \tag{3.7}$$

where h is the height of the stable layer.

It is important to note the following properties of the weakly nonlinear internal solitary waves shown by the above results:

1) The solitary wave is a isolated smooth symmetric crest, not periodic.

2) In the proper waveguide without friction, solitary waves can propagate with unchanging form.

3) Solitary waves propagate at supercritical phase speeds which are larger than the long-wave speed c_0 in the same medium.

4) The speed difference $c-c_0$ between the solitary wave and the long wave is proportional to the amplitude of the solitary wave. It means the wave with larger amplitude propagates faster.

5) There is an unique relation between wavelength λ and amplitude a. It implies if the amplitude of a solitary wave is given, the wavelength is determined.

6) The amplitude of solitary wave in the neutral layer decreases with height.

For an incompressible fluid with infinite depth, the normalized vertical modal function $\varphi(z)$ satisfies the eigenvalue problem (Christie 1989):

$$\frac{\partial}{\partial z}(\rho_o(c_o - u_o)^2 \frac{\partial \varphi}{\partial z}) + \rho_o N^2 \varphi = 0 \qquad (3.8)$$

$$\varphi = 0 \qquad \text{on} \qquad z=0$$

$$\frac{\partial \varphi}{\partial z} \to 0 \qquad \text{as} \qquad z \to \infty$$

Through the transformation $\overline{\varphi} = (u_o - c_o)\varphi$, Eq.(3.8) can be rewritten as the Taylor-Goldstein equation.

$$\frac{\partial^2 \overline{\varphi}}{\partial z^2} + l^2(z)\overline{\varphi} = 0 \tag{3.9}$$

where $l^2(z) = \dfrac{N^2}{(u_o - c_o)^2} - \dfrac{\partial u_o / \partial z}{(u_o - c_o)}$ is the Scorer parameter (Scorer 1949) and u_o is the horizontal velocity of the sheared background flow.

For a homogeneous incompressible fluid, the coefficients α and β in the BDO equation are given by

$$\alpha = \frac{3\int_o^\infty \rho_o (c_o - u_o)^2 (\frac{\partial \varphi}{\partial z})^3 dz}{2\int_o^\infty \rho_o (c_o - u_o)\,(\frac{\partial \varphi}{\partial z})^2 dz} \tag{3.10}$$

and

$$\beta = \frac{\{\rho_o (c_o - u_o)\varphi^2\}_{z \to \infty}}{2\int_o^\infty \rho_o (c_o - u_o)\,(\frac{\partial \varphi}{\partial z})^2 dz} \tag{3.11}$$

Chapter

4

Numerical Simulations of Solitary Waves

4.1 Propagation of solitary waves

To test and improve the numerical model, a number of simulations were conducted to show the evolution of solitary waves under the same background field as used to derive the analytical solutions for weakly nonlinear waves. We consider a neutral layer over a stable layer with constant Brunt- Väisälä frequency N, no friction, no temperature difference at the interface between neutral and stable layer, and no ambient wind. Under this simple background field, the analytic solution can be obtained. Thus we can compare the results of the numerical simulations with the analytic solution to check our model.

In this case, in the stable layer the eigenvalue problem becomes

$$\frac{\partial^2 \varphi}{\partial z^2} + \frac{N^2}{c_o{}^2}\varphi = 0 \tag{4.1}$$

with the boundary condition on the surface

$$\varphi(0) = 0$$

and at the interface

$$\frac{\partial \varphi(h)}{\partial z} = 0$$

obtained by matching the gradient of vertical velocity (Doviak, 1988).

The solution of this eigenvalue problem in the stable layer is given by

$$\varphi(z) = (-1)^{n+1} \sin(\frac{2n-1}{2h} \pi z),\ n=1,2,3,... \tag{4.2}$$

$$c_o = \pm \frac{Nh}{(n - 1/2)\pi} \tag{4.3}$$

By using Eq.(3.9) and (3.10), the coefficients for this case in the BDO equation can be obtained as follow

$$\alpha = \frac{2c_o}{h} \tag{4.4}$$

and

$$\beta = \frac{4hc_o}{[(2n-1)\pi]^2} \tag{4.5}$$

The phase speed of solitary wave and the relation between amplitude and wavelengths of the solitary wave for this case are derived from Eq.(3.5) and (3.8):

$$c = c_0(1+\frac{a}{2h}) \tag{4.6}$$

$$\lambda = \frac{8h^2}{[(2n-1)\pi]^2}. \tag{4.7}$$

To simplify the problem, the lowest mode (n=1) is chosen to calculate the wavelength in order to set up a solitary wave with matched amplitude and wavelength by using Eq.(3.5) at the initial time in the model. Fig.4.1 shows the schematic diagram of a solitary wave.

In this section, all simulations are conducted with the same background field as described at the beginning of this section. The specific parameters are shown in Table 4.1.

Table 4.1. Parameters in the solitary wave simulations.

h	N	θ_o	θ_n	U_b	ν	κ
1km	0.0233Hz	300k	316.6K	14.83m/s	0	0

where θ_o and θ_n are the potential temperatures on the ground and at the interface between stable and neutral layers, respectively; U_b is the inflow speed; υ and κ are the kinematic and thermal viscosity.

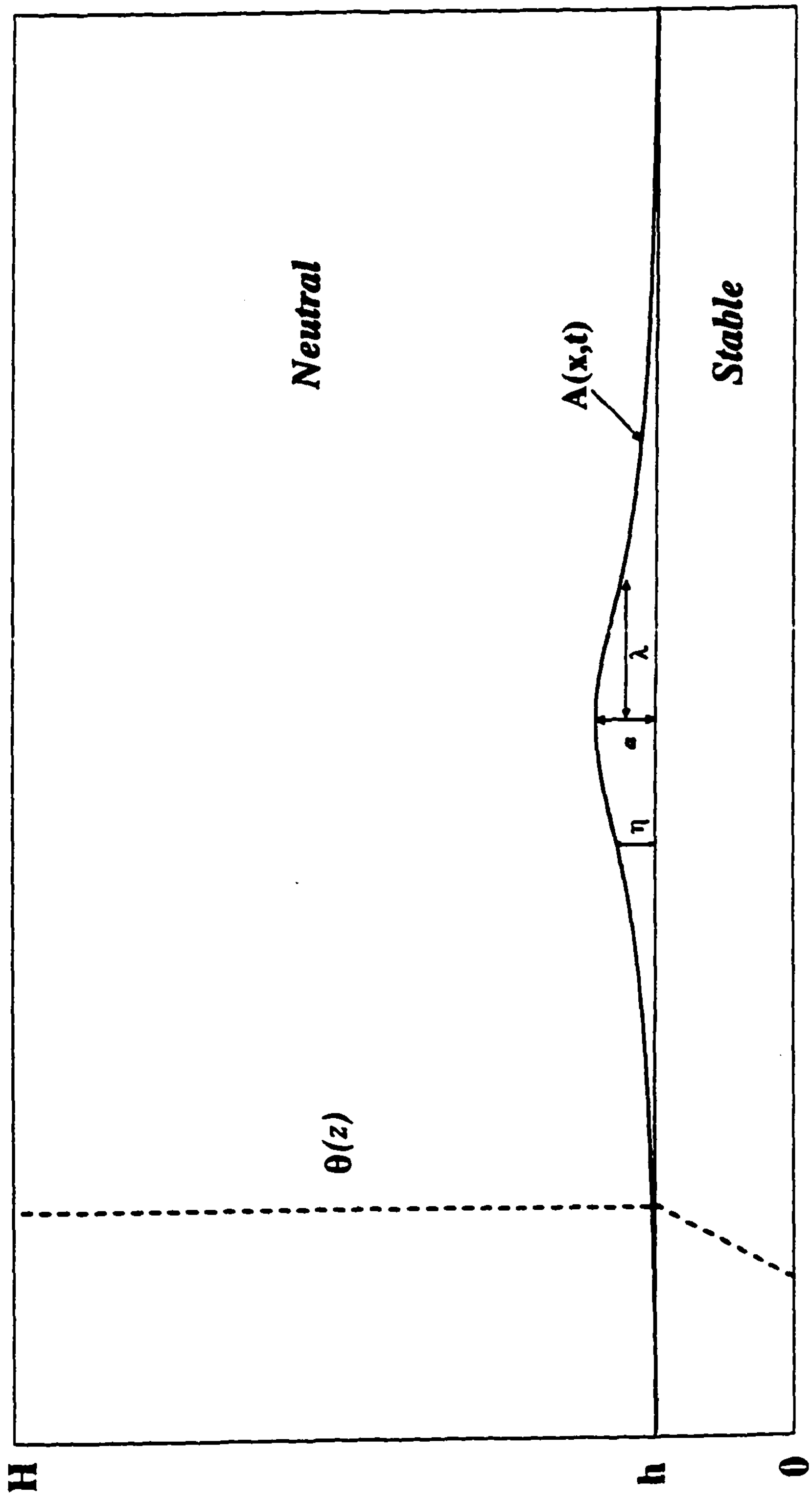

Fig.4.1 Schematic diagram of a solitary wave.

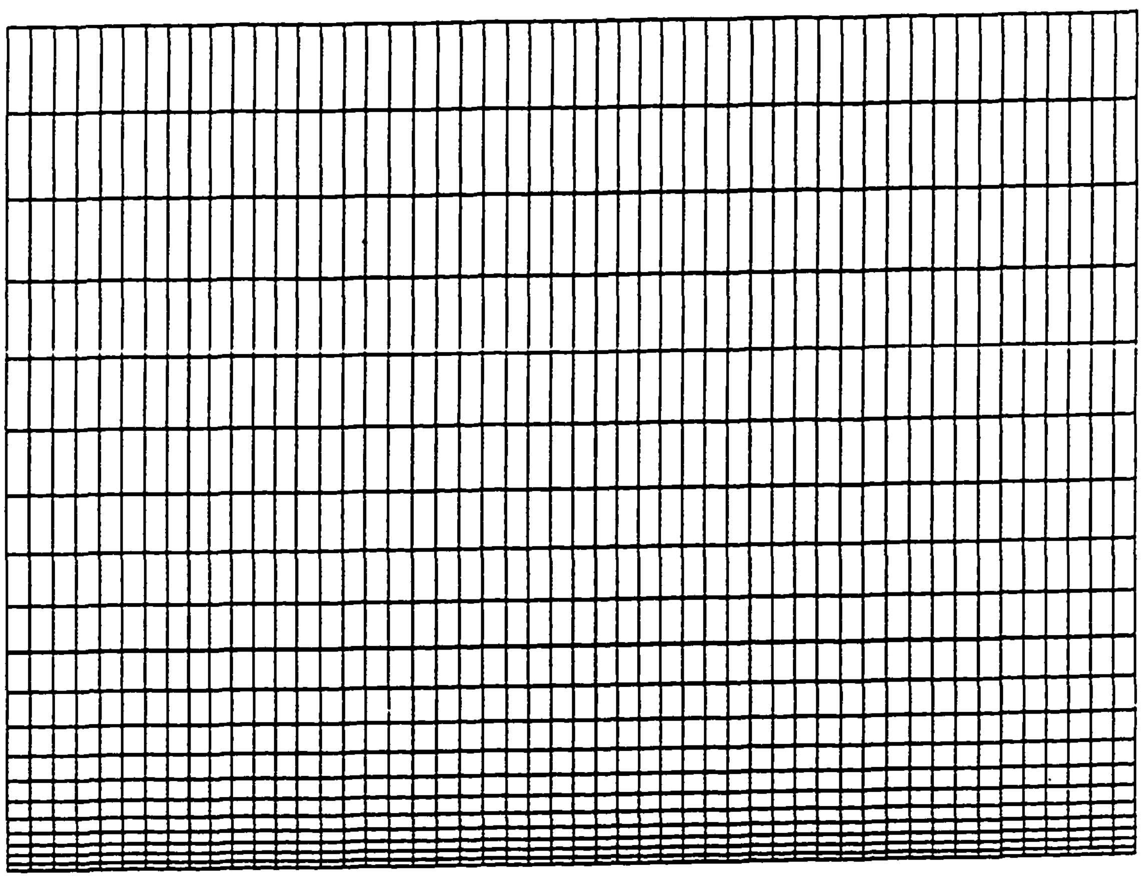

Fig.4.2 Schematic diagram of the distribution of grid points in the domain.

The model domain is 200 km long and 10 km high with 1 km horizontal and stretched vertical grid spacing which varies from 38.5m near the surface to 518.3m near the top of domain. Fig.4.2 shows schematic diagram of the distribution of grid points in the domain. The time step is 2 seconds. To keep the solitary waves in the numerical domain for a longer time, an inflow without vertical shear is imposed at the right side boundary. The speed of the inflow is set to equal the long wave speed c_0

In the model the evolution of the solitary wave is simulated to test if this model is correctly coded and able to accurately duplicate the theoretical results. We take the solitary wave solution of BDO as the initial input of our model. A small amplitude (100m) solitary wave which satisfies the weakly nonlinear condition ($a/h \ll 1$) is set up at the initial time. The wavelength of the mode 1 (i.e. n=1) wave, obtained from Eq.(4.7), is 8106 m. When these conditions are met, the solitary wave should propagate at constant speed c without change of form for all time as shown by weakly nonlinear theory.

The time-dependent horizontal velocity at z=0 for the solitary wave with amplitude a=100 m is shown in Fig.4.3 which clearly records the propagation of the solitary wave during 40,000 seconds (about 11h). We found that the initial perturbation evolved into a solitary wave and a series of very small amplitude dispersive waves during the first 4000 sec. The generation of these dispersive waves perhaps is caused by the fact the initial soliton-like perturbation derived from the weakly nonlinear theory is not exactly a soliton (i.e. a solitary wave of permanent form) for the fully nonlinear model, as well as the rigid top boundary condition of the model which is different from

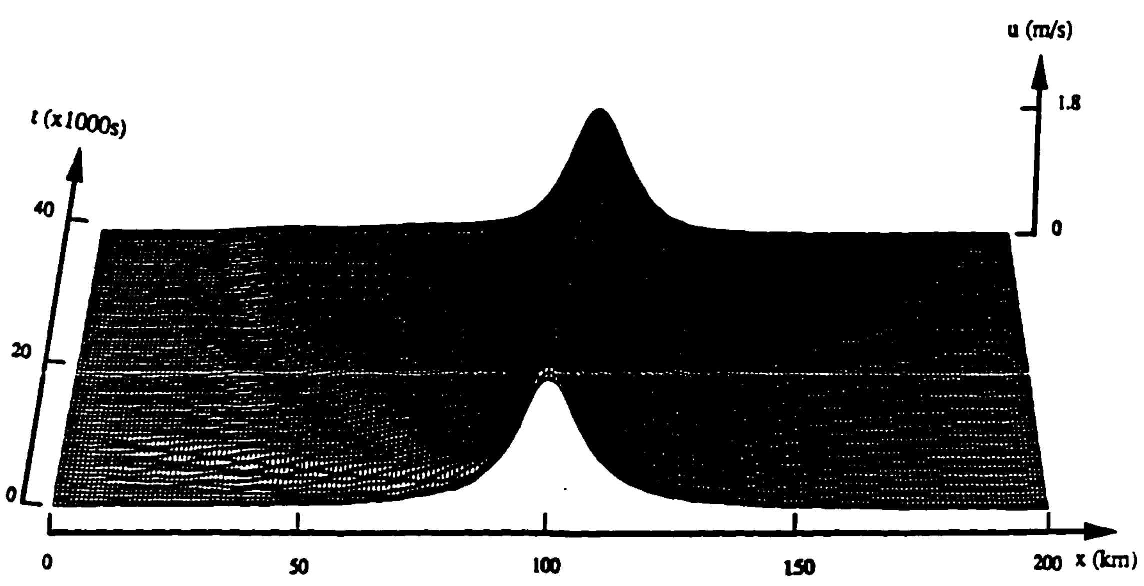

Fig.4.3 The time-dependent horizontal velocity on the surface for the solitary wave with amplitude a=100m.

the infinite expanse of homogeneous fluid of the weakly nonlinear theory. Actually the initial soliton-like perturbation adjusts itself to become a solitary wave to match the numerical model during this initial period. One should also noticed that the adjustment is quite small, to a certain extent, which implies the 9 km thick neutral layer with an 1 km thick "sponge" layer near the top is a good alternative to the infinitely deep neutral layer. After the initial adjustment, the solitary wave is formed and propagates with the constant phase speed and almost permanent shape for all the time (~11h).

To compare the model results with the weakly nonlinear theory in detail, the vertical and horizontal velocity fields, streamlines and buoyancy field in x-z plane at initial time and t=40,000 sec are shown in Figs. 4.4 and 4.5. The features of solitary wave at initial time represent the results derived from the weakly nonlinear theory. It is clear that the position of maximum horizontal velocity is on the surface and the maximum and minimum vertical velocities are near the interface between the stable and neutral layers. The pattern of positive and negative vertical velocity are symmetric with respect to the center axis of the solitary wave. It is worth noticing that we found, for large amplitude solitary waves, the location of maximum horizontal velocity is no longer on the surface; this finding will be discussed in succeeded Chapter 5.

To quantitatively compare the results, the phase speed of solitary waves in the model is estimated using the zero vertical velocity contour in the middle of the solitary wave to locate the position of the wave at different times. We obtained a 15.1m/s phase speed for the solitary wave with amplitude a=100 m, which is slightly smaller than the phase speed 15.6m/s calculated from Eq.(4.6) with c_0=14.85m/s obtained from Eq.(4.3).

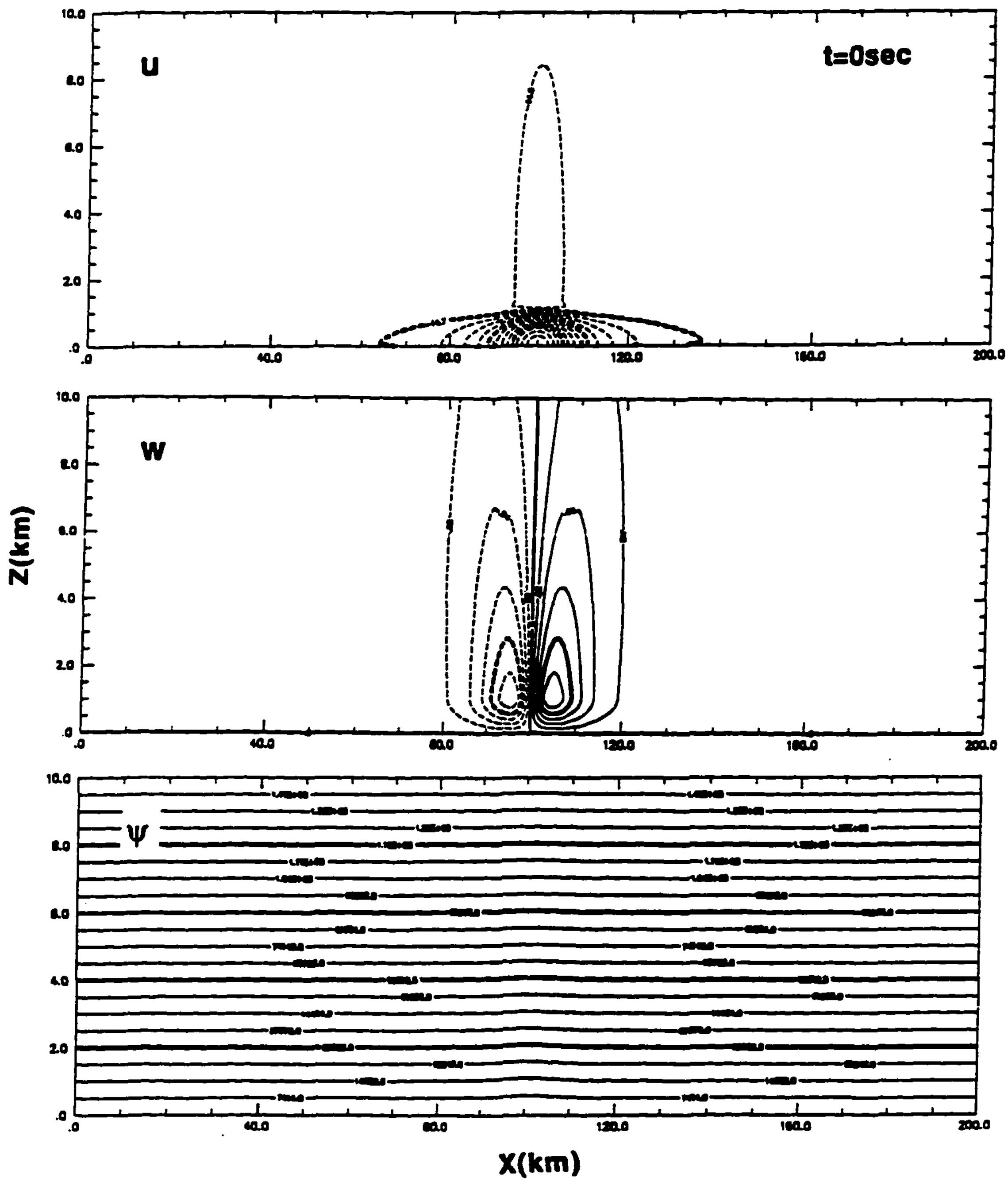

Fig.4.4 Horizontal velocity u, vertical velocity w fields, and streamlines ψ for 100m amplitude solitary wave at initial time.

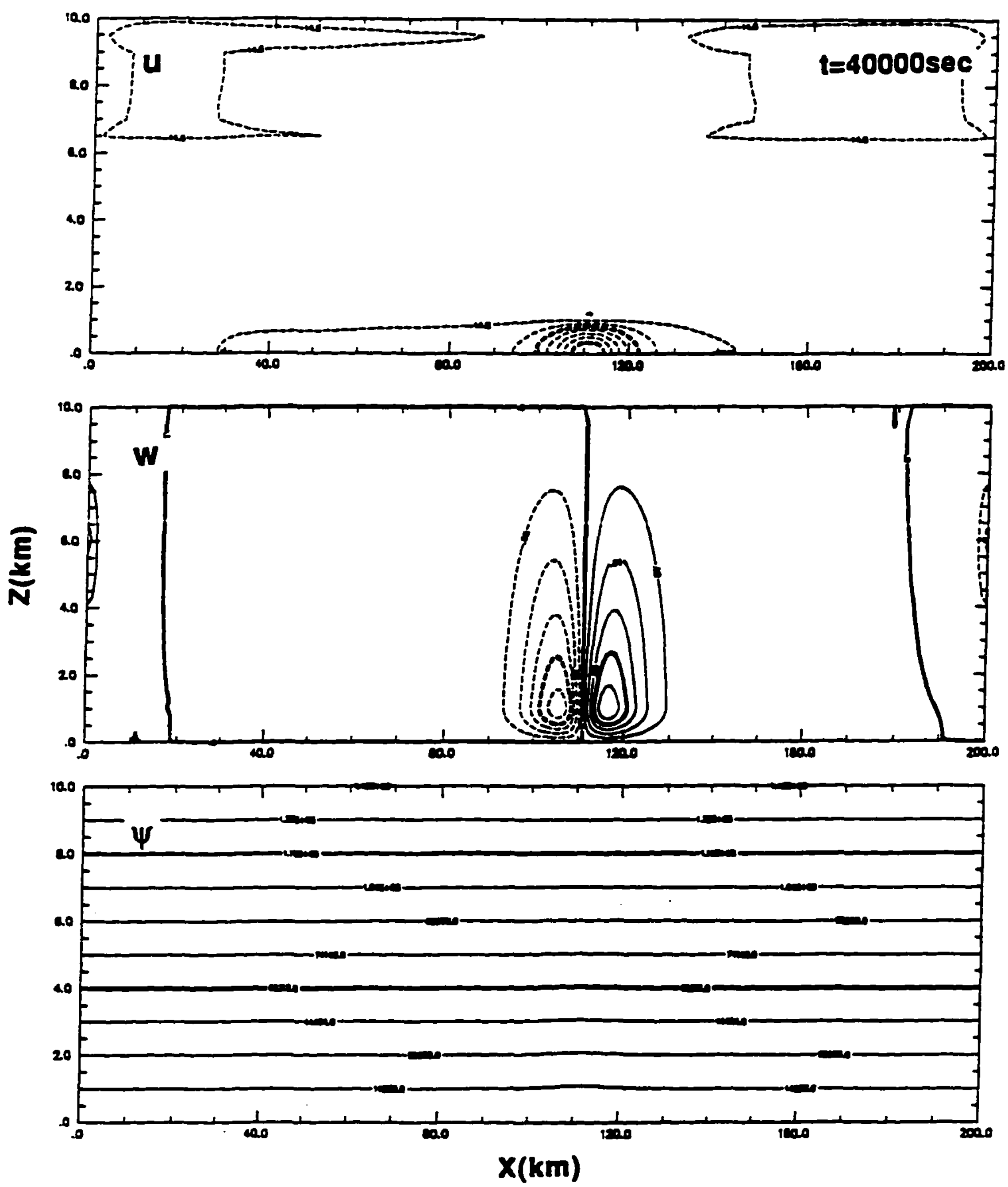

Fig.4.5 As in Fig.4.4 except for t=40000sec.

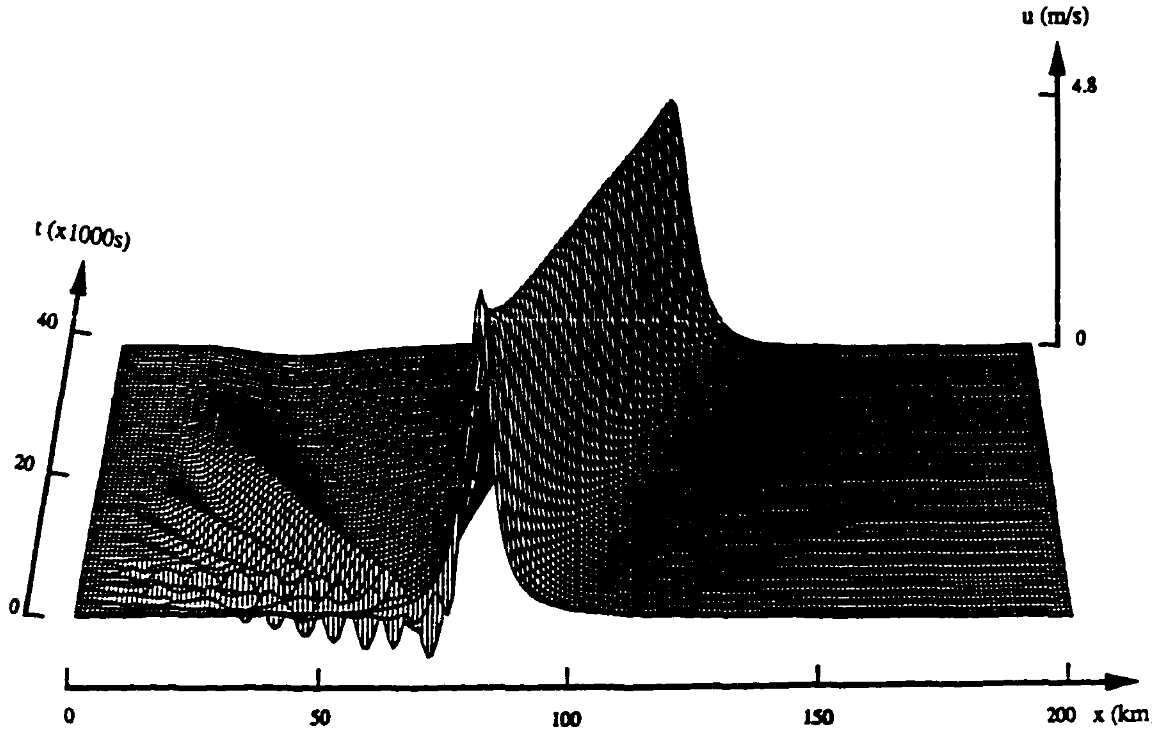

Fig.4.6 As in Fig.4.3 except for a 300m amplitude solitary wave.

Fig.4.6 shows the propagation of a larger amplitude (300m initially, a/h=0.3) solitary wave. We also found a series of small amplitude waves propagating away from the solitary wave during the initial stage, but with relatively larger amplitudes compared to those seen in Fig.4.3 as the solitary wave evolves into a stationary state, its amplitude decreases from the initial 300m to about 250m. This suggests the initial soliton-like perturbation based on weakly nonlinear theory is not as well satisfied as for the case when the amplitude is small. This is reasonable because the larger the amplitude, the larger is the departure from the assumptions of weakly nonlinear theory.

Using the above method, the phase speed of this solitary wave is found to be 15.8m/s which is also smaller than the speed 16.7m/s calculated from Eq.(4.6) for a solitary wave with amplitude 250m, but larger than 15.1m/s, the speed of solitary wave with amplitude a=100 m. This result accords with the character of solitary waves (i.e., the phase speed of the wave is proportional to the amplitude).

4.2 Collisions of two solitary waves

For a further test of the model, the collision of two solitary waves with different amplitudes, one 100m and the other 300m, is designed and examined using our model. In order to catch the behavior of these two solitary waves before, during and after the collision, we changed the inflow speed to 15.50m/s, the value between the phase speed of 100m and 300m solitary waves, to enable one solitary wave to propagate forward and the other backward in the domain. Thus the collision will occur near the center of the domain.

Before describing the model results, we first introduce the previous theoretical and numerical studies about the interactions of solitary waves as the criterion for judging our model's performance.

Matsuno (1980) presented the nature of the interaction of two solitary waves in detail and divided them into two classes based on the ratio of the initial amplitudes of two solitary waves. For $\frac{a_2}{a_1} < 3 + 2\sqrt{2} \approx 5.83$, during the period of interaction, the larger solitary wave decreases its amplitude a_2 to a_1 and increases its speed whereas the small one increases its amplitude from a_1 to a_2 while its speed decreases. After the interaction they propagate with their previous forms and phase speeds respectively. This is why one finds a "phase shift" in Fig.4.7. For $\frac{a_2}{a_1} > 3 + 2\sqrt{2}$, the small solitary wave penetrate through the larger one (Fig.4.8). Unlike the former case, the two solitary waves pass through each other and propagate as before in their own ways.

Fig.4.7 presents the whole course of the collision of two solitary waves with amplitudes 100m and 300m respectively, the ratio of their amplitude is 3.0 smaller than 5.83. Fig.4.8 shows another collision with a_1=30m and a_2=300m, the ratio is 10.0 larger than 5.83. It is apparent, from our model results, that the interaction of two solitary waves reveal the same nature as described by Matsuno (1980).

These numerical experiments indicate that the 2D vorticity-stream function model can successfully simulate the propagation and collision of solitary waves. Moreover, it shows this model is correctly coded and suggest it has capability to simulate more complicated phenomena related to solitary waves.

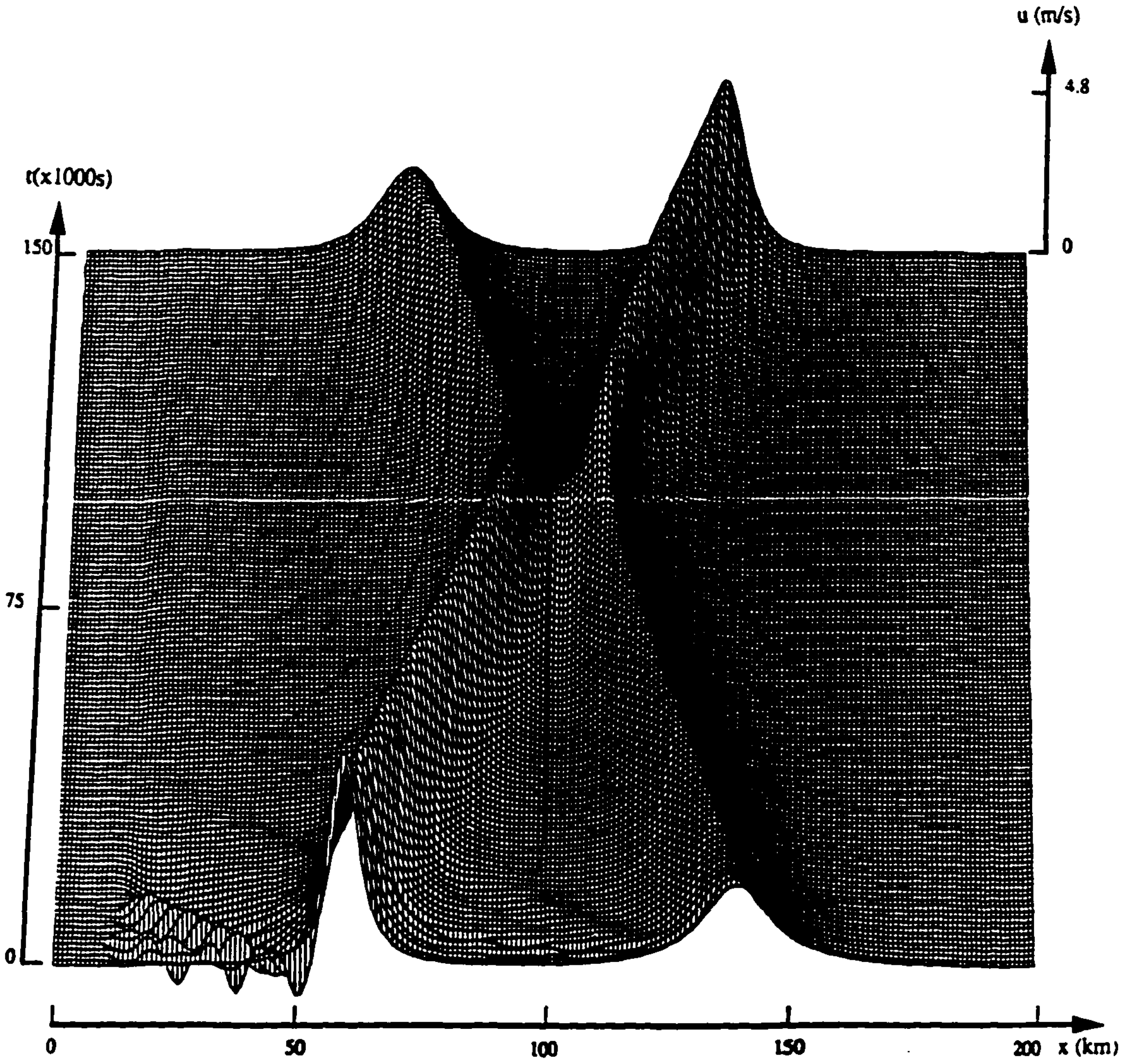

Fig.4.7 Time-dependent horizontal velocity on the surface z=0 for showing the collision of 100m and 300m amplitude solitary waves. The inflow speed is 15.5m/s.

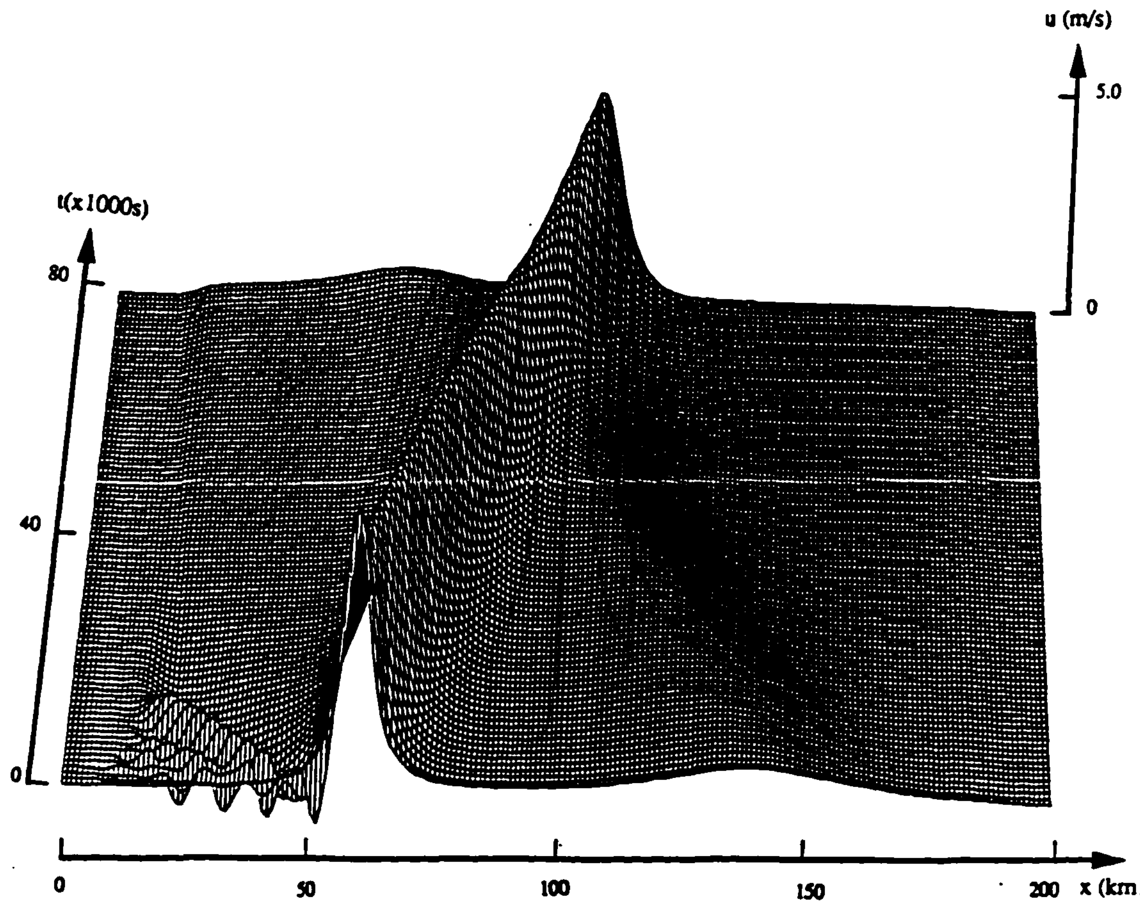

Fig.4.8 As in Fig.4.7 except for 30m and 300m amplitude solitary waves.

4.3 Generation of solitary waves by thunderstorm outflow

In the atmosphere, there are a number of mechanisms for solitary wave generation. In this section, we focus on the interactions of the thunderstorm outflow with a stable layer covered by a neutral layer as the mechanism of wave generation.

To simulate this kind of phenomena in the atmosphere using our model, we first produce a cold density current as the outflow and let it excite solitary waves. To generate a density current in the model, a block of cold air, 20 km wide and 3 km high, centered at x=30 km and on the surface, is built up by applying a cooling function to this area of the domain over a period of time. The cooling function is as follow

$$\begin{aligned} F_c(x,z,t) = r_c(1/2)^4[1+\tanh(a_1(x-x_l))][1-\tanh(a_1(x-x_r))] \\ [1-\tanh(a_2(z-z_{top}))][1-\tanh(a_3(t-t_o))] \end{aligned} \tag{4.8}$$

where r_c is the cooling rate and a_1 and a_2 are constants which determine the sharpness of the boundaries of the cooling area, a_3 represents the rate of shutting off the cooling, x_l, x_r and z_{top} are the positions of left, right and top boundaries, t_o is the cooling period. The shape of function used above is illustrated in Fig.4.9. As the cold air is being built up, it also spreads out forming a density current.

In this experiment, except for the inflow speed and Brunt- Väisälä frequency which are set to zero and 10^{-2}Hz respectively, the other background field parameters are the same as before(i.e. h=1 km, θ_o=300K, ν=0 and κ=0). t_o and r_c are set equal to 400 sec and -0.05K/sec (these can be changed to control the intensity of the density

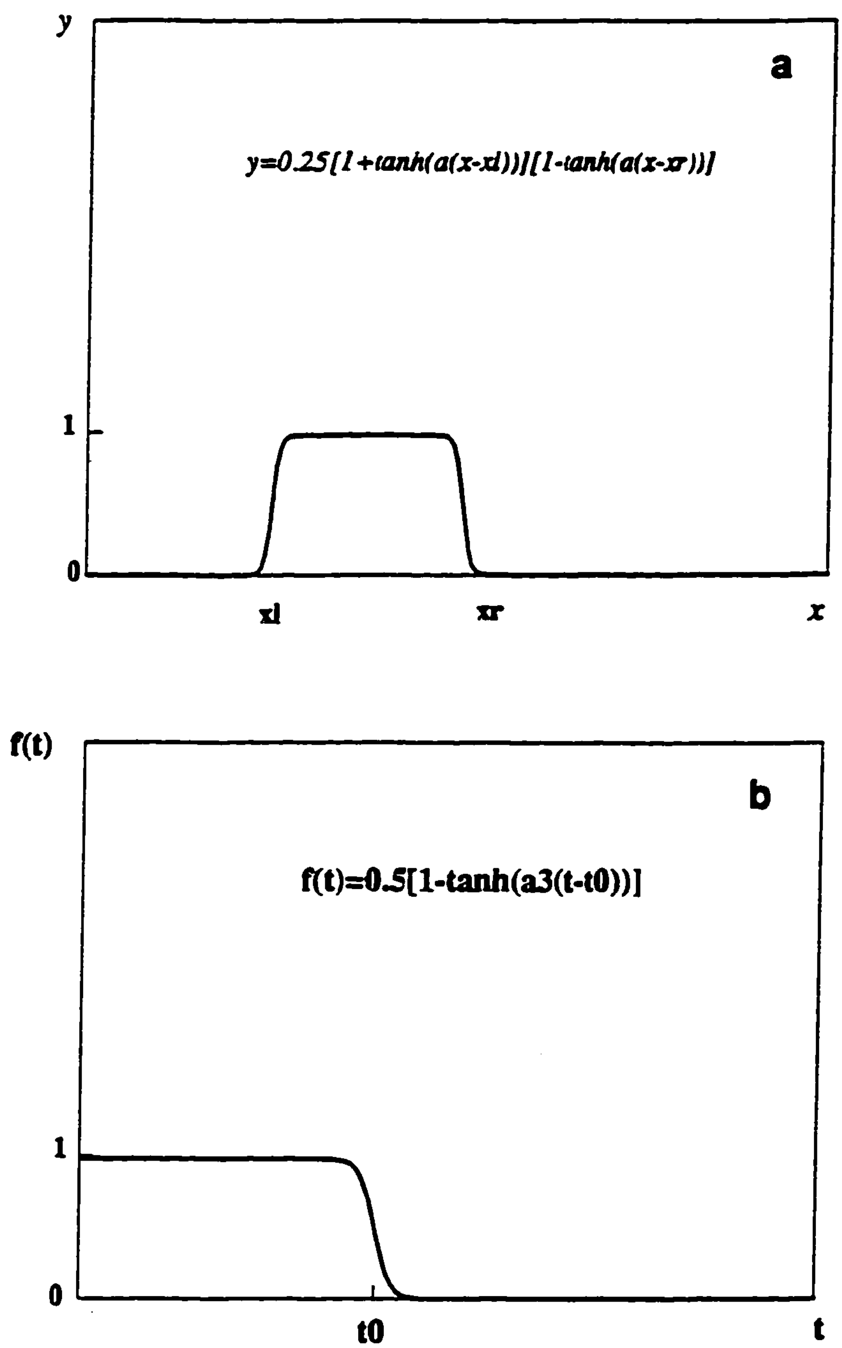

Fig.4.9 Sketch map of functions: (a) y=0.25[1+tanh(a(x-xl))][1-tanh(a(x-xr))]; (b) f(t)=0.5[1-tanh(a3(t-t0))].

current). a_1, a_2 and a_3 are 5×10^{-4}(1/m), 5×10^{-3}(1/m) and 1.25×10^{-1}(1/sec) respectively. x_l, x_r and z_{top} are 20 km, 40 km and 3 km respectively. At the effective end of cooling period(i.e. at t=400 sec), the maximum temperature difference between cold and ambient air is about 3.5K which is a reasonable value for the thunderstorm outflow in the atmosphere (Goff, 1975). The temperature profiles of cold air (at the center of cooling area) and the background field, at the end of cooling period, are presented in Fig.4.10.

Fig.4.11 shows a series of buoyancy fields at different times. At t= 5000 sec, we find that at least two well-defined waves are fully developed and cold air within them is trapped; this will be discussed and proved in section 4.4. To determine whether these waves are solitary waves, we compared the horizontal and vertical velocity fields of these waves with the solitary waves obtained in the previous section and found the basic features of them are the same. The patterns of the positive and negative vertical velocities and the pattern of horizontal velocity of the wave are symmetric about the central axis of the wave. The locations of the maximum and minimum vertical velocities are near the interface between the stable and neutral layers. But the location of the maximum horizontal velocity is above the surface, this is different from the small amplitude solitary wave. Fig.4.11 also clearly shows these waves with different amplitudes propagate at different phase speeds. For further and qualitative verification, the amplitude and phase speed of these waves are estimated from Fig.4.11. The leading wave with amplitude about 1700m propagates at average speed of 13m/s, the second one with 600m at 10m/s. This results indicates the speeds of these waves are directly proportional to their amplitudes which is the unique characteristic of evolving solitary waves. Hence we conclude these waves generated by the density current are evolving

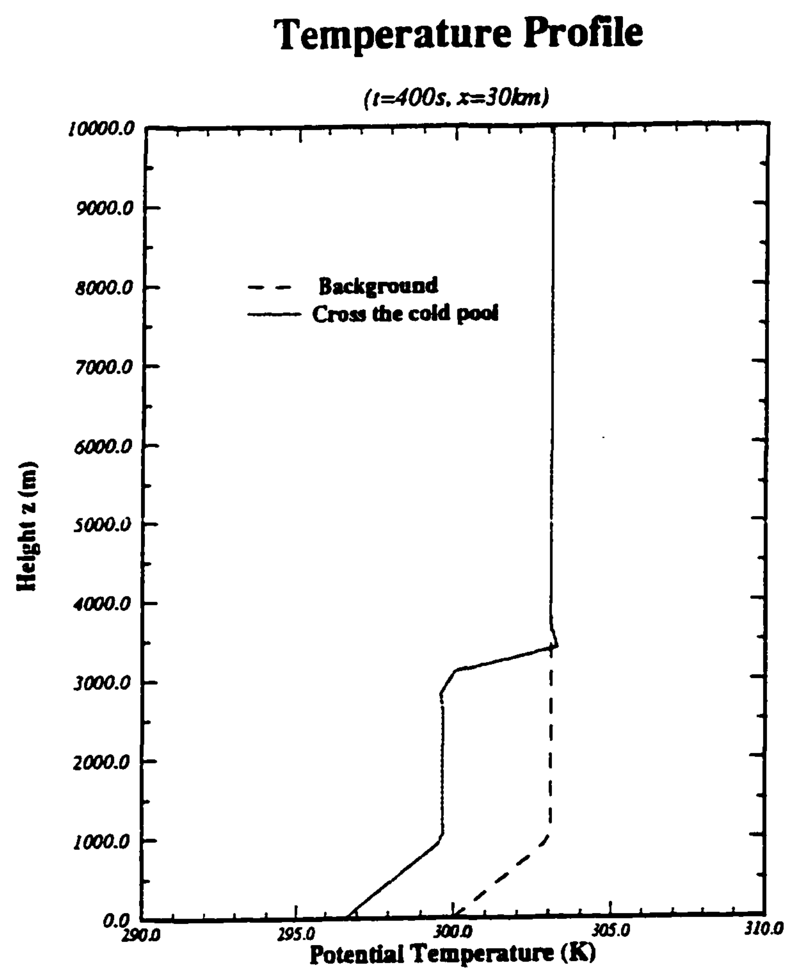

Fig.4.10 Potential temperature profiles of the coldpool and background field at the end of cooling.

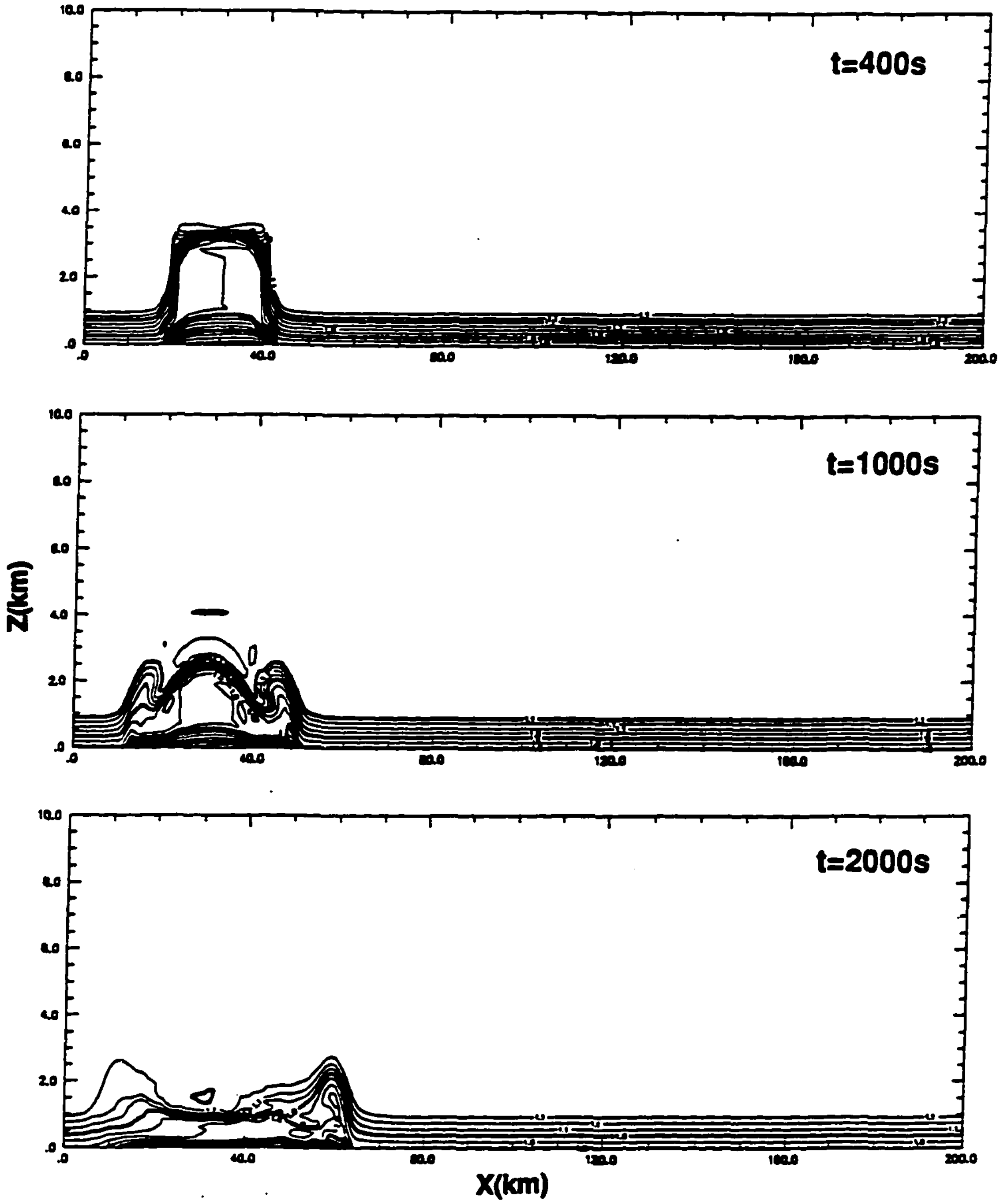

Fig.4.11 Time series of buoyancy b fields for showing various stages of generation and evolution of an undular bore.

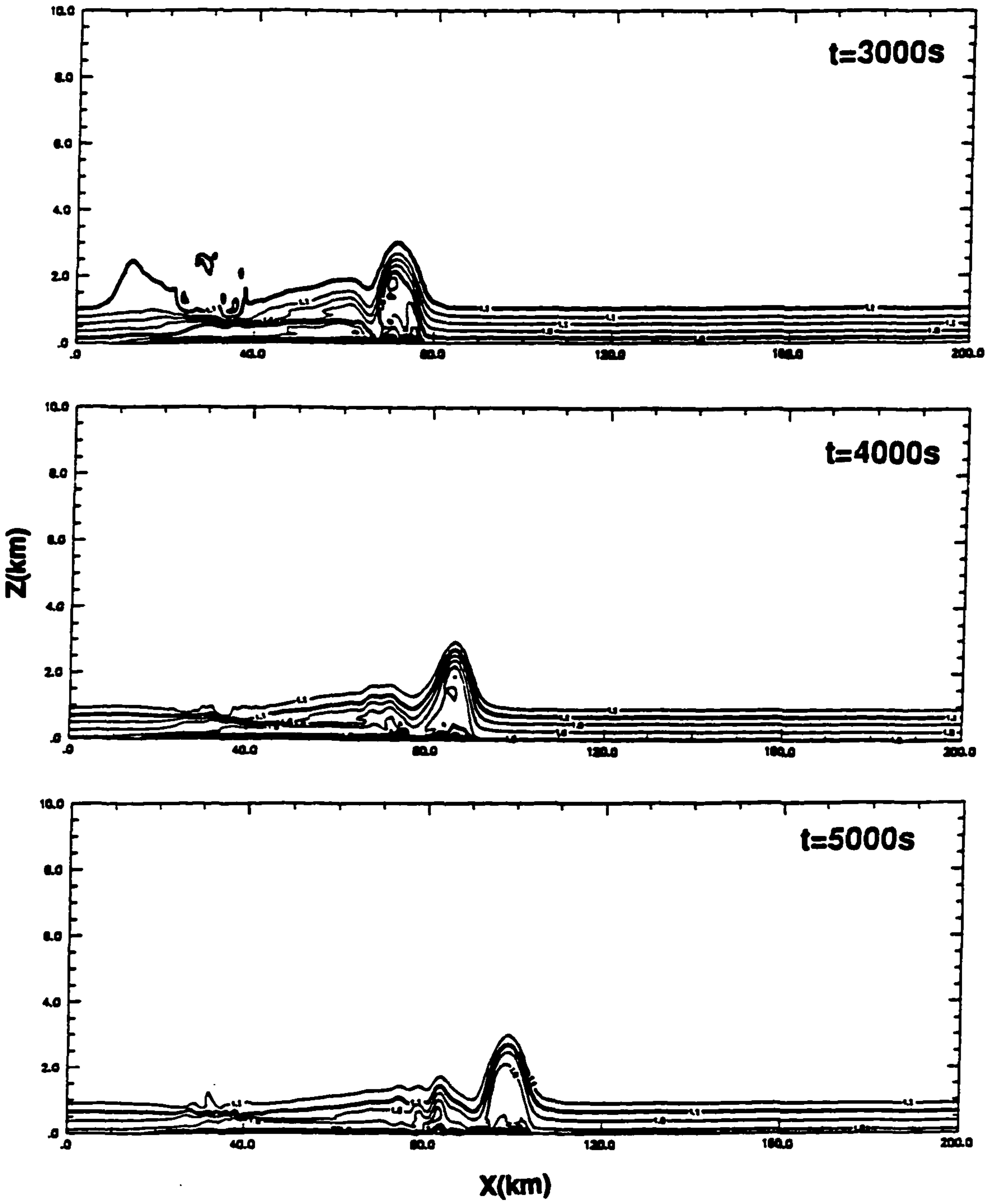

Fig.4.11 (Continued)

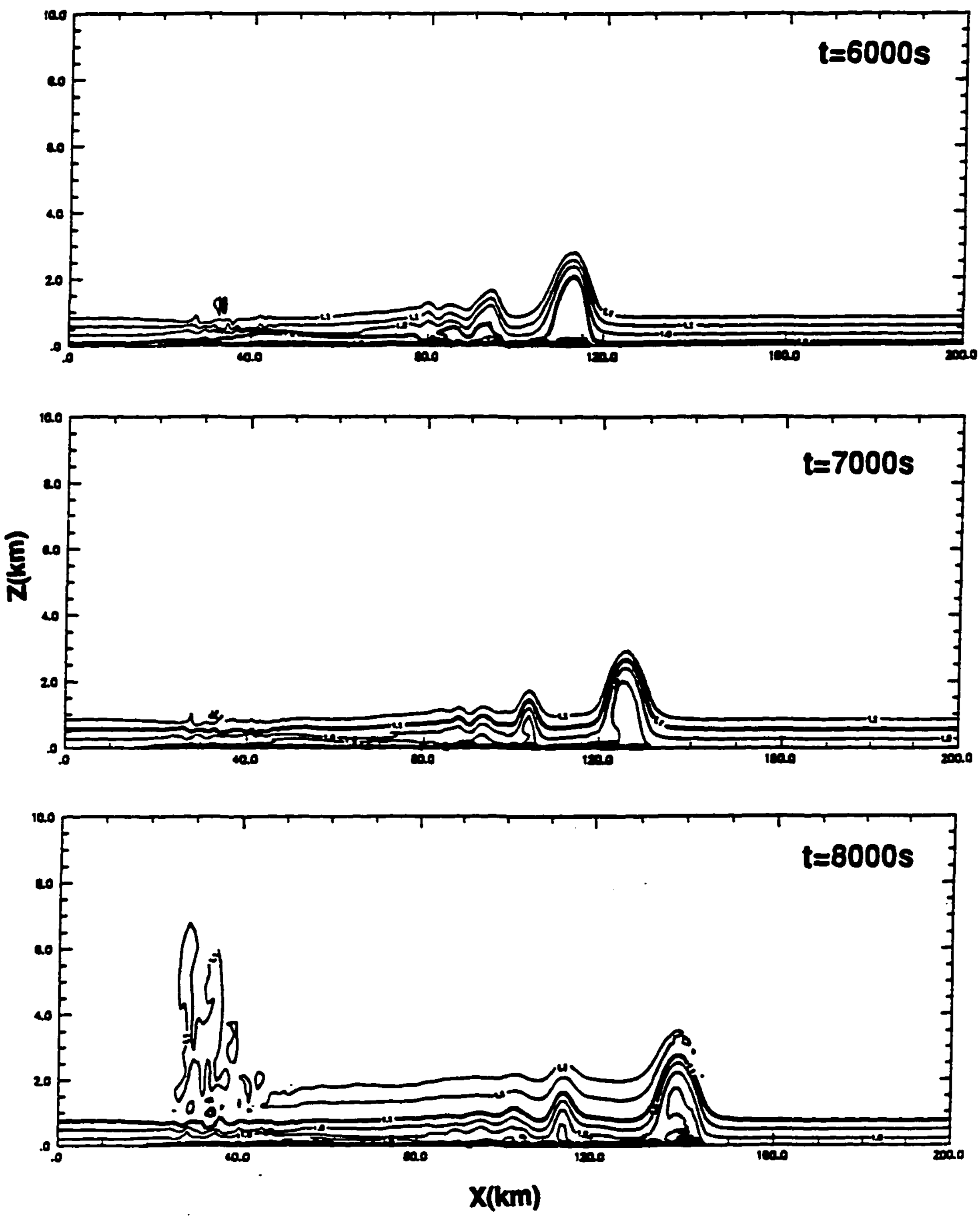

Fig.4.11 (Continued)

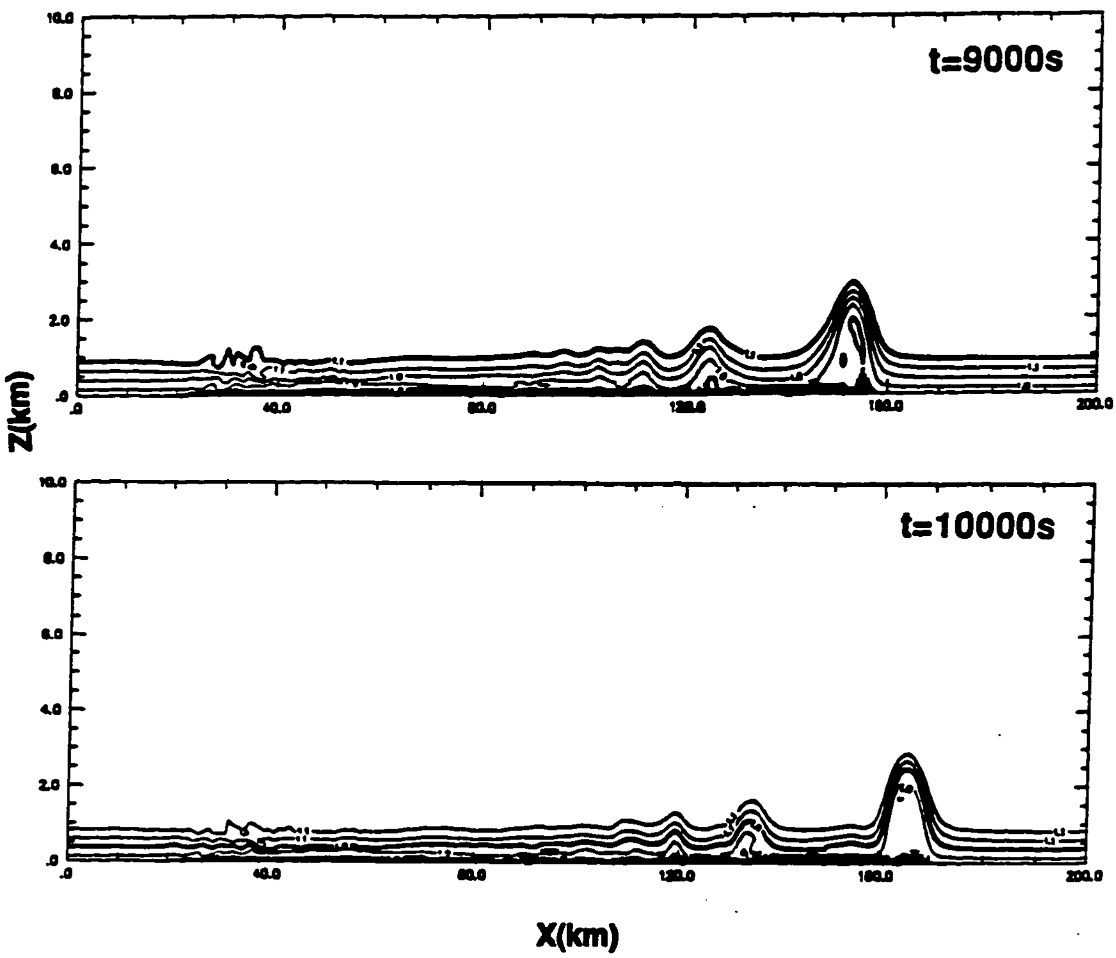

Fig.4.11 (Continued)

solitary waves.

Several similar numerical experiments with different sizes and maximum temperature defects of cold air have been conducted. Different numbers of internal solitary waves with different amplitudes were excited. The results indicate the internal solitary wave are easily generated in the numerical model. This conclusion is consistent with that given by Maxworthy (1980).

4.4 Trajectories of air parcels

In order to follow the motion of an air parcel, a particle tracer technique is applied as a tool in our model. When a particle is located, the velocity of it is calculated based on the velocities at the nearest four grid points using the Cressman interpolation method

$$\vec{v}(x,z) = \sum_{i}^{i+1}\sum_{j}^{j+1}\left[\frac{r^2 - d_{i,j}^2}{r^2 + d_{i,j}^2}\vec{v}_{i,j}\right] / \sum_{i}^{i+1}\sum_{j}^{j+1}\left[\frac{r^2 - d_{i,j}^2}{r^2 + d_{i,j}^2}\right] \qquad (4.2)$$

where $r^2 = (\Delta x)^2 + (\Delta z)^2$, $d_{i,j}$ is the distances between the particle and four adjacent grid points separately. If the particle is on a the grid point, the velocity at that grid point will used instead of the one obtained from the above method. As the velocity of the particle is obtained, the position of it at next time step $t + \Delta t$ can be calculated

$$\vec{x}(t + \Delta t) = \vec{x}(t) + \vec{v}(x,z)\Delta t \qquad (4.3)$$

Repeating this process at each time step, a trajectory of the particle over a period of time can be drawn.

By utilizing this technique, we prove another unique characteristic of solitary waves: An air particle will be shifted a certain distance as a solitary wave passes over it. This is unlike sinusoid waves which only drive the air particle around their balanced positions (Kundu, 1990). Fig.4.12 shows the trajectory of a particle initially located in front of solitary wave with amplitude 300m at a height of 100m. The trajectory clearly recorded the motion of the particle, being lifted by the wave during the first half period of the wave moving toward it, and then lowering it as the wave moves away. Comparing the initial and final positions of particle, we found the particle is moved about 4400m horizontally in the direction of wave propagation without any net vertical shift. It is obvious the maximum lift height and net horizontal shift depend on the size of solitary wave and the initial location of the particle.

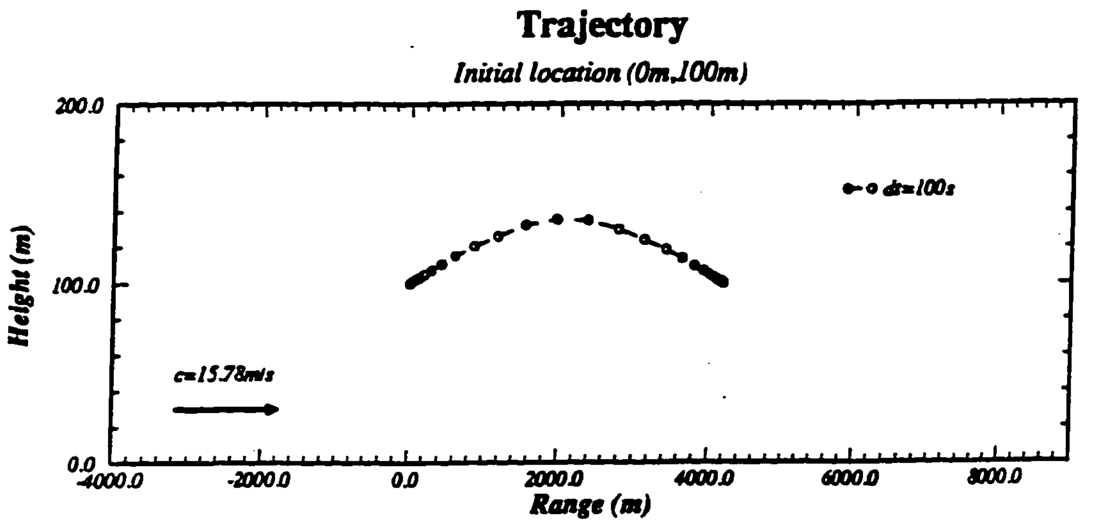

Fig.4.12 Trajectory of a air parcel as a small amplitude solitary wave pass over.

The most useful application of this technique is to show that large amplitude solitary waves can trap and transport a mass of air from the wave source for a quite long distance. The phenomena was observed by Doviak and Ge (1984) in an evolving solitary wave generated by a thunderstorm outflow. Christie (1992) found a visible cloud of smoke along the Morning glory wave originated in bush fire in the area of wave generation. Doviak et al. (1991) also give a detailed description of the observations in 1984. In addition, this trapping mechanism of large amplitude solitary waves is supported by the numerical model results reported by Hasse and Smith (1989). Using a volume of tracers, they found the waves generated by the inflow trap an amount of inflow fluid when the fluid is under supercritical conditions (i.e. the phase speed of infinitesimal amplitude long waves on a stable layer smaller than the speed of the gravity current in the absence of the stable layer). The authors mentioned the tracer suffers some long-term diffusion which makes it an unreliable indicator for a longer time.

Comparing with a volume of tracers, the parcel tracer adopted in some of our experiments avoids the diffusion problem and is able to depict the trajectory of an air parcel instead of motion of a volume of tracers which diffuse as well as being advected by the flow.

In order to determine the effects that large amplitude buoyancy waves generated by thunderstorm outflow have on the environment, four tracers are initially located at different positions. The trajectories of these four tracers during the numerical experiment period are displayed in Fig.4.13. Comparing the paths of the tracers with the motion of the wave (see Fig.4.11), we found that tracer 1, initially at x=40 km, z=10 m and on the boundary of the block of cold air, is trapped and advected by the leading solitary wave (Fig.4.13a). Tracer 2, placed at x=36 km, z=200 m at the beginning time, is trapped by the front of the wave during the initial stage (t<2600 sec), then slowly dropped out of the leading wave and trapped by a second wave. But during the final stage (t>9000), it leaks out from the second wave (Fig.4.13b). Tracer 3, which represents the ambient air is initially positioned at x=50 km, z=100 m. As the front of the wave passes over it, tracer 3 was collected by the wave and trapped within the leading solitary wave (Fig.4.13c). Tracer 4 placed at x=50 km, z=300 m, 200m higher than tracer 3 at the initial time, also represents the ambient air (Fig.4.13d). But its behavior is different from that of tracer 3. Instead of being collected by the wave, this tracer is lifted up and then laid down by the front of the wave. After that, it is only slightly moved by the following perturbations.

To further illustrate the relation between the motion of the air parcels and the large amplitude waves, the horizontal velocities of the tracers during the numerical experiment period are displayed together with the speed of the leading wave in Fig.4.14. The speed of the leading wave is calculated from Fig.4.11. From Fig.4.11 and Figs.4.14a, and 4.14c, we notice the leading solitary wave has fully developed at about t=3000 s. Tracers 1 and 3 are trapped by the wave, and their horizontal velocities approach the speed of the wave, but vibrate around that value. These results confirmed the former finding of trapping and existence of recirculation within the wave. Fig.4.14c and d show tracer 3 and 4 have similar patterns of horizontal velocities during the first 2000 sec, a peak at about t=1100 sec and following by a valley at t=1500 sec. Fig.4.14b shows tracer 2 has approximately same speed as the leading wave, then slows down to about 3m/s when it is dropped out from the leading wave. Then the horizontal speed of

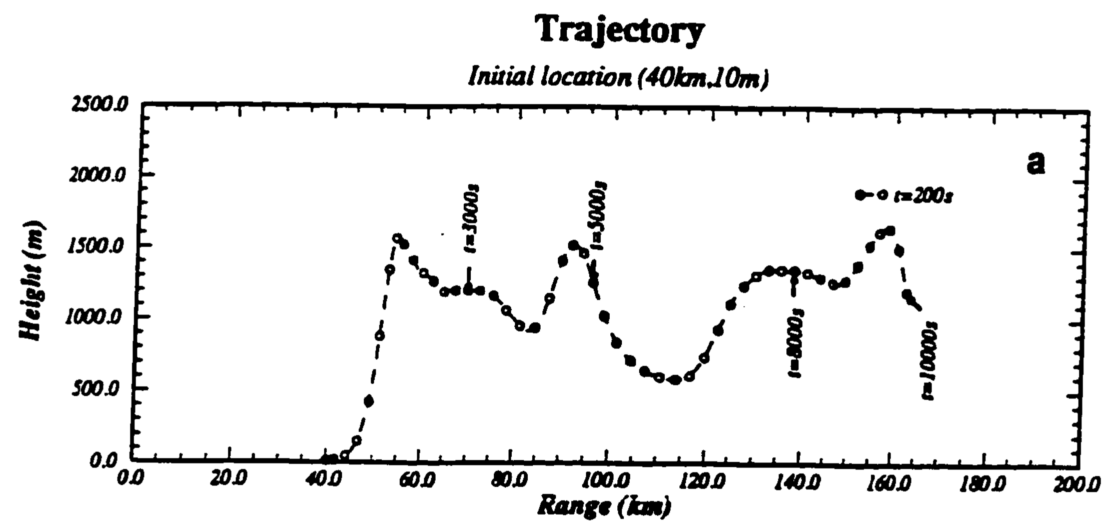

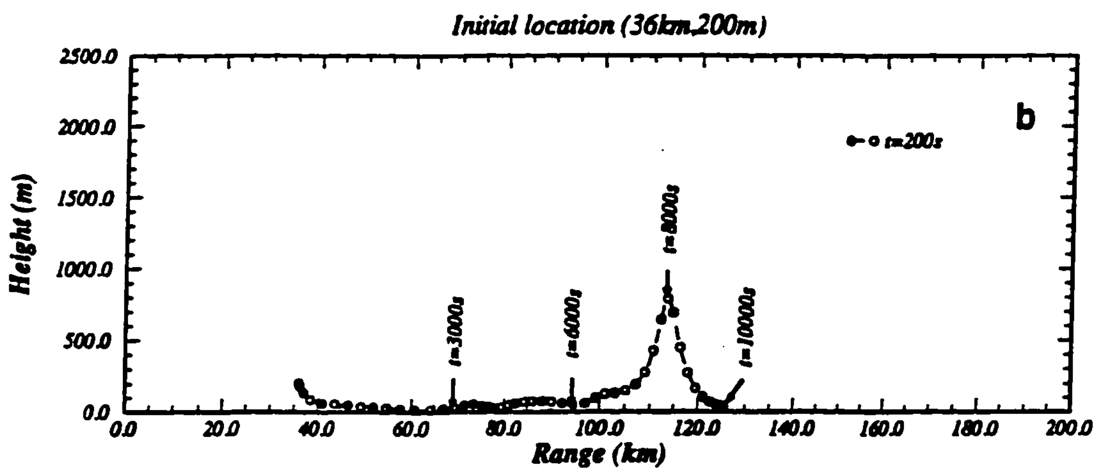

Fig.4.13 Trajectories of four air parcels initially located at (a) x=40km, z=10m; (b) 36km, 200m; (c) 50km, 100m; (d) 50km, 300m.

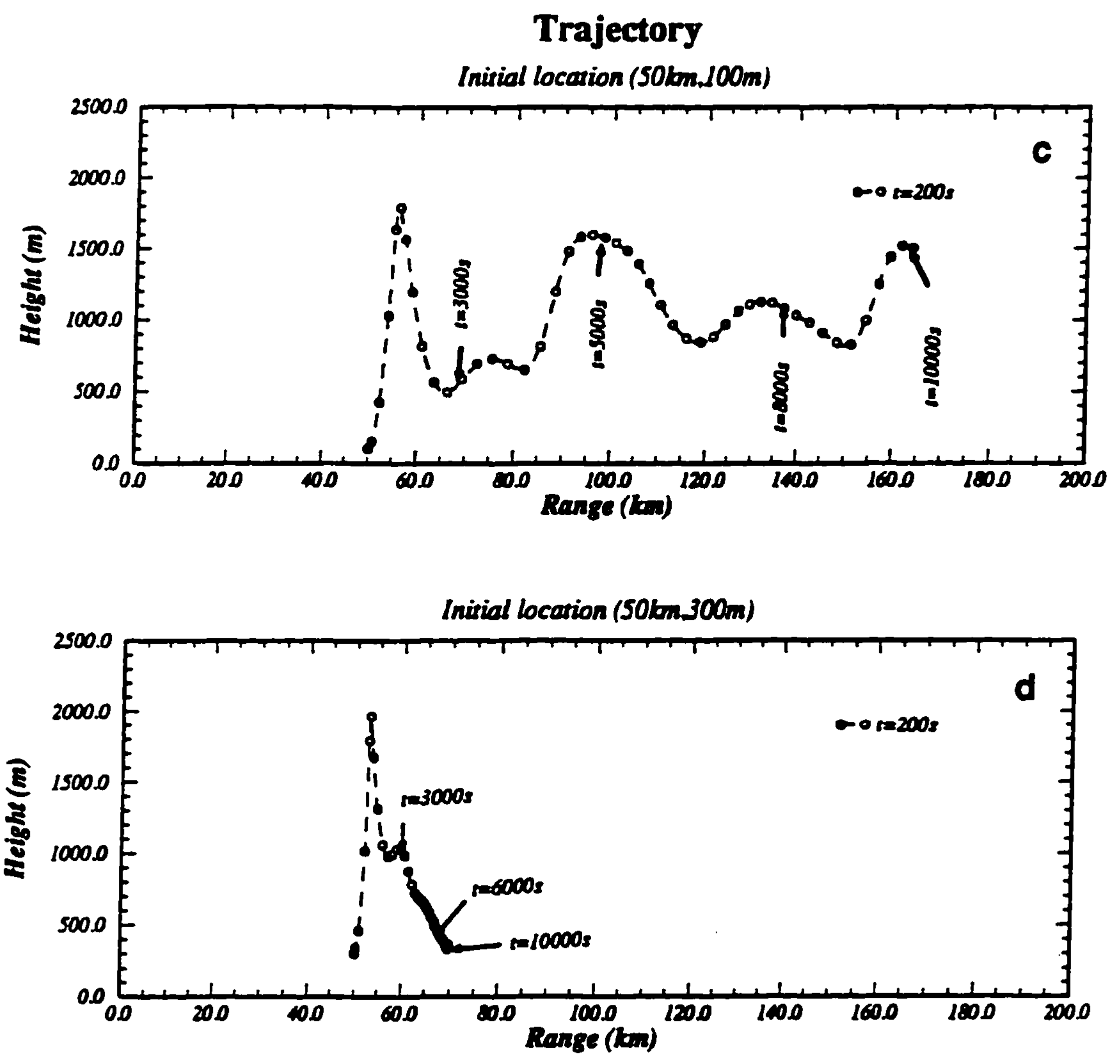

Fig.4.13 (Continued)

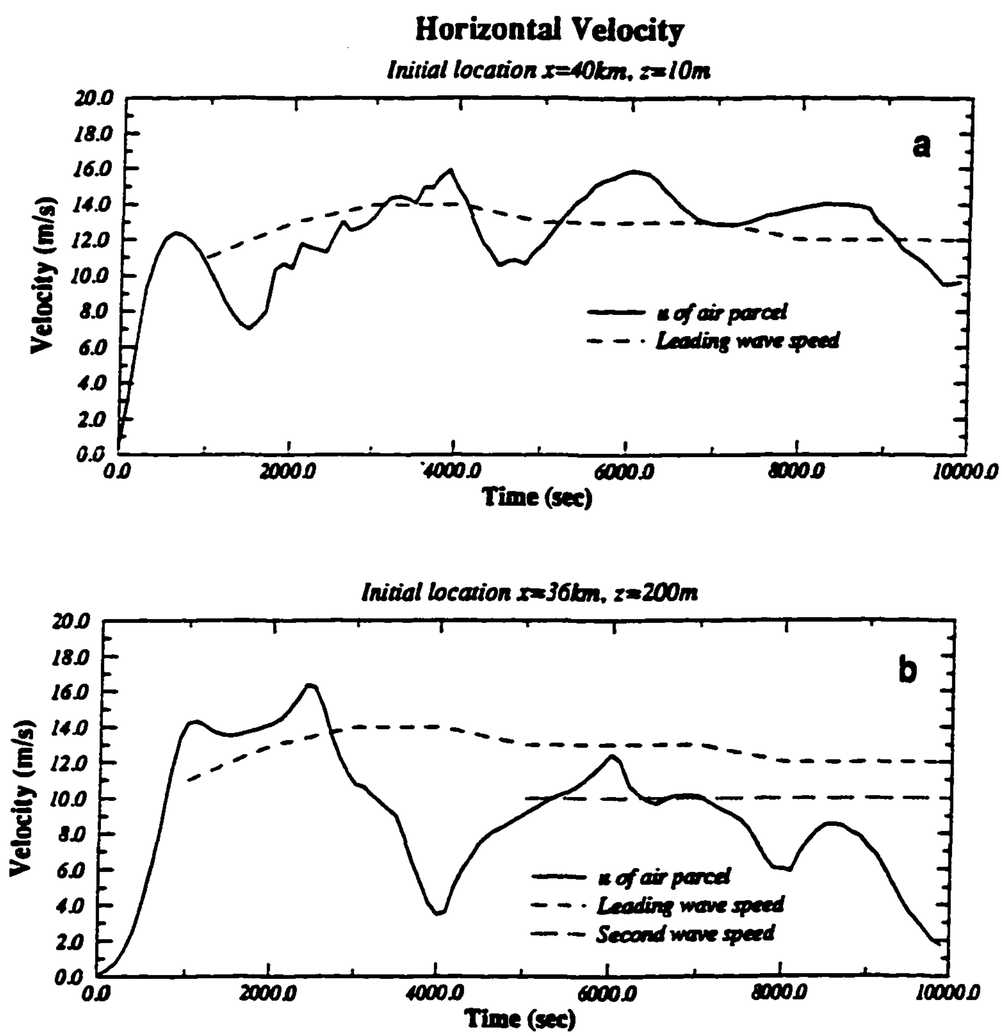

Fig.4.14 Time-dependent horizontal velocities of four air parcels shown in Fig.4.13 and the speeds of solitary waves. The speed of second wave also shown in (b).

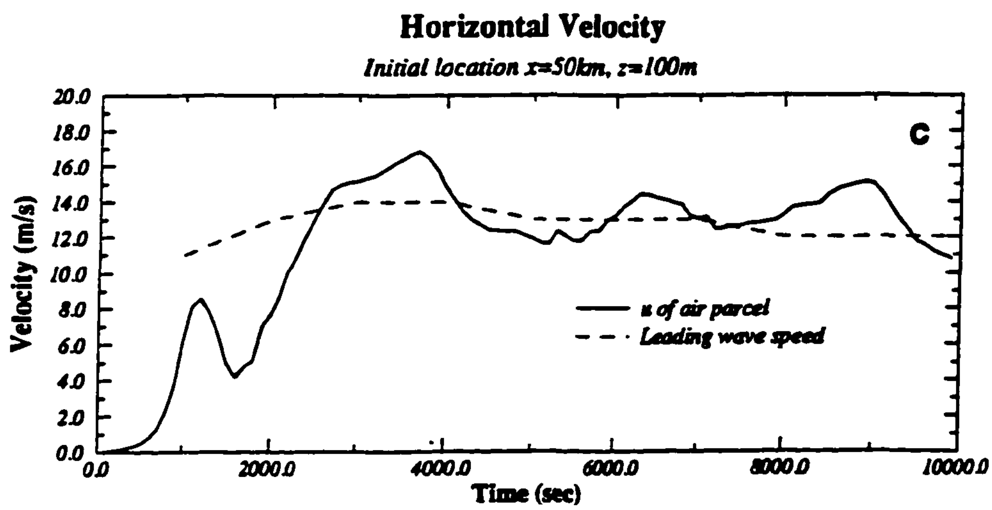

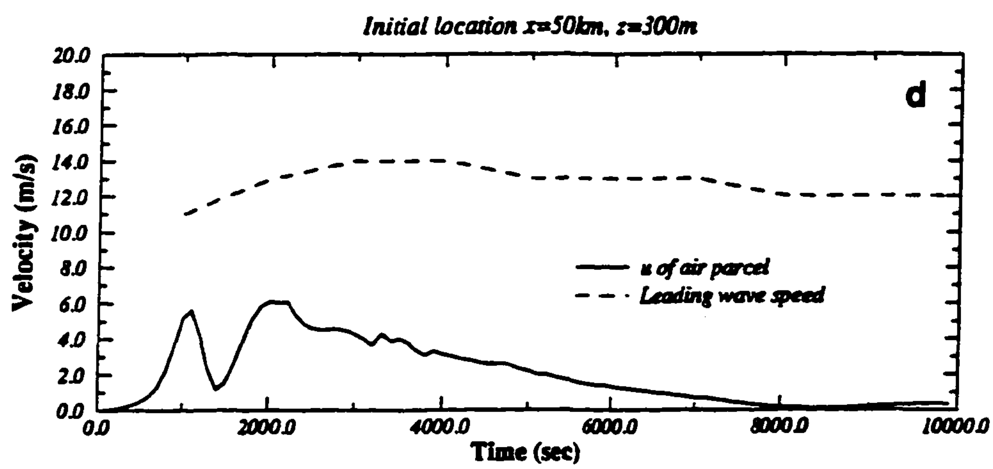

Fig.4.14 (Continued)

tracer 2 increases to a maximum 12m/s and remains around 9m/s for about 3000 sec when it is captured by following second wave. Finally its horizontal speed monotonously decreases to 1m/s when it is gradually released from the second wave.

Referring to Fig.4.11, 4.13c and d, and 4.14c and d, we found the tracers 3 and 4 are first pushed forward and raised up from the static state, during this period they gain their peak horizontal velocities respectively. After that, tracer 3 is collected by the leading wave and its horizontal velocity approaches the speed of leading wave. Tracer 4 is pushed by the following perturbations to achieve the maximum horizontal velocity about 6.1m/s. Then tracer 4 slows down to static state with net horizontal shift about 20 km in the direction of the motion of the waves.

The behaviors of these tracers clearly exhibit the effects of large amplitude solitary waves. The model results show the large amplitude solitary waves can trap, not only the air of thunderstorm outflow (tracer 1) that generated the waves, but also the ambient air (tracer 3). The results also indicate once the tracers are trapped by the wave, they not only translate with the wave, but also oscillate within the core area of the wave. The oscillations of the tracers moving with the wave reflect the existence of recirculation within the wave. The trajectory of tracer 2 implies that trapped air leaks out from the rear of the wave. These numerical findings of trap and leakage effects of large amplitude solitary wave are consistent with observations (Doviak et al. 1991). More detailed studies of trapping and leaking mechanism of large amplitude solitary waves and a case related to this mechanism are described in Chapter 5 and 7.

Chapter

5

Structures and Properties of Large Amplitude Solitary Waves

5.1 Generation of pure large amplitude solitary waves

A pure large amplitude solitary wave is defined as a solitary wave with a recirculation in it, but the potential temperature of fluid in the recirculation region is not colder than the ground temperature outside of this region. This definition is used to distinguish pure waves from the large amplitude solitary waves generated by a cold outflow which is trapped by the wave, thus creating a recirculating region cooler than the environment. If a wave is stationary in a moving frame, the recirculation region within this wave is defined by a family of closed streamlines.

In order to generate a large amplitude solitary wave in the numerical domain, a large amplitude solitary wave-like perturbation, described in Appendix A, is specified at the initial time t=0. Fig.5.1 shows the initial buoyancy b, horizontal velocity u and vertical velocity w fields. There is no recirculaton region within the initial large amplitude

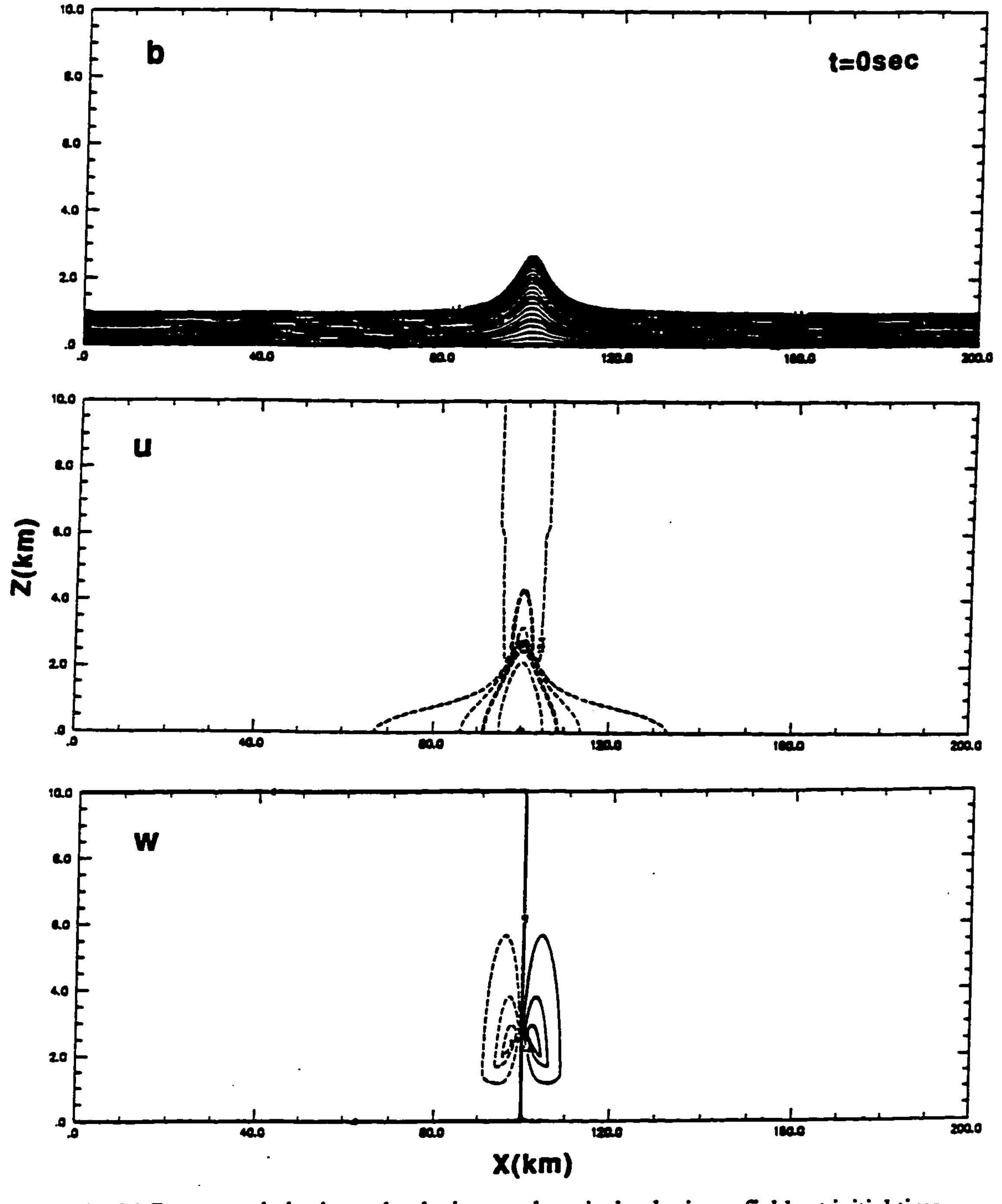

Fig.5.1 Buoyancy b, horizontal velocity u and vertical velocity w fields at initial time.

perturbation. After a period of time, this large perturbation develops into a large amplitude solitary wave and several small amplitude waves. Due to the speed differences of these waves, the largest solitary wave in which we are interested propagates at the fastest speed and separates from the smaller waves. To keep the largest one in the numerical domain for a longer time, an inflow with a guessed speed in the direction opposite to the speed of wave is set up. After one simulation, the exact speed of the largest solitary wave can be estimated. Then the inflow speed is chosen as this speed. Thus the largest wave can be made stationary in the numerical domain.

5.2 Configurations of reversed recirculation within large amplitude solitary waves

For investigating the detail structure of the large amplitude wave after recirculation has set in and the wave is quasi-stationary, a part of the wave is enlarged. The width of this highlighted area is 40 km and the height is 3 km. Fig.5.2 shows the horizontal velocity u, vertical velocity w, and buoyancy b fields of a pure large amplitude solitary wave in the relatively steady stage in the frame moving with the wave. The symmetric pattern of the u, and b fields, opposite vertical velocities with respect of the vertical central line of the wave, similar to small amplitude solitary waves, are found in these fields.

We also notice, besides these similar structures that a recirculation region does exist within the large amplitude solitary waves in our numerical simulations in agreement with the results observed in theoretical studies (Tung et al, 1982) and laboratory experiments (Stamp and Jacka, 1995). In Fig.5.2 there are two special features which are used to affirm the appearance of recirculation within the wave. One is small positive-

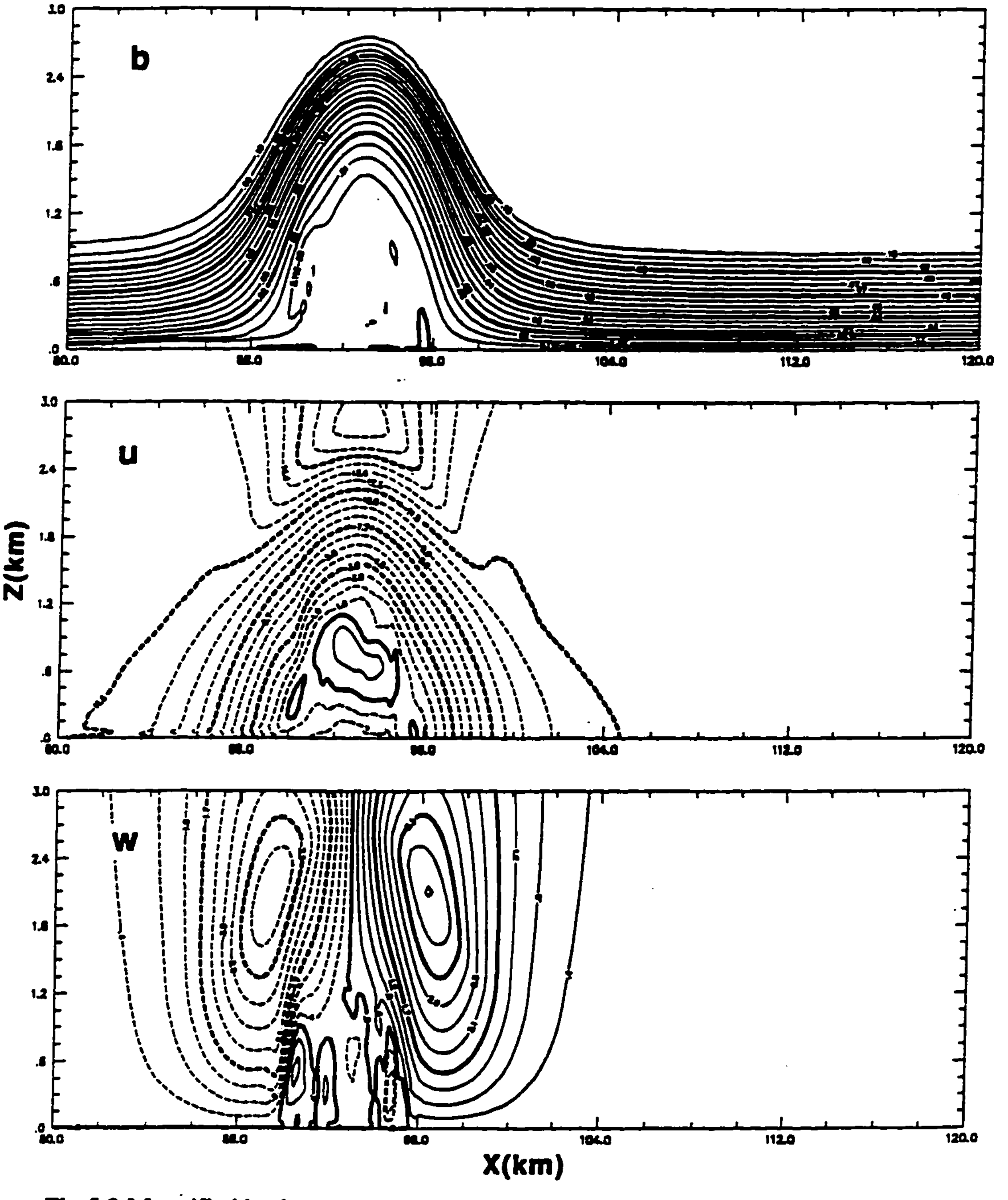

Fig.5.2 Magnified horizontal velocity u, vertical velocity w, buoyancy b fields, and streamlines of a pure large amplitude solitary wave in the frame moving with the wave.

negative pair of vertical velocity beneath the large pair in the w field. The other is the region with positive horizontal velocity (solid lines) in the core region of the wave in u field. Note the word 'recirculation' with prefix 're' is used to especially describe the circulation inside the large amplitude solitary wave in order to distinguish it from the outside circulation induced by the wave.

In comparison with previous theoretical studies and laboratory experiments, our numerical simulations have the advantage of being capable of showing the detailed structures of the recirculation region. For the theoretical studies (Tung et al., 1982), the numerical solutions of large amplitude solitary wave are derived based on the assumption of open streamlines. In other words, information of the wave is obtained from the upstream flow. When recirculation appears in the wave, closed streamlines will show up in the flow domain. But there is no way to get any information on the flow within the recirculation region. Hence, Tung et al. (1982) assumed the direction of the flow in this region.

In the laboratory experiments it is difficult to observe the fine structure in the recirculation region. Because viscosity cannot be avoided in the real fluid, the inviscid assumption is invalid and strong diffusion will mix up the fine structures within the recirculation region of laboratory experiments. In addition, the scale of fluid movement becomes so small that detecting the motion directions in the recirculation region is very difficult in the laboratory experiment.

In the simulations, the w field inside the recirculation region shows a pair of upward and downward vertical motions (Fig.5.2). The impressive point is that the

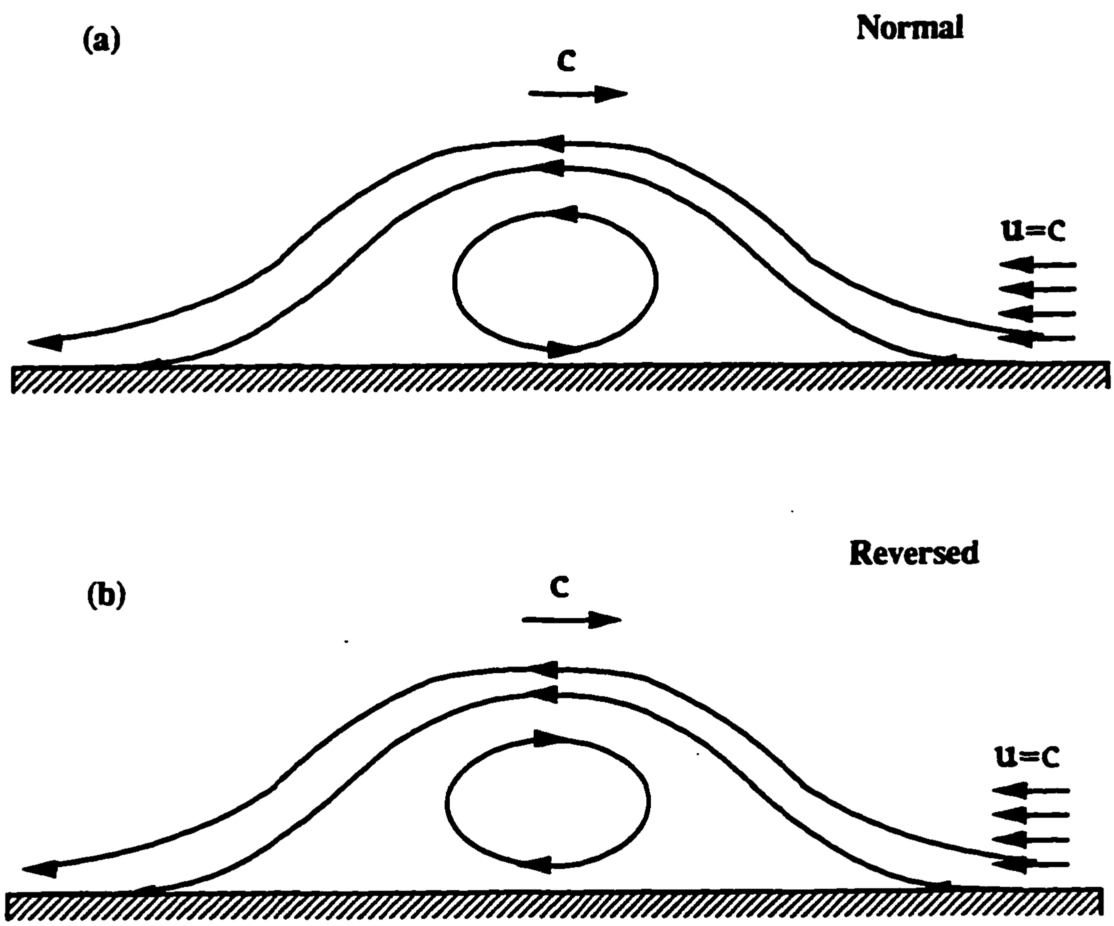

Fig.5.3 Schematic diagram of (a) normal and (b) reversed recirculation within a large amplitude solitary wave in the frame moving with the wave.

direction of this recirculation is opposite to the motion of outside flow. This recirculation is opposite in direction assumed in previous theoretical studies (Tung et al, 1982). We call it reversed recirculation.

In the previous theoretical studies (Tung et al, 1982), the rotation direction of the recirculation assumed to be the same as the flow outside the recirculation region as depicted in Fig.5.3a. If the fluid is viscous, the drag effect will force the inner fluid to rotate in the same direction as the outside flow. But if we assume there is no viscosity in the fluid, the inner fluid may rotate in the direction opposite to the outside flow (Fig.5.3b). Our simulations show that the inner fluid does rotate in this way. Certainly, even without viscosity the inner fluid might recirculate in the same direction as the outside flow.

Following Orlanski (1969), we can show that reversed recirculation does not violate any physical principals. Assume that the amplitude of solitary wave is so large that within the wave above the ground there is a region in which the horizontal velocity u is larger than the wavespeed c. Thus there must be a closed boundary C1-C2 along which u is equal to c (Fig.5.4). Hence in the frame moving with the wave, u on this closed boundary is zero, with positive u inside and negative u outside. For simplicity, we assume only one maximum u in the shaded region R bounded by curves C1 and C2. A vertical line AB can be found, such that horizontal velocity u on the left of AB is always less than u on the right. The intersection points between line AB and boundary C1-C2 are defined as points A and B respectively (See Fig.5.4).

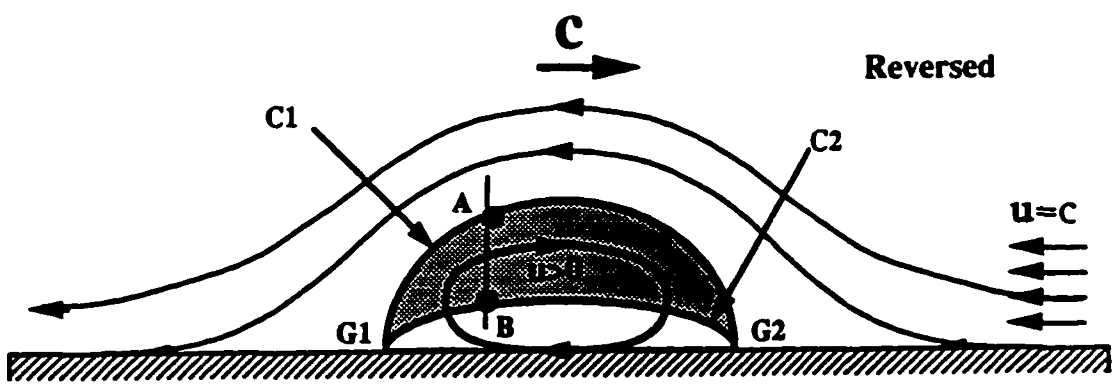

Fig.5.4 Schematic diagram of reversed recirculation. In the shaded region u>0.

In the moving frame, the wave is stationary. So the adiabatic equation can be simplified by neglecting the local change term:

$$u\frac{\partial\theta}{\partial x}+w\frac{\partial\theta}{\partial z}=0\ . \tag{5.1}$$

At point A, u=0, the first term of Eq.5.1 is zero, and thus $w\dfrac{\partial\theta}{\partial z}$ must be equal to zero. $\dfrac{\partial\theta}{\partial z}$ cannot be zero because the ambient air flowing above A is stable (because waveguide is stable) and we assume gradients are continuous. Hence, w=0 at point A. According to the continuity equation:

$$\frac{\partial u}{\partial x}+\frac{\partial w}{\partial z}=0. \tag{5.2}$$

Along line AB, $\frac{\partial u}{\partial x} > 0$ by construction, so we get $\frac{\partial w}{\partial z} < 0$ along AB. Since w=0 at point A, w must be positive below point A. At point B, w must not be zero and positive as well, otherwise the continuity equation is violated. Therefore, $\frac{\partial \theta}{\partial z}$ must be zero at point B in order to satisfy Eq.5.1. Similarly, we can apply this analysis all over the region R and find that on the left hand side of the u maximum, the fluid moves upward, and on the right hand side, the fluid moves downward. Moreover, w on the boundary C1 of region R is zero, but not zero along C2.

From our simulations, we found that the upper boundary C1, along which u=w=0, extends to the ground. The intersection points between curve C1 and ground are labeled G1 and G2 in Fig.5.4. The boundary C1 and the rigid ground surface between points G1 and G2 form a closed boundary. This implies that there is no flow in or out through this closed boundary. In the frame moving with the wave the streamlines inside the region is closed. The region contained by the boundary C1 and ground is the recirculation region Rr. The region R is formed by the boundary C1 and C2 and located above the ground.

In the previous discussion it has been shown that the fluid on the right (left) side of u maximum moves downward (upward). In addition, u>0 in region R and u=w=0 on the boundary C1, like a rigid boundary, the fluid between boundary C2 and ground must flows from right to left to satisfy the mass continuity and the incompressible assumption. Thus a reversed recirculation is formed, which violates no physical principals.

Furthermore, it can be shown that, inside region R, the fluid is convectively unstable. Differentiating Eq.(5.1) by z, we get

$$\frac{\partial u}{\partial z}\frac{\partial \theta}{\partial x}+u\frac{\partial^2 \theta}{\partial x \partial z}+\frac{\partial w}{\partial z}\frac{\partial \theta}{\partial z}+w\frac{\partial^2 \theta}{\partial z^2}=0 \tag{5.3}$$

At point B, $\frac{\partial \theta}{\partial z}=0$ and u=0 because point B is on the boundary of R. Therefore Eq.(5.3) becomes

$$\frac{\partial u}{\partial z}\frac{\partial \theta}{\partial x}+w\frac{\partial^2 \theta}{\partial z^2}=0 \tag{5.4}$$

$\frac{\partial \theta}{\partial x}\neq 0$ at point B because the region outside R is stable, and $w \neq 0$, and $\frac{\partial u}{\partial z}\neq 0$. Then based on Eq.(5.4), $\frac{\partial^2 \theta}{\partial z^2}\neq 0$ must not be zero. Hence point B is not an inflection point; it must be a maximum or minimum point. Because $\frac{\partial \theta}{\partial z}>0$ (i.e. stable) outside region R, there must be a region just above point B in which $\frac{\partial \theta}{\partial z}<0$ (i.e. unstable). This demonstrates that the fluid within the region R is convectively unstable. There must be small scale turbulence in this region and the stable stratification will be eroded, at the same time the recirculation is developing. Due to recirculation, the fluid inside R will also mix with fluid outside R but inside recirculation region Rr. After a period of time, a relative steady state has been reached. This process is observed in our simulations (Fig.5.5).

In the reversed recirculation case, we find that the maximum horizontal velocity u is not on the ground and across the center of the waves. Fig.5.6 shows the vertical profile of horizontal velocity u and potential temperature θ across the center of a large

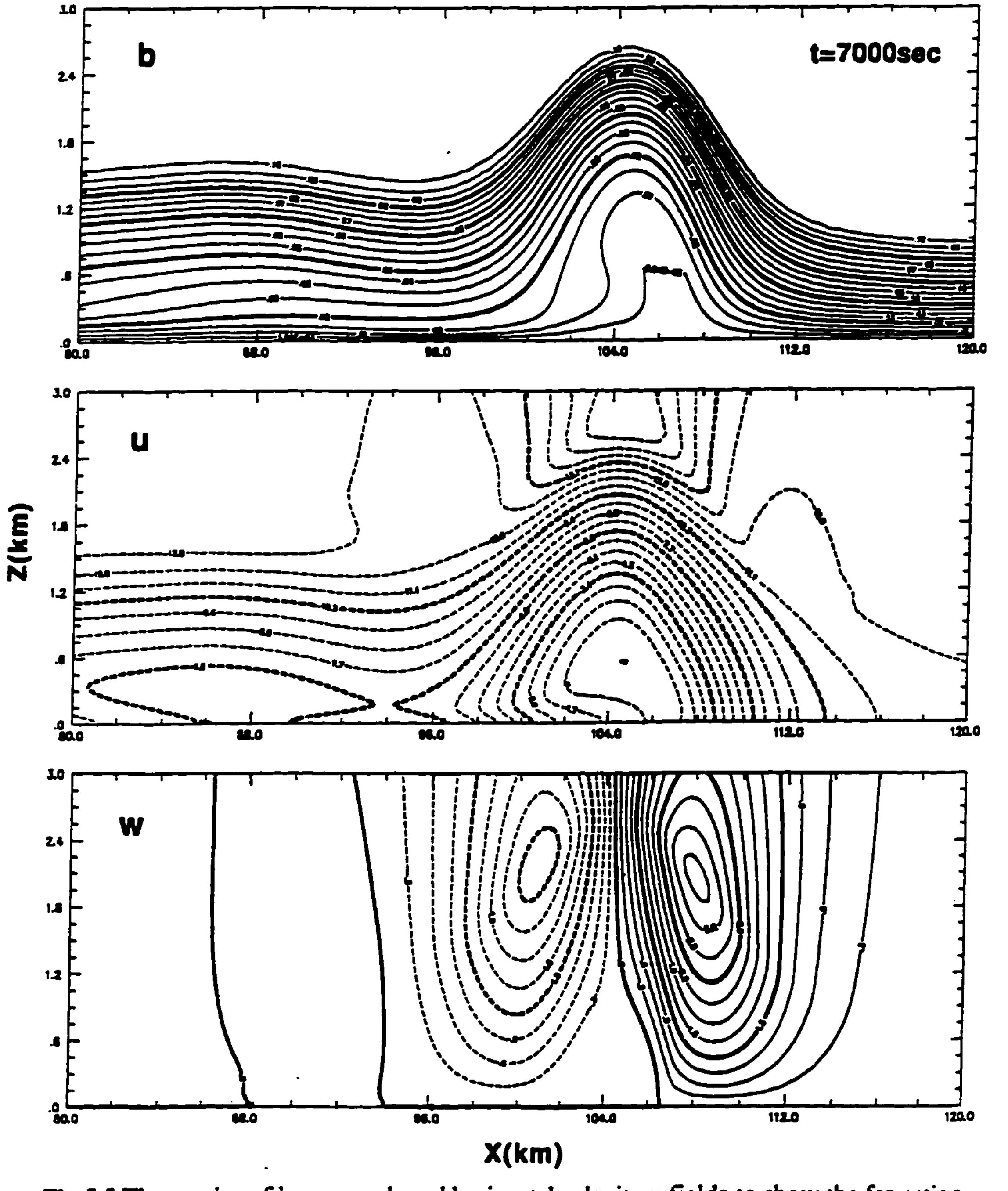

Fig.5.5 Time series of buoyancy b and horizontal velocity u fields to show the formation of reversed recirculation region.

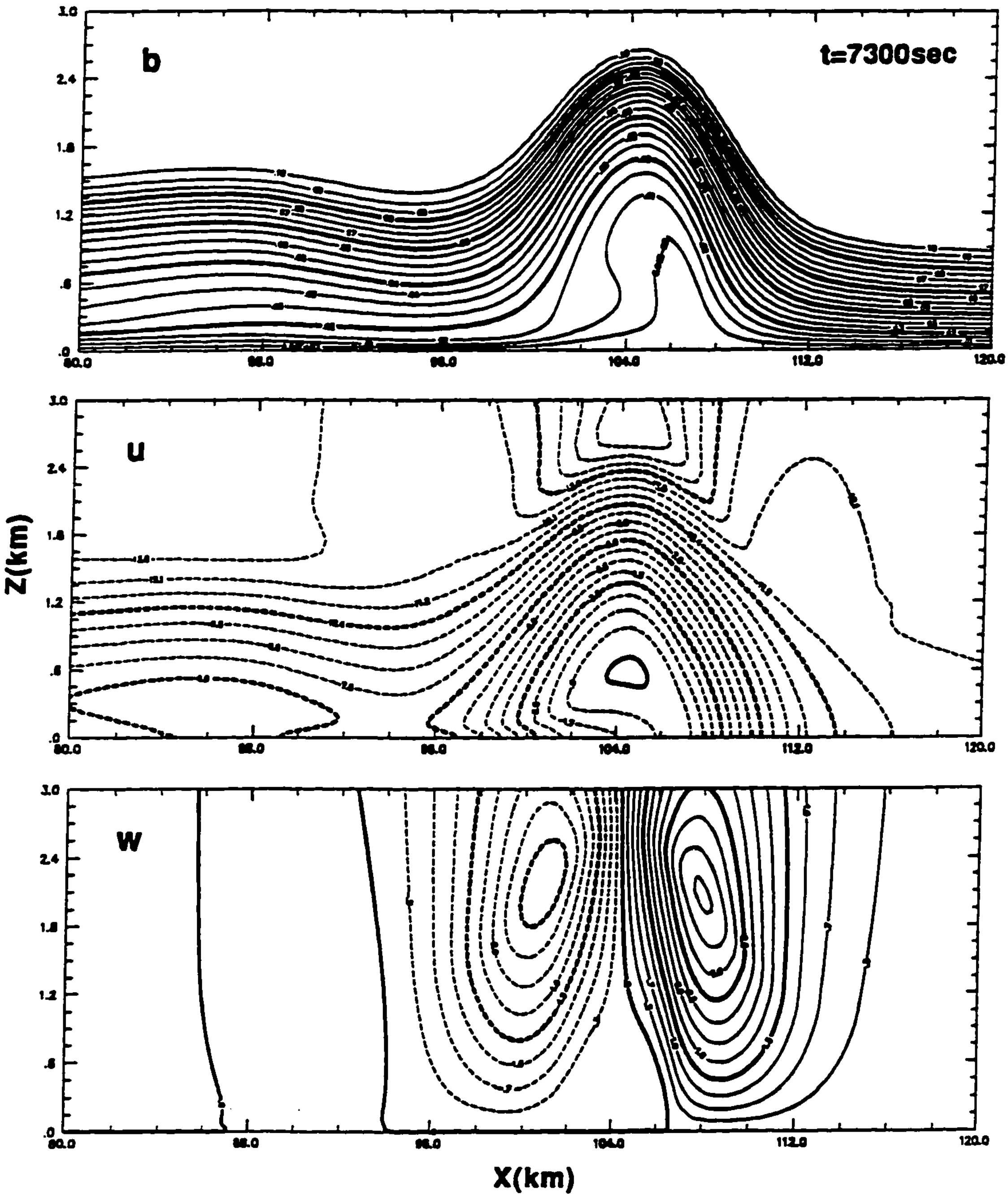

Fig.5.5 (Continued)

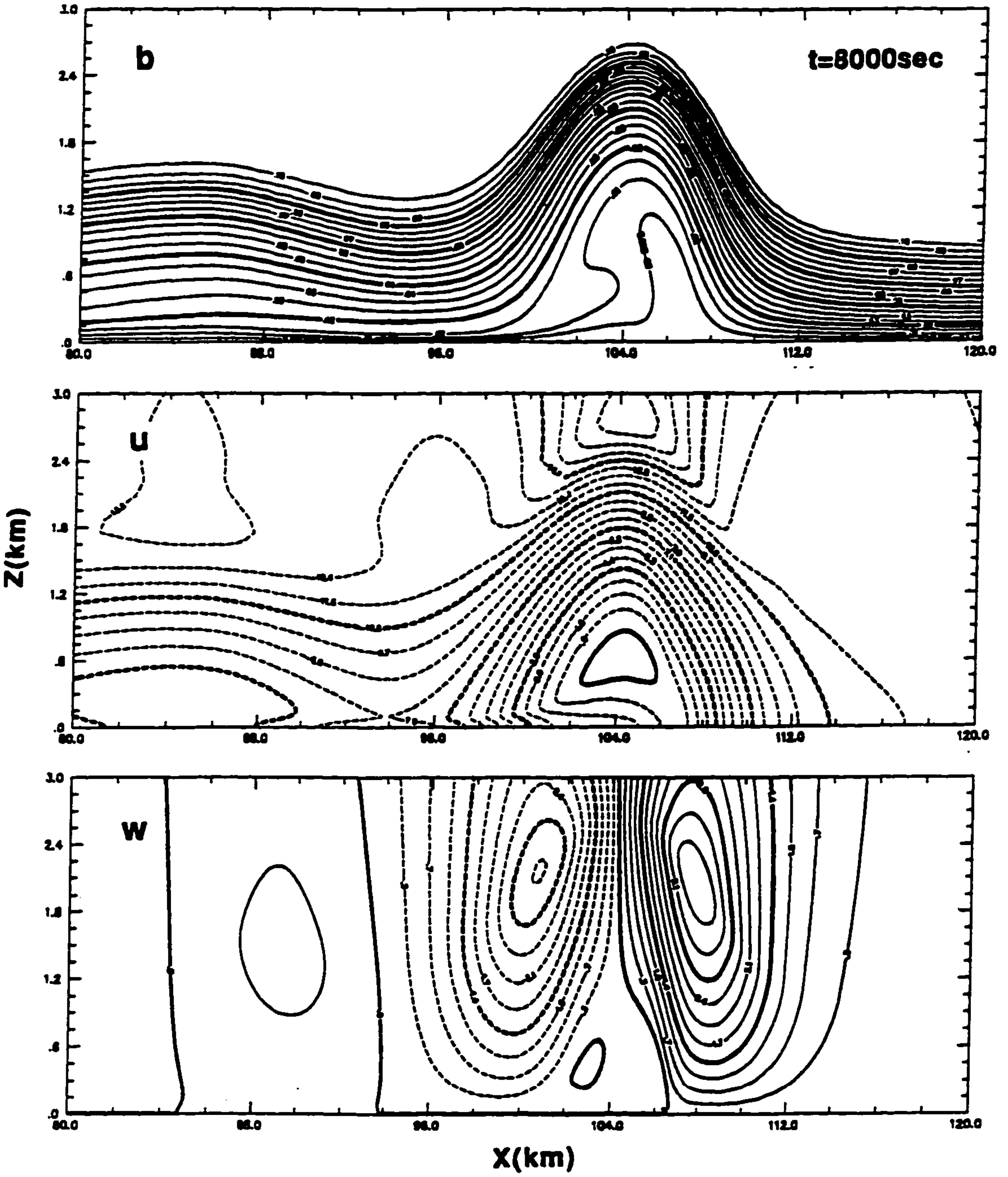

Fig.5.5 (Continued)

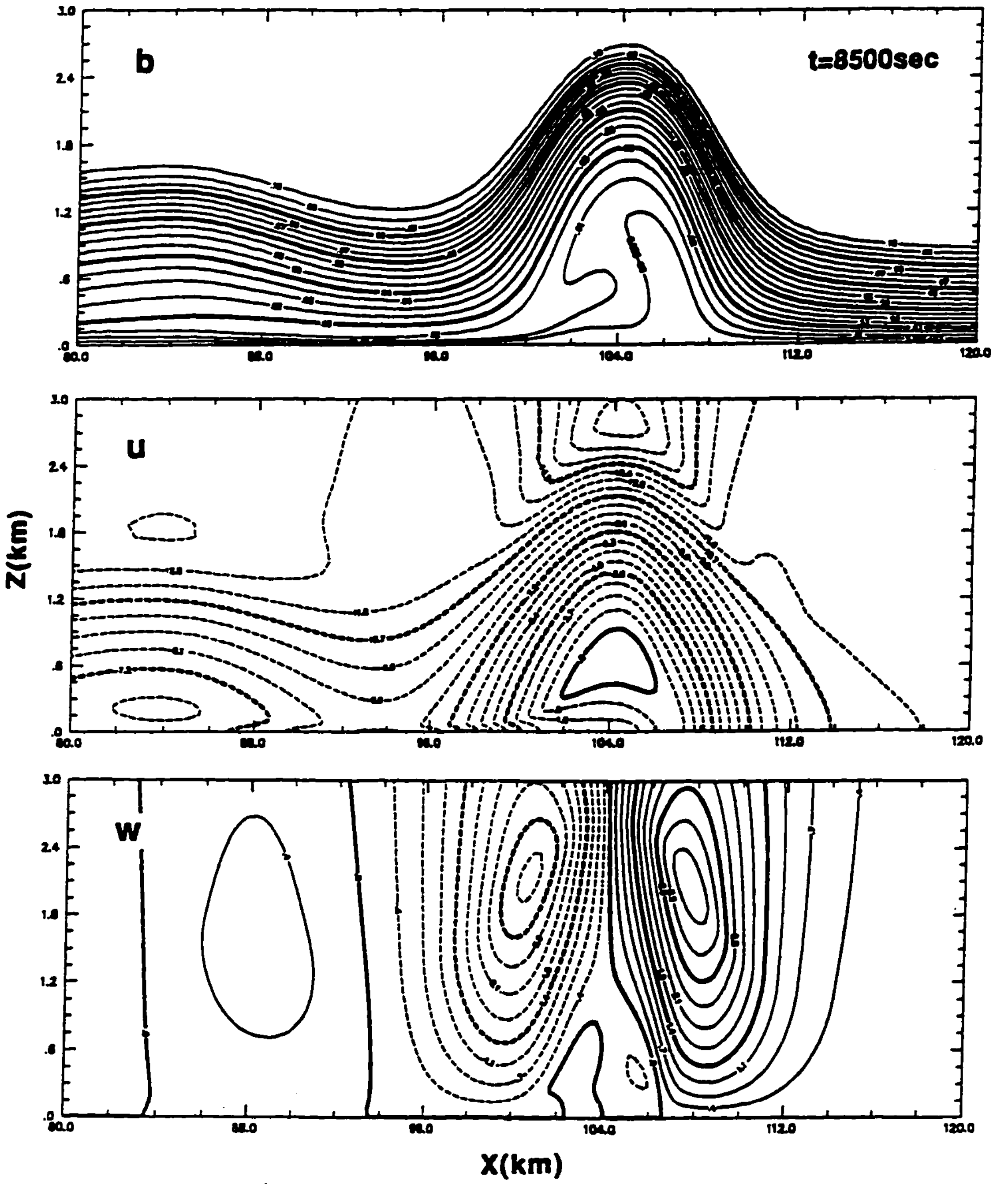

Fig.5.5 (Continued)

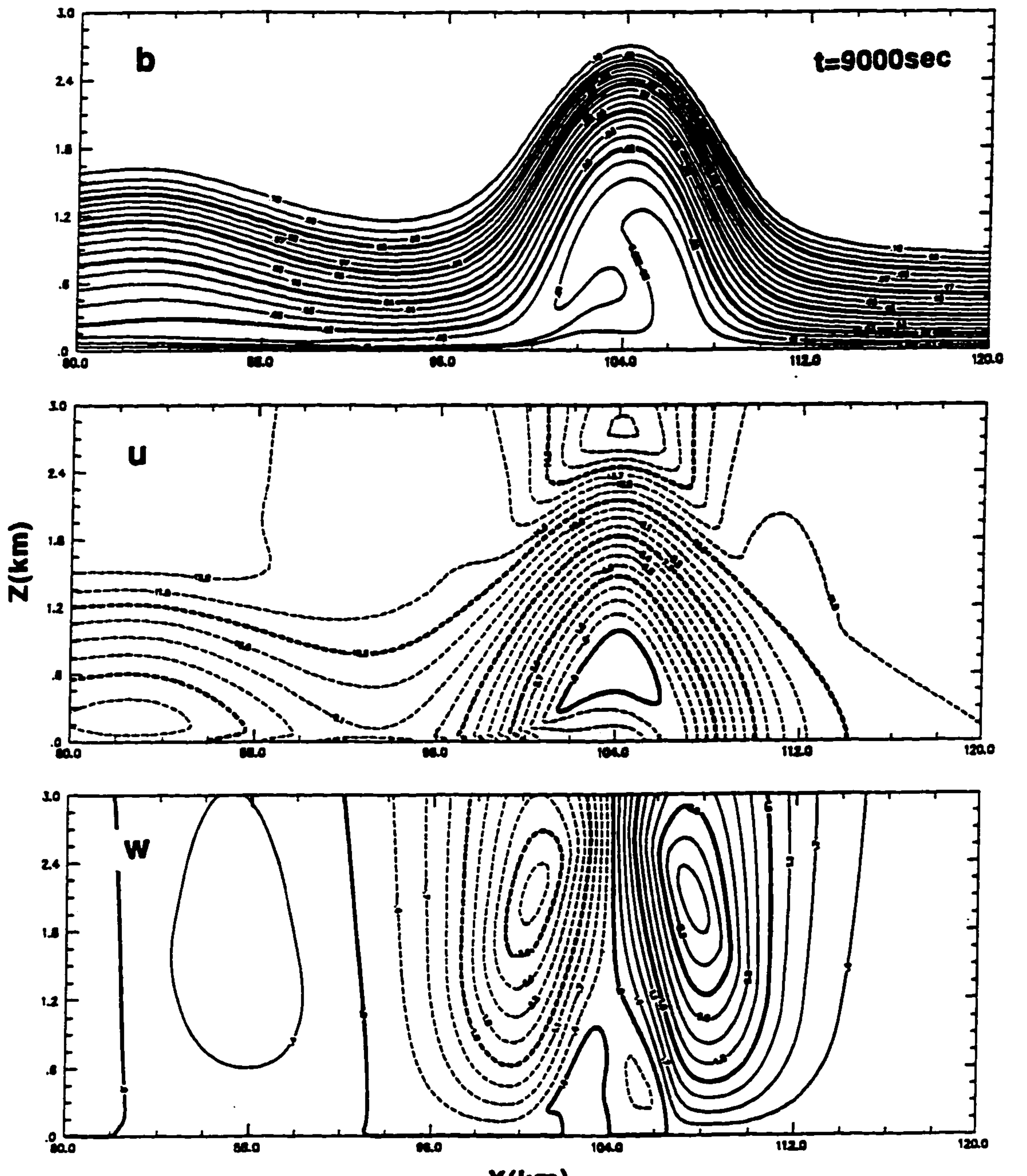

Fig.5.5 (Continued)

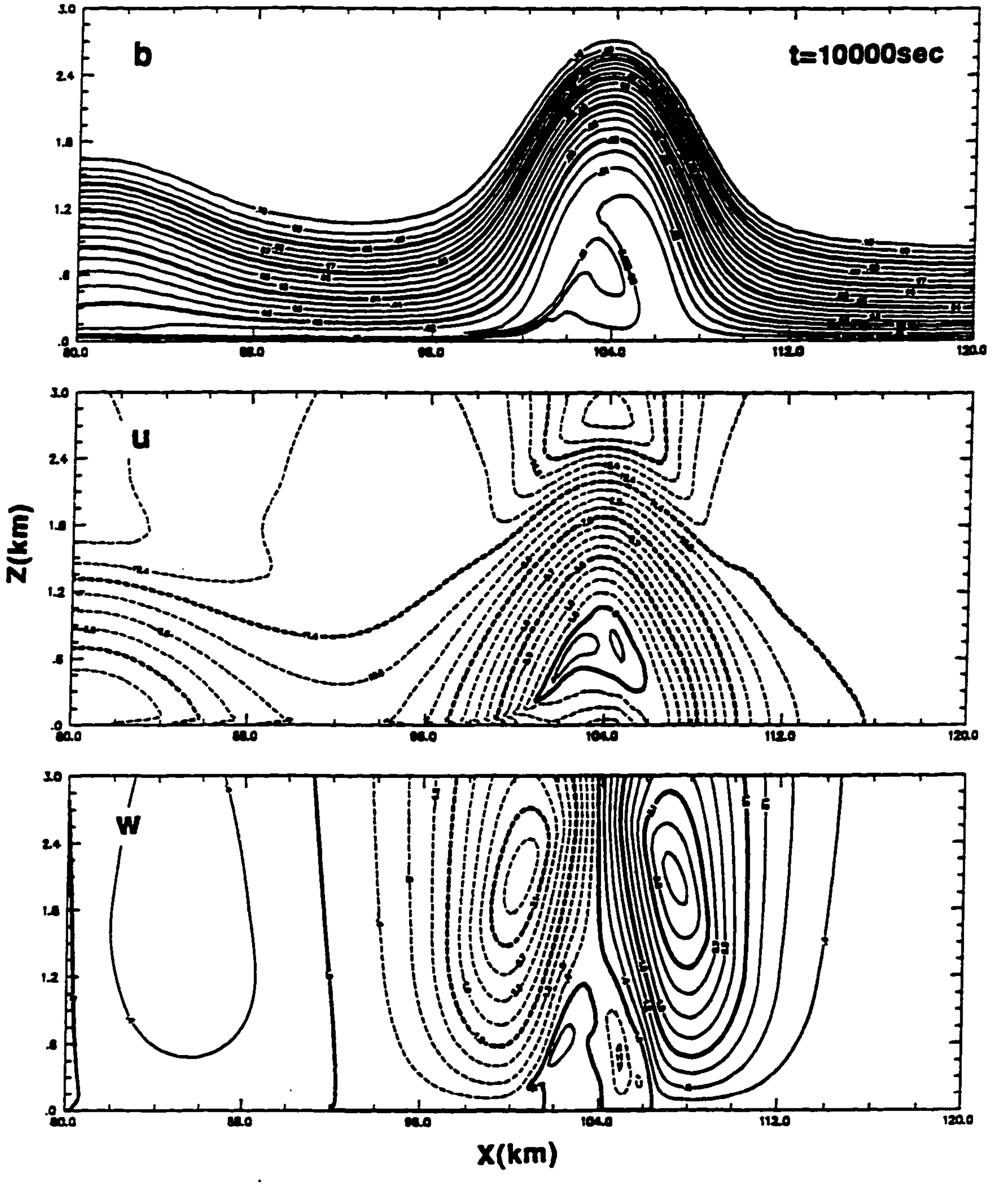

Fig.5.5 (Continued)

amplitude pure solitary wave with amplitude (1800m) displayed in Fig.5.2. The maximum u is located at about 1100m height above the ground. Note that the ground is frictionless in these simulations.

Horizontal velocity u and vertical velocity w fields also show there are smaller scale movements in the recirculation region. In some simulations, more than one positive-negative pair of vertical velocity appears in the recirculation region. The reason is that although in this numerical simulation the fluid is inviscid physically in the model equations, the numerical dissipation induced by the lowest-order (6th order in our advection scheme) term of truncation error in the numerical scheme can not be avoided. This kind dissipation plays a role like viscosity to reduce all gradients and generate turbulence in the fluid. After a period of time the fluid in the recirculation region is further mixed by numerical dissipation. The almost constant potential temperature θ within this region, observed in Fig.5.2 (b field) and 5.6, confirms the mixing effect of numerical dissipation. The dissipation also affects the fluid outside of the recirculation region, the amplitude of the solitary wave is slowly decreasing during the simulation. But comparing with the fluid within the recirculation region the velocity gradients are weaker outside, the dissipation effect is not so obvious.

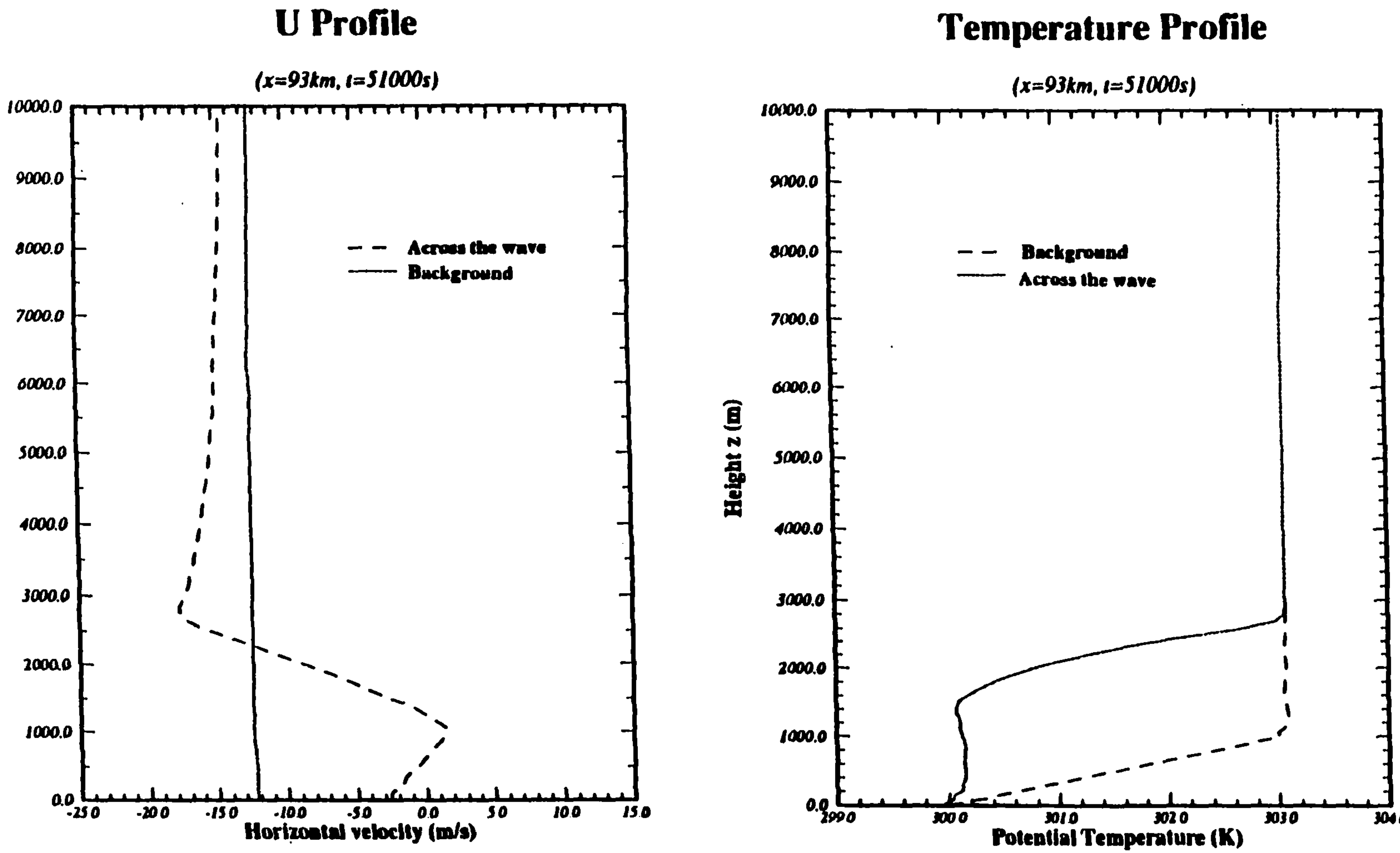

Fig.5.6 Vertical profiles of (a) horizontal velocity u and (b) potential temperature θ across the center of a large amplitude pure solitary wave with amplitude (1800m) obtained from the simulation.

5.3 Configurations of normal recirculation within large amplitude solitary waves

Fluid inside of recirculation region has the possibility to rotate in the same direction as the outside flow. We call this normal recirculation. As seen in Fig.5.3a, in this case positive horizontal velocity region R' will also be inside of recirculation region Rr' like the reversed recirculation case, but the bottom of region R' attaches the ground.

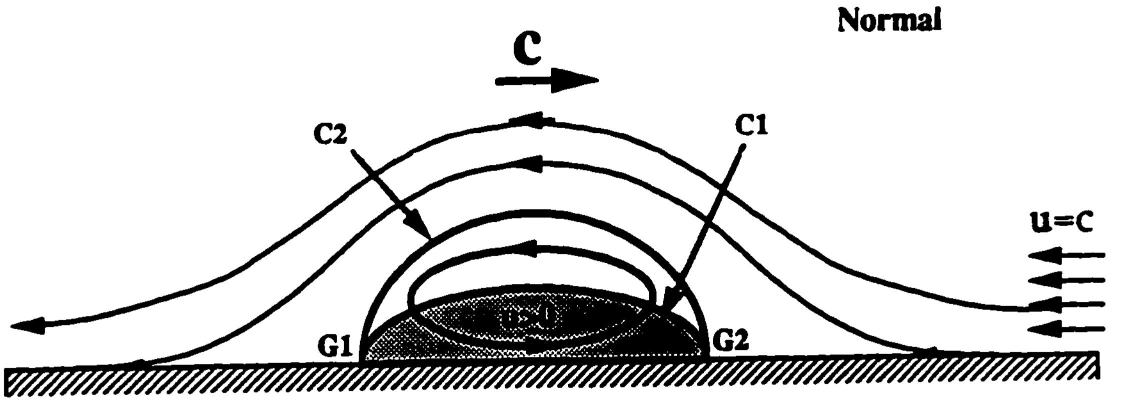

Fig.5.7 As in Fig.5.4 but for normal recirculation.

Assuming the upper boundary of R' as C1 (Fig.5.7) on which u is equal to zero, but w is not because fluid flows through it. Based on Eq.(5.1), $\frac{\partial\theta}{\partial z}$ must vanish on the boundary C1. Note w=0 on the ground. Following the similar arguments used in previous section, with maximum u on the ground fluid within the Rr' circulate in the same direction as the outside flow (Fig.5.7). The most outside closed streamline marks the upper boundary C2 of Rr' along which u and w are not equal to zero. Hence it can also be demonstrated that the normal recirculation does not violate any physical principals as well.

However, so far normal recirculations have not been found in our simulations.

5.4 Trapping and leaking effects of recirculation region

Generally, in a moving frame zero velocity indicates that fluid at those points is stationary relative to the frame. If this frame moves with the wave, those points with zero velocity are stationary relative to the wave or, from other point of view, are moving with the wave.

Referring to our previous analysis, we know the recirculation region, in a frame moving with the speed of a large amplitude pure solitary wave, can be closed by a boundary and ground. It means that there is no fluid across this boundary. Hence in a fixed frame the fluid on this boundary moves with the solitary wave. In other words, the fluid within the recirculation region is trapped by this large amplitude solitary wave.

But our numerical results show that the boundary of region Rr is not totally closed. It can be found that, in the u field (in Fig.5.2), the zero contour of u is not attached to the ground at the lee side of the recirculation region where the horizontal velocity is negative. This gap is observed after the large solitary wave formed. It implies that fluid within the recirculation region is continuously leaking backward from the solitary wave.

In order to confirm and clearly reveal this fact, we used a passive tracer technique to mark with a positive number the fluid within the region Rr, and the rest of fluid with zero. This allow us to trace the movement of fluid originating within the region Rr. This procedure is exactly analogous to injecting a amount ink into a certain block of fluid within the region Rr. A block of ink is injected at t=0 sec when the large solitary wave is well formed, then the ink flows within this block of fluid. A time series of ink field from t=0 sec to t=10000 sec is displayed in Fig.5.8. It clearly visualized the leaking process.

The reason of leaking is viscosity. As we mentioned in the previous section, although the fluid in our numerical experiment is physically inviscid, numerically it is not. The wave is affected by the numerical viscosity, strongly on the interface, where there is strong shear due to the reverse circulation, between the recirculation and outside regions. The fluid near the interface is mixed by the fluid inside and outside Rr due to the strong shear. Thus a portion of trapped fluid persistently diffuses out whereas a portion of outside fluid blends into the recirculation region. Once diffusing out of the recirculation region, the trapped fluid will flow with the outer flow. The fluid inside Rr is continuously being "peeled off" from the boundary of Rr by the outside flow. Since, in this moving, frame the outside flow is always moving against the stationary wave and the fluid inside Rr, the fluid leaks backward. In a fixed frame, the trapped fluid is continuously leaking and depositing behind the wave as the wave propagates forward.

On the other hand, we found that the major part of ink is kept in the recirculation region. It confirms the trapping effect of the recirculation region. However even with continuous leaking, the trapped fluid still lasts quite long time in the recirculation region.

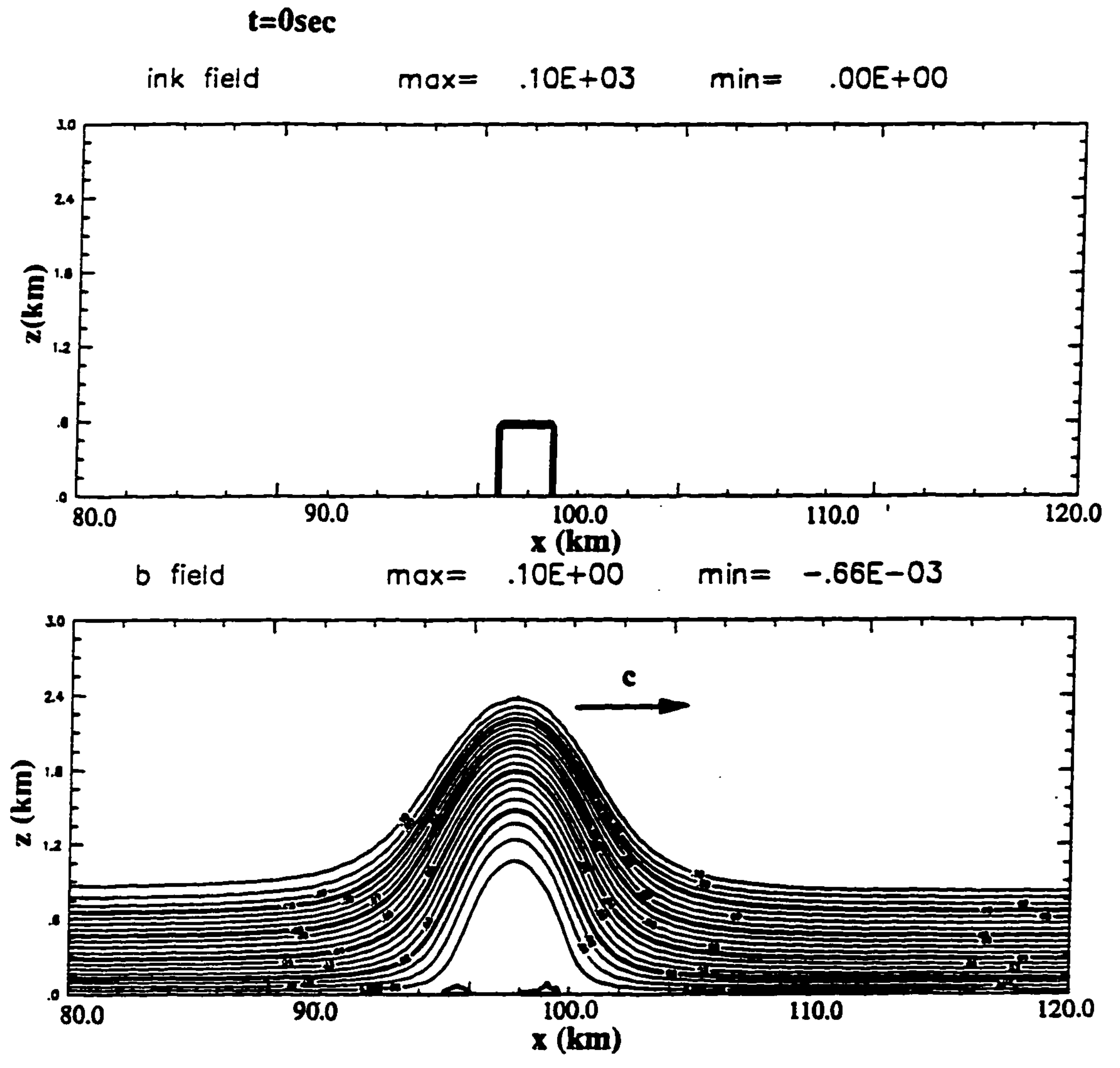

Fig.5.8 Time series of ink field to show the trapping and leaking effects of a large amplitude solitary wave.

t=1000sec

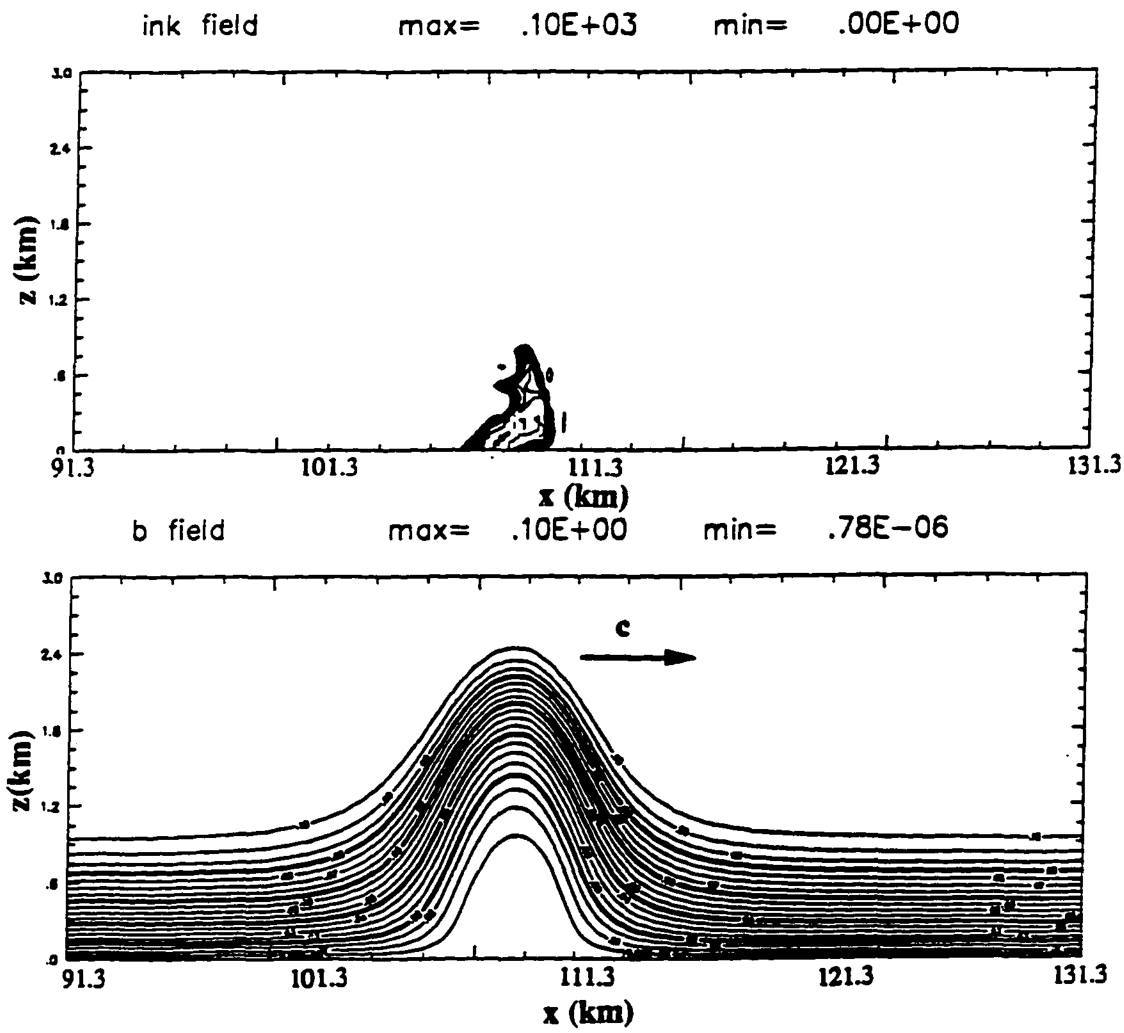

Fig.5.8 (Continued)

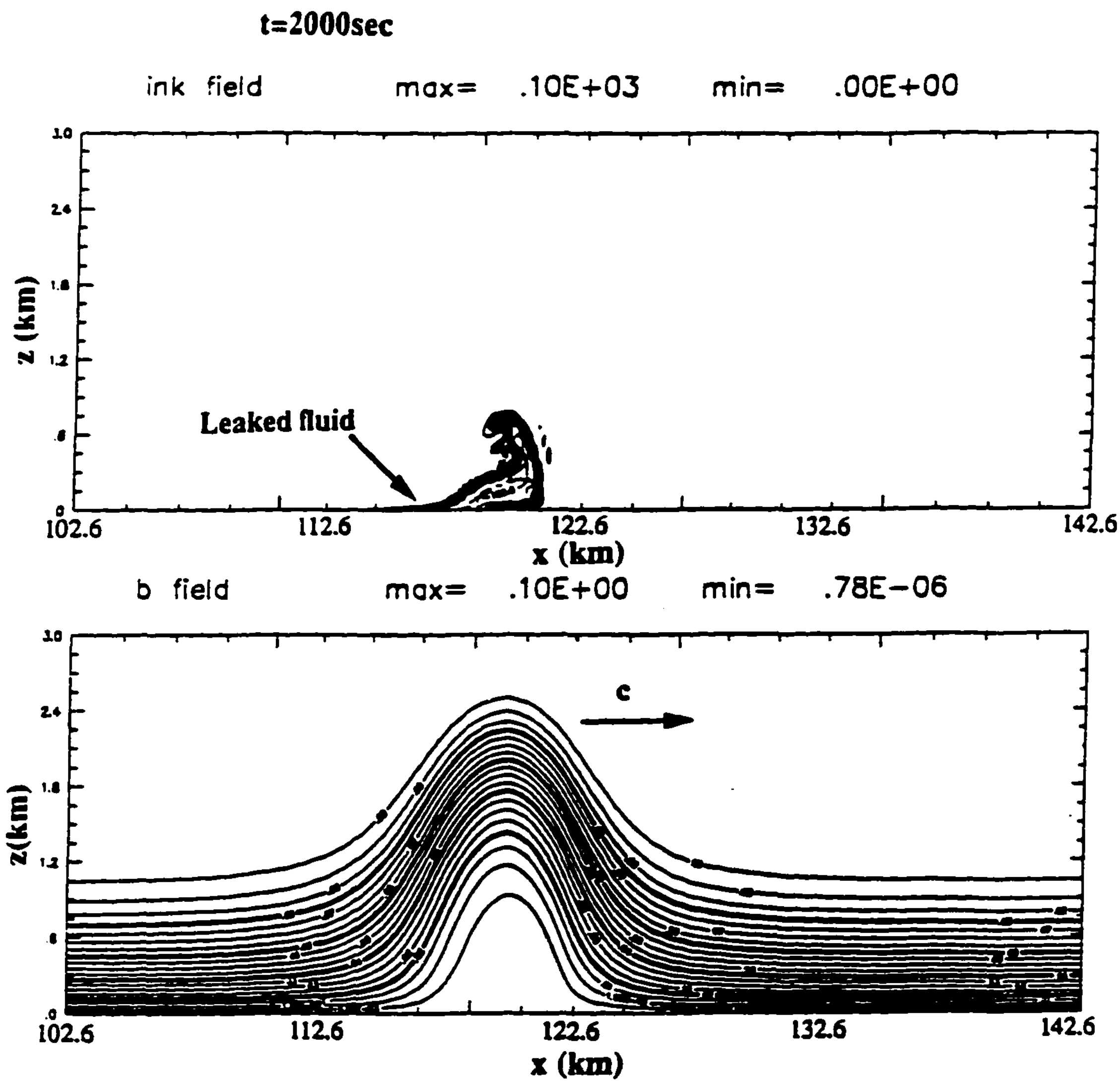

Fig.5.8 (Continued)

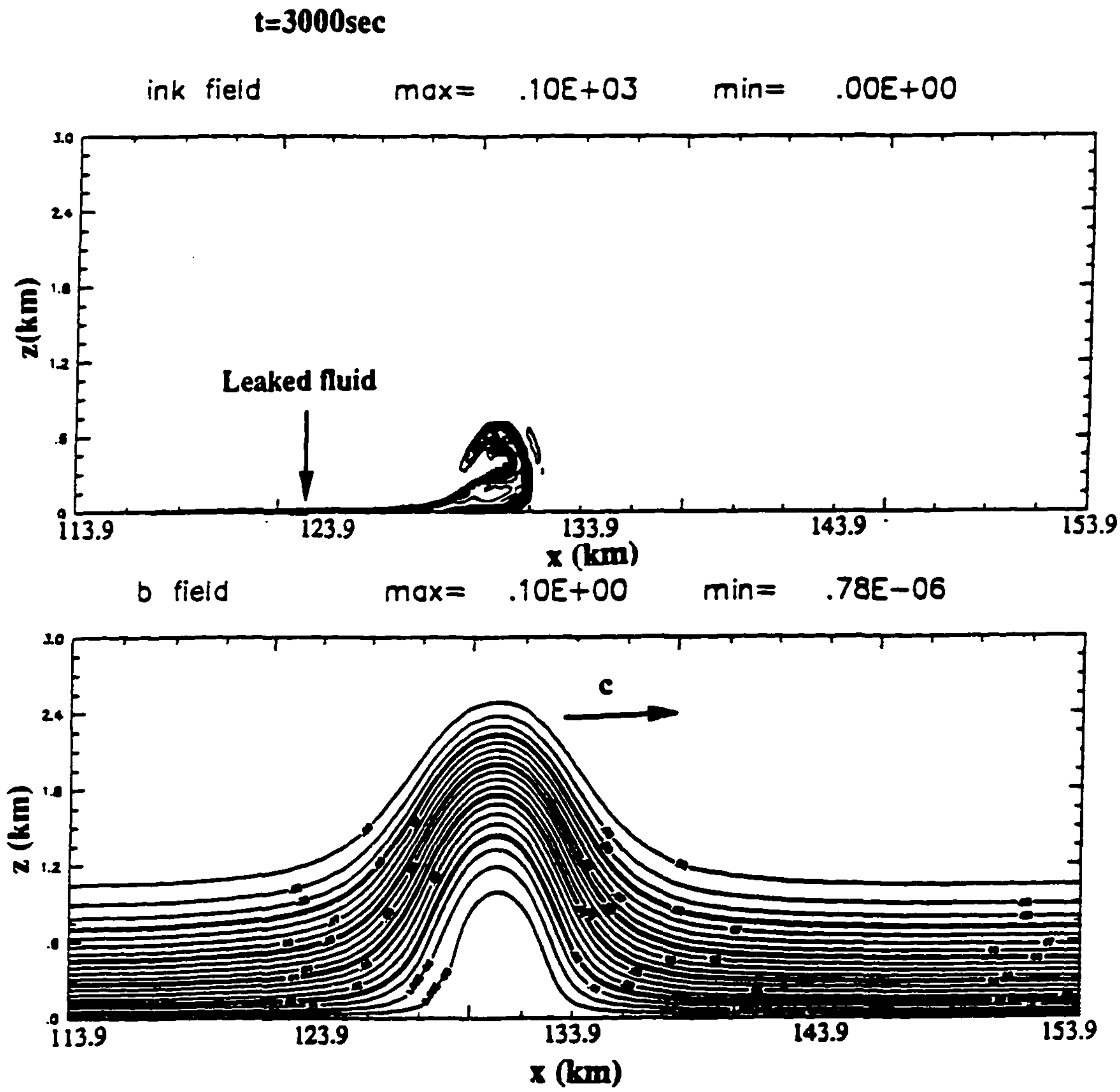

Fig.5.8 (Continued)

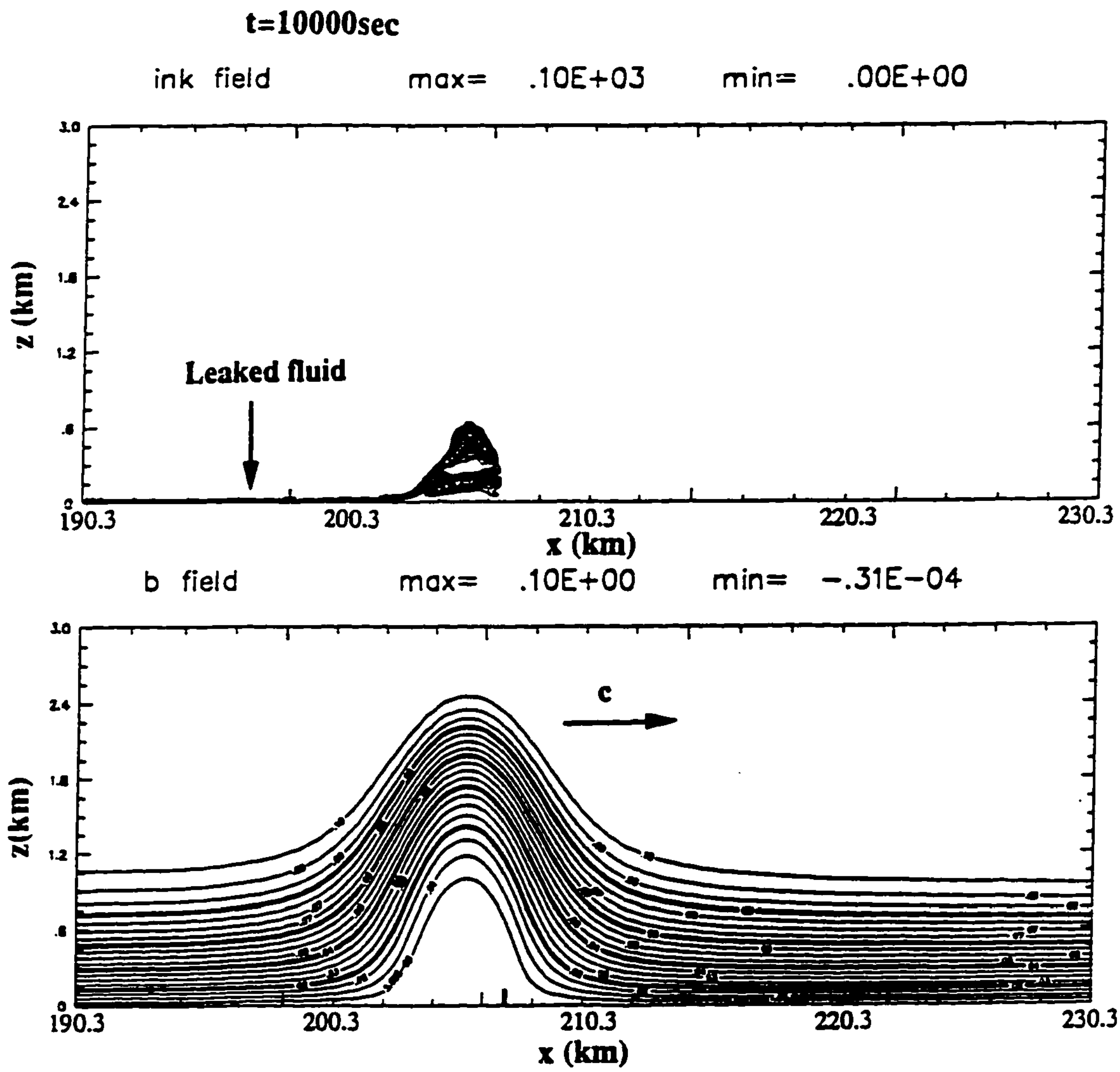

Fig.5.8 (Continued)

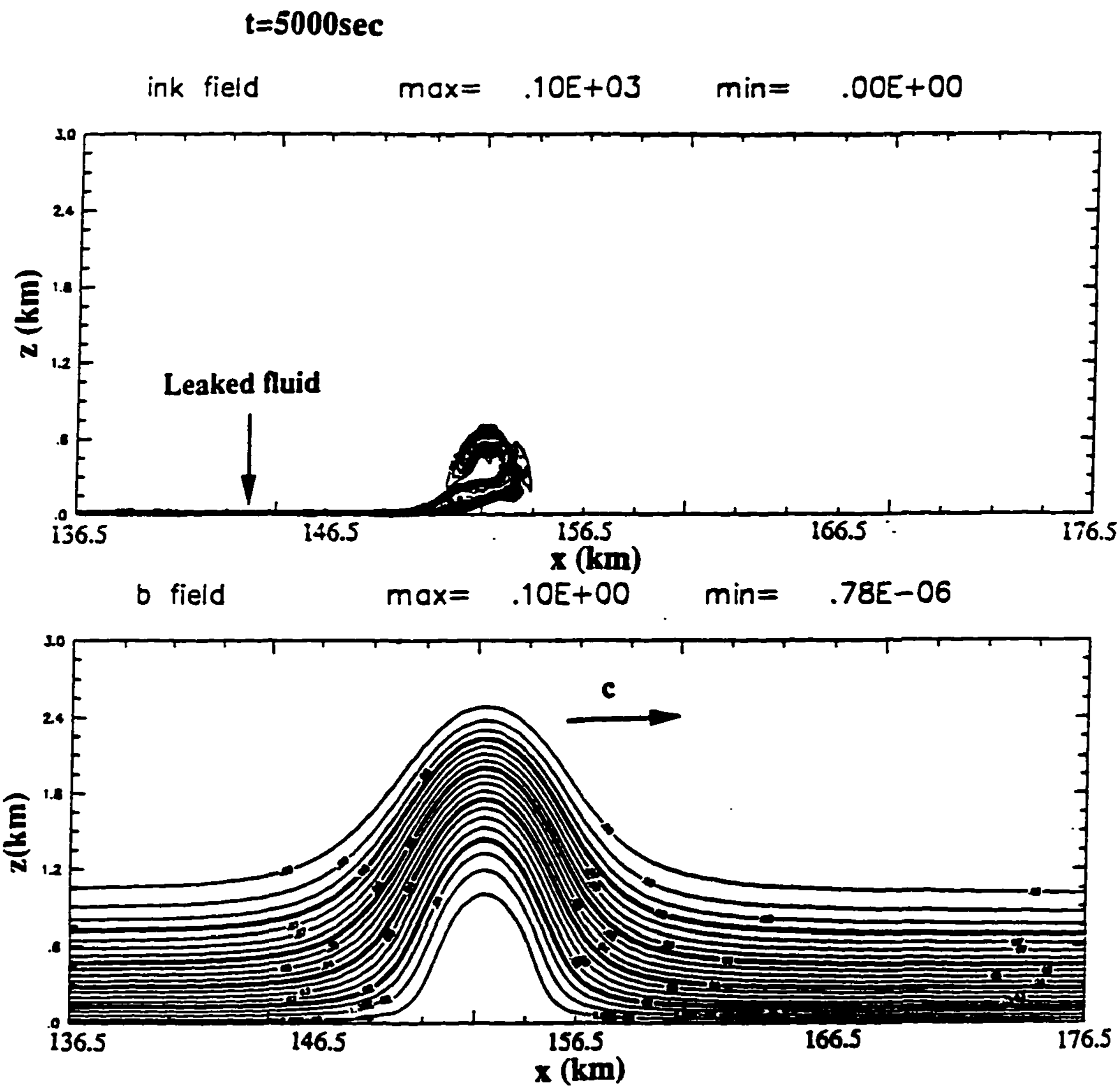

Fig.5.8 (Continued)

In our numerical simulation without any physical viscosity, ink injected inside of recirculation region can last at least several thousand seconds. The evolution of ink density in the recirculation region in the simulation displayed in Fig.5.8 is shown in Fig.5.9.

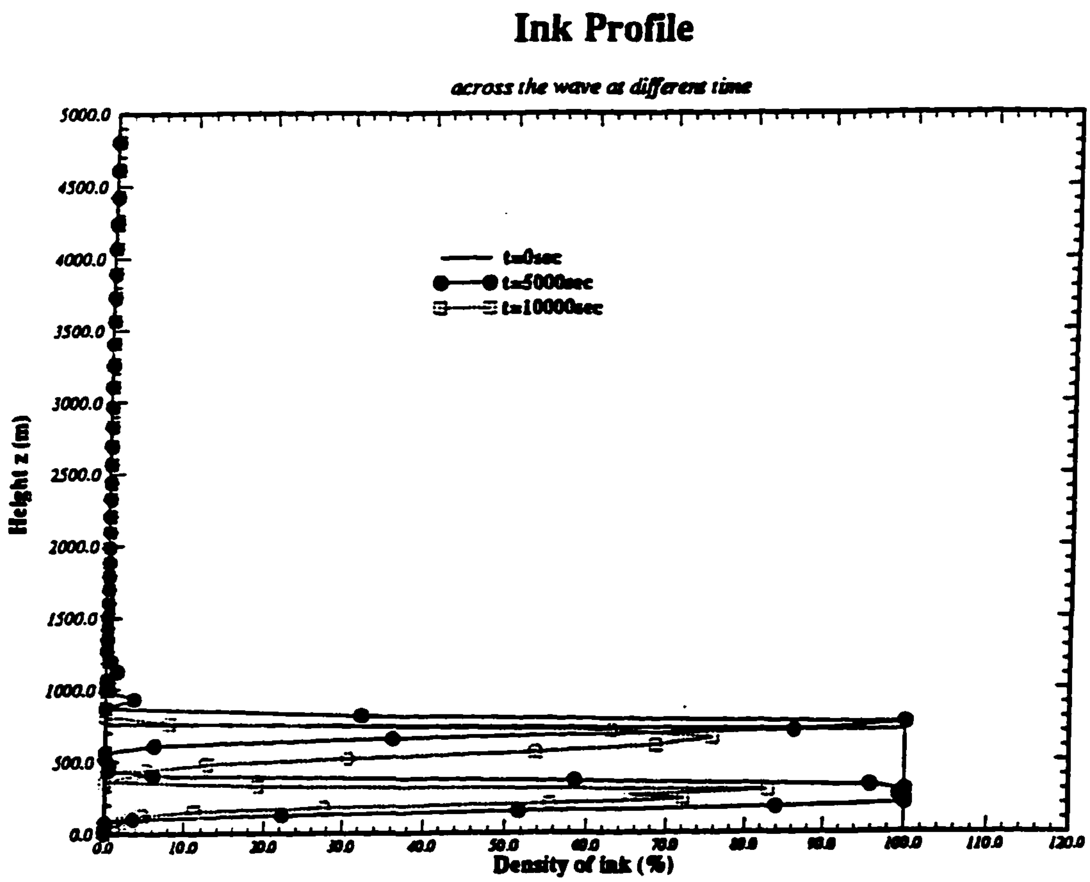

Fig.5.9 Ink profiles across the center of a large amplitude solitary wave with a reversed recirculation at t=0 (solid line), 5000sec (dot-dashed line), and 10000sec (square-dashed line).

At initial time, the density is 100% when ink is injected. After 5000 sec, due to recirculation the ink has been redistributed, and two density maxima (100%) appear. At t=10000 sec, even though with further mixture and leaking, the density maximum has only dropped 18%. With 11.3m/s wavespeed, during this period of time (10000 sec), the solitary wave and trapped fluid have traveled for about 110 km. This result denotes that large amplitude solitary waves can transport trapped fluid for a long distance in a proper environment. Theoretically, if fluid is inviscid numerically as well as physically, the fluid within the recirculation region will be totally trapped by a large amplitude solitary wave without any leaking.

So if hazardous materials originates in or near the source of large amplitude waves, they may not only be spread out by the wind or diffusion, but also transported by waves. It is important for monitoring and warning of potential danger over a larger area.

An interesting and strong evidence of trapping in the atmosphere is reported by Christie (1992). He states a visible cloud and strong smell of smoke, which is originated in the bush fire in the area of generation of waves and is about 200 km away from the observation site, appeared with the solitary waves.

When Stamp and Jacka (1995) investigated deep-waters waves with recirculation regions by using laboratory experiments, he also observed "fluid was continuously entrained into and ejected from this region". But he mentioned the boundary of recirculation region is not clear because turbulence develops in this region.

5.5 Relations among amplitude, wavelength, and wave speed of solitary waves

Using the background potential temperature field and the method described in the previous section, solitary waves with different wavelengths and amplitudes can be generated in the simulations. By adjusting the inflow speed, we can keep one solitary wave stationary in the domain. The wavelengths and amplitudes of solitary waves can be estimated through analysis of the numerical results.

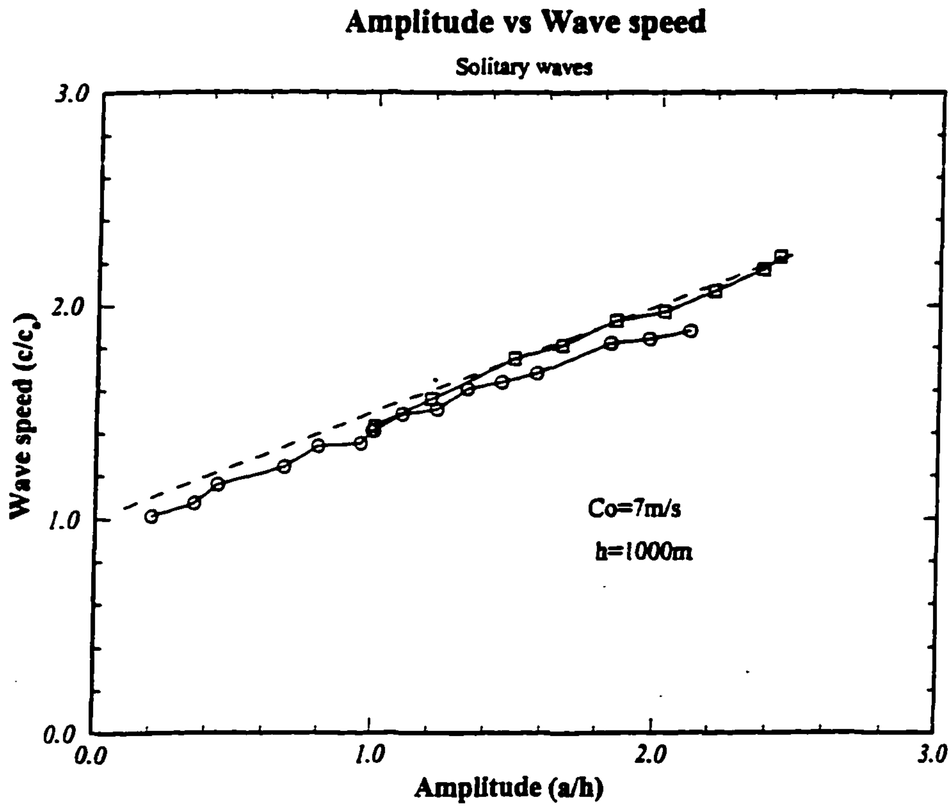

Fig.5.10 The relations between amplitude and speed of solitary waves. Circle solid line represents our simulation results; Square solid line Stamp's results; Dashed line weakly nonlinear theory's results.

The relation, attained from the simulations, between amplitude and speed of solitary waves is shown in Fig.5.10. We found the wave speed increases almost linearly as amplitude increases. In order to compare our results to others, the results obtained by Stamp and Jacka (1995), and prediction of weakly nonlinear theory are also plotted in the same figure. The results of weakly nonlinear theory are calculated by using Eq.(4.6) The simulation results coincide with others quite well for all waves, even with weakly nonlinear theory.

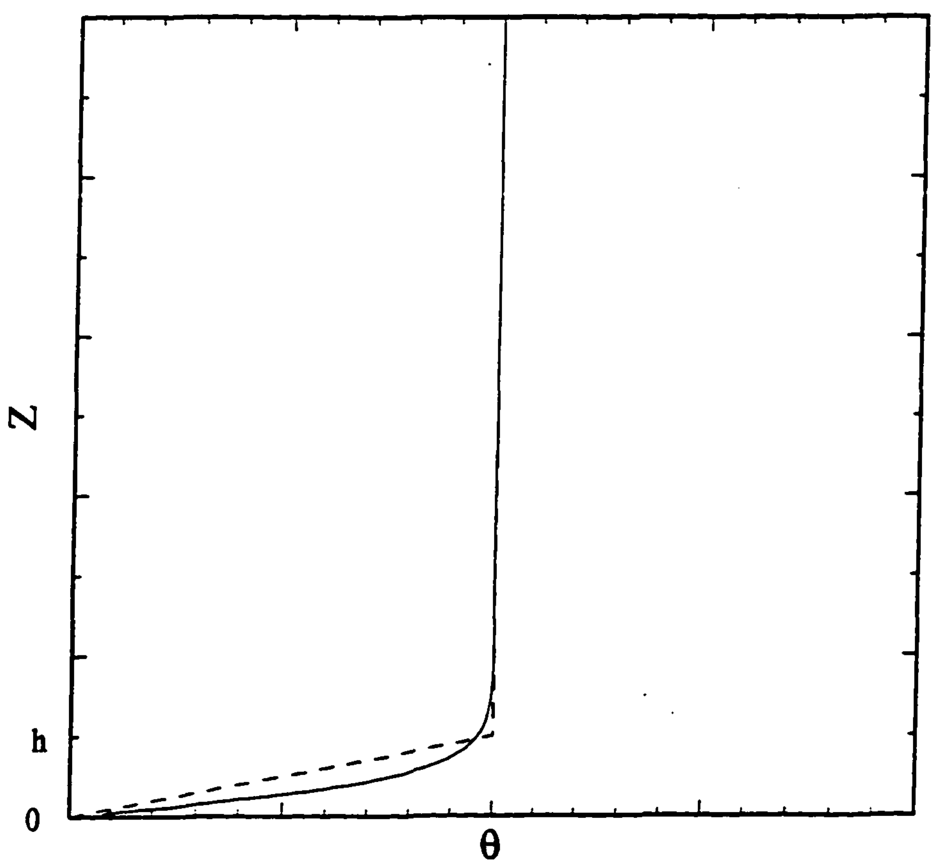

Fig.5.11 Potential temperature profiles (1) tanh (solid line); (2) linear (dashed line). H is the height of stable layer.

Note that, in the experiments of Tung et al. (1982) and Stamp and Jacka (1995), the density profile of background field is described or approximated by a hyperbolic tangent function. Whereas in our experiments, the potential temperature of background field constantly increases in the stable layer (i.e. with constant Brunt- Väisälä frequency) above the ground, and is constant above the stable layer. It is known that the shape of density profile is the same as the shape of potential temperature in an incompressible fluid. Hence the results they obtained are comparable to ours under the similar background field. Note that these two profiles are only slightly different near the transition zone (Fig.5.11).

Fig.5.12 is the plot of the amplitude versus the wavelength. The results of weakly nonlinear theory, Stamp and Jacka (1995) and Tung et al. (1982) are also shown in this plot. It can be clearly seen that the wavelength decreases as amplitude increases for small amplitude solitary waves ($a/h<1$). When the amplitude exceeds the height of the stable layer h, the wavelength increases with increasing amplitude.

It is evident that the simulation results shown in Fig.5.12 are consistent with the results obtained in the laboratory (Stamp and Jacka, 1995). Because weakly nonlinear theory is valid only for small amplitude solitary waves ($a/h<<1$), the large difference between the results predicted by weakly nonlinear theory and the simulation are expected. But, c/c_0 *vs* a/h is surprisingly in good agreement with weakly nonlinear theory. However we should not be mislead by this agreement because it does not extend to λ. Only for the smallest amplitude (200m, i.e. $a/h=0.2$) is the solitary wave in the simulation close to the theoretical prediction.

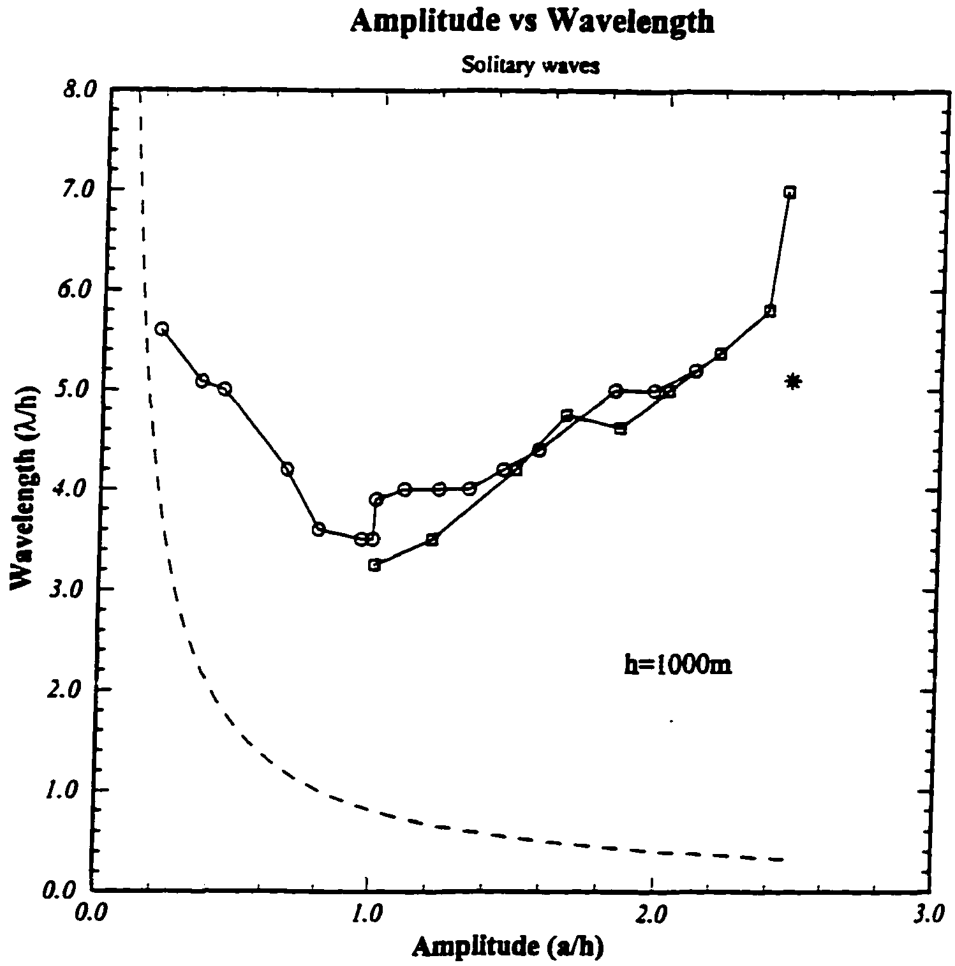

Fig.5.12 As in Fig.5.10 except for the relations between amplitude and wavelength. 'Star' represents the result of Tung et al..

For large amplitude solitary waves, as we discussed previously, one significant difference from small amplitude waves is that recirculation appears within the waves when the amplitude is reaching the height of stable layer. It is just the turning point of the curve of the relation of the amplitude and the wavelength. For this reason, we believe the recirculation within the waves critically affects the relation between the amplitude and the wavelength.

Chapter

6

The Effects of Eddy Diffusivity and Wind Shear on Solitary Waves

6.1. K Theory

The flow in the real atmosphere near the surface of the earth is strongly affected by the surface. The velocity at the surface vanishes due to the surface irregularities. As a consequence, even a small movement of air near the surface will cause a large wind shear, and it will generate turbulence. Meanwhile surface heating due to solar radiation will cause convective eddies. Such shear induced and convective eddies transfer momentum and heat between the lower and upper layers. Hence, the turbulent diffusion determines the dynamic structure of atmospheric boundary layer (ABL) rather than viscosity.

In the stable or neutral boundary layer, the generation of turbulence largely comes from the instability associated with wind shear. The traditional method to close the momentum and heat equations is to assume that turbulent flux is proportional to the local mean gradient of the quantity being transferred. Under horizontally homogeneous condition, the two dimensional momentum and heat equations give the momentum flux

$$\overline{u' w'} = -K_m \left(\frac{\partial \overline{u}}{\partial z}\right) \qquad (6,1)$$

and the heat flux

$$\overline{\theta' w'} = -K_h \left(\frac{\partial \overline{\vartheta}}{\partial z}\right) \qquad (6,2)$$

where K_m and K_h are the diffusivities of momentum and heat respectively. This closure is often referred to as K theory.

6.2. Effects of eddy diffusivity

6.2.1 *Model results for uniform eddy diffusivity*

In this section we shall investigate the effects of eddy diffusivity on solitary waves in the ABL. First, as a reference, we make a simulation without any kind surface friction. Then simulations will be executed with surface friction and different diffusivity coefficients under the same initial and boundary conditions, and background potential temperature and wind fields. By comparing the formation, development and propagation of the waves, and the speed, amplitude and structure of the wave with and without surface friction and eddy diffusivity, we can acquire the knowledge about the effects of surface friction and eddy diffusivity.

In the first simulation (S6.1), $K_m = K_h = 0$. A coldpool built up during the initial stage (t from 0 to 400 sec), is used to generate solitary waves in a calm (i.e. $u_{in} = 0$) stable layer. The height of coldpool is 3 km. After cooling, the maximum temperature difference between coldpool and the environment on the ground is about 4K. In order to show the motion of the cold air during the simulation period, the coldpool region is marked by 'ink'(a passive tracer) at the initial time.

Fig.6.1 is a series of buoyancy b field to show the generation, development and propagation of the waves in S6.1. Two solitary waves can be clearly found in the buoyancy fields. The first wave (with larger amplitude) has amplitude a=1290 m and propagates at speed c=10.6 m/s. The wavelength of the first wave is 3890m. The maximum vertical velocity w_{max} induced by the first wave is 3.0m/s. The second one has a=820 m, λ=3610 μ and c= 8.7m/s.

The detailed structure of these two waves in u, w and b fields in shown in Fig.6.2. The maximum horizontal velocity u_{max} induced by the first wave is 11.4m/s which is larger than the speed of the wave and locates above the ground at z=521 m. In the w field beneath the large positive-negative w pair there is small positive-negative pair with opposite motion to the outside pair. According to the analysis in Chapter 5, it means reversed recirculation exists within the first solitary wave.

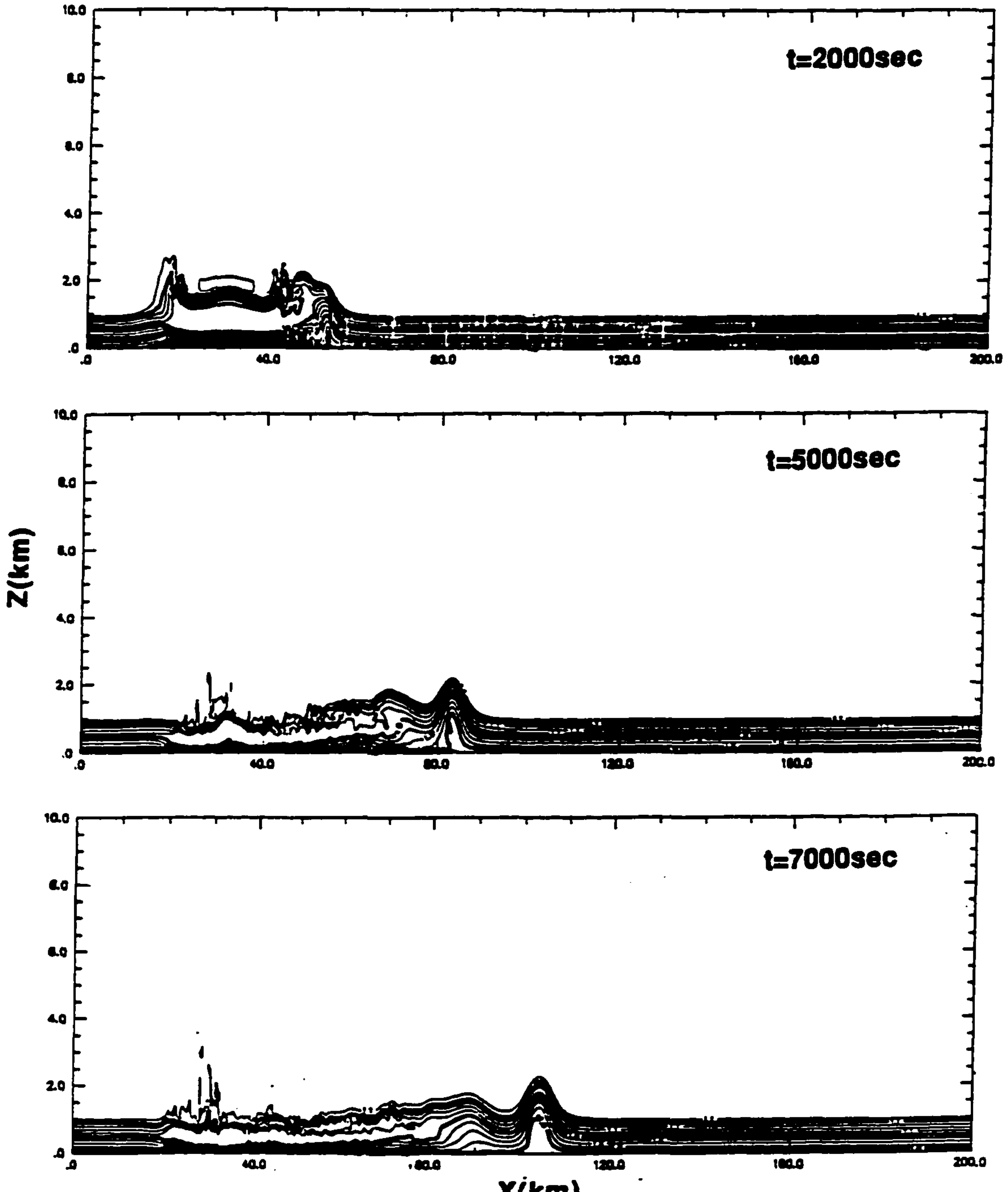

Fig.6.1 Time series of buoyancy b field for $K_m = K_h = 0.0\,m^2/s$.

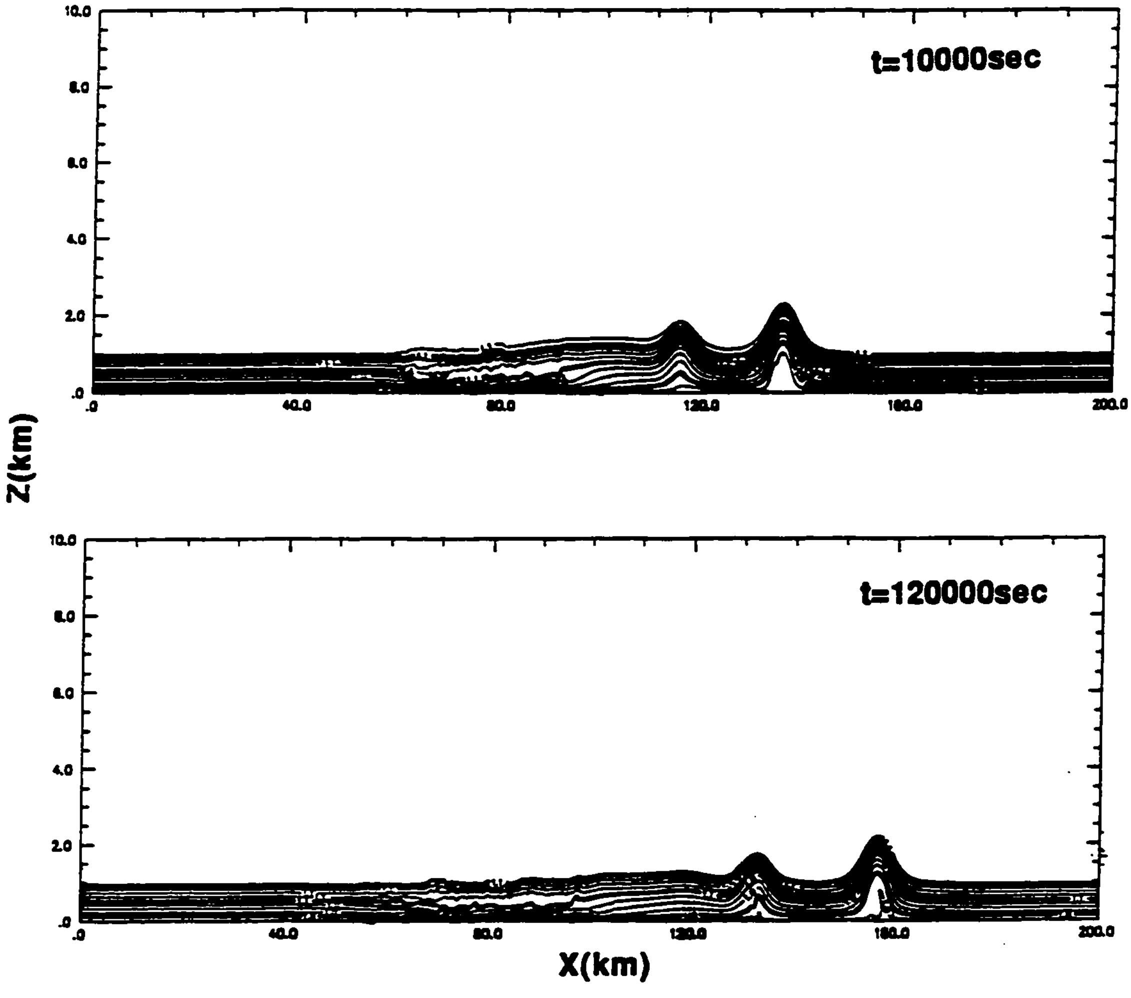

Fig.6.1 (Continued)

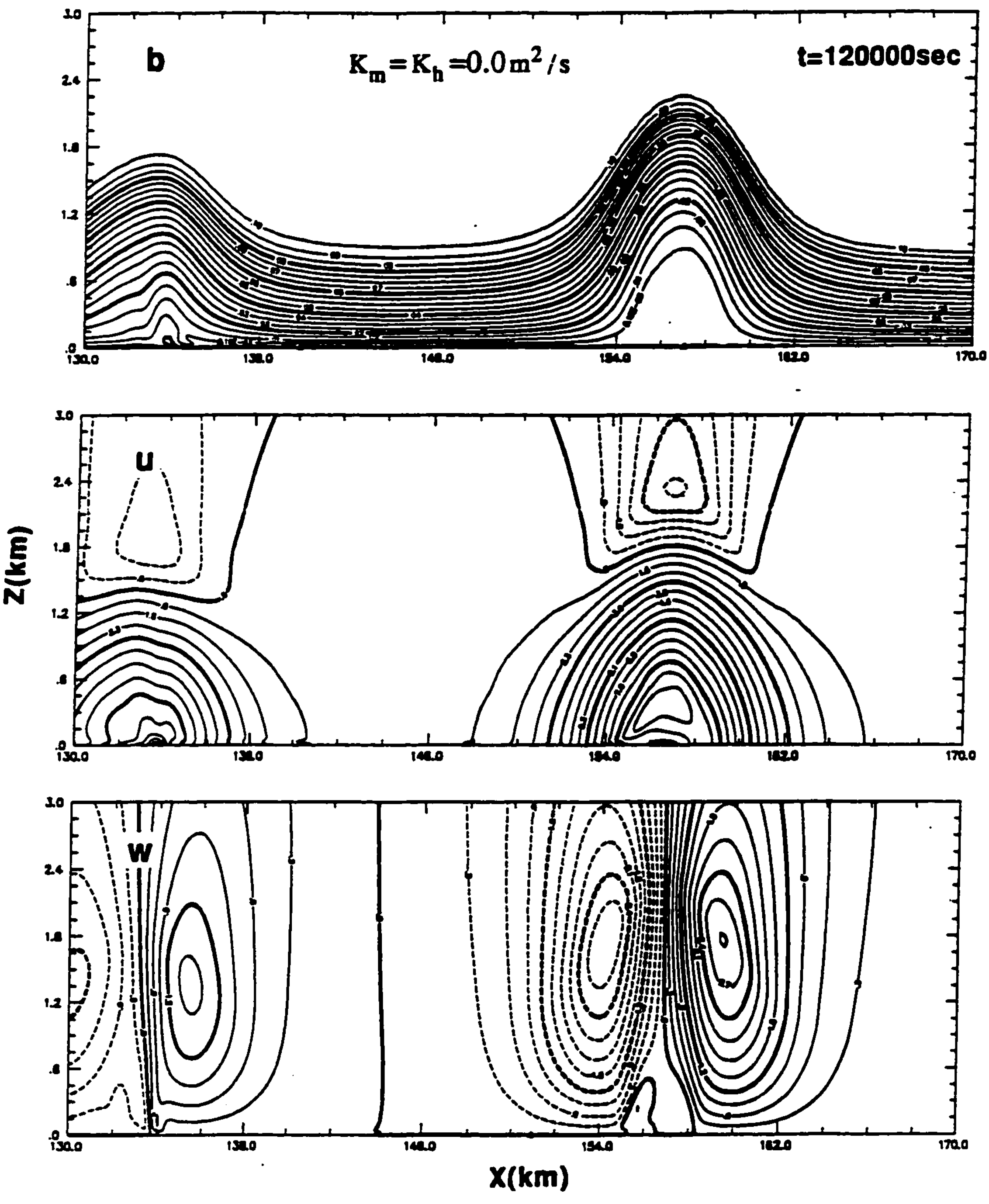

Fig.6.2 Magnified buoyancy b, horizontal velocity u, and vertical velocity w fields at t=12000sec for $K_m = K_h = 0.0\,m^2/s$.

After conducting the reference simulation, several simulations with surface friction and different viscosity coefficients are carried out. For simplicity, K_m and K_h are assumed constant. Typically, in the ABL $K_m \approx 1m^2/s$ (J.R. Garratt, 1992). First, to investigate the effects of weak diffusivity, relative small value of the eddy viscosity coefficient K_m and diffusivity K_h are chosen. They are $0.1 m^2/s$ and $0.12 m^2/s$ respectively, because Brost and Wyngaard (1978) found that the ratio between K_h and K_m is about 1.2. The height of boundary layer (1 km) is the same as the height of stable layer. u is set to be zero on the ground. So the heat and momentum exchanges due to turbulent eddies only affect the waves in the layer below 1 km. To avoid a sudden influence on the flow, which may generate unrealistic perturbations if the diffusivity terms are turned at the a certain time during the simulation, these heat and momentum exchanges act from the beginning of the simulation including the coldpool building stage.

Fig.6.3 shows a time series of buoyancy b field for the simulation (S6.2) with eddy diffusivity. We also found two solitary waves are generated and the evolution of these waves in this simulation is similar to the evolution in S6.1. The amplitude and speed of the leading solitary wave is 1270m and 10.4m/s, which are slightly smaller comparing with the wave in S6.1. The wavelength and u_{max} decrease to 3750m and 11.0m/s at t=12000 sec. Because u_{max} is still larger than the speed of the wave, the recirculation occurs within the wave. The detailed structures of solitary waves shown in Fig.6.4 confirm the existence of reversed recirculation. In the w field, a reversed motion pair appears within the wave. However, the w_{max} is 3.0m/s, the same as in S6.1. These results indicates that eddy diffusivity does have some effects on the waves (i.e., decreasing the amplitude, speed, and u_{max} of the wave), but not too much with relatively small values of K_m and K_h that were chosen.

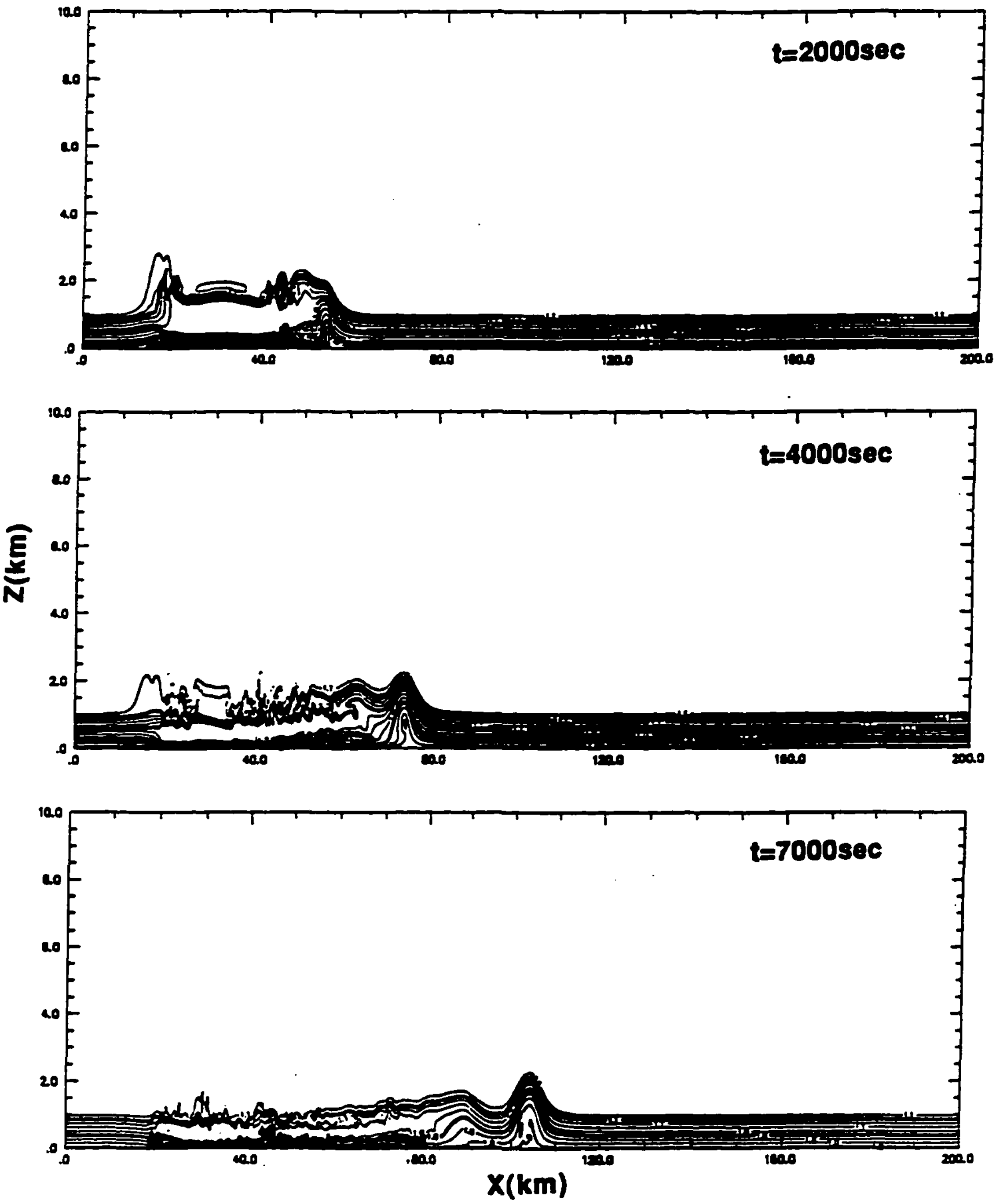

Fig.6.3 Time series of buoyancy b field for uniform $K_m = 0.1\,m^2/s$ and $K_h = 0.12\,m^2/s$.

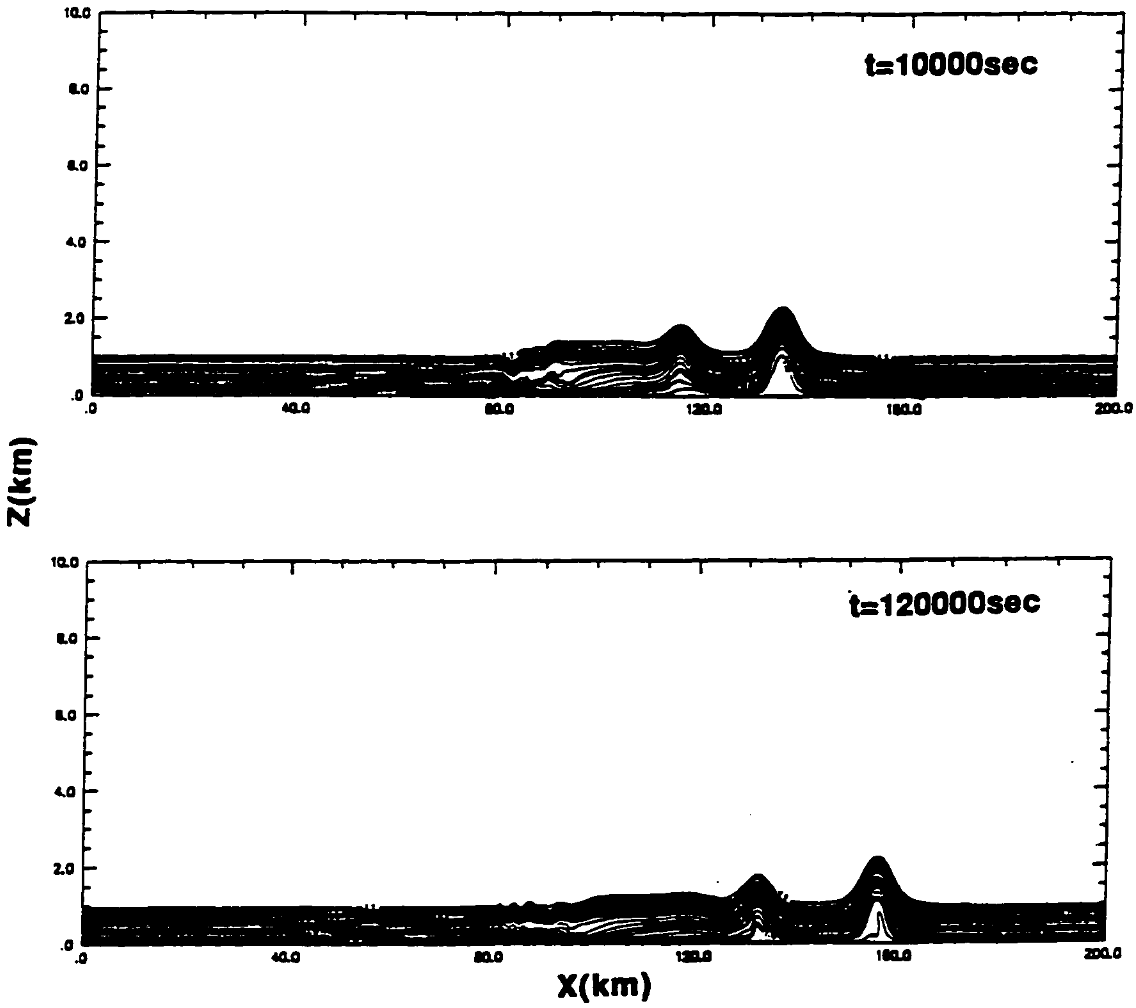

Fig.6.3 (Continued)

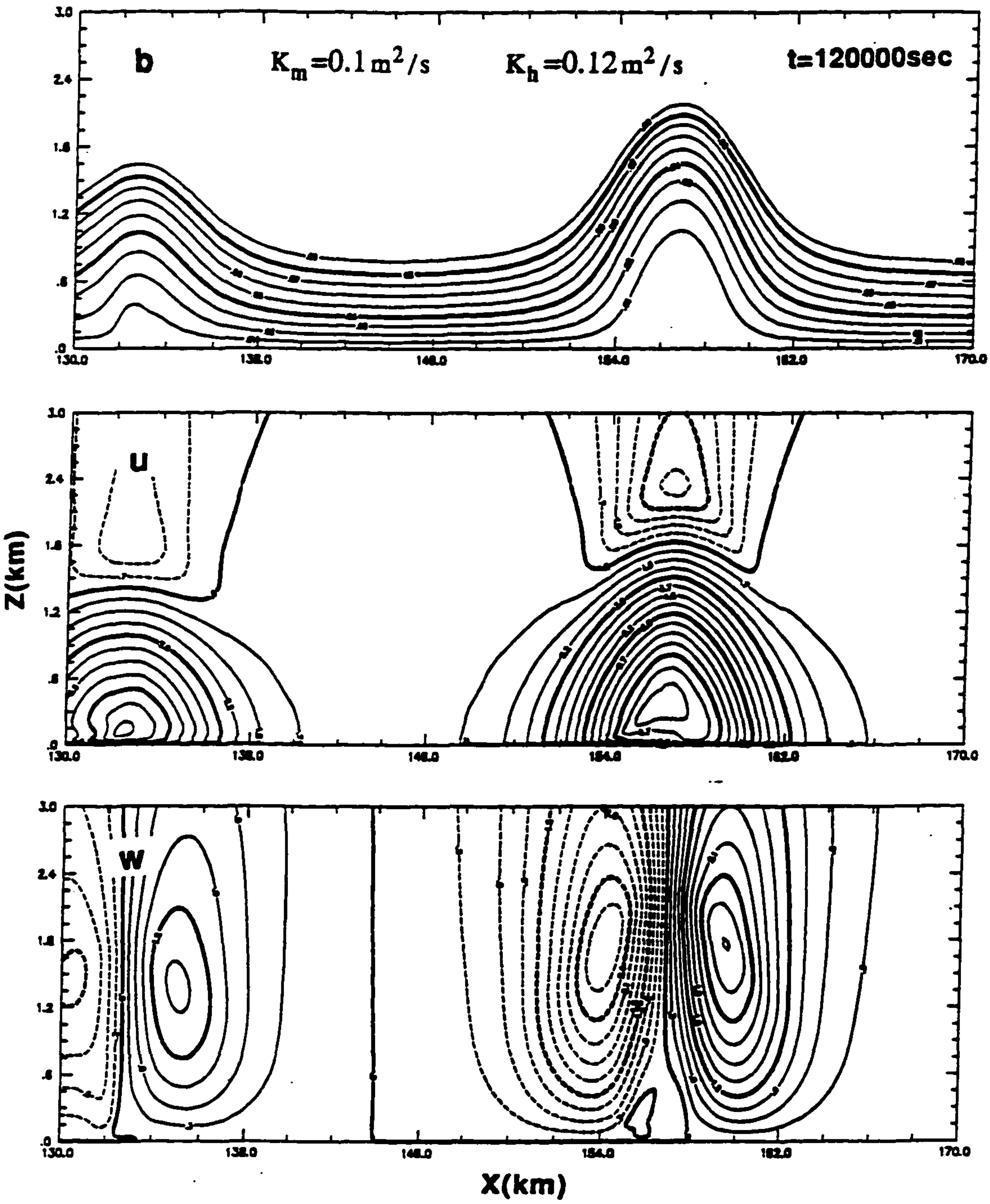

Fig.6.4 Magnified buoyancy b, horizontal velocity u, and vertical velocity w fields at t=12000sec for K_m=0.1 m^2/s and K_h=0.12 m^2/s.

In order to enhance the effects of turbulent diffusivity in ABL, the typical eddy viscosity coefficient K_m and diffusivity K_h in the ABL are increased to $1.0 m^2/s$ and $1.2 m^2/s$ in this simulation (S6.3). Because the generation and evolution of the solitary waves in this simulation are similar to the previous one (S6.2), the time series of b, u and w fields are not shown here. Fig.6.5 shows the detailed structures of the two solitary waves which are generated under the condition of increased diffusivity. In this case, the amplitude a and the speed c of the first solitary wave are reduced to 1220m and 10.3m/s respectively. The wavelength also shrank to 3470m. The most important point is that u_{max} decreases to 10.0m/s which is smaller than c. It indicates the recirculation does not exist within the first large amplitude solitary wave although $a/h \approx 1.22$ which is slightly larger than 1.2 for the criterion of the existence of recirculation (Davis and Acrivos, 1967). In Fig.6.5 the small positive-negative pair no longer appears beneath the large pair in w field. It is another evidence of disappearance of recirculation. So strong eddy viscosity in ABL will impede the formation of recirculation.

6.2.2 *Model results for a more realistic vertical dependence of eddy diffusivity*

Generally, in the real ABL turbulent fluxes usually are not simply proportional to the local mean gradients. Supposing K theory provides a reasonable estimate of the turbulent exchange, it still would not be proper to assume constant K_m and K_h. They vary rapidly with height. Based on their numerical studies, Brost and Wyngaard (1978) give a formula of eddy diffusivty as a function of z/h and h/L,

$$K_m = \kappa u_{*0} h \frac{(\frac{z}{h})(1-\frac{z}{h})^{1.5}}{1+4.7(\frac{z}{h})(\frac{h}{L})} \qquad (6,3)$$

where κ is von Karman constant, and a generally accepted value for it in the stable ABL is 0.4 (Kaimal and Finnigan, 1994). u_{*0} is friction velocity on the surface, h is the depth of stable ABL, and L is Monin-Obuhov length. They also found Eq.(6,3) "works about as well for K_h if 1.2 is inserted on the right side" of Eq.(6.3). That is,

$$K_h = 1.2\kappa u_{*0} h \frac{(\frac{z}{h})(1-\frac{z}{h})^{1.5}}{1+4.7(\frac{z}{h})(\frac{h}{L})} \qquad (6,4)$$

In the following simulations, Eq.(6,3) and Eq.(6,4) are used instead of constant K_m and K_h in Eq.(6,1) and Eq.(6,2). In S6.4, u_{*0}, L, and h are chosen as 0.3m/s (Garratt, 1992), 50m (Brost and Wyngaard, 1978), and 1000m. In S6.5, u_{*0} and h are the same as in S6.4 except L=500 m. We intend to make evidently different degrees of eddy diffusivity by choosing these two values of L. Fig.6.6 shows the profiles of $K_m 1(z)$ (L=50 m) and $K_m 2(z)$ (L=500 m) in whole boundary layer. The maximum value of $K_m 2(z)$ is about $6\,m^2/s$ which is 6 times K_m in S6.3.

Because structures of the waves generated in S6.4 are similar to the structures seen in S6.5, they are not shown here. Fig.6.7 displays magnified buoyancy b, horizontal velocity u, and vertical velocity w fields at t=12000 sec for $K_m(z)$ with L=500 m. But the values of amplitude, wave speed, wavelength, u_{max} and w_{max} in S6.4 differ considerably from that in S6.5.

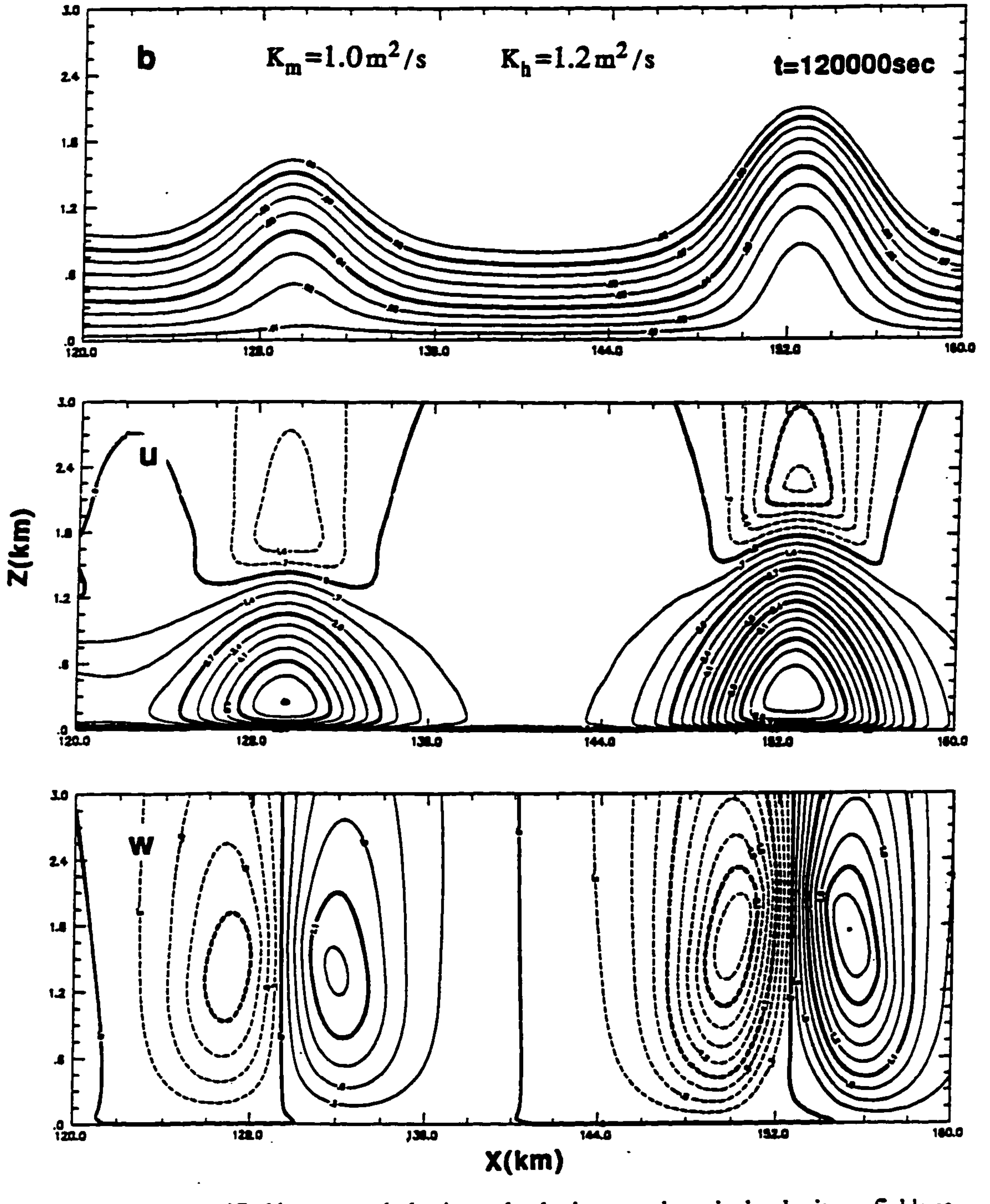

Fig.6.5 Magnified buoyancy b, horizontal velocity u, and vertical velocity w fields at t=12000sec for $K_m=1.0\,m^2/s$ and $K_h=1.2\,m^2/s$.

The results of S6.5 reflect the significant effect of eddy viscosity in ABL on the waves. Two solitary waves are still generated and propagate in steady shape with almost constant speeds. But the amplitude and speed of the first wave reduce to 1180m and 10.0m/s, respectively. u_{max} and w_{max} also decrease to 8.9m/s and 2.3m/s, respectively. Clearly u_{max} is smaller than the speed of the wave, hence recirculation does not exist in the first wave. Fig.6.7 exhibits the detailed structures of these two solitary waves. As in S6.3, the small positive and negative w pair does not appear beneath the large pair for the first wave. Furthermore the constant b area totally disappears within the first wave.

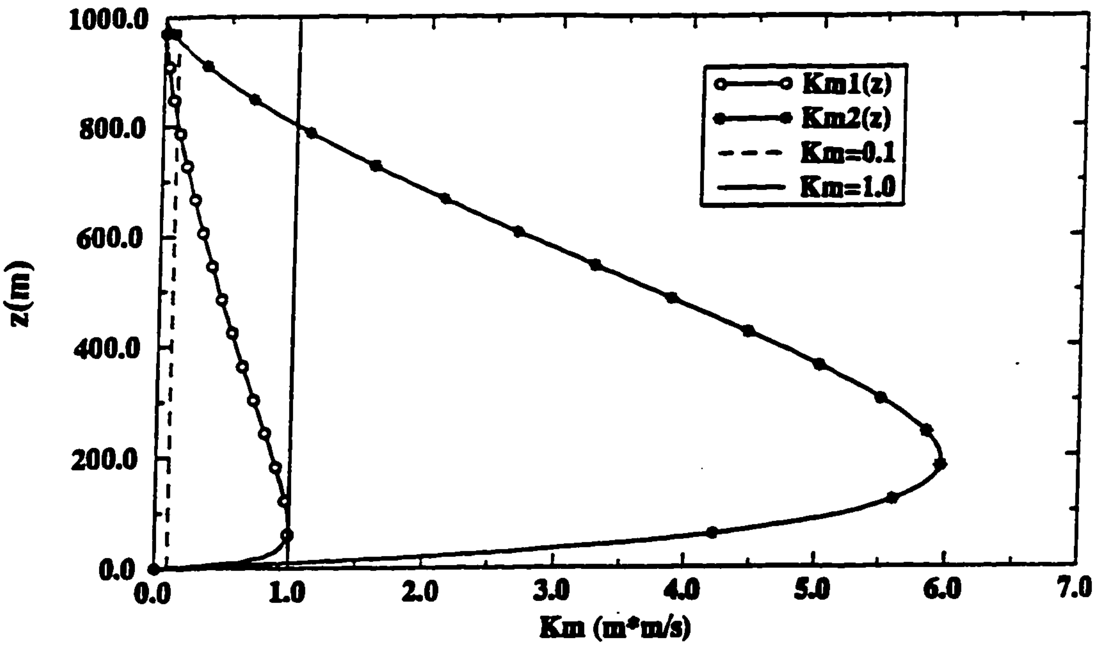

Fig.6.6 Profiles for uniform eddy diffusivity $K_m=0.1\,m^2/s$ and $K_m=1.0\,m^2/s$, and for more realistic profiles $K_m(z)$ with Monin-Obuhov length L=50m ($K_m1(z)$) and L=500m ($K_m2(z)$).

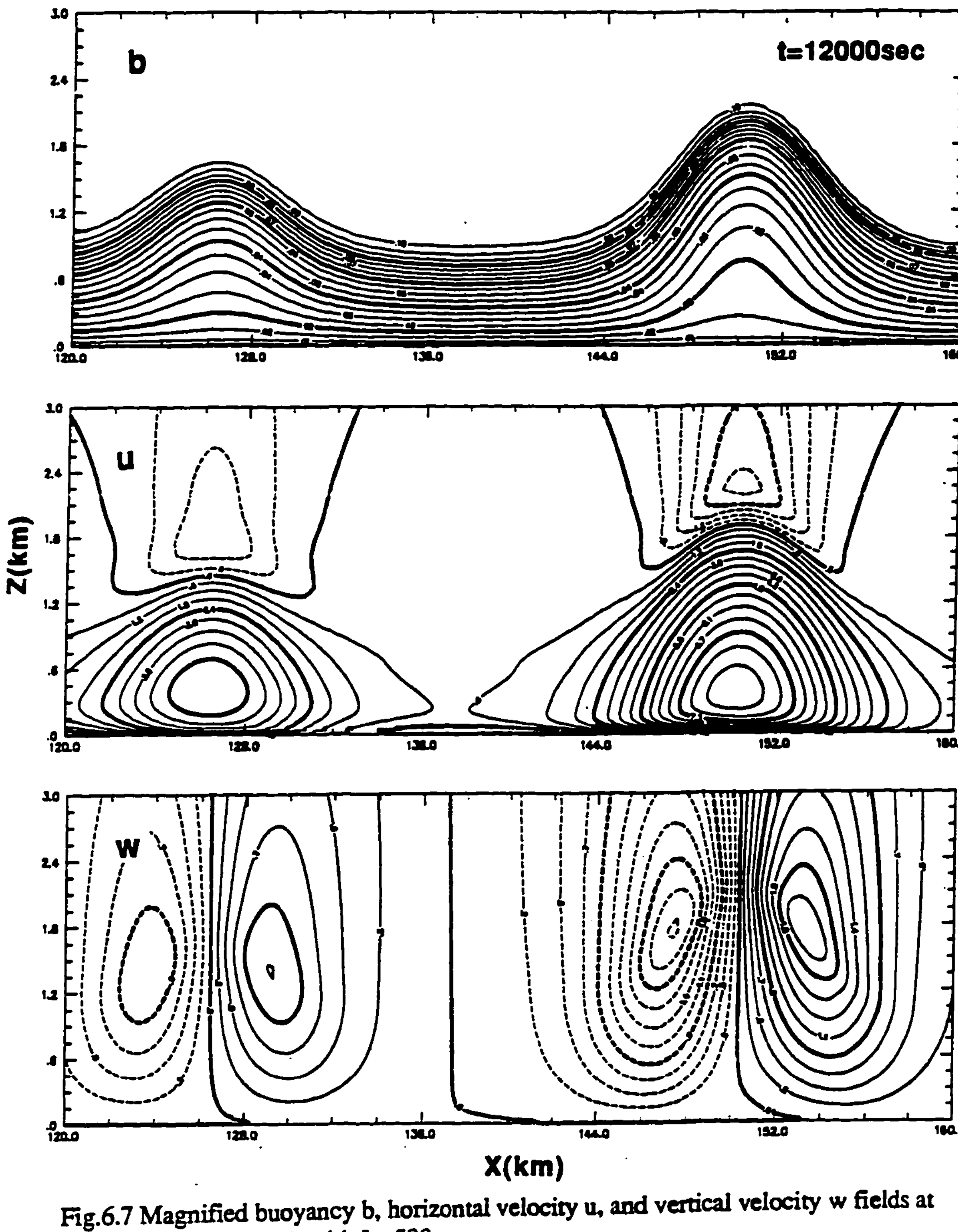

Fig.6.7 Magnified buoyancy b, horizontal velocity u, and vertical velocity w fields at t=12000sec for $K_m(z)$ with L=500m.

Note that the eddy viscosity acts on the fluid motion from the initial time, even when the coldpool is collapsing to form a density current. So the strength of density current which generates the waves is weaker with stronger eddy diffusion.

6.2.3 *Relations of amplitude a vs wavespeed c, and amplitude a vs wavelength λ*

For the convenience of comparison, the major properties of the first solitary wave and second solitary wave under different eddy viscosity conditions are listed together in Table 6.1 and Table 6.2 respectively.

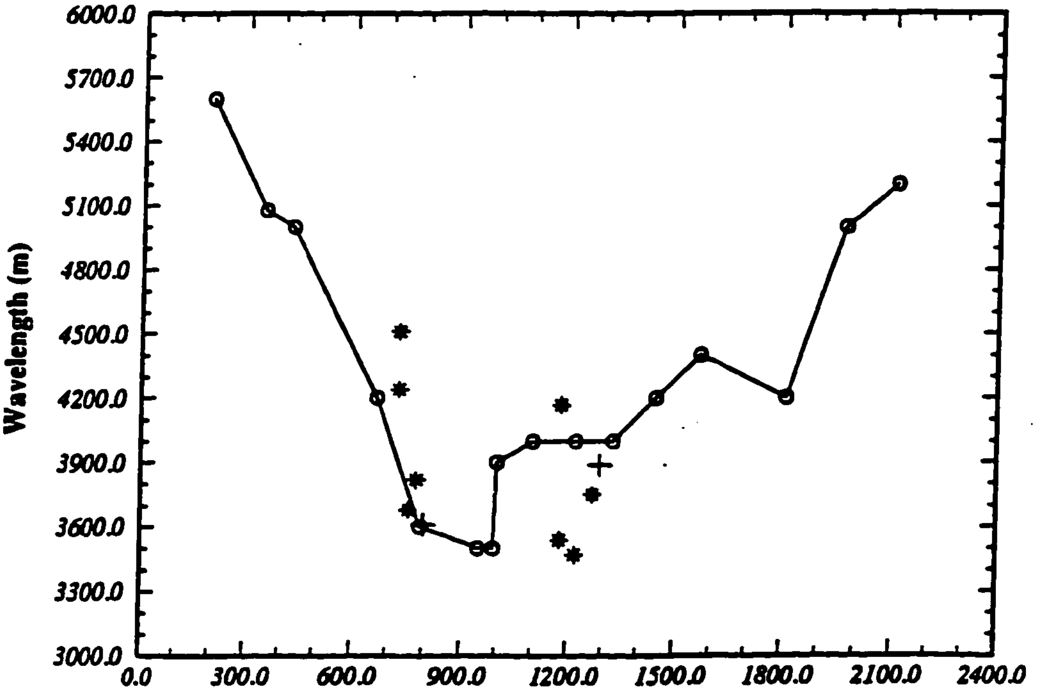

Fig.6.8 Wavelength λ vs wave amplitude a. Open circle with solid line represents the results described in section 5.5. '+' signs are the results from S6.1 without eddy diffusivity. '*' signs from S6.2-6.5 with eddy diffusivity.

To clearly display the differences of the properties of between the solitary wave generated by a density current with and without eddy diffusivity, and waves generated by a solitary wave-like perturbation in the inviscid fluid, the results of wave amplitudes, speeds, and wavelengths in Table 6.1 and Table 6.2 with results obtained in Chapter 5 are shown together in Fig.6.8 and 6.9. Fig.6.8 gives the relation between amplitude a and wavelength λ. The relation of amplitude a and wave speed c is presented in Fig.6.9. In both figures, open circles with solid lines represent the results from Chapter 5. '+' sign represents result in S6.1 without eddy diffusivity. '*' signs stand for the results in S6.2-6.5 with eddy viscosity.

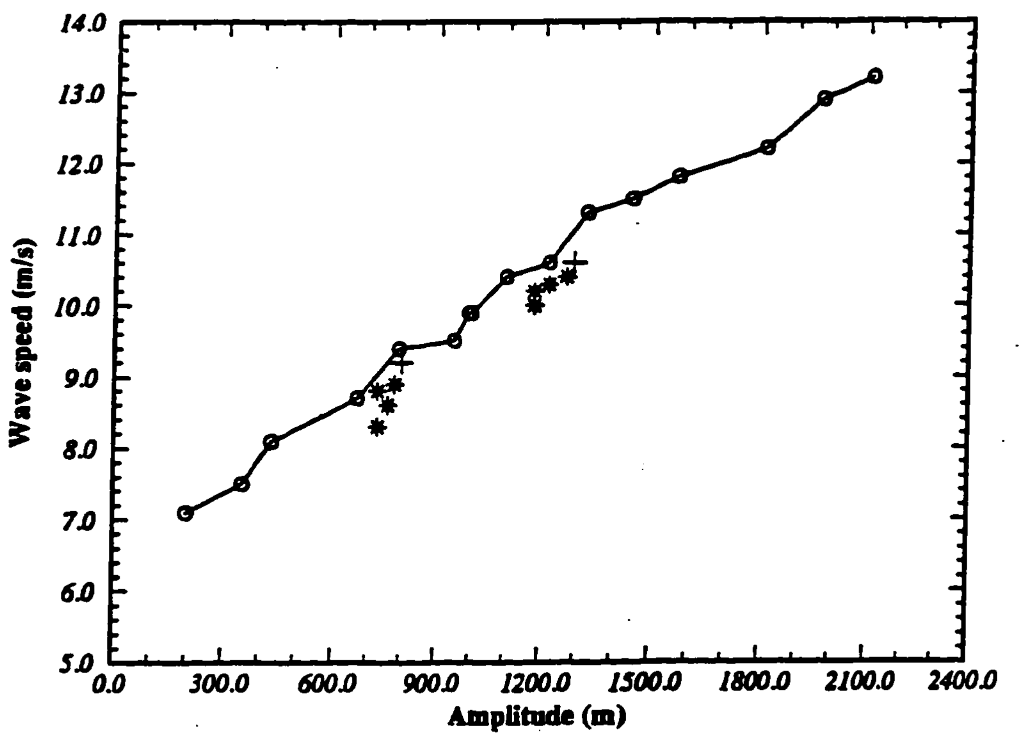

Fig.6.9 Wavespeed c *vs* wave amplitude a. The signs represent the same as in Fig.6.8.

In an inviscid fluid the wavelength shrinks as the amplitude decreases for large amplitude solitary wave (a/h>1.0). In contrast, the wavelength increases as the amplitude

Table 6.1: The properties of the first waves at t=12000 sec with different eddy viscosity in the ABL.

	$K_m(m^2/s)$	*a (m)*	*c (m/s)*	*λ (m)*	$u_{max}(m/s)$	$w_{max}(m/s)$	*R*
S6.1	0.0	1290	10.6	3890	11.4	3.0	Yes
S6.2	0.1	1270	10.4	3750	11.0	3.0	Yes
S6.3	1.0	1220	10.3	3470	10.0	2.7	No
S6.4	$K_m1(z)$	1180	10.2	3540	10.0	2.7	No
S6.5	$K_m2(z)$	1180	10.0	4170	8.9	2.3	No

where R indicates the existence of recirculation.

Table 6.2: The properties of the second waves at t=12000 sec with different eddy viscosity in the ABL.

	$K_m(m^2/s)$	*a (m)*	*c (m/s)*	*λ (m)*
S6.1	0.0	800	9.2	3610
S6.2	0.1	780	8.9	3820
S6.3	1.0	730	8.8	4240
S6.4	$K_m1(z)$	760	8.6	3680
S6.5	$K_m2(z)$	730	8.3	4510

decreases for small amplitude solitary waves (a/h<1.0). Without eddy diffusivity, the shape and speed of the solitary waves ('+' signs in Fig.6.8 and 6.9) created by a density current fairly agree with the waves (open circle signs in Fig.6.8 and 6.9) generated by a solitary wave-like perturbation. The results presented in Fig.6.8 show similar relationship between amplitude and wavelength for the waves in the fluid with eddy diffusivity, except for $K_m = K_m(z)$ in S6.4 and S6.5.

The amplitude of the wave in S6.4 and S6.5 are 1180m, so the ratio (a/h) of amplitude and the height of stable layer is 1.18 which is near to 1. Perhaps the increase of wavelength reflects the characteristic of small solitary waves. Comparing the results of S6.4 with S6.5, we also find that there is very little change in amplitude for a large increase in K_m and K_h. More close examinations are needed to understand these wave behaviors under the influence of eddy diffusivity.

Fig.6.9 shows that the wave speed increases with amplitude with or without viscosity. For the same amplitudes, the wave speeds in S6.2-6.4 (i.e., viscosity is present) are slightly smaller than the wave speeds without any viscosity; the stronger viscosity is, the slower the wave propagates (Tables 6.1 and 6.2).

Examining Fig.6.8 and Fig.6.9, we find that the *a vs c* results with eddy diffusivity are consistent with those results without diffusivity. But the *a vs* λ results with eddy diffusivity show significant difference from the previous results in the inviscid fluid. The large variability on the plot of amplitude vs wavelength results suggests that they are much more sensitive to the different diffusivities than amplitude vs wavespeed results. In other words, it is more dependable to predict solitary wave amplitude in the light of wave speed rather than wavelength when there is difficulty to observe wave amplitude. On the other hand, the measurement of wavelength introduces errors in a-λ results. The wavelengths of these waves are measured at half amplitude by eye, and are based on the plots shown in figures such as Fig.6.1. In addition, Δx (grid interval in x direction) in the simulations is 200m. These two factors introduce at least a 200m uncertainty in the measurement of wavelengths.

6.2.4 u_{max} *and recirculation*

Comparing the decreases of wave speed and u_{max} with eddy diffusivity increases (Tables 6.1 and 6.2), we find u_{max} declines faster than wave speed. It is because strong local wind shear, due to reverse recirculation, near the center of the wave causes strong eddy diffusivity. Meanwhile, u_{max} is just located in the center area. Thus, strong viscosity makes u_{max} reduce faster than the wave speed. As u_{max} becomes less than the wave speed, the recirculation will disappear within the solitary waves, even if the ratio of amplitude a of the wave to the height h of stable layer is larger than 1.2. It implies that large amplitude solitary waves may not trap fluid if the eddy viscosity is strong enough. For example, recirculation does not appear in the first solitary wave in S5.3 although the ratio a/h is 1.22. The 'ink' field in S6.3 confirmed that no fluid is trapped in the wave.

6.2.5 *Trapping in an eddy diffusivity environment*

The previous results show that when K_m is equal to $1.0 m^2/s$ (in S6.3) or equivalently larger than $1.0 m^2/s$ (in S6.4 and S6.5), recirculation disappeared. Does this mean $K_m = 1.0 m^2/s$ is so strong that no solitary wave can trap fluid? If the answer is yes, it implies it is difficult to observe trapped fluid by solitary waves in the atmosphere because $1.0 m^2/s$ is a typical value for K_m in the stable ABL (J.R. Garratt, 1992). In order to answer this question, simulation (S6.6) was conducted.

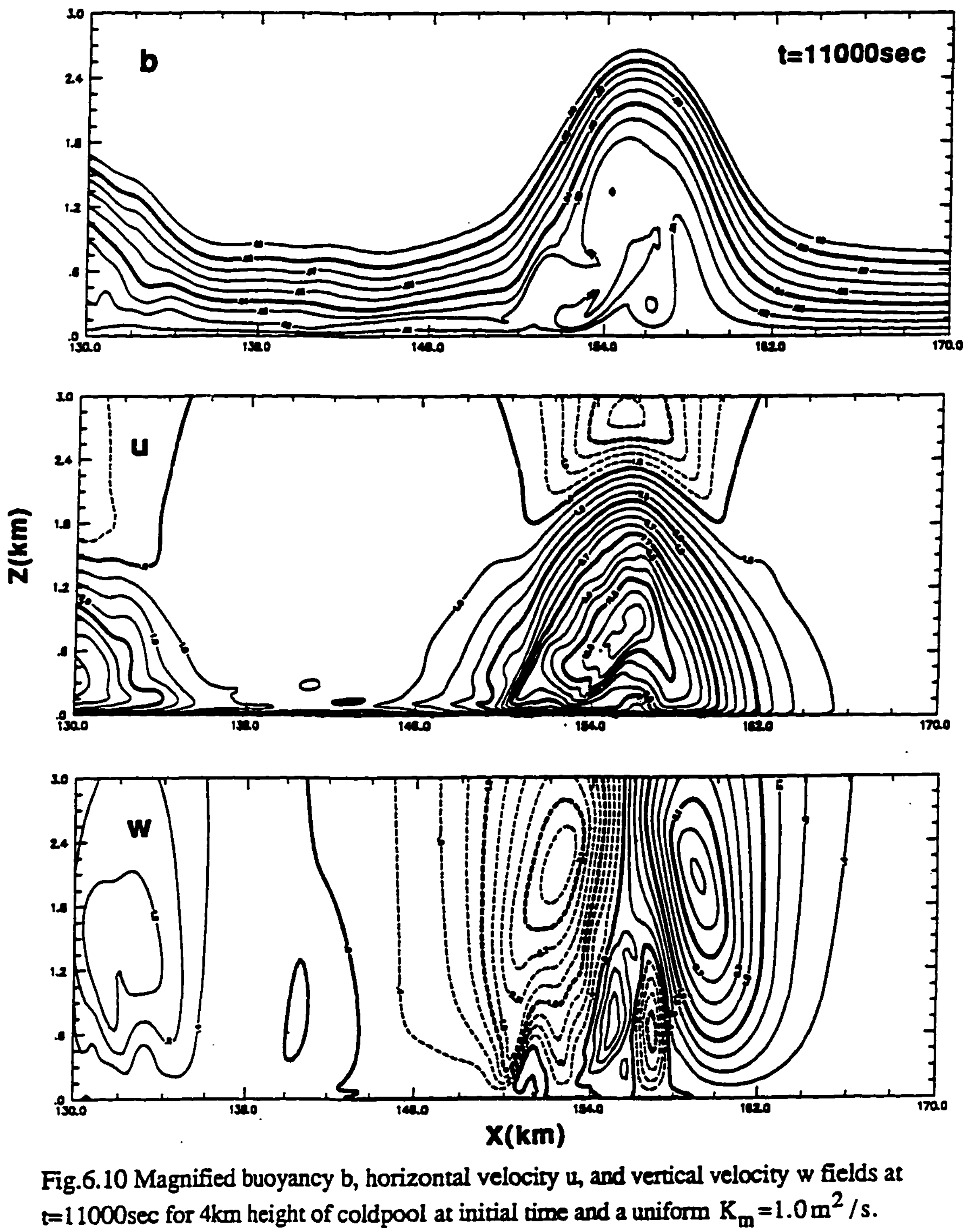

Fig.6.10 Magnified buoyancy b, horizontal velocity u, and vertical velocity w fields at t=11000sec for 4km height of coldpool at initial time and a uniform $K_m = 1.0\,m^2/s$.

In S6.6, the height of coldpool is increased from 3 km to 4 km during the cooling period to generate a larger amplitude solitary wave than the waves in S6.1-6.5. The rest initial and background conditions are the same as in S6.3. The simulation results show that two solitary waves are generated. The first wave propagates in speed 11.5m/s with amplitude 1670m. u_{max} is 14.1m/s at t=11000 sec. The recirculation appears within the first wave. Fig.6.10 shows the detailed structures of the first wave at t=11000 sec. w field clearly displays a positive-negative pair within the wave which indicates the existence of a reversed recirculation. The 'ink' field (not shown here) shows that a portion of cold air is inside of the wave which confirms the existence of recirculation and trapping effect of the wave.

Hence in such a background field if the amplitude of solitary wave is large enough, the wave still can have recirculation and trap fluid with typical values of turbulent eddy diffusivity in ABL.

6.3 Effects of wind shear

In this section, two simulations will be introduced to investigate the effects of wind shear on the generation and propagation of solitary waves. The ambient wind with shear in the simulations can be defined by

$$U(z)= \begin{cases} \pm \alpha z, & 0 \le z < h_s \\ \pm \alpha h_s, & h_s \le z \le H \end{cases} \qquad (6.5)$$

where constant α represents the shear, h_s the depth of shear layer, and H the depth of model. α and h_s in both simulations are the same and equal to 10^{-2} 1/s and 1 km, but the wind is in opposite directions. So the ambient wind is 0m/s at the surface (z=0) and $\pm$10m/s at the top of shear layer (z=1 km). Above 1 km, ambient wind speed is constant $\pm$10m/s. If the wind is in the direction of wave propagation, it generates a downstream shear; if wind is opposite to the direction of wave propagation, it generates a upstream shear. Coldpool, the source of solitary waves, is also the same in both simulations. The location and strength of the coldpool are identical as in S6.1.

The solitary waves displayed in the buoyancy field in these two simulations are shown in Fig.6.11. They propagate from the left of domain to the right. The leading solitary wave generated in the downstream shear ambient wind field (Fig.6.11a) has a dramatically large amplitude of about 3 km. In contrast, the amplitude of leading wave (about 500m) in the upstream shear ambient wind field (Fig.6.11b) is about 6 times smaller than the first one.

The significant difference of the locations of the leading waves at the same time (t=8000 sec) indicates that their speeds relative to the ground are very different. The average speeds of these two leading waves are 15.5m/s and 6.5m/s, respectively. Recall the simulation 6.1 with the same ambient temperature field but without ambient wind, the speed and amplitude of leading wave are 10.6m/s and 1.3 km. Hence, as expected, the wave in the downstream ambient wind shear propagates faster than without ambient wind; in contrast, the wave in the upstream ambient wind shear propagates slower. The speed deficit between the downstream wave and the wave in S6.1 is 4.9m/s which is near the average ambient wind speed (i.e. 5m/s) in the shear layer, but the deficit for upstream one

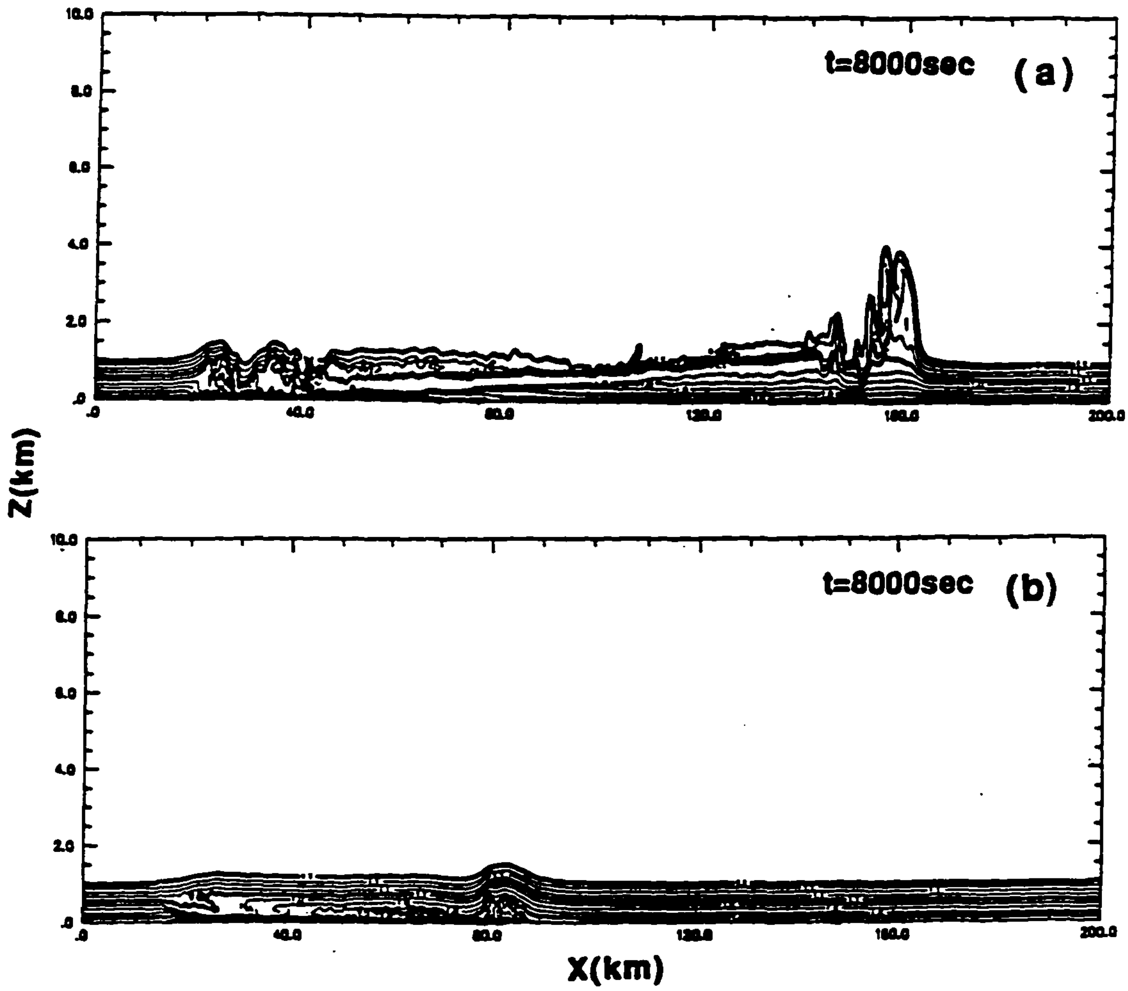

Fig.6.11 Buoyancy fields at t=8000sec with same shear but two wind directions: (a) downstream wave; (b) upstream wave.

is 4.1m/s which obviously differs from 5m/s. Therefore, based on these two simulations, we cannot conclude that the wave is advected by the average ambient wind in a shear environment. More simulations could further clarify the relation between average ambient wind speed and wavespeed.

Here we still call the leading waves as solitary waves because they have a single main crest and a large negative-positive pair of vertical velocity (Fig.6.12) and they propagate at almost constant speed which is the basic character of solitary waves. However, the fine structure within the leading solitary waves are noticeably different from the solitary wave in S6.1. Unlike one smooth single peak in the solitary wave in the calm ambient wind, there are some wavelike perturbations within the leading solitary wave. The shear instability, which results in these perturbations, creates Kelvin-Helmholtz (KH) waves. This is confirmed by the low Richardson number (<1/4) in the region (shaded regions in Figs. 6.13 and 6.14) where KH waves coexist with large shear. We also find that the fine structures within the leading waves are not steady, especially for the downstream wave. Liu and Moncrieff (1996) shows unsteady vertical velocity maximum induced by the density current head when they studied the effects of ambient wind shear on a density current advancing in a neutral environment. They also found that the height of the density current head is not proportional to the shear, but the highest head occurs in a moderate-shear environment.

A passive tracer (ink) is also applied in the simulations to mark the location of the air that was initially placed in the coldpool. In both simulations (i.e. up and downstream wave propagation) a portion of ink appeared to be trapped by the leading waves. For the downstream case, the ambient wind speed above 1 km (height of shear layer) is +10m/s

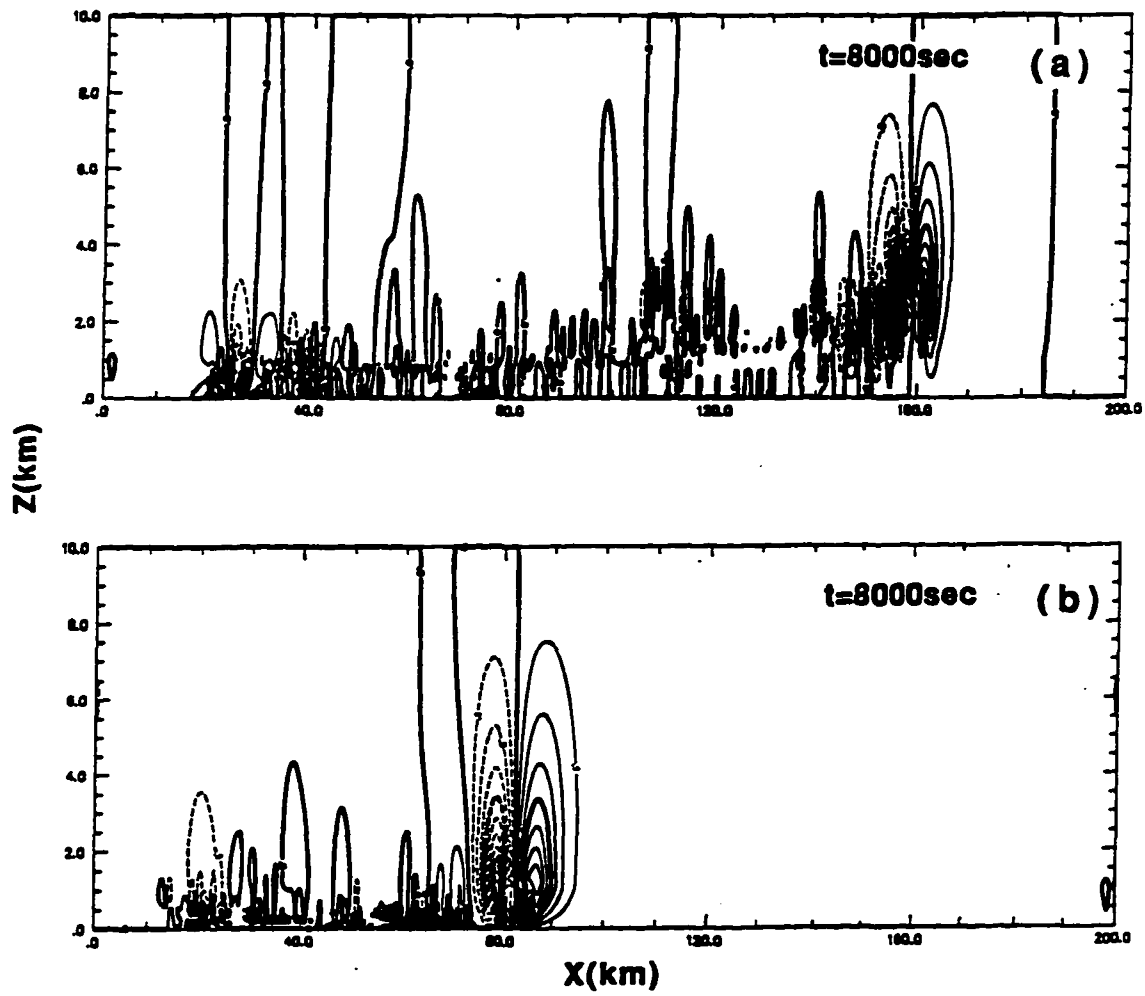

Fig.6.12 As in Fig.6.12 but for the vertical velocity fields.

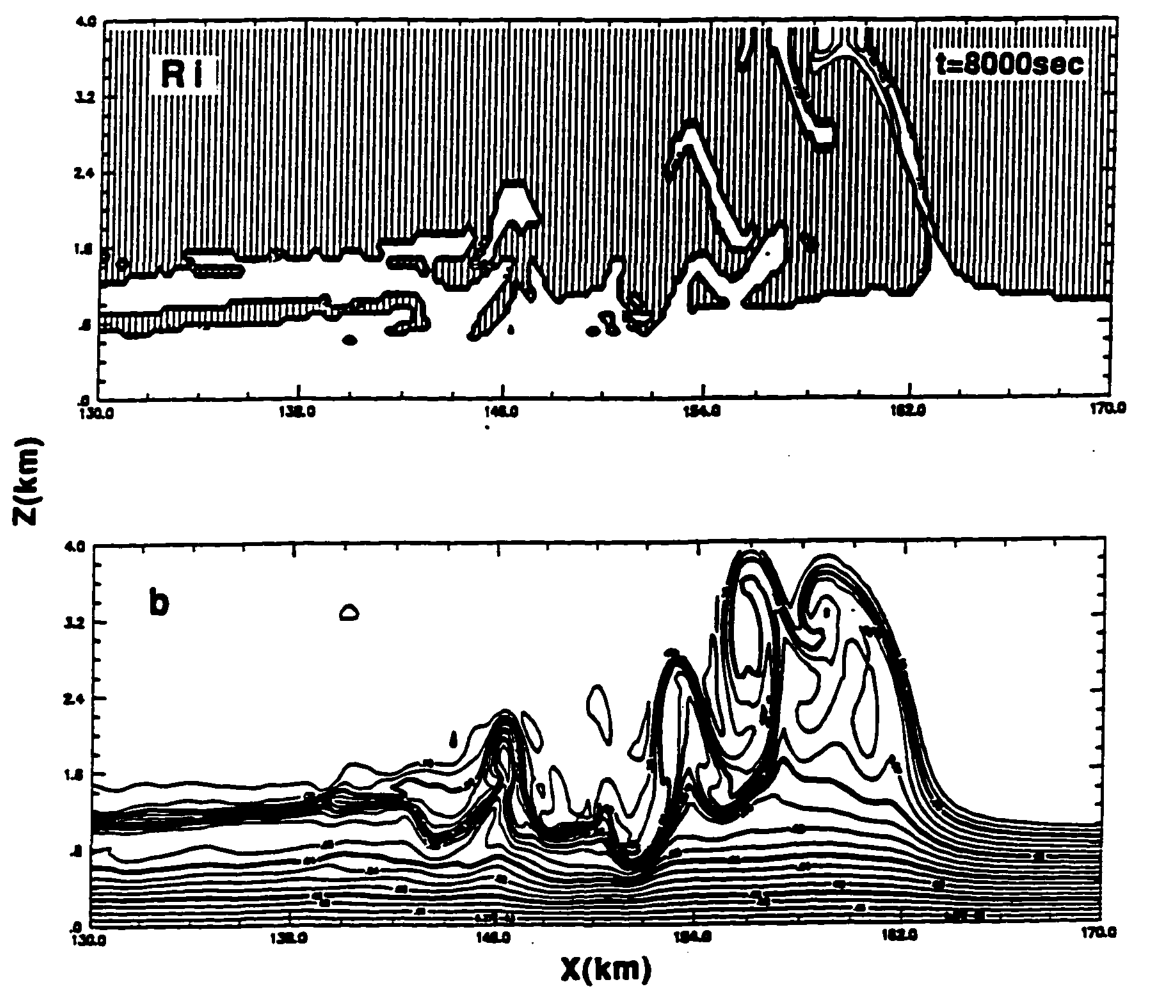

Fig.6.13 Magnified Richardson number Ri and buoyancy b fields at t=8000sec for a wave propagating downstream in a wind shear. Shaded region represents Ri< 1/4.

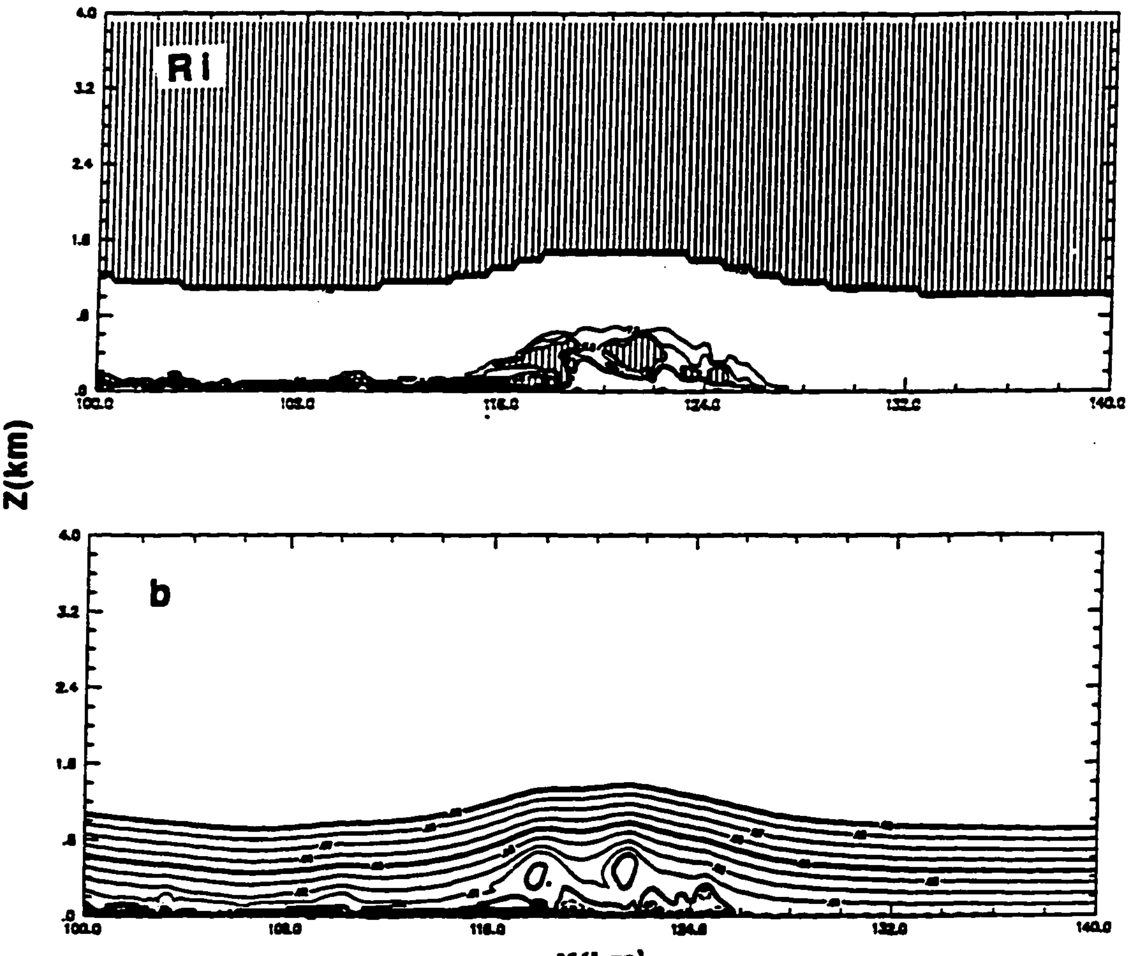

Fig.6.14 Magnified Richardson number Ri and buoyancy b fields at t=14000sec for a wave propagating upstream in a wind shear. Shaded region represents Ri< 1/4.

and the coldpool initially centers at 30 km, so a block of 'ink' centered about 110 km indicates that the ink residue of the coldpool has been advanced by ambient wind (Fig.6.15). Three segments of ink located around 158 km, corresponding to the position of leading wave (Fig.6.11a), demonstrate they are trapped by the leading wave. Note that the ink does not necessarily represent the cold air even though it was initially located in the coldpool. Although ink is injected at t=0 into the coldpool, the air in the coldpool was gradually cooling down during first 400 sec, some of ink moves downward and then advances with the cold air near the ground as a density current, some of ink, where the air does not become cold yet, is advected by the ambient wind.

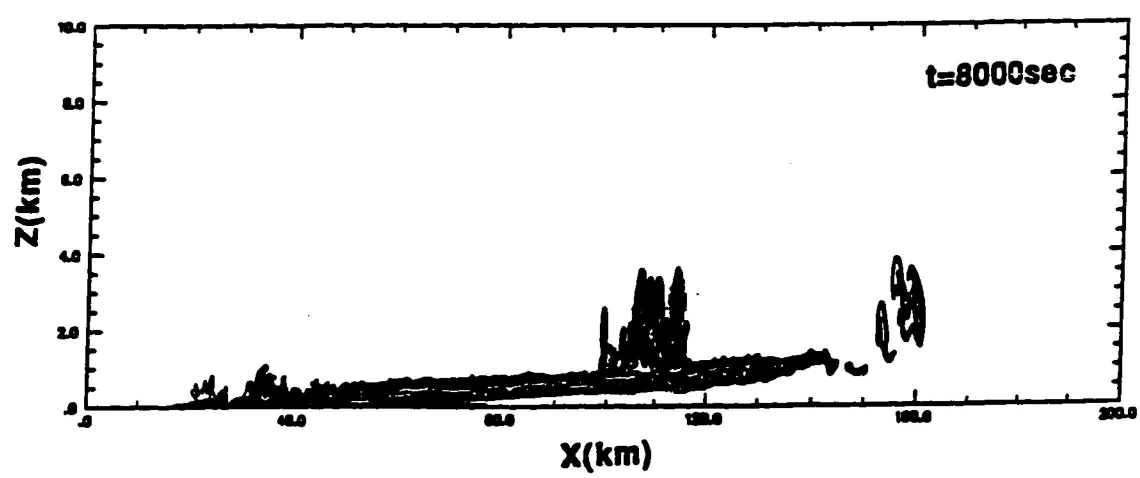

Fig.6.15 Ink field for downstream wave at t=8000sec.

For the upstream case, in order to compare the location of ink with the waves, the ink and buoyancy fields at t=14000 sec are shown together in Fig.6.16. Ink field at this time mainly represents the cold air produced by coldpool initially, since the rest of ink has been advected by the ambient wind out of the model domain. It is clearly displayed that a portion of cold air is trapped by the leading wave although the amplitude of leading solitary wave is only about 900m. So in a sheared environment the ratio of wave amplitude and height of the stable layer is not a proper parameter to determine if the wave is capable of trapping fluid.

Hence, shear plays a critical and complex role in modulating the structure and the behavior of solitary wave. As in the real atmosphere, wind fields are always inhomogeneous; more simulations could shed further light on the effects of wind shear on the generation and propagation of solitary waves.

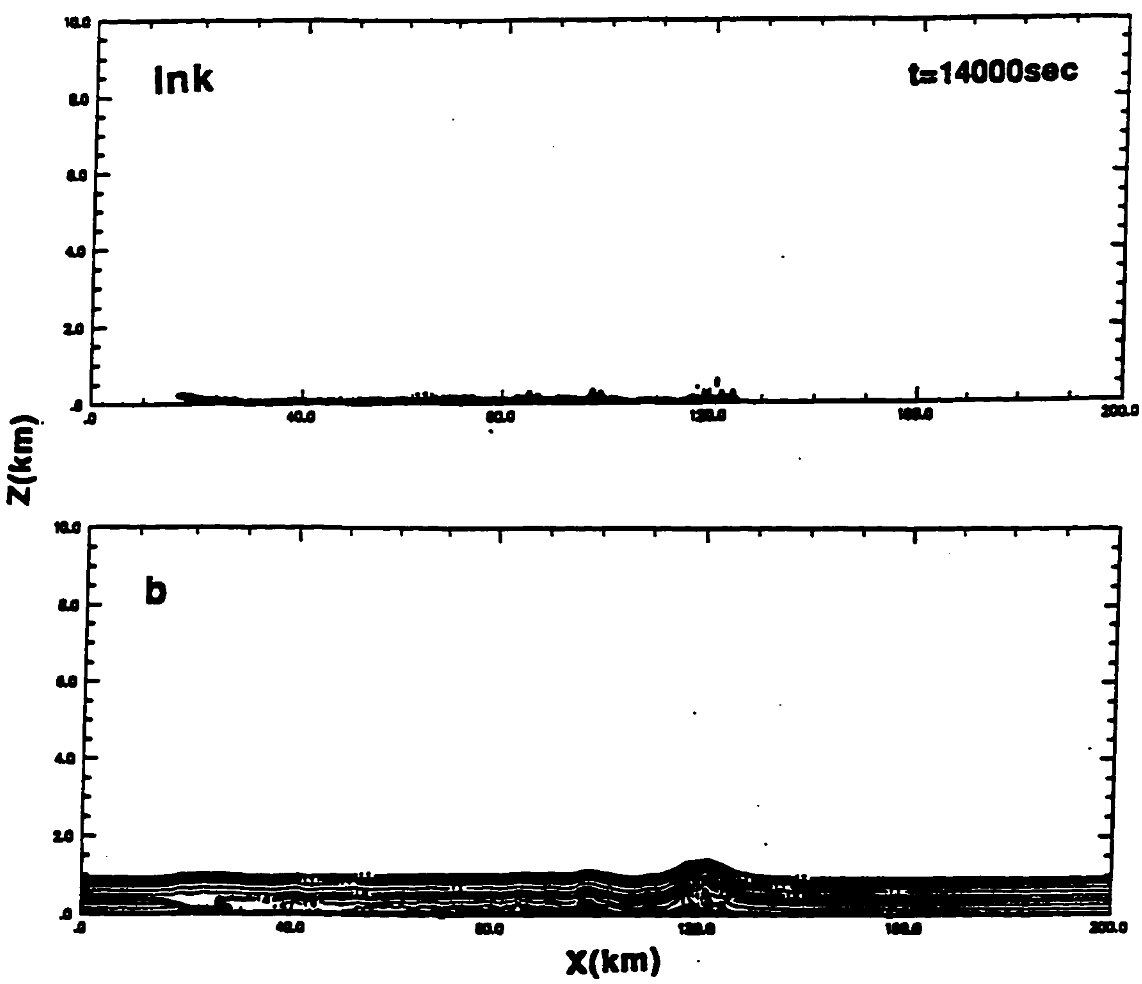

Fig.6.16 Ink and buoyancy fields for upstream wave at t=14000sec.

Chapter

7

A Solitary Wave Related Case Study by Using the Model

In the previous chapters, we have shown that this model has successfully simulate large and small amplitude solitary waves in different background fields. The many properties of solitary waves have been studied and understood.

In this chapter, this model is used to study solitary wave related case observed with a Doppler radar, a tall tower and a surface network. This case has been reported (Doviak and Ge, 1984) and studied previously (Doviak et al, 1991). But because of previous theory could not provide solutions under condition of complicated environmental temperature and wind fields, some features in the case were not totally understood.

7.1 Brief introduction of the case

The case we studied is a solitary wave which propagates over 100 km from its source in the central Oklahoma in the late evening of 11 May 1980. The wave is generated by a thunderstorm outflow and the whole phenomenon lasts about 1.5 hours. This event was observed with NSSL's Doppler weather radar, meteorological instruments on a 444m tall tower and with a surface network.

Observation indicates that before wave passage in central Oklahoma, an earlier thunderstorm outflow has moved southerly over the tower at 2130 CST (Central Standard Time). This outflow formed a cold and strong stable layer about 600m in depth above the ground.

At 2207 CST, a solitary gust generated by another thunderstorm outflow was first detected by the radar. This solitary gust evolved into a solitary wave propagating in the stable layer. Doppler radar detected the propagation of the wave from 2226 CST to 2316 CST. Fig.7.1 shows isochrones of solitary wave position determined by the leading edge of zero Doppler velocity, and the location of the tower (Δ), and instruments of surface network (o). The arrival time of the solitary wave and peak surface wind speed induced by the solitary wave at each site are also shown in the parentheses. The radar reflectivity and radial velocity fields show the leading wave essentially as a plane wave. It indicates that structure along the wave is approximately the same.

As the wave passes the tower, it records time series of vertical and horizontal velocities at different heights above the ground. The record provides detailed structures of

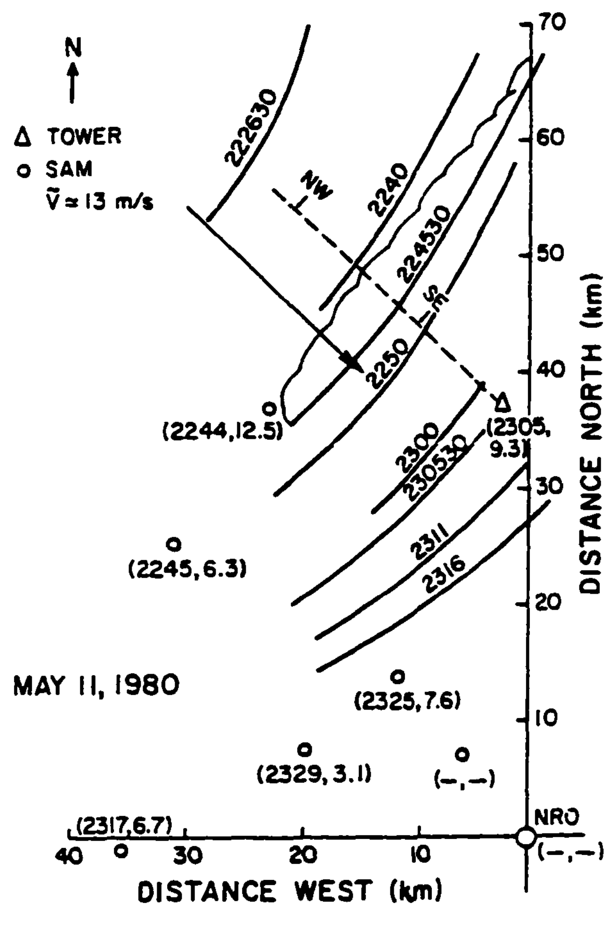

Fig.7.1 Isochrones of leading solitary wave position and location of the tall tower, sites of the automated meteorological instruments (SAM) and radar. The arrow indicates the approximate direction of wave propagation and the dashed line is the location of the cross section of the wave observed at the tower. The time of arrival of the wave at each surface site is indicated in parentheses next to the station where peak wind speed induced by the wave is also listed. (from Doviak and Ge, 1984).

the wave and pre-wave environmental temperature, moisture, and wind profiles in the lower atmosphere. The temperature and wind profiles above the tower top is deduced from rawinsonde data before and after this event. Doppler radar also provides wind profiles up to 2 km in front of the propagating wave.

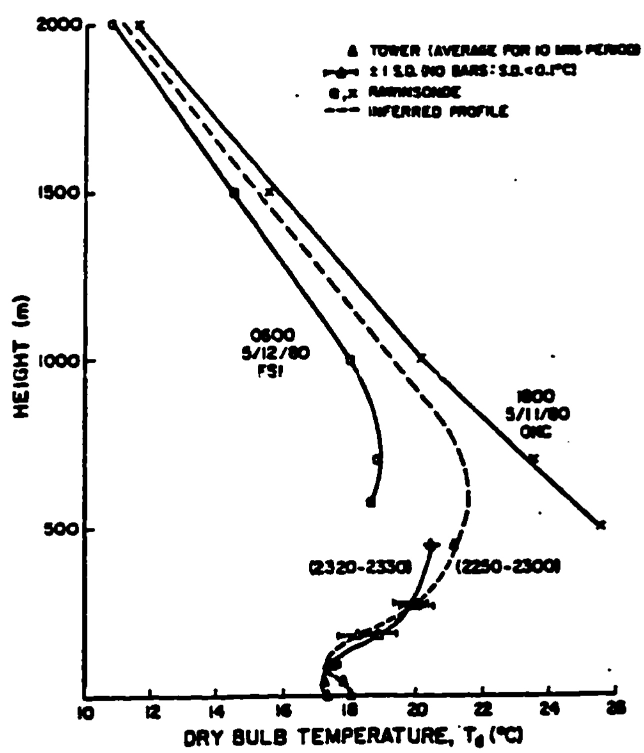

Fig.7.2 Vertical profiles of temperature measured by rawinsonde and tower (from Doviak and Ge, 1984).

The temperature profiles observed by rawinsonde, located at Oklahoma City (OKC) about 15 km south of the tower and Fort Sill (FSI) about 100 km to the southwest, 5 hr before and 7 hr after the event and by tower for 10 min. average before and after the leading wave are shown in Fig.7.2. The vertical profile of the ambient wind components parallel to the cross section of the wave measured by tower (below 444m) and Doppler radar (from 444m to 2 km) at around 2245 are plotted in Fig.7.3.

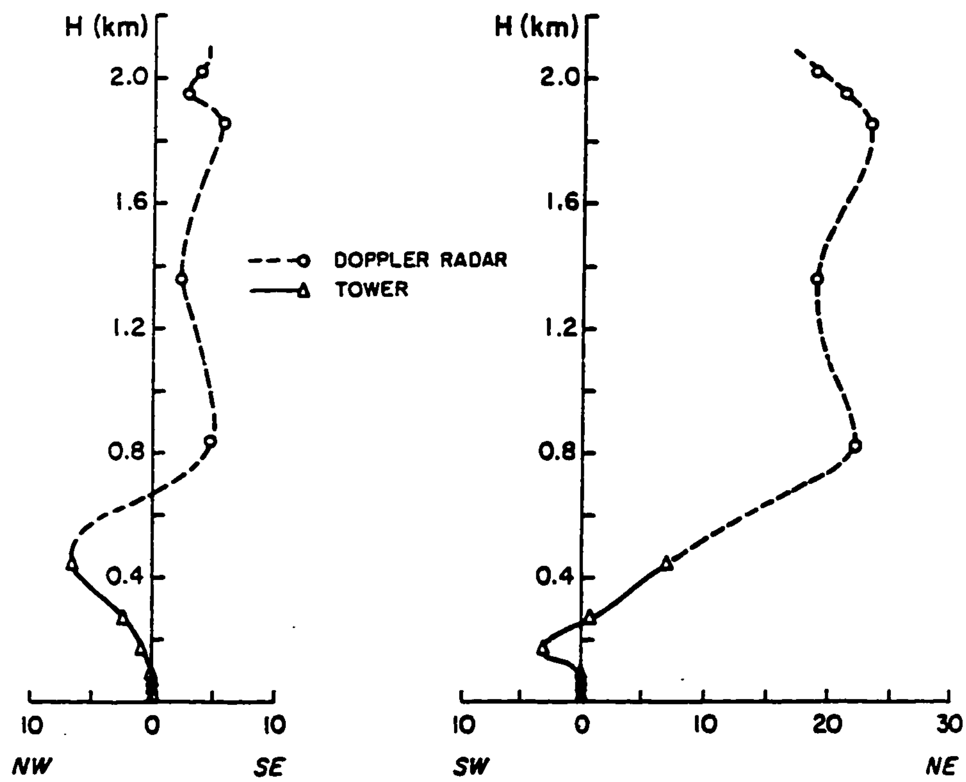

Fig.7.3 Ambient wind profiles measured by tower and Doppler radar (a) in the propagation direction of the leading solitary wave; (b) perpendicular to the propagation direction. The rawinsonde sites are ~20 km NW (OKC) and 120 km SW (FSI) of the Norman Doppler radar. The Doppler radar estimate of wind is an average over a 40° sector 40 km north of radar. (from Doviak and Ge, 1984).

7.2 The set up of the model for the case study

The model used to simulate this case is described in Chapter 2. The background fields (potential temperature and horizontal wind) are given based on the observed temperature and wind profiles (assumed horizontally homogenous).

The potential temperature profile (Fig.7.4) is calculated from the inferred temperature profile which is shown in Fig.7.2. Hydrostatic assumption is used in the calculation of potential temperature. Due to lack of observation data, a constant potential temperature above 2 km is given in the model.

Fig.7.4 provides pre-wave ambient wind profiles perpendicular and parallel to the solitary wave from ground to 2 km. But it has been suspected that the radar data may be contaminated by the birds or/and insects (Doviak and Chen, 1988). Because in the radar observations the peak in horizontal velocity perturbations lags behind the peak of reflectivity. Doviak and Zrnic' (1984) found that the reflectivity factor Z of the ambient has a strong vertical gradient (-17 dBZ/km). The peak reflectivity is expected to coincide with the peak horizontal velocity. Thus insects and/or flying birds or mammals might respond to the lag. The large scatter of the mean Doppler velocity estimates from one resolution volume V6 to the next V6 (Doviak and Zirnic', 1984) and the unusually high equivalent reflectivity factor (10 dB Z_e at 300m altitude) also support this suspicion.

Contamination of radar data by the migration of birds and insects has been known for many years. Vaughn (1985) states that "From spring through fall, birds and/or insects are generally common to abundant in the atmosphere to an altitude of 1 to 2 km over most

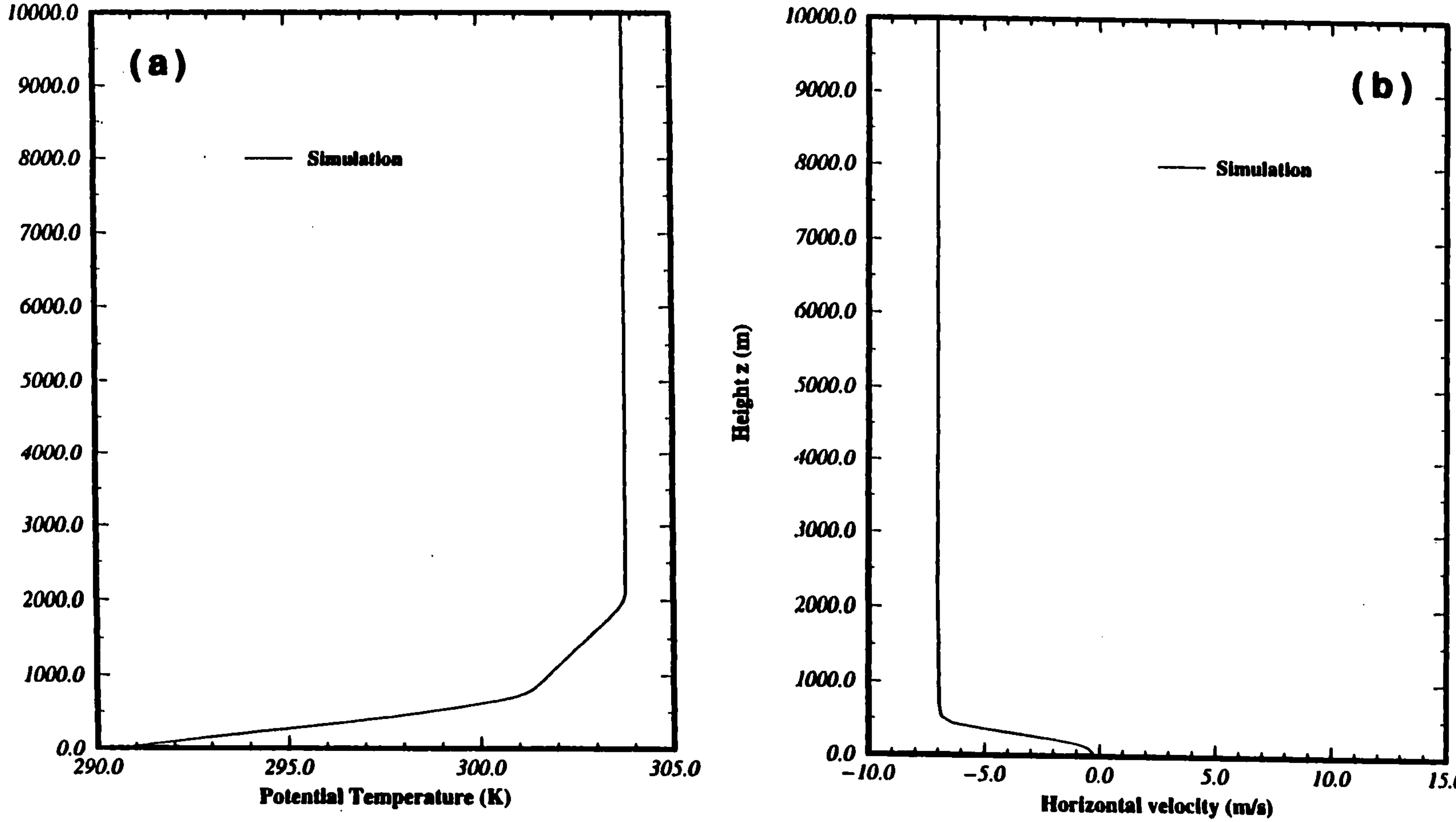

Fig.7.4 Vertical profiles of (a) potential temperature and (b) horizontal wind perpendicular to the wave front used in the simulation.

land areas of the world". Especially at night during spring (March-May) seasonal migrations of birds and insects increases dramatically (Vaughn, 1985; Wilson et al, 1994; Wilczak et al, 1995). Flying birds can contaminate the radar observed velocity by vectorially adding about 7 to 15m/s to the wind. Southward migration called "reverse" migration of birds in spring season has also been found(Wilczak et al, 1995).

For our case, the radar data was collected in night during spring season (2245, 11 May). It is reasonable to believe that the ambient wind deduced from radar measurements above 444m (Fig.7.4) is contaminated by southward movements of birds or/and insects. In addition, wind profiles observed by rawinsondes might not represent the realistic wind field in front the wave because they were measured 5 h before and 7 h after the event. Thus we removed the wind profile portion above 444m and simply assume a constant velocity which is equal to the value at 444m observed by the tower.

The observation shows the gust front was initiated by a thunderstorm outflow. However, the three dimensional, moisture and rain related thermodynamic and kinematic mechanism in the generation of the thunderstorm outflow can not be simulated by this two-dimension dry model. Moreover, paucity of existing observation in the thunderstorm outflow is the other reason why the real outflow in the observation is hard to be reproduced by this model.

In our experiments the thunderstorm outflow is simulated by a block of air which is gradually cooled to reach a certain temperature lower than ambient temperature. The colder air then continuously spreads out to form two density currents in both left and right directions in the numerical domain. The density current moving toward right direction is the one used to simulate the outflow. The left density current will move out of the domain soon and not be concerned in our study.

Also because the lack of observational data about the characteristics of the thunderstorm outflow, it is difficult for us to choose an unique model for cooling the block of air and the block dimensions. After many trials with different combinations of block dimensions, cooling rate, and period of cooling time, the following parameters, height of the block h_{cp}=610m, width of the block w_{cp}=10 km, period of cooling time ΔT=600 sec, were chosen such that the leading wave speed is comparable with the observed wave speed. The block of air which is cooled is located 35 km from the left side of the domain. The cooling rate γ is linearly changing with time and approaching to zero at the end of cooling period:

$$\gamma = \gamma_0 \left(\frac{t - \Delta T}{\Delta T} \right) \tag{7.1}$$

where γ_0=5.5 $^{\circ}$C/sec and t is simulation time. As $t > \Delta T$, γ is set to be zero.

The passive tracer technique is also used in this simulation. The value of the passive tracer in the cooling block is prescribed as 100 and 0 in the rest of domain at the initial time. It is like a cold block air dyed with 'ink'. Thereafter 'ink' flows with the cold air and displays the shape and movement of the density current created by the collapsing coldpool. Thus we clearly distinguish the density current as the source of waves from ambient air and the waves generated by the interaction of the density current with the ambient stable layer.

Surface friction and turbulent eddy viscosity in the boundary layer are considered in the simulation. K theory discussed in Chapter 6 is applied in the model below 2 km in which a constant eddy viscosity coefficient K_m=2.0 $m^2/s$and eddy diffusivity of heat K_h=2.4 m^2/s are used.

For numerical stability, kinematic viscosity υ_h (in horizontal direction) and υ_v (in vertical direction), and thermal viscosity κ_h and κ_v in the model equations (see Eq.(2.12) and (2.14)) are all given a constant $1.0\,m^2/s$. But the viscosity terms only act in the region where Richardson number R_i>1/4.

7.3 Evolution of the solitary wave in the simulation

The goal of our numerical study is 1) to demonstrate that simulated undular bore does evolve into a family of solitary waves observed; 2) to exhaustively investigate the whole process of formation, development, and decline of the wave, a process not completely observed in the short term of observation; 3) to reveal the fine features of the phenomenon, some of them could not be observed; 4) to verify the hypothesis made by Doviak et al. (1991) that when recirculation exists within the leading solitary wave, a mass of air will be trapped and transported by the wave.

In order to give the detailed features of density current and waves for our investigation, the horizontal component of wind, the 'ink' (passive tracer) fields, and buoyancy fields are magnified in wave front area in Fig.7.5. After close examination, we found that the whole process can be divided into the three following stages based on the evolution of leading solitary wave.

1) Initial stage(0-1000 sec): In this stage, a density current (i.e. the thunderstorm outflow) is created by collapsing of the coldpool. As the density current intrudes the lower atmosphere, perturbations in the ambient stable and neutral layers are excited simultaneously.

The fields of buoyancy, b, and ink in Fig.7.5a (t=500 sec) clearly show that a density current formed in the lower stable layer. The density current is evidenced in the b field by its increase in height behind the leading perturbation which moves to about 44.5 km at this time. The height of the current head is about 390m. Moreover, a single hump in the stable layer appears above the head of the current in the b field. The 'ink' field at the same time (Fig.7.5a) also confirms the shape and location of the density current deduced from the b field.

Recall from the previous section, the coldpool is continuously cooled until t=600 sec. The current gains more momentum from the transformation of potential energy as the coldpool collapses. The maximum horizontal velocity u_{max} in the head has increased a little (from 21.2m/s at t=500 sec to 21.5m/s at t=1000 sec). During the same time period the density current speed has increased from 9.0m/s to 14.4m/s. The speed of density current is estimated by measuring the location of the leading edge of the density current at different times.

A bore with a smooth tail has evidently evolved from the single hump above the density current.

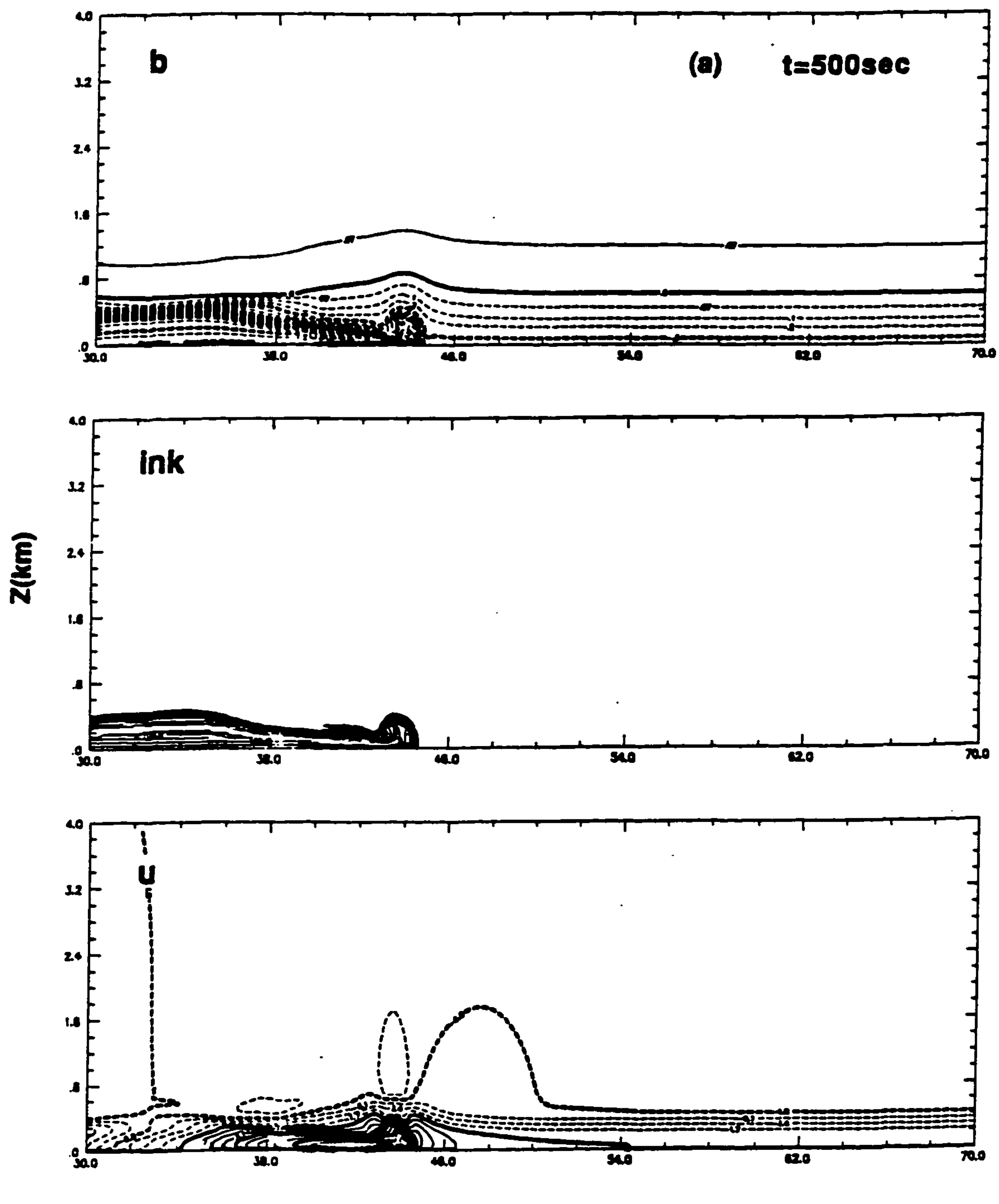

Fig.7.5 A time series of magnified horizontal velocity, 'ink' and buoyancy fields at (a) t=500sec; (b) t=1000sec; (c) t=1500sec; (d) t=2000sec; (e) t=2500sec, (f) t=3000sec; (g) t=3500sec; (h) t=4000sec; (i) t=4500sec; (j) t=6500sec.

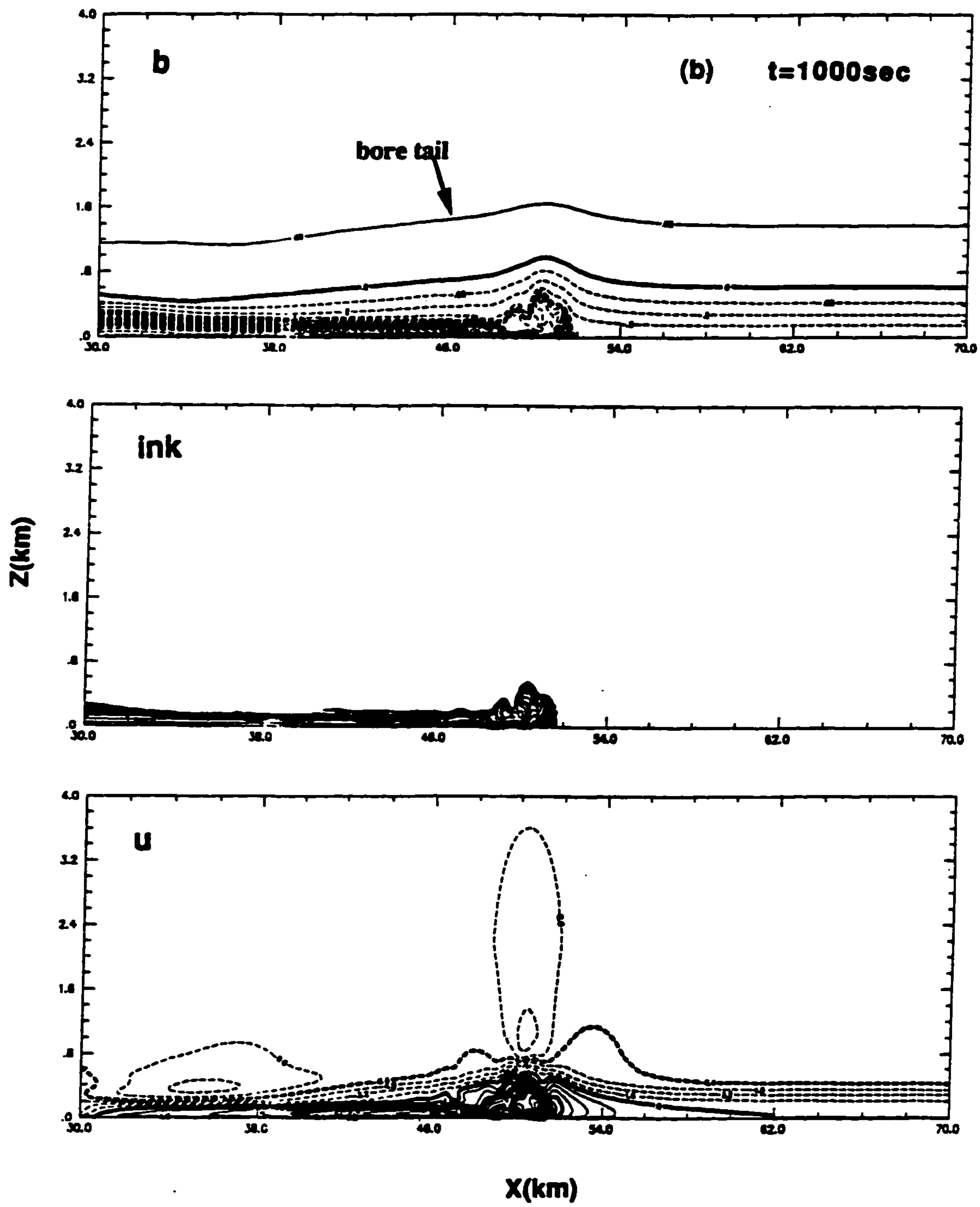

Fig.7.5 (Continued)

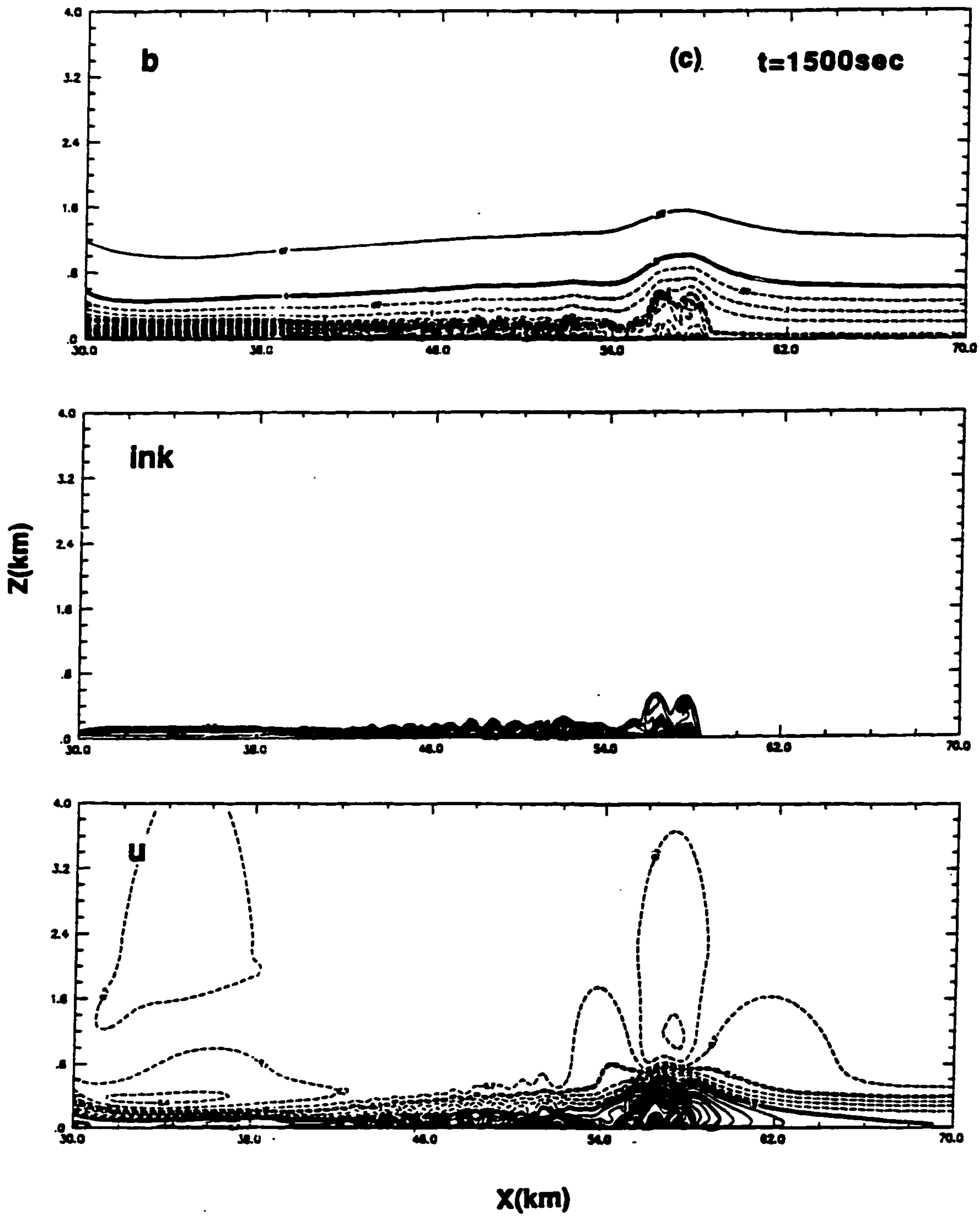

Fig.7.5 (Continued)

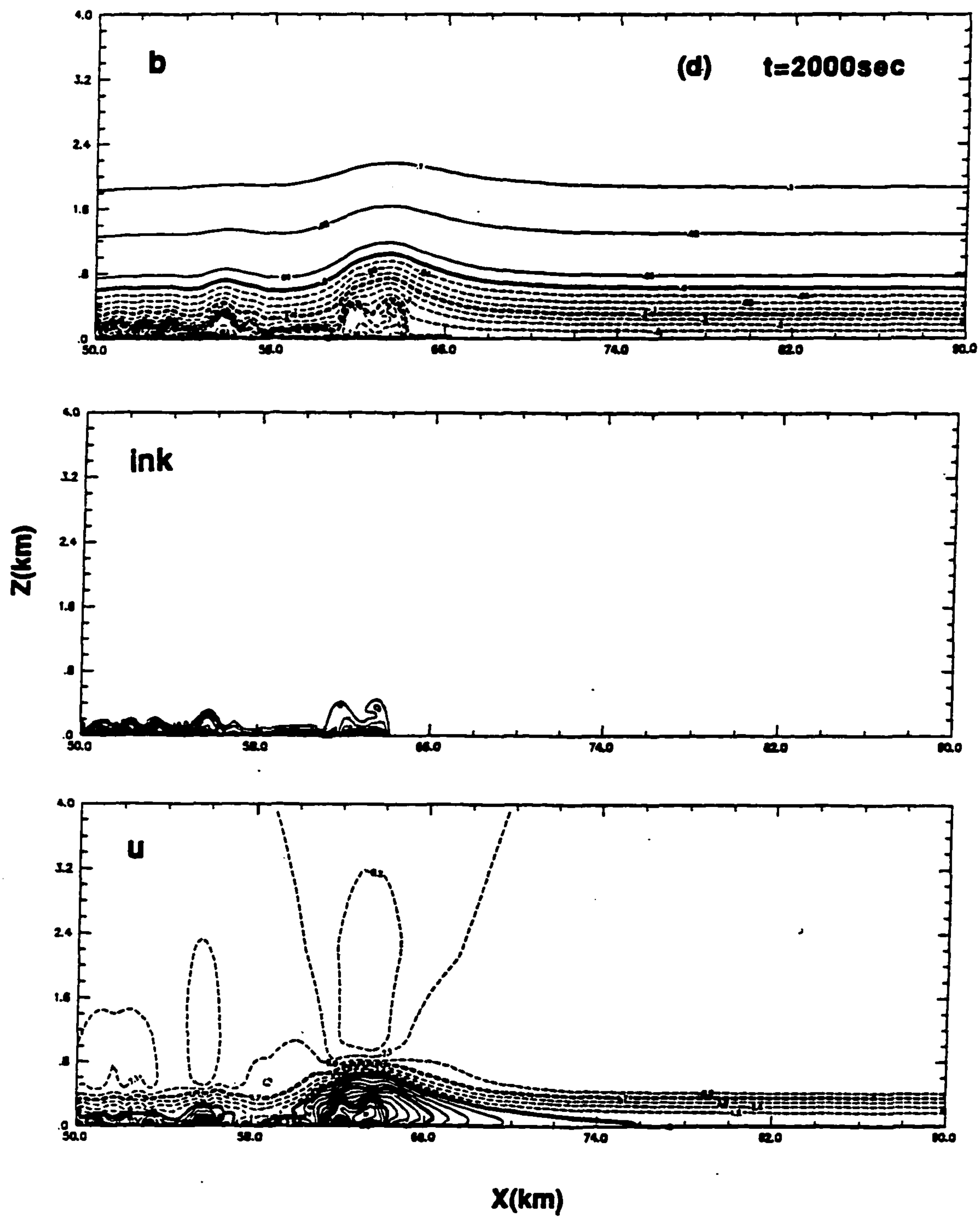

Fig.7.5 (Continued)

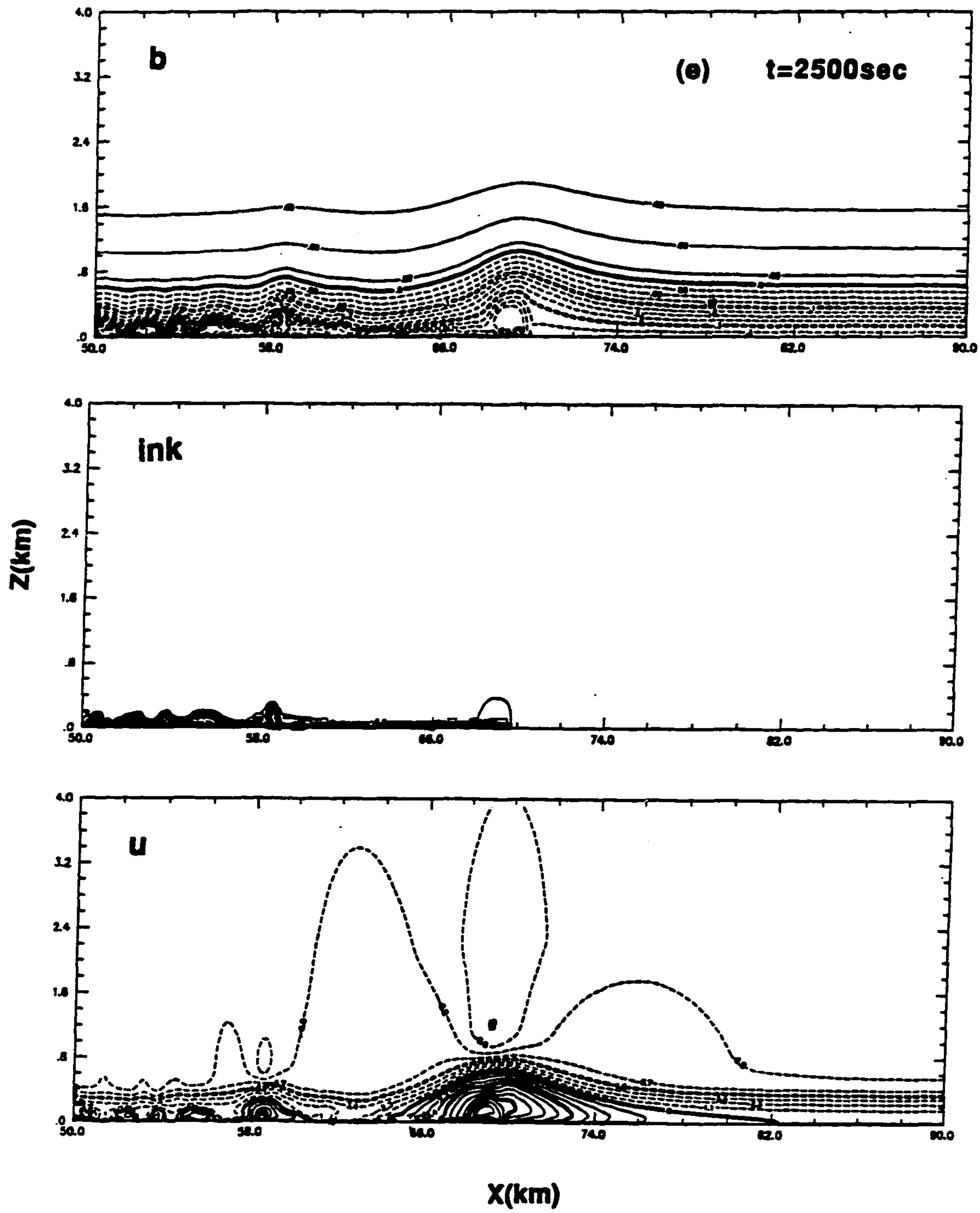

Fig.7.5 (Continued)

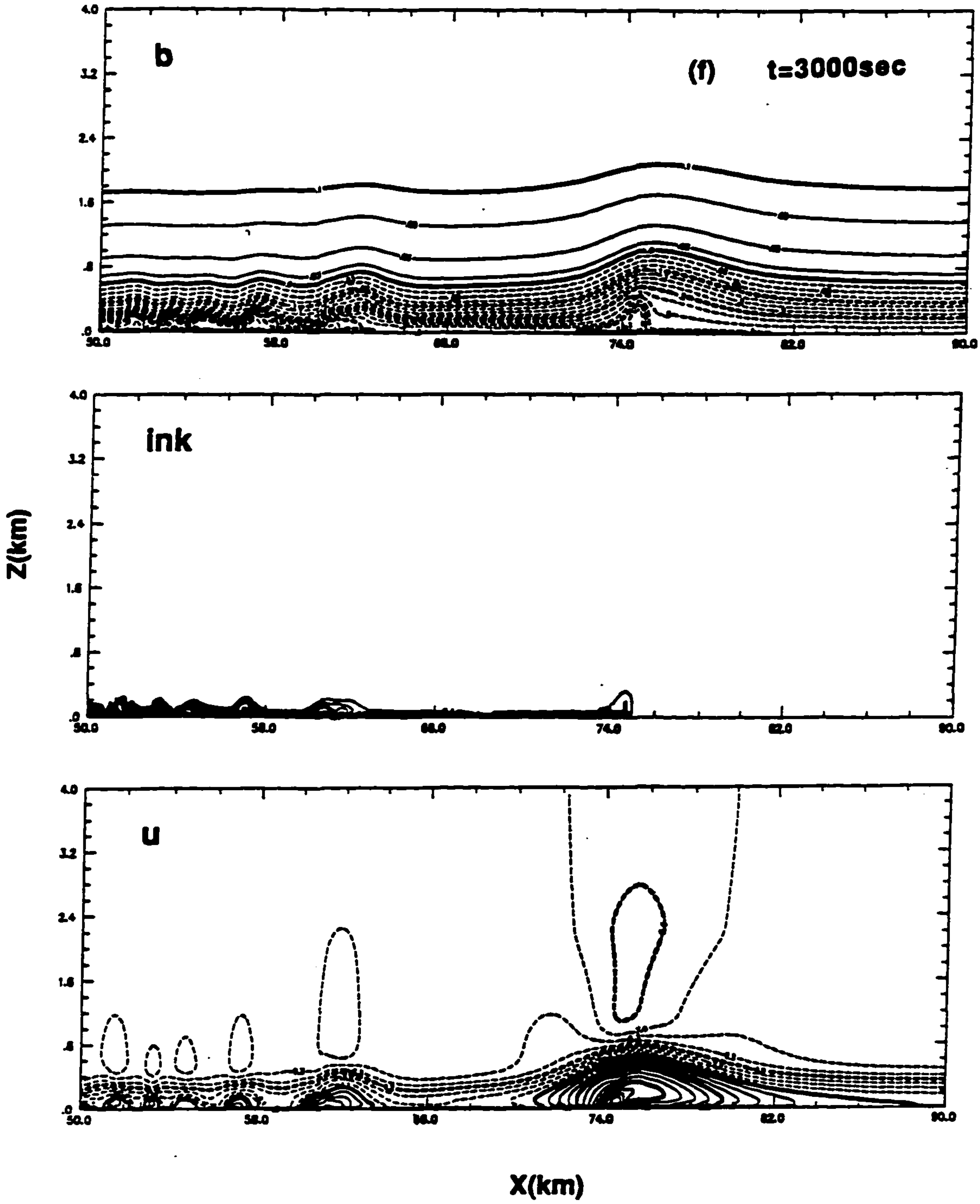

Fig.7.5 (Continued)

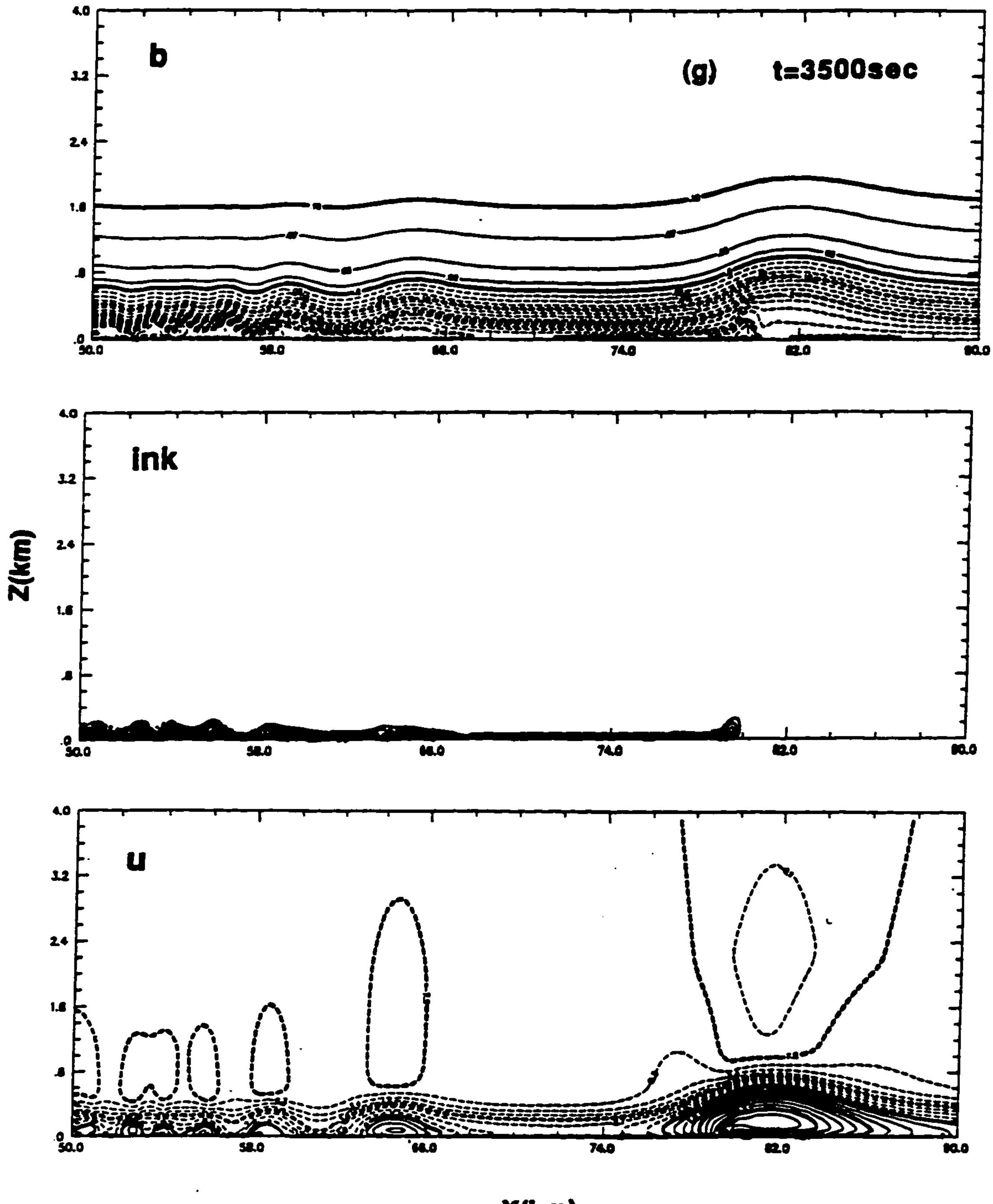

Fig.7.5 (Continued)

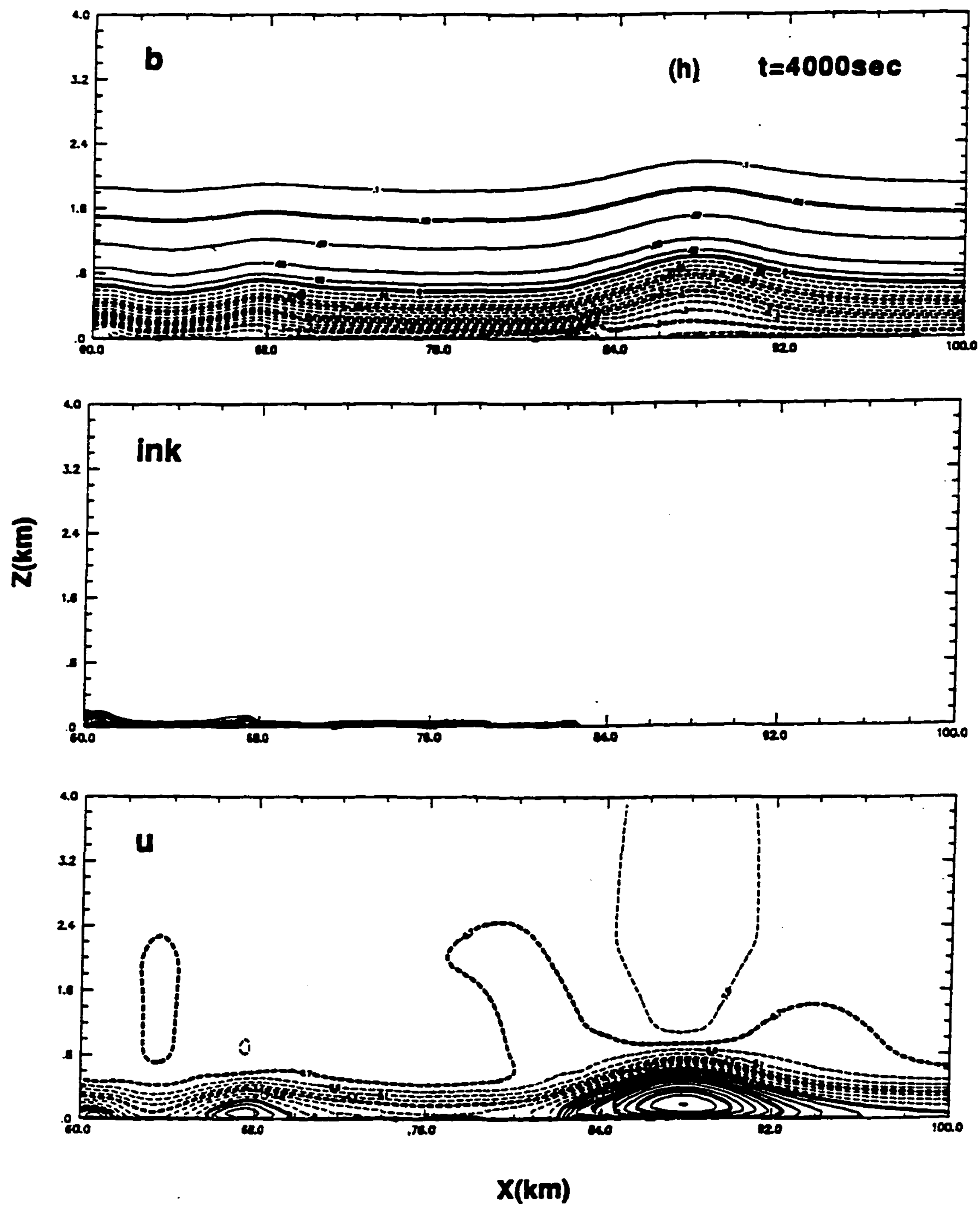

Fig.7.5 (Continued)

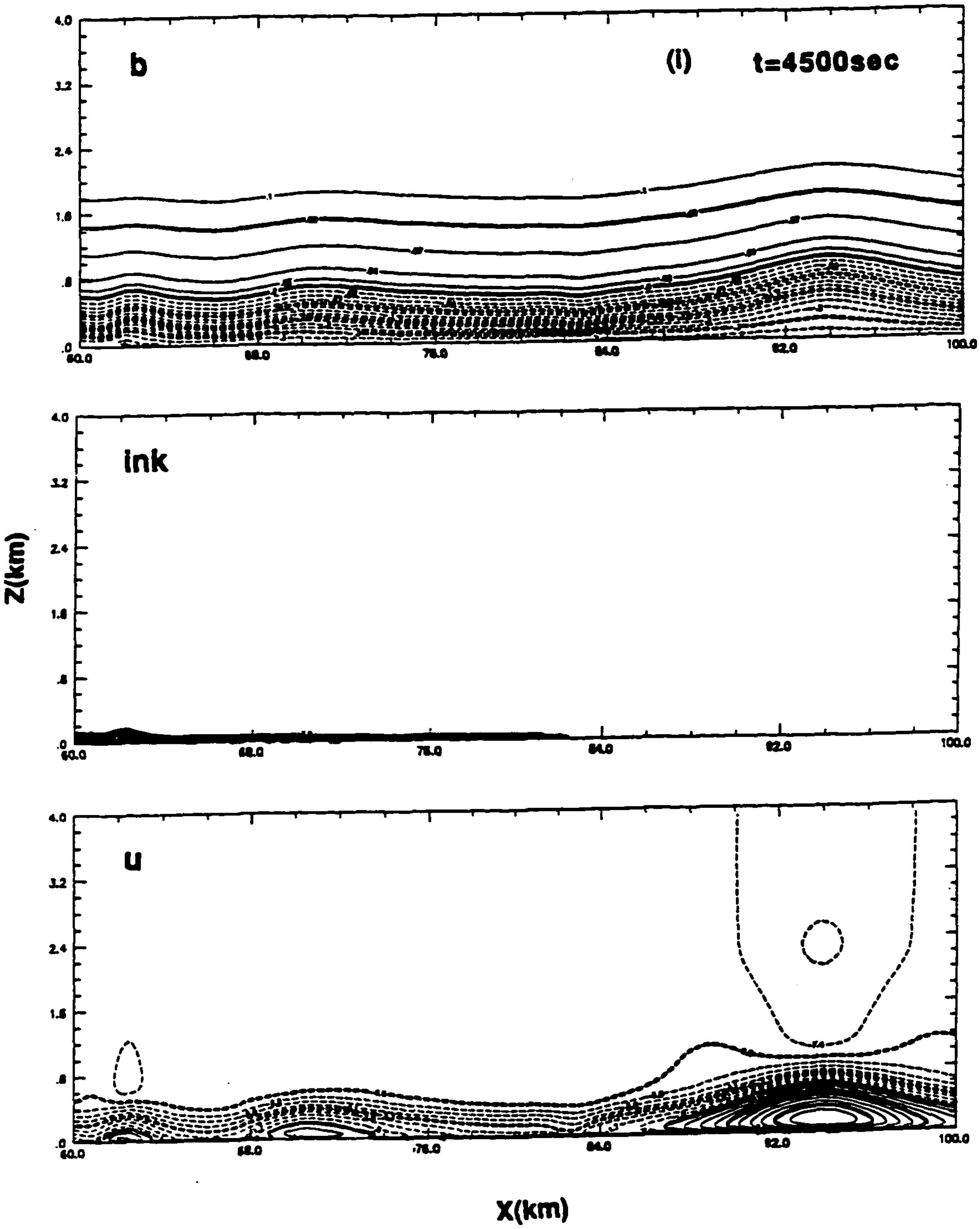

Fig.7.5 (Continued)

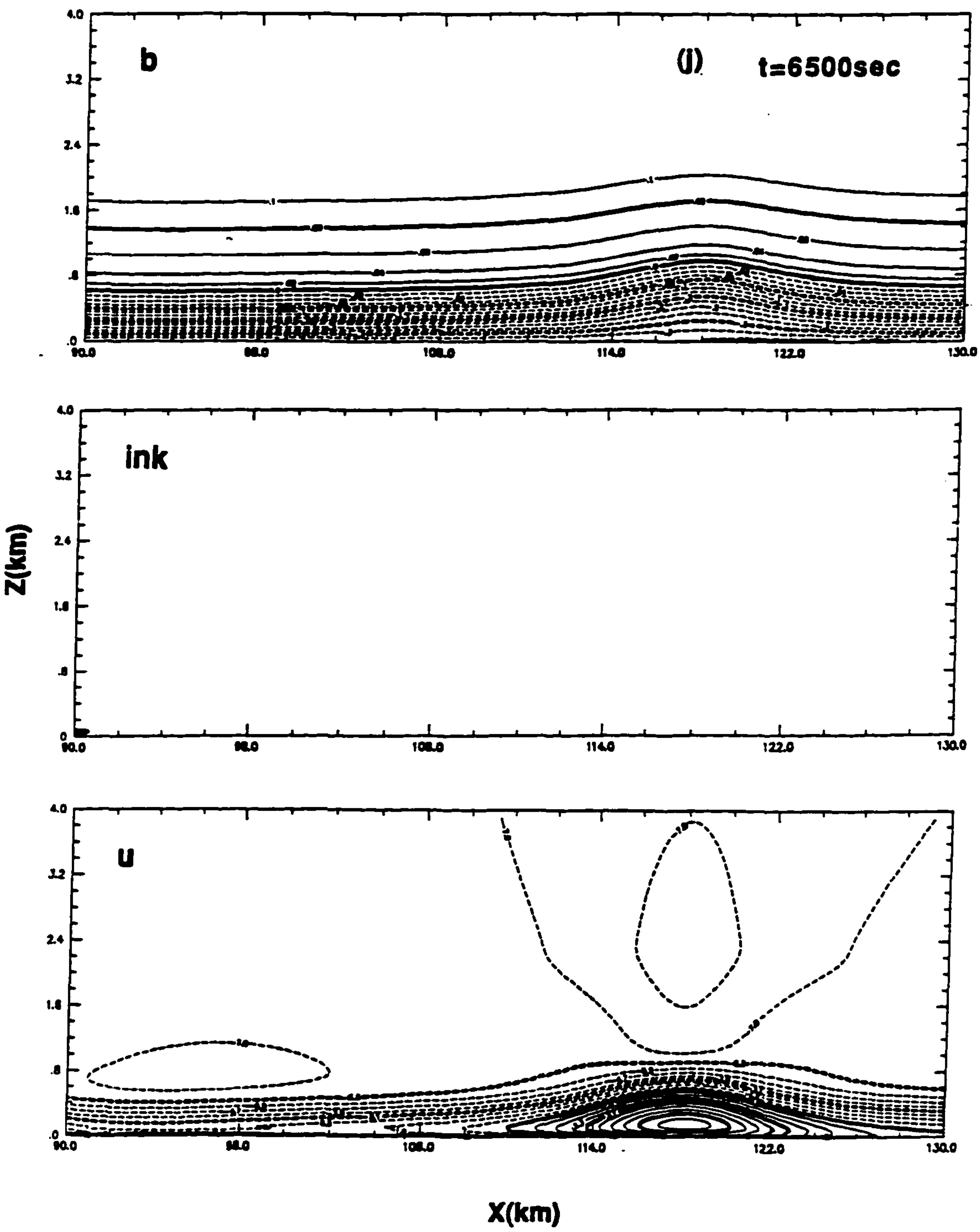

Fig.7.5 (Continued)

It was also found that there are two peaks in the current head in the b and 'ink' fields. They are produced by Kelvin-Helmholtz (KH) waves due to the strong wind shear at the interface between the current and ambient air (Droegemeier, 1987).

In view of above observation, we found that at the initial stage the density current is dynamically dominant. The motion of the current and the bore is primarily driven by the pressure difference between the current and ambient air. In addition, the birth of the bore is an important fact, later the bore will dramatically change the nature of the phenomenon.

2)Wave development stage (1000-3000 sec): The density current is still moving forward, but gradually losing its momentum because of the spreading out of the current, and because of surface friction. The speed of the current decreases from 14.4m/s at t=1000 sec to 10.4m/s at t=3000 sec. During the same period of time u_{max} declines by almost 50%, from 21.5m/s to 12.4m/s.

At t=2000 sec, small wavelike perturbations occurs in the body of the bore, and the head of the bore become more evident in b field (Fig.7.5d). It indicates the bore is evolving into an undular bore. The density current is modulated by the bore to exhibit undulations at the interface between current and ambient air. The 'ink' field at t=2000 sec in Fig.7.5d distinctly demonstrates these undulations.

At t=2500 sec (Fig.7.5e) the bore head clearly separates from the small perturbations and is evolving into a solitary wave, while the current head moves with the wave and becomes smaller and smaller. 500 sec later(Fig.7.5f) the current head slightly falls back from the wave and becomes even smaller.

During this period of time (from t=1000 sec to 3000 sec), perturbations in the stable layer accomplished the evolution from a bore to an undular bore, and then to a family of amplitude ordered solitary waves. The waves can been confirmed as solitary waves by the increase of distances between the waves because the propagation speed of solitary waves are proportional to the amplitude. The similar evolving process has been found in the laboratory (Maxworthy, 1980), in the atmosphere (Clark et al, 1981; Clark, 1983; Doviak and Ge, 1984; Fulton et al, 1990) and has been theoretically investigated by using the BDO (Benjamin-Davis-Ono) equation Christie (1989).

After the density current reaches its maximum strength at about t=1000 sec, it slowly losses its momentum and is no longer dynamically dominant after this time. In contrast, the leading solitary wave is gradually maturing and plays the prevalent role after 1000 sec.

3) Wave decaying stage (3000-6500 sec): At this stage the leading solitary wave outruns the dying density current and continuously propagates forward at nearly constant speed(12.0m/s). The detailed variation in the wave speed will be discussed later.

Comparing the 'ink' field at t=4000 sec(Fig.7.5h) with t=4500 sec (Fig.7.5i), it is seen that the leading edge of density current stops at 82.7 km. This indicates that the density current ceases at about t=4000 sec. The density current's demise might be caused by a combination of three factors: 1) insufficient depth of cold air over a long range; 2) surface friction; and 3) mixing between the cold air and ambient air.

As the density current spreads out on its way, its depth is gradually becoming lower and lower. Meanwhile mixing leads the temperature deficit to decrease. Both of these two factors are weakening the strength of the current and reducing the current speed. Surface friction is an other obvious factor to slow down the current.

As the density current rapidly weakens in the interval from t=3500 sec to 4500 sec, the leading solitary wave, generated by the current, begins to separate from the current. Comparing 'ink' field with buoyancy field at t=4500 sec, it is found that the air tagged by the ink field is left behind the wave (Fig.7.5i).

At this time (4500 sec), the leading solitary wave is without closed recirculation and is in a quasi-stationary state in which it propagates at nearly constant speed. By slowly decreasing their magnitudes, the maximum horizontal velocity, u_{max}, and maximum vertical velocity w_{max} purely induced by the wave show the dissipation effects of surface friction and eddy viscosity . u_{max} decreases from 8.2m/s at t=4500 sec to 7.5m/s at t=6500 sec, and w_{max} from 1.1m/s to 0.96m/s in the time interval from 4500 sec to 6500 sec.

7.4 Comparison between observation and simulation results

7.4.1 Speeds of the density current and the wave

The temperature difference between the current and ambient air results in a pressure gradient force which acts on the cooler air to drive it forward thus forming a density current. The speed of density current relative to the ambient wind can be roughly estimated by using the following formula (Charba, 1974):

$$V = k\sqrt{gh\frac{\Delta\theta}{\theta}} \tag{7.1}$$

where k, the dimensionless Froud number, had been evaluated in laboratory, atmosphere, and numerical models. It varies from 0.74 (Georgi, 1936) to $\sqrt{2}$ (Benjamin, 1968). h is the mean height of the density current, and $\Delta\theta$ is average potential temperature difference between the current and the ambient fluid with potential temperature θ.

Because of the complexity of the background temperature and wind field and because of the lack of sufficient data, it is very difficult to estimate, for our observation, the parameters like $\Delta\theta$ and k in Eq.(7.1). Nevertheless Eq.(7.1) can still be used to estimate, based on limited observational data, the density current speed.

In order to compare the evolution of the simulated and observed leading solitary waves, their speeds are plotted in Fig.7.6. In the succeed sections, the wave speed refers to the speed of the leading solitary wave in a frame relative to the ground. In the simulation, the speeds of wave and density current are estimated by measuring the location of the wave peak and leading edge of the current at different times, respectively. The speeds are the average speed between two measuring times, the measuring time interval is 500 sec in this experiment.

Observations suggest that the wave speed quickly drops from 26.3m/s to 11.6m/s in about 2500 sec; it then reaches to a steady state with speed of about 11.5m/s. The simulation exactly replicates this evolution from 1500 sec to 3000 sec. Except for a small jump in speed at t=3500 sec, the wave speed determined from simulation attains a relative steady speed 12.0 m/s which is slightly higher than observed 11.5 m/s.

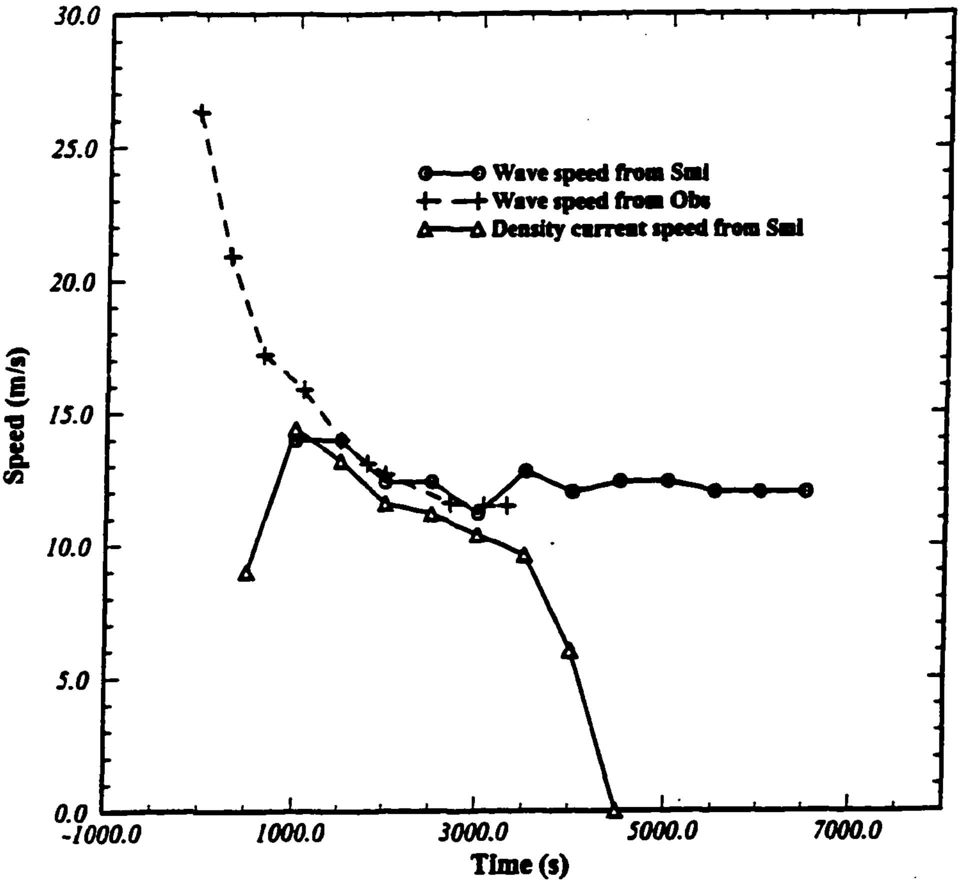

Fig.7.6 The evaluation of wave and density current speeds. Dot-solid line is wave speed of simulation; cross-dash line is wave speed of observation; triangle-solid line is density current speed of simulation.

During the initial 1500 sec period of time, the difference of wave speed between observation and simulation is obvious. Actually the model could not simulate the evolution of the wave during this period time. There are several reasons: 1) the environment near the thunderstorm which generated the wave is very different from the horizontally homogeneous environment used in the simulation; 2) the coldpool used in the 2D model cannot totally duplicate the real 3D thunderstorm outflow neither dynamically nor thermodynamically; 3) the involvement of moisture as the outflow is forming makes the processes more complicated. It cannot be simulated by this dry model.

Many similar simulations, with different source strengths and ambient fields, suggest that there is always a small jump of the wave speed right after the departure of the density current head from the wave. This jump is not an occasional phenomena or measurement error in this simulation. It implies that the denser air in the current head somehow drags the wave when they move together. As the current head leaves the wave, the drag force is released from the wave, so the wave can move faster. Besides, the slope formed by the head perhaps accelerates the motion of wave peak when the current head is leaving the wake of the wave. After the small jump, the wave speed slightly reduces and the wave no longer has any density current. The wave then adjusts to a relative steady state.

This small jump is not seen in the wave speed plot of the observation, adopted from Fig.9 (Doviak et al., 1991), in Fig.7.6. But when we carefully investigate the isochrones of wave position at different times (Fig.7.1), it is found that the leading wave propagates for a longer distance in the 5.5 minutes time interval 2305:30 to 2311, than for the same period in the interval from 2300 to 2305:30. This means a faster wave speed at a later time. It is in a good agreement with simulation. The wave speed jump of the simulation is observed at 3500 sec right after the leading wave passed the virtual tower located at 74.8 km. In addition, the small jump in bore front speed had the appearance in another similar observation (Fulton et al., 1990) although it had not been discussed in the paper. Certainly, observational errors or horizontal inhomogeneousness of wave guide, which may also make the small jump in wave speed, cannot be excluded. So more observations are needed to prove this finding.

In the foregoing part, we have examined the small wave speed jump after the density current head leaves the wave. Furthermore, we notice that the speed of the density current quickly declines from 9.6m/s to 0m/s after the jump increase in wave speed. This sudden density current speed decline suggest that, without wave drag, the density current would not have advanced as fast as it did, nor move as fast move as fast as before the jump.

It is not difficult to understand this wave drag effect on the density current. Generally, a solitary wave propagating in a waveguide attached the ground induces a horizontal velocity field in which the wind direction is the same as the wave propagation direction near the ground, and opposite above a certain height which depends on the wave amplitude (Fig.7.5j). The solitary wave provides a local positive wind field, even in an negative ambient wind field, for a density current head when it advances beneath the wave. This local positive wind field helps the density current advance more rapidly than in the environment without the wave.

7.4.2 Kinetic and thermodynamic structures of the leading wave

Tower data provides a vertical profile (from z=0 to 444m) of horizontal velocity induced by the leading solitary wave. At the corresponding simulation time (t ≅3000 sec), the profile of horizontal velocity computed at 74.8 km in the numerical domain shows almost same shape as the observed one below 444m (Fig.7.7).

Because of low spatial resolution of observation in vertical direction , the maximum of u located between 90m and 176m may not be resolved. The value might be larger than 11.7m/s. The simulation with higher resolution in vertical direction than tower shows that the maximum u is 12.4m/s at height 103.6m. Thus the values and locations of maximum u in the simulation are in quite good agreement with in the observation.

The feature of the u profile with a maximum located above the surface is similar to the feature across a large amplitude solitary wave with a reversed recirculation shower in Chapter 5. It easily leads us to conclude that the existence of reversed recirculation in the simulated and observed solitary wave. But after close examination (see section 7.4.5), we found thatalthough they have similar features, the mechanism is different. For this case, surface friction instead of reversed recirculation results in the monotonous decrease of u near the surface below about 100m. So the u profile exhibits a maximum above the surface.

Tower observation not only provides an estimate of the vertical profile of horizontal velocity across the center of the leading wave, but also a time series of horizontal and vertical velocities (u and w) at several observation levels. For the sake of

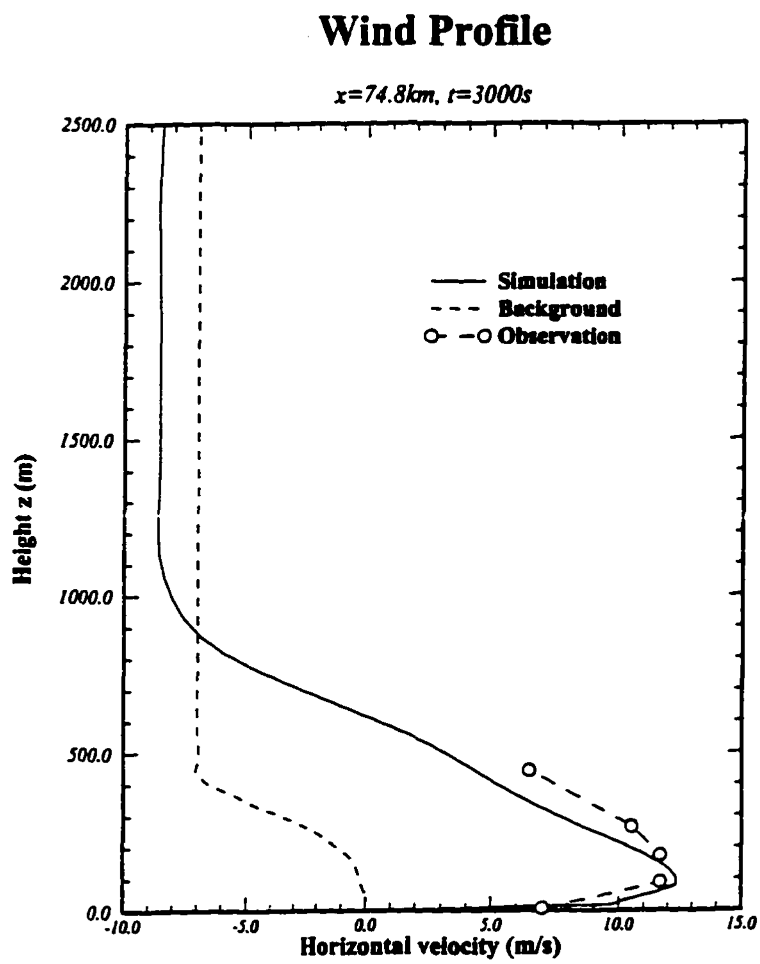

Fig.7.7 Vertical profiles of horizontal velocity relative to the ground of observation (open circle-dash line) and simulation (solid line) across the center of leading solitary wave. Dash line is background wind profile.

comparison, u and w are recorded at the virtual tower at almost same heights as the real one, except the lowest level because the first level in the model is 18.7m which is higher than 7m for the observation. The plots of the evolution of observed and simulated u at four different levels as the leading wave passes the tower are displayed in Fig.7.8. The plots in Fig.7.8 show a good agreement between the simulation and observation.

Due to coarse spatial resolution of the model, the small wave like perturbations overlaid on the main feature in the observation are not well represented in the simulation. Some of these small perturbations, more evident at the 7m level, are thought to be produced by KH waves and turbulence (Doviak et al., 1989). Recall b field at t=3000 sec (Fig.7.5f) when the leading solitary wave passes the tower, the density current is with the wave. Tower instruments at the lower height are inside the density current head where the stability is relative weak and wind shear is relative strong due to surface friction in the simulation, as well as in the observation. Thus KH wave is a reasonable interpretation.

Closely comparing the wavelengths between the observation and simulation (Fig.7.8), we found that the wavelength of the simulated wave is larger than the observed one, especially at two higher heights (z=266 m and 444m). Horizontally inhomogeneous ambient wind and temperature fields in the real atmosphere might result in these wavelength differences because in the model the ambient wind and potential temperature fields are horizontally homogeneous. In addition, a constant ambient wind above 444m in the simulation might not accurately represent the real ambient wind. This could also affect the structure of the simulated solitary wave. The differences between the simulation and observation are more evident in the comparison of w fields.

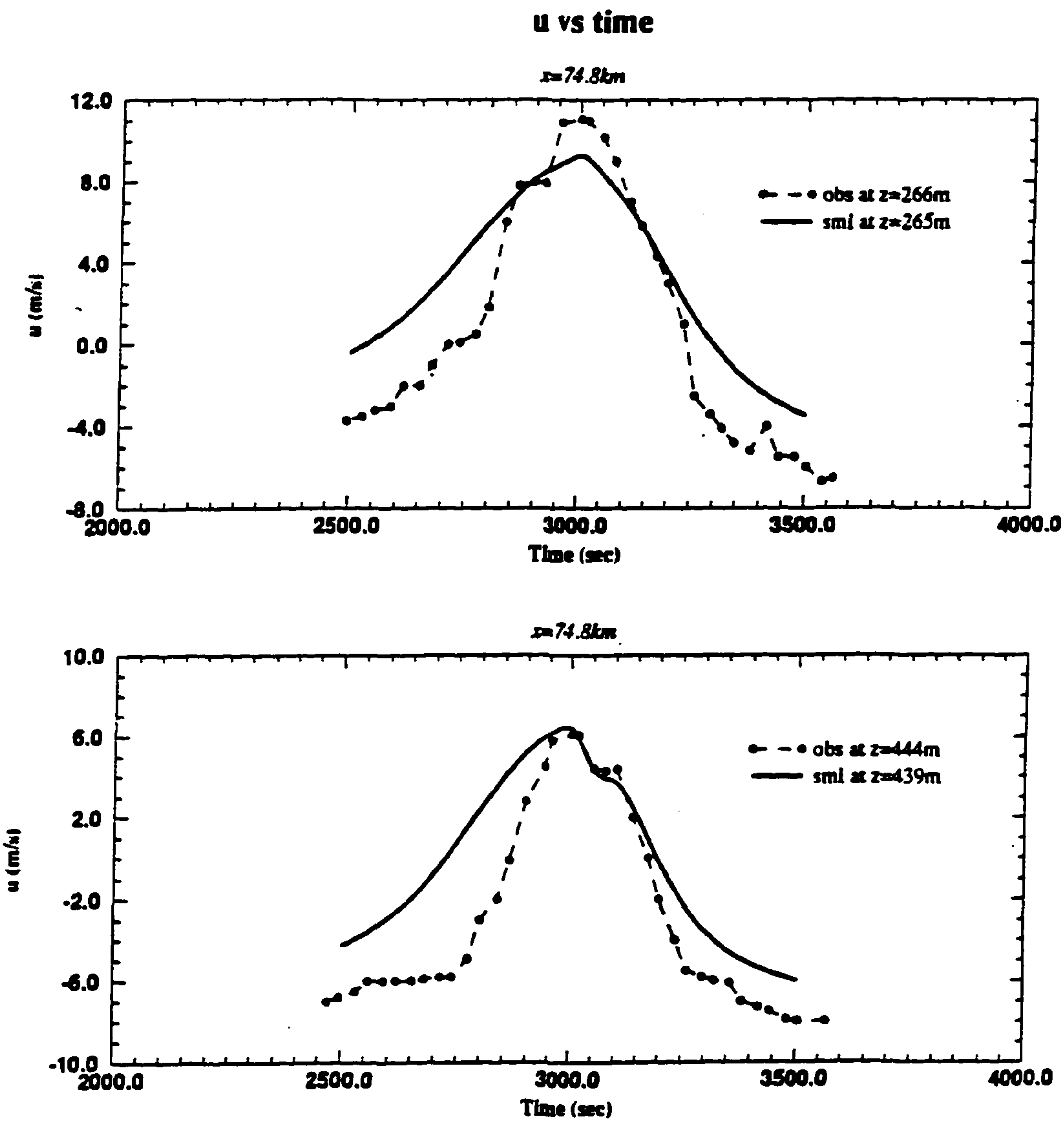

Fig.7.8 Horizontal velocity of observation (dot-dash line) and simulation (solid line) *vs* time at four levels.

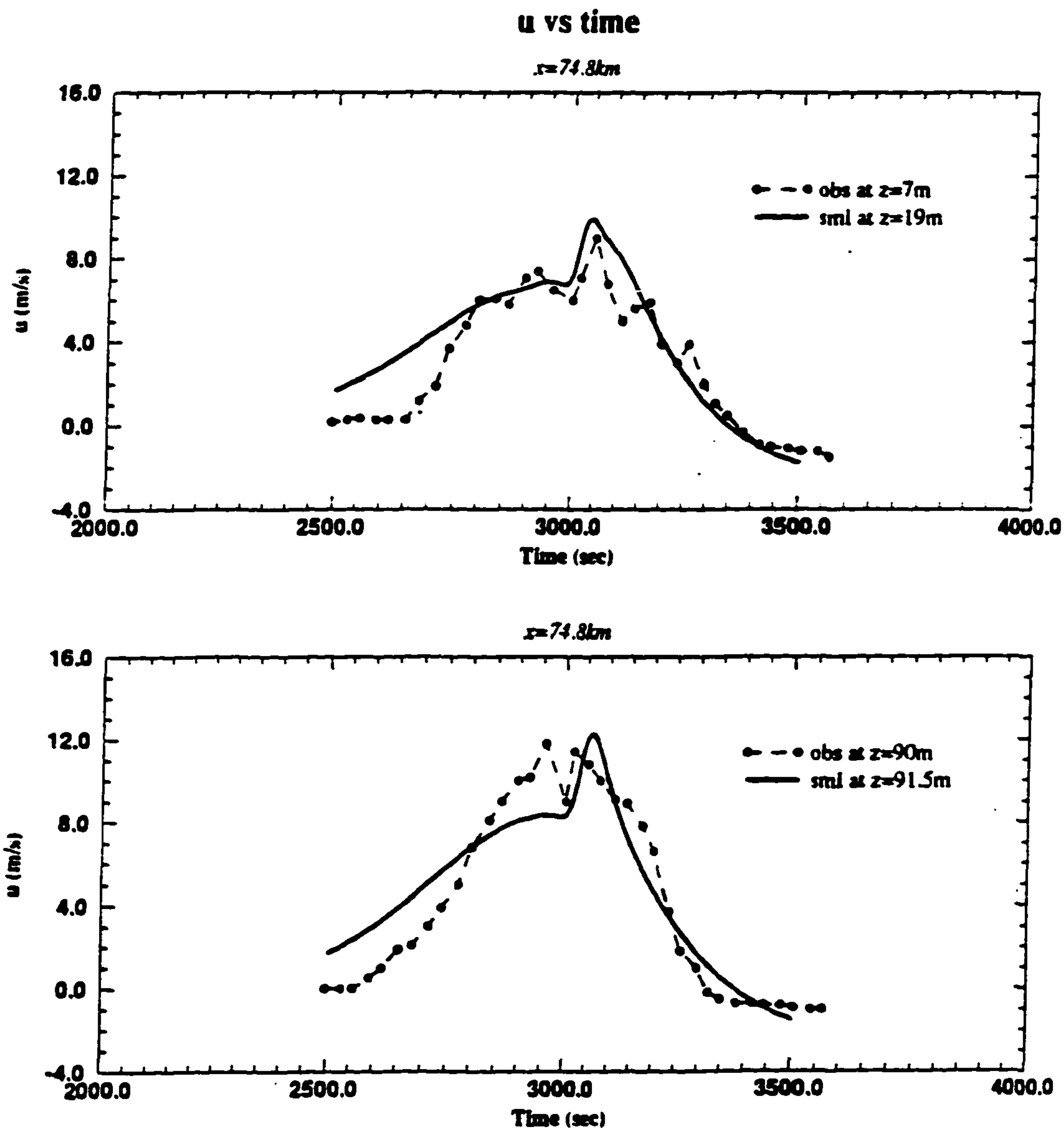

Fig.7.8 (Continued)

Fig.7.9 shows the time series of w component at two different heights. Unlike u component, w maximum and minimum from the simulation are much smaller than observation. The reasons why the simulation failed to reproduce the large observed variation of w component may be due to 1) the relative coarse spatial resolution of the model; 2) not well representation of real turbulence in the model. The reasons, given in the above paragraph, which cause the differences between the simulation and observation in the wavelengths might also lead the simulation failure of w fields.

Small positive peaks of simulation at both heights near center of the wave are result from the circulation induced by the density current head. So the peak at 265m near the head of the density current is relatively higher than at 439m. The small disturbances modulated on the solitary wave feature at 266m level in the observation are thought to be KH waves. Like the u component, the simulation does not reveal these KH waves in the w time series.

However, the wavelengths of simulation shown in Fig.7.9 is in a fairly close agreement with the observation. Moreover, w of observation shows an unsymmetric feature. The positive portion is smoother and smaller than negative. This feature is also clearly visible in the simulation although the magnitude of w is smaller. Closely inspecting the shape of the u component in Fig.7.8, the unsymmetric feature is also found. The front half (left half in Fig.7.8) of the wave is smoother than rear half. The entire unsymmetric feature of the leading wave can be distinctly seen in Fig.7.5f.

These unsymmetric features are created by the density current head within the wave. The direction of circulation induced by a solitary wave is downward (upward) at

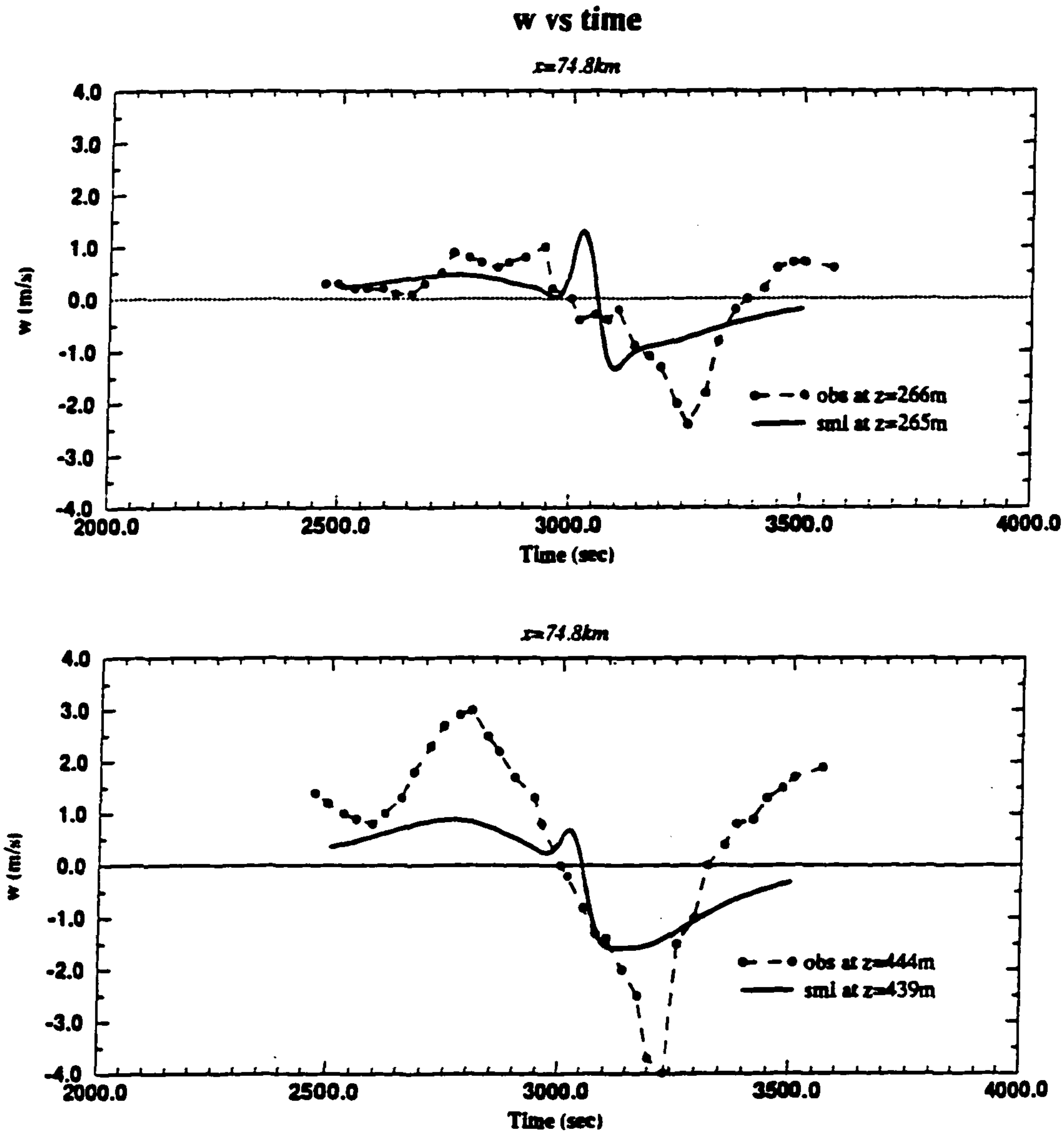

Fig.7.9 Vertical velocity of observation (dot-dash line) and simulation (solid line) *vs* time at two levels.

the rear (front) of the wave and forward (backward) at lower (upper) level. The flow of the circulation in the wave is partially blocked by the density current which is no longer symmetrically landed in the wave. Thus, there are sharper gradients of u and w and stronger downward motion in the wake to keep the continuity of the flow. Its external manifestation is unsymmetric b, u, and w fields. When the current leaves the wave, the wave regains its normal symmetric form even though the environment has wind shear (Fig.7.5j).

7.4.3 Temperature structure of the wave

The retrieved temperature field based on the tower data is plotted in Fig.7.10. Assuming the wave is relatively steady as it passes over the tower, it will propagate about 13.4 km in 20 min. at its speed of 11.2 m/s. The temperature field at 3000 sec of simulation with corresponding spatial distance of 14 km is shown in Fig.7.12 as well.

The resemblance between observation and simulation is obvious. The unsymmetric feature of the wave also exhibits in both observed and simulated temperature fields. A cold core centered at about 250m with a small tail in the simulation indicates the position of density current head. The tail in the observation is not very obvious. But the core temperature minimum in the simulation is 2 degrees colder than the observation. The small wiggles on the contours in the core region at about 75.5 km in the simulation, which is not found in the observation, reflect the fine structure of the density current. The relatively coarse spatial resolution in the vertical direction in the observation might not be capable of resolving these small structures (i.e. the tail and wiggles) displayed in the simulation. On the other hand, the observed small perturbations on the contours of 19°C,

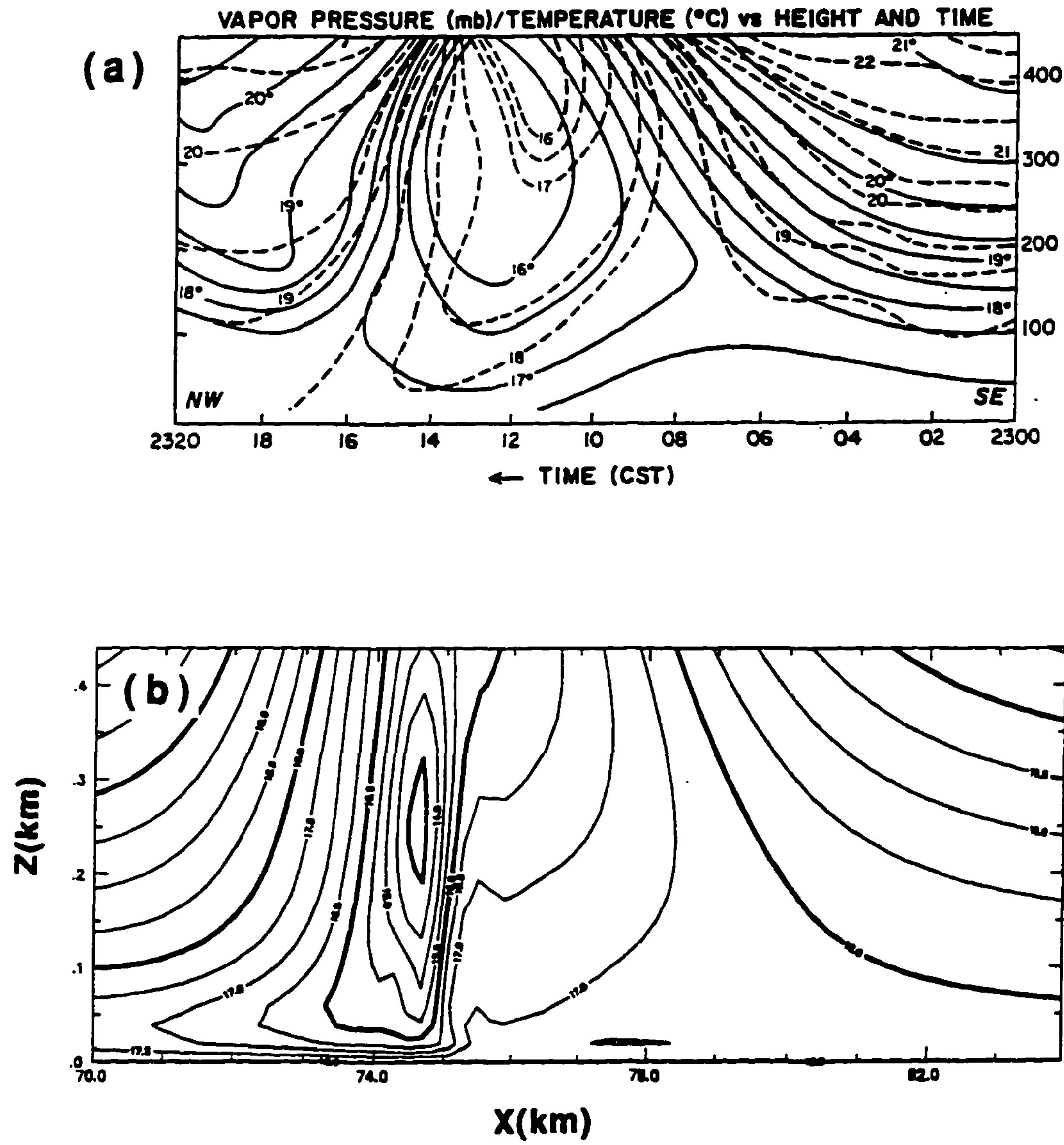

Fig.7.10 Temperature field of (a) observation (solid line) (from Doviak and Ge, 1984) and (b) simulation. The contour interval is $0.5^{\circ}C$.

19.5 °C, and 20 °C in the wake are not found in the simulation. Turbulence observed in the wake of the wave (Doviak and Ge, 1984) could cause these small perturbations.

7.4.4 Second wave

A second wave following the leading wave was observed by the tall tower. Its peak passed the tower at about 23:40 CST, 30 min. late after the leading wave. The simulation shows that several waves, at least four at t=6500 sec (Fig.7.4), are generated. The second wave of the simulation passed the virtual tower at about 5000 sec, about 33 min. late after the first one. It agrees with 30 min. found in the observation. Tower data have not shown third and fourth waves, perhaps because their amplitudes are too small to be detected.

7.4.5 Discussion on the existence of recirculation

After a close study, we found that the recirculation does not exist in the leading solitary wave in the observation and simulation. One could argue that observed and simulated u maximum located above the ground is a sign to show the existence of the recirculation. A small couplet of positive-negative vertical velocity beneath the leading wave at t=3000 sec (Fig.7.11) seems to support this argument. But as the head of density current leaves the leading wave at t=4500 sec, the couplet vanishes as well (Fig.7.12). But u maximum is still located above the ground (see u field in Fig.7.5i). This suggests that the couplet is produced by the density current and the decrease of u near the ground results from the surface friction rather than the recirculation within the wave.

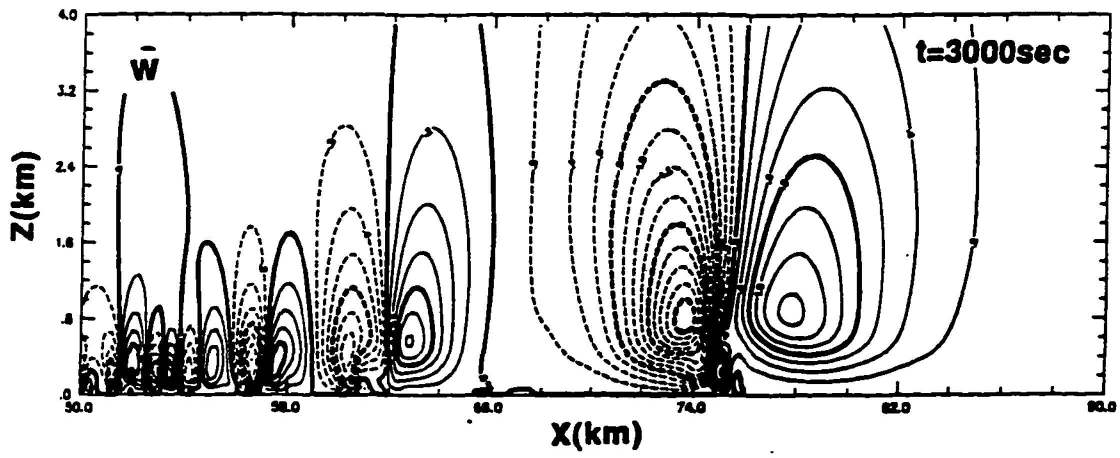

Fig.7.11 Magnified vertical velocity field of leading solitary wave at 3000sec.

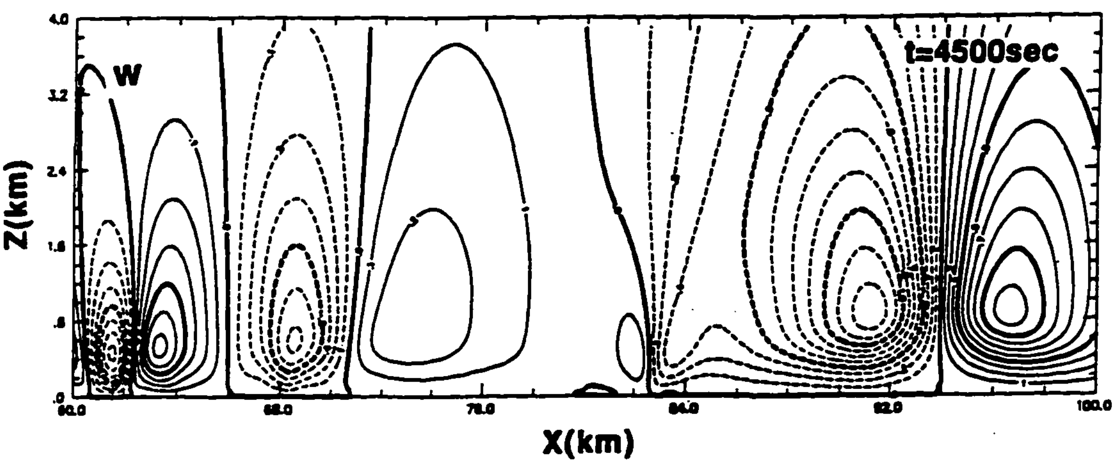

Fig.7.12 Magnified vertical velocity field of leading solitary wave at 4500sec.

One could continue to argue that the recirculation does exist within the leading solitary wave when the wave has the density current, but it is dissipated by the eddy viscosity in the observation and simulation. Thus the trapped current head leaks out from the wave in the simulation. However, small change in wave speed, before and after the current leaks completely out from the wave in the simulation, suggests that the wave amplitude does not change too much because solitary wave speed is amplitude-dependent. The fact of no recirculation in the wave after the departure of the density current head implies that the amplitude of the leading solitary wave is not large enough to have a recirculation within it even in the initial stage in the simulation.

Note that in a complicated background potential temperature field with wind shear, it is almost impossible to use the criterion $a/h>$ (or$<$)1 used in simple background fields to judge if a solitary wave is a large amplitude one. In addition, checking the b field at t=6500 sec (Fig.7.5j), the largest vertical displacement induced by solitary wave is no longer right at the interface between stable and neutral layers.

Moreover, the study in the Chapter 6 has demonstrated that strong surface friction hampers the formation of recirculation in a solitary wave.

Thus we conclude that for both simulation and observation the leading solitary wave generated by the density current is not large enough to have a recirculation inside, and the head of density current is not trapped, if the word 'trap' is strictly used to describe the trapping effect of large amplitude solitary wave with recirculation, by the leading solitary wave. But the wave did propagate with and 'drag' the density current head for a period time. After density current loses its momentum and spreads out on the ground, the wave leaves it.

Some observations (Fulton et al., 1990; Smith and Morton, 1984) suggest that this 'trapped' phenomena take place 'only in the early, formative stages of bores when they are very near the source.'. Their findings support our conclusion.

7.4.6 Scenario for the evolution of the solitary waves

According to the previous study of this case, Doviak et al. (1991) suggest a scenario for the evolution of the solitary waves (Fig.7.13). Gathering the buoyancy fields at different times of the simulation into one picture (Fig.7.14), it shows dramatic similarity with the observation. In order to avoid unnecessary repetition of section 7.3, the detailed description of the evolution will not be presented here.

The similarity demonstrates that the evolution of the solitary waves has been successfully simulated.

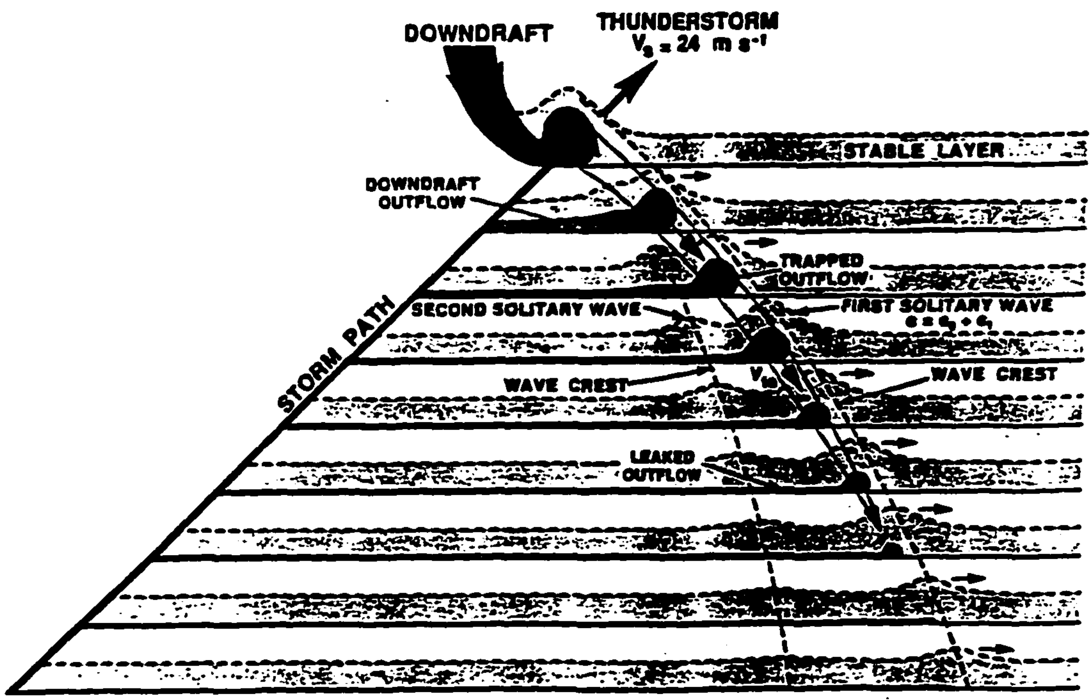

Fig.7.13 A scenario for the evolution of thunderstorm-generated solitary waves (From Doviak et al., 1991).

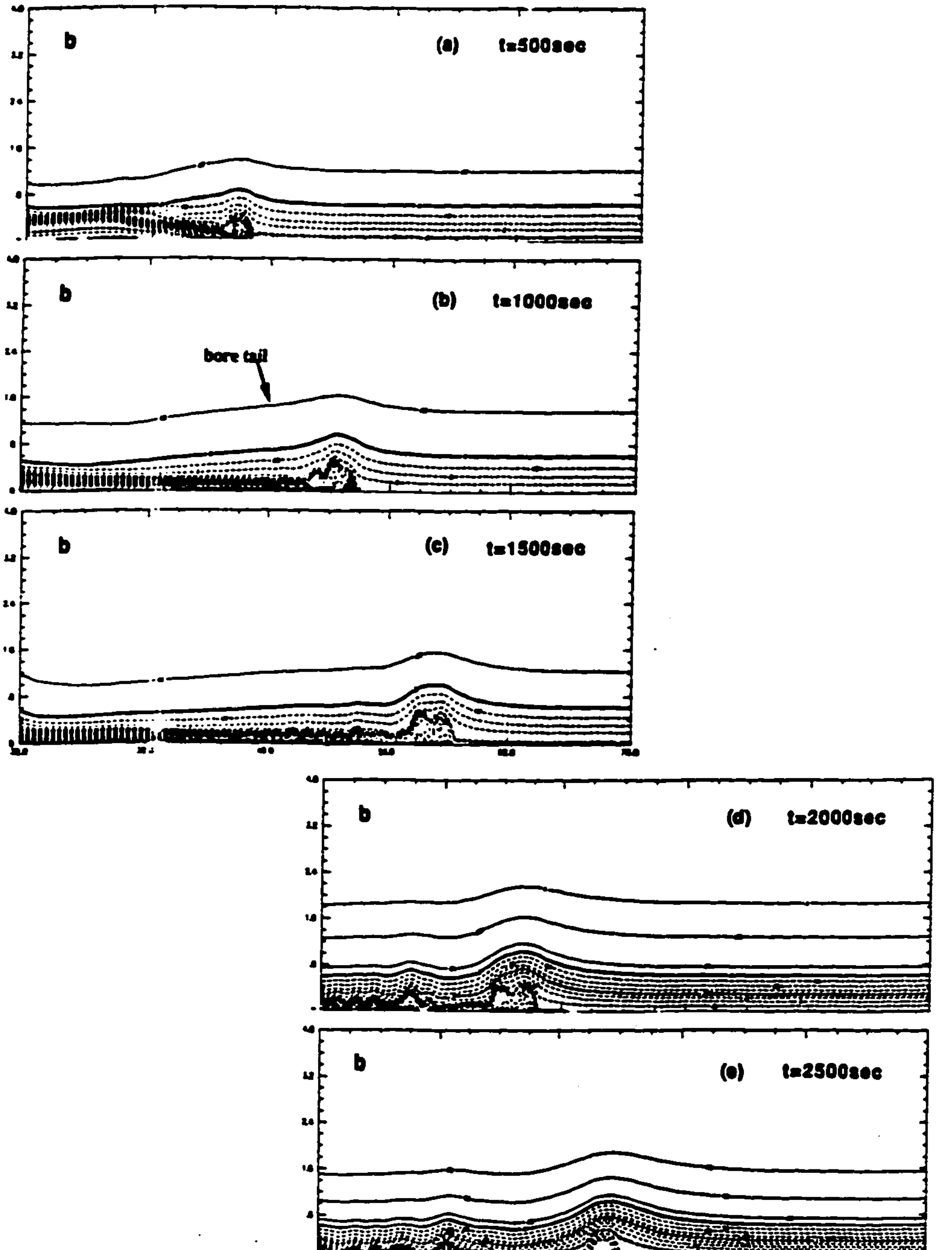

Fig.7.14 The evolution of the solitary wave and density current in the simulation displayed in buoyancy fields at different times. The time interval is 500sec, except the bottom one.

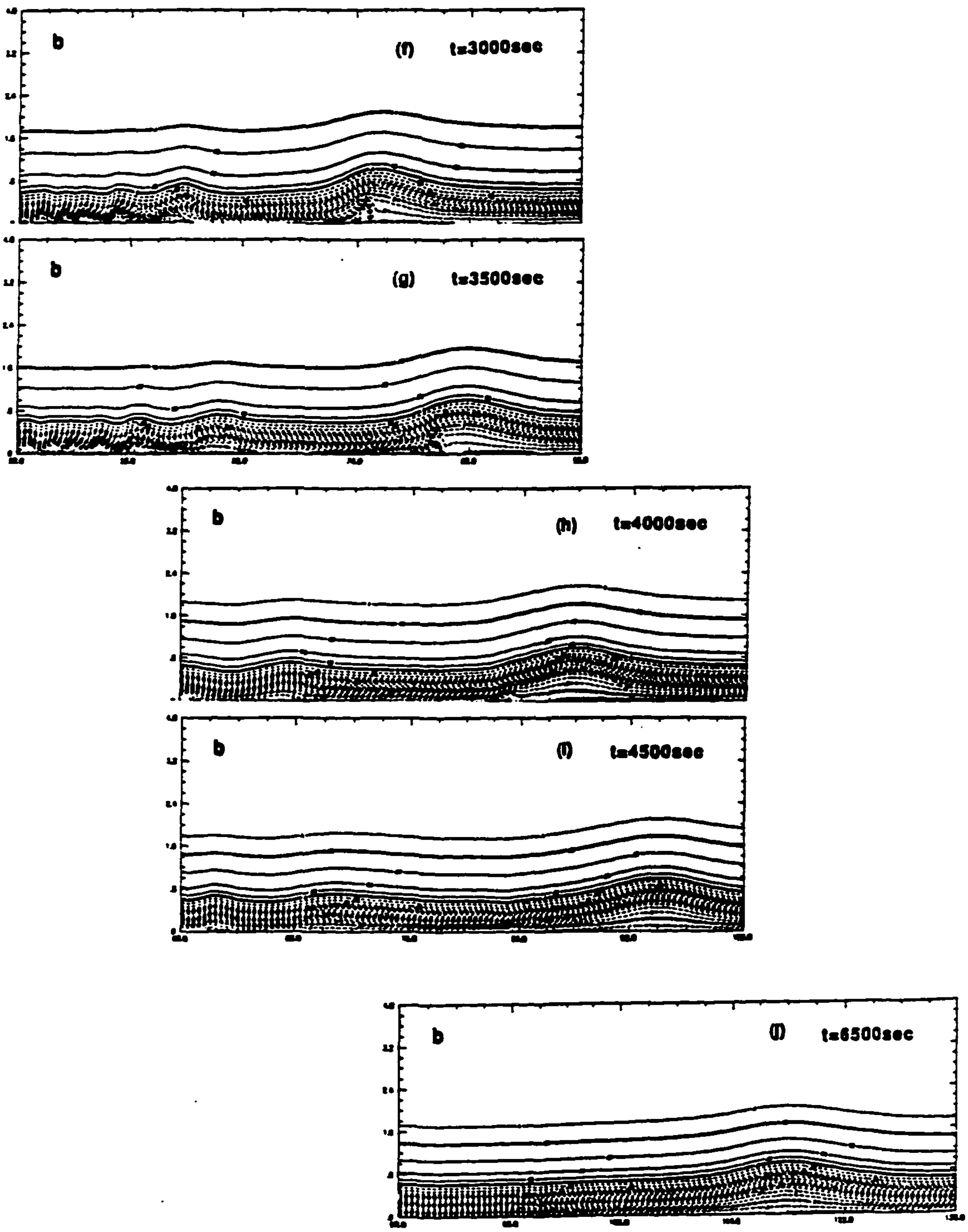

Fig.7.14 (continued)

7.5 Conclusion

The model simulation has successfully duplicated the evolution of the solitary wave observed by multisensers and provided more useful information, which was not observed, to help us to have a better understanding of the phenomena we studied.

In comparison with previous case studies of solitary waves (e.g. Doviak and Ge, 1984; Doviak et al., 1991; Fulton et al., 1990; Smith and Morton, 1988), this simulation has advantage to reproduce the evolution, generation, propagation and decay, of the wave in detail. It makes possible to examine the internal structures of the wave, such as velocity and temperature fields, and compare them with the observation with a relatively high resolution.

Chapter

8

Summary and Conclusions

A two-dimensional dry incompressible vorticity-stream function model is developed for the purpose of studying internal nonlinear buoyancy waves and related phenomena in the lower atmosphere. The model equations are vorticity, Poisson, and conservation of potential temperature equations with three variables: vorticity, stream function, and buoyancy. Kinematic and thermal viscosity terms are included. These time-dependent nonlinear partial differential equations are 'discretized' into finite-difference representations and the variables exist only at grid points. The third-order Adams-Bashforth scheme is adopted for time integration, and the fifth-order upstream advection scheme is applied to spatial derivatives. A stretched vertical coordinate is used to increase the spatial resolution near the ground. because the most rapid changes in the variables occur there. The lateral boundaries are open in order to allow internally generated waves to pass out freely. To avoid reflections of the waves, 'sponge' boundary conditions are applied at and near the lateral and top boundaries.

For testing the model, several simulations of solitary waves are conducted in a relatively simple background field: a deep neutral layer over a shallow stable layer near the ground with constant Brunt-Väisälä frequency, in absence of surface friction, physical dissipation, and ambient wind shear. The simulation results are in good agreement with the results of weakly nonlinear theory. Two kinds of collision of two small amplitude solitary waves predicted by a theoretical study (Matsuno, 1980) are successfully reproduced. In the simulations, several solitary waves are generated by a thunderstorm outflow and propagate in the numerical domain. With the aid of a parcel tracer technique, the influence of the waves on the ambient air parcels is tentatively examined.

In contrast to theoretical and laboratory studies, the numerical simulation described in this dissertation enables investigation of the detailed structure inside the recirculation region. In the simulations, reversed recirculation within large amplitude solitary waves has been found for the first time. The rotation direction of reversed recirculation is opposite to the outside flow and the direction of normal recirculation assumed by the previous theoretical study. It has been proven that both normal and reversed recirculation do not violate any physical principals. However, so far, normal recirculations have not been found in our simulations. Because of coarse spatial resolution, it is very difficult to observe the rotation direction of recirculation in laboratory experiments. Hence, no observation of either reversed or normal recirculation has been reported.

The existence of recirculation enables large amplitude solitary waves to trap air and transport it, because recirculation forms a closed region within the wave. Theoretically, in an ideal waveguide without any dissipation the trapped fluid will forever be transported by the unchanging wave. However viscosity is inevitable, even in our simulations. Though no physical viscosity term was included in this simulation, the truncation error in the numerical scheme plays a similar role. Because of viscosity, the amplitude of a solitary wave gradually decreases, the size of recirculation region also shrinks, and the trapped fluid leaks out. Furthermore, for the reversed recirculation the fluid near the interface between recirculation region and outside flow is continuously mixing due to strong wind shear. Partially trapped fluid is entrained out and flows with the outside fluid, which moves backward relative to the wave, eventually leaking out. Using a passive tracer technique, the trapping and leaking effects are clearly visualized.

The relations among amplitude, wavelength, and wave speed of solitary waves are obtained through many numerical simulations. For small amplitude solitary waves ($a/h<1$), the wavelength shrinks with the increase of wave amplitude. In contrast, for large amplitude solitary waves ($a/h>1$), the wavelength increases with amplitude. The wave speed is nearly linearly proportional to amplitude for both small or large amplitude solitary waves. These results are consistent with the results obtained from the laboratory experiments and weakly nonlinear theory for extremely small amplitude solitary waves ($a/h<<1$).

The balance between dispersive and nonlinear effects results in steady solitary waves of small amplitude ($a/h<<1$). It can be employed to explain the relation between amplitude and wavelength. Nevertheless, the relation for large amplitude solitary wave is totally different from the one for small waves. I believe that the existence of recirculation within large amplitude solitary waves critically influences the relation between amplitude and wavelength.

As expected, turbulent eddy diffusivity in the atmospheric boundary layer reduces the amplitude and wave speed of solitary waves propagating in the stable layer. The induced horizontal and vertical velocity maximums by the waves are also reduced. The stronger the degree of the turbulent eddy diffusivity, the further the reduction of these parameters. Recirculation within the large amplitude solitary wave in absence of eddy diffusivity can be eliminated by large eddy diffusivity.

The effects of low-level wind shear on solitary waves are relatively complicated. First, the downstream (i.e. wave propagates in the ambient wind direction) wave propagates faster than the upstream (i.e. wave propagates opposite the ambient wind direction) wave. The wave speed increase or decrease is not simply equal to the average ambient wind. Second, the structures of solitary waves are modulated by the ambient wind shear. For example, in the simulation with 10^{-2} 1/s shear in the lower layer, the amplitude of the downstream wave is 2.3 times larger than the wave in a calm environment. Due to strong shear, KH waves appear in the solitary waves. The shape of wave becomes rough and unsymmetric. We also found that it is not proper to determine whether the wave can trap fluid from the ratio of wave amplitude and height of the stable layer if shear is present.

An internal solitary wave generated by a thunderstorm outflow, observed by NSSL's Doppler weather radar, a 444m tall tower and a surface network in central Oklahoma in the late evening of 11 May 1980, is modeled. The simulation results show a quite good agreement with the observation in several aspects. The kinematic and thermal features of the simulated wave are basically coincident with the observed features. The evolution of the wave is reproduced by the simulation.

It has been demonstrated that the density current, which generated the solitary wave, is not trapped by the wave because no recirculation has been found in the wave. However the wave does help the current move farther and faster than it would without a wave in the initial stage. The simulation shows remarkable similarity with the scenario depicted by the previous study based on the analysis of the observation.

Although the major aspects of the observation are successfully simulated, the model failed to reproduce the very early stages of the formation of the observed solitary wave. The magnitude of vertical velocity induced by the simulated wave is smaller than that observed. Thus further investigations with a more comprehensive model (three-dimensional, moisture included) are still required to explore the three-dimensional properties of the solitary wave, moisture effects on the waves in more realistic environment.

It is known that solitary waves can initiate or enhance deep convection, and induce a strong wind shear which can jeopardize aircraft flying near the ground, and trap and transport hazardous materials in an emergency situation at faster speed than wind advection and diffusion. Through studies, such as this, more characteristics of solitary waves, especially those with large amplitude in the lower atmosphere may be explored further. Eventually, such studies may be useful in developing better technologies for predicting severe weather under circumstance in which solitary waves play a vigor role.

Reference

Abdullah, A. J., 1955: The atmospheric solitary wave. *Bull. Amer. Meteor. Soc.* **36**, 511-518.

Anderson, D. A., J. C. Tannehill, and R.H. Pletcher, 1984: Computational fluid mechanics and heat transfer. *Heisphere Publishing Corporation*. 92pp

Baines, P. G. 1984: A unified decription of two -layer flow over topography. *J. Fluid Mech.,* **146,** 127-167.

Benjamin, T. B., 1967: Internal waves of permanent form in fluids of great depth. *J. Fluid Mech.*, **29,** 559-592.

Brost, R. A., and J. C. Wyngaard, 1978: A model study of teh stably stratified plantary boundary layer. *J. Atmos. Sci.* **35,** 1427-1440.

Carbone, R. E., J. W. Conway, N.A. Crook and M. W. Moncrieff, 1990: The generation and propagation of a nocturnal squall line. Part I: Observations and implications for mesoscale predictability. *Mon. Wea. Rev.*, **118,** 26-49.

Chen, H. H., Y. C. Lee and N.R. Pereira, 1979: Algebraic internal wave solitons and the integrable Calogero-Moser-Sutherland N-body problem. *Phys. Fluids,* **22,** 187-188.

Christie, D. R., 1989: Long nonlinear waves in the lower atmosphere. *J. Atmos. Sci.* **46,** 1462-1491.

----, 1992: The morning glory of the Gulf of Carpentaria: a paradigm for non-linear waves in the lower atmosphere. *Aust. Met. Mag.* **41,** 21-46.

----, and K. J. Muirhead, and A. L. Hales, 1978: On solitary waves in the atmosphere. *J. Atmos. Sci.* **35,** 805-825.

Clark, R. H., 1972: The morning glory: an atmospheric hydraulic jump. *J. Appl. Meteor.* **11,** 304-311.

Crook, N. A., and M. J. Miller,1985: A numerical and analytical study of atmospheric undular bores. *J. Atmos. Sci.* **43.** 171-181

Davis, R. E., and A. Acrivos, 1967: Solitary internal waves in deep water. *J. Fluid Mech.* **29,** 593-607.

Doviak, R. J., and S. Chen and D. R. Christie, 1991: A thunderstorm-generated solitary wave observation compared with theory for nonlinear waves in a sheared atmosphere. *J. Atmos. Sci.* **48**, 87-111.

----, and S. Chen, 1988: Observations of a thunderstorm generated gust compared with solitary wave theory. Final report, DOT/FAA/SA-88/1, Dept. of Transportation, FAA, Advanced System Acquisition Service, Washington, DC, 20590, 24pp.

Doviak, R. J., and D. S. Zrnic', 1984: *Doppler Radar and Weather Observations*. Academic Press, Orlando, Florida, 458pp.

Durran, D. R., 1991: The third-order Adams-Bashforth method: An attractive alternative to Leapfrog time differencing. *Mon. Wea. Rew.*, **119**, 702-720.

Fulton, R., D. S. Zrnic, R. J. Doviak, 1990: Initiation of a solitary wave family in the demise of a nocturnal thunderstorm density current. *J. Atmos. Sci.* **47**, 319-337

Garratt, J. R., 1992: *The atmospheric boundary layer*. Cambridge University Press, 28pp.

Goff, R. C., 1975: Thunderstorm outflow kinematics and dynamics. NOAA Tech. Memo ERLTM-NSSL, No. 75, 63pp

Goncharov, V. P., and A. K.Matveyev, 1982: Observations of nonlinear waves on an atmospheric inversion. *Izv. Acad. Sci.* USSR *Atmos. Oceanic Phys., Engl. Transl.*, **18**, 61-64

Grimshaw, R., 1981a: Evolution equations for long, nonlinear internal waves in stratified shear flows. *Stud. Appl. Math.*, **65**, 159-188.

----,1981b: Slowly varying solitary waves in deep fluids. *Proc. Roy. Soc.* London, **376**, A 319-332.

Kaimal, J. C., and J.J. Finnigan, 1994: *Atmospheric boundary layer flows*. Oxford University Press, 11pp.

Mahaptra, P. R., R. J. Doviak and D. S. Zrnic, 1991: Multisensor observation of an atmospheric undular bore. *Bull. Amer. Meteor. Soc.* **72**. 1468-1480.

Maslowe, S. A., and L. G. Redekopp, 1979: Solitary waves in stratified shear flows. *Geophy. Astrophys. Fluid Dyn.* **13**, 185-196.

----, and ---, 1980: Long nonlinear waves in stratified shear flows. *J. Fluid Mech.*, **101**, 321-348.

Hasse, S., and R. K. Smith, 1984: Morning glory wave clouds in Oklahoma: a case study. *Mon. Wea. Rev.* **112**, 2078-2089.

----, 1989: The numerical simulation of atmospheric gravity currents. Part II: Environments with stable layers. *Geophy. Astrophys. Fluid Dyn.* **46**, 35-51

Hirota, R., 1971: Exact solution of the Korteweg-de Vries equation for multiple collisions of solitons. *Phys. Rev. Lett,* **27**, 1192-1194.

Kao, T. W., F. S. Pan, and D. Renouard, 1985: Internal solutions on the pycnocline: generation, propagation, and shoaling and breaking over a slope. *J. Fluid Mech.,* **159**, 19-53

Korteweg, D. J. and G. de Vries, 1895: On the change of form of long wave advancing in a retancular canal and on a new type of long stationary waves. *Phil. Mag.* **39**, 422-443.

Kundu, P. K., 1990: Fluid Mechanics. *Academic press.* 196pp

Liu, C. and M. W. Moncrieff, 1996: A numerical study of the effects of ambient flow and shear on density current. *Mon. Wea. Rew.* **124**, 2282-2303.

Matsuno, Y., 1979: Exact multi-soliton solution of the Benjamin-Ono equation. *J. Phys. A: Math. Gen.,* **12**, 1519-1536.

Maxworthy. T. 1980: On the formation of nonlinear internal waves from the gravitational collapse of mixed regions in two and three dimensions. *J. Fluid Mech.,* **96**, 47-64.

Miura, R. M., C.S. Gardner and M. D. Kruskal, 1968: Korteweg-de Vries equation and generalizations. II: Existence of conservation laws and constants of motion. *J. Math. Phys.,* **9**, 1204-1209.

Nakamura, A., 1979: Backlund transform and conservation laws of the Benjamin-Ono equation. *J. Phys. Soc.* Japan, **47**, 1335-1340.

Neal, A. B., I. J. Butterworth, and K. M. Murphy, 1977: The morning glory. *Weather* **32**, 176-183.

Ono, H. 1975: Algebraic solitary waves in the stratified fluids. *J. Phys. Soc.* Japan, **39**, 1082-1091.

Pullin, D. I. and Grimshaw, R. H. J. 1988: Finite-amplitude solitary waves at the interface between two homogeneous fluids. *Phys. Fluids,* **31**, 3550-3559.

Ramamurthy, M. K., Collins, B.P., Rauber, R.M. and Kennedy, P.C. 1990: Evidence of very-large-amplitude solitary waves in the atmosphere. *Nature,* **348**, 314-317.

Rottman, J. W. and J. E.Simpson, 1989: The formation of internal bore in the atmosphere: A laboratory model. *Quart. J. Roy. Meteor. Soc.,* **115**, 941-963.

Shreffler, J. H., and F. S. Binkowski, 1981: Observations of pressure jump lines in the midwest, 10-12 August 1976. *Mon. Wea. Rew.*, **109**, 1713-1725.

Skyllingstad, E. D. 1991: Critical layer effects on atmospheric solitary and cnoidal waves. *J. Atmos. Sci.*, **48**, 1613-1624.

Stamp A. P., and M. Jacka, 1995: Deep-water internal solitary waves. *J. Fluid Mech.*, Publishing.

Tung, K. K., Chan, T. F. and Kubota T. 1982: Large amplitude internal waves of permanent form. *Stud. Appl. Math.*, **66**, 1-44.

Vaughn, C. R., 1985: Birds and insects as radar targets: A review. *Proc. IEEE*, **73**, 205-227

Wilczak, J. M., et al., 1995: Contamination of wind profiler data by migrating birds: Charateristics of corrupt bird data and potential solutions. *J. Atmos. Oceanic Technol.*, **12**, 449-467

Wilson, J. W., T.M. Weckewerth, J. Vivekanadan, R. M. Wakimoto, and R.W. Russell, 1994: Boundary layer clear-air radar echoes: origin of echoes and accuracy of derived winds. *Atmos. Oceanic Technol.*, **11**, 1184-1206

Wood, J. R. and J.E.Simpson, 1984: Jumps in layered miscible fluids. *J. Fluid Mech.*, **104**, 329-342.

Zabusky, N. J. and M. D. Kruskal, 1965: Interaction of "solitons" in a collisionless plasma and the recurrence of initial states. *Phys. Rev. Lett.* **15**, 240-243.

Zhang, D. L., and J. M. Fritsch, 1988: Numerical simulation of the Mesoβ-scale structure and evolution the 1977 Johnstown flood. Part III: Internal gravity waves and the squall line. *J. Atmos. Sci.*, **45**, 1252-1268.

Appendix

A

Initial conditions for small and large amplitude solitary waves

When we study the basic properties of small and large solitary waves , the potential temperature background field is set up as a deep neutral layer over a stable layer with constant Brunt- Väisälä frequency N near the ground.

In the cases without wind shear, inflow speed u_{in} is constant. The stream function field $\psi(x,z)$ is

$$\psi(x,z)=u_{in}\eta(x,z) \tag{A,1}$$

and

$$\eta(x,z)=z-\delta(x,\eta(x,z)) \tag{A,2}$$

where η is the streamline height in the original unperturbed flow; $\delta(x,z)$ is vertical displacement of a streamline (Fig.A.1) and can be written as follow for each of two regions:

(1) In the stable layer (i.e. when $0 < z < h + \dfrac{a\lambda^2}{(x-x_0)^2+\lambda^2}$):

$$\delta(x,z) = A(x)\varphi(\eta(x,z)) \qquad \text{(A,3)}$$

where $A(x) = \dfrac{a\lambda^2}{(x-x_0)^2+\lambda^2}$, and $\varphi(\eta) = \sin(\dfrac{\pi\eta}{2h})$. For small amplitude waves $\eta(x,z)$ in $\varphi(\eta)$ is approximately equal to z as same as Eq.(4.2) for n=1. Because η appears in both sides of Eq.(A,2) for large amplitude waves, an iteration method is used to calculate η field.

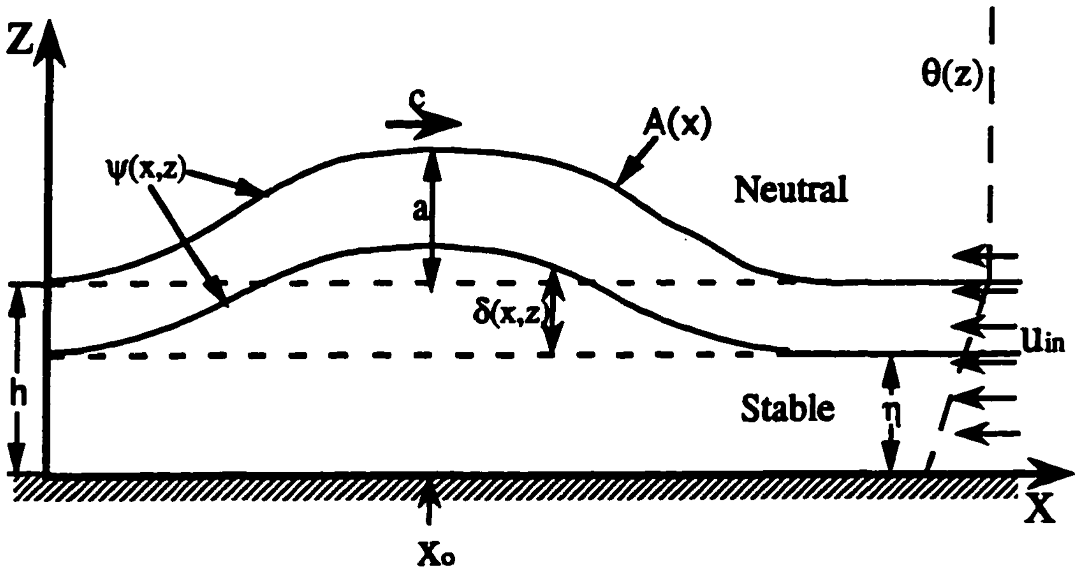

Fig.A.1 Schematic diagram for the definitions of the parameters used in the appendix.

(2) In the neutral layer (i.e. when $h+\dfrac{a\lambda^2}{(x-x_0)^2+\lambda^2}<z<H$):

$$\delta(x,z)=\frac{a\lambda(\lambda+z-h)}{(x-ct)^2+(\lambda+z-h)^2} \tag{A,4}$$

Then the initial vorticity ζ(x,z) and buoyancy b(x,z) fields can be obtained:

$$\zeta(x,z)=\frac{\partial^2\psi}{\partial x^2}+\frac{\partial^2\psi}{\partial z^2} \tag{A,5}$$

In the stable layer:

$$b(x,z)=N^2\eta(x,z) \tag{A,6}$$

In the neutral layer:

$$b(x,z)=N^2h \tag{A,7}$$

Hence, by giving the inflow speed and the shape of perturbation the initial stream function, vorticity and buoyancy fields are obtained.

Appendix

B

Derivation of equations used in Chapter 6

We assume that any field variables can be separated into two parts, one is the mean component to represent the large-scale flow indicated by overbars, the other is the fluctuating components to represent the small-scale turbulence indicated by primes. Thus v, w, θ and π can be written as

$$
\begin{aligned}
u &= \overline{u} + u' \\
w &= \overline{w} + w' \\
\theta &= \overline{\theta} + \theta' \\
\pi &= \overline{\pi} + \pi'
\end{aligned}
\tag{B.1}
$$

Substitute Eq.(B.1) into Eq.(2.6), (2.7) and (2.8), then average them, we get the mean equations as follow

$$\frac{\partial \overline{u}}{\partial t} + \overline{u}\frac{\partial \overline{u}}{\partial x} + \overline{w}\frac{\partial \overline{u}}{\partial z} = -\Theta_0 \frac{\partial \overline{\pi}}{\partial x} - \frac{\partial \overline{u'u'}}{\partial x} - \frac{\partial \overline{u'w'}}{\partial z} + F_x \tag{B.2}$$

$$\frac{\partial \overline{w}}{\partial t} + \overline{u}\frac{\partial \overline{w}}{\partial x} + \overline{w}\frac{\partial \overline{w}}{\partial z} = -\Theta_0 \frac{\partial \overline{\pi}}{\partial z} + g\frac{\overline{\theta}}{\Theta_0} - \frac{\partial \overline{u'w'}}{\partial x} - \frac{\partial \overline{w'w'}}{\partial z} + F_z \tag{B.3}$$

$$\frac{\partial\overline{\theta}}{\partial t}+\overline{u}\frac{\partial\overline{\theta}}{\partial x}+\overline{w}\frac{\partial\overline{\theta}}{\partial z}=-\frac{\partial\overline{u'\theta'}}{\partial x}-\frac{\partial\overline{w'\theta'}}{\partial z}+F_\theta \tag{B.4}$$

where $F_x=\upsilon_h\frac{\partial^2\overline{u}}{\partial x^2}+\upsilon_v\frac{\partial^2\overline{u}}{\partial z^2}$, $F_z=\upsilon_h\frac{\partial^2\overline{w}}{\partial x^2}+\upsilon_v\frac{\partial^2\overline{w}}{\partial z^2}$, and $F_\theta=\upsilon_h\frac{\partial^2\overline{\theta}}{\partial x^2}+\upsilon_v\frac{\partial^2\overline{\theta}}{\partial z^2}$.

For simplicity by assuming that the horizontal turbulent fluxes are horizontally homogeneous, so that horizontal turbulent flux divergent terms can be neglected. For w momentum equation, comparing with pressure gradient and buoyancy terms turbulent flux terms are relative small and neglectable. By applying K theory given in the Chapter 4, Eq.(B.2), (B.3), and (B.4) become

$$\frac{\partial\overline{u}}{\partial t}+\overline{u}\frac{\partial\overline{u}}{\partial x}+\overline{w}\frac{\partial\overline{u}}{\partial z}=-\Theta_o\frac{\partial\overline{\pi}}{\partial x}+\frac{\partial}{\partial z}(K_m\frac{\partial\overline{u}}{\partial z})+F_x \tag{B.5}$$

$$\frac{\partial\overline{w}}{\partial t}+\overline{u}\frac{\partial\overline{w}}{\partial x}+\overline{w}\frac{\partial\overline{w}}{\partial z}=-\Theta_o\frac{\partial\overline{\pi}}{\partial z}+g\frac{\overline{\theta}}{\Theta_o}+F_z \tag{B.6}$$

$$\frac{\partial\overline{\theta}}{\partial t}+\overline{u}\frac{\partial\overline{\theta}}{\partial x}+\overline{w}\frac{\partial\overline{\theta}}{\partial z}=\frac{\partial}{\partial z}(K_h\frac{\partial\overline{\theta}}{\partial z})+F_\theta \tag{B.7}$$

Differentiating Eq.(B.5) with respect to z and Eq.(B.6) with respect to x and subtract one from the other, mean vorticity equation can be obtained.

$$\frac{\partial\overline{\zeta}}{\partial t}+\overline{u}\frac{\partial\overline{\zeta}}{\partial x}+\overline{w}\frac{\partial\overline{\zeta}}{\partial z}=-\frac{\partial^2}{\partial z^2}(K_m\frac{\partial\overline{u}}{\partial z})+F_\zeta \tag{B.8}$$

where $\overline{b}=g\frac{\overline{\theta}}{\Theta_o}$, and $F_\zeta=\upsilon_h\frac{\partial^2\overline{\zeta}}{\partial x^2}+\upsilon_v\frac{\partial^2\overline{\zeta}}{\partial z^2}$.

If K_m and K_h are assumed as constants. Eq.(B.7) and (B.8) are simplified to

$$\frac{\partial\overline{\theta}}{\partial t}+\overline{u}\frac{\partial\overline{\theta}}{\partial x}+\overline{w}\frac{\partial\overline{\theta}}{\partial z}=K_h\frac{\partial^2\overline{\theta}}{\partial z^2}+F_\theta \tag{B.9}$$

$$\frac{\partial\overline{\zeta}}{\partial t}+\overline{u}\frac{\partial\overline{\zeta}}{\partial x}+\overline{w}\frac{\partial\overline{\zeta}}{\partial z}=-K_m\frac{\partial^3\overline{u}}{\partial z^3}+F_\zeta \tag{B.10}$$

But turbulent fluxes are usually not simply proportional to the local mean gradients in the ABL., so formula.(4.3) and (4.4) given by Brost and Wyngaard (1978) are used in our other simulations instead of constant K_m and K_h. For reader's convenience, Eq.(4.3) and (4.4) are shown here again.

$$K_m=\kappa u_{*0}h\frac{(\frac{z}{h})(1-\frac{z}{h})^{1.5}}{1+4.7(\frac{z}{h})(\frac{h}{L})} \tag{4.3}$$

$$K_h=1.2\kappa u_{*0}h\frac{(\frac{z}{h})(1-\frac{z}{h})^{1.5}}{1+4.7(\frac{z}{h})(\frac{h}{L})} \tag{4.4}$$

In this case the Eq.(2.7) and (2.8) become more complicated. They are

$$\frac{\partial\overline{\theta}}{\partial t}+\overline{u}\frac{\partial\overline{\theta}}{\partial x}+\overline{w}\frac{\partial\overline{\theta}}{\partial z}=K_h\frac{\partial^2\overline{\theta}}{\partial z^2}+\frac{\partial K_h}{\partial z}\frac{\partial\theta}{\partial z}+F_\theta \tag{B.11}$$

$$\frac{\partial\overline{\zeta}}{\partial t}+\overline{u}\frac{\partial\overline{\zeta}}{\partial x}+\overline{w}\frac{\partial\overline{\zeta}}{\partial z}=$$

$$-K_m \frac{\partial^3 \overline{u}}{\partial z^3} - 2\frac{\partial K_m}{\partial z}\frac{\partial^2 \overline{u}}{\partial z^2} - \frac{\partial^2 K_m}{\partial z^2}\frac{\partial \overline{u}}{\partial z} + F_\zeta \tag{B.12}$$

where the gradient terms of K_m and K_h. in Eq.(B.11) and (B.12) can be calculated by substituting Eq.(4.3) and (4.4) into them. After a straightforward computation, we find,

$$\frac{\partial K_m}{\partial z} = \kappa u_{*o}\left[\frac{(1-\frac{z}{h})^{1/2}(1-2.5\frac{z}{h})}{1+4.7\frac{z}{L}} - \frac{4.7z(1-\frac{z}{h})^{3/2}}{(1+4.7\frac{z}{L})^2 L}\right] \tag{B.13}$$

$$\frac{\partial^2 K_m}{\partial z^2} = \kappa u_{*o}\left[\frac{2-1.25\frac{z}{h}}{h(1-\frac{z}{h})^{1/2}(1+4.7\frac{z}{L})}\right.$$

$$\left. - \frac{9.4(1-\frac{z}{h})^{1/2}(1-2.5\frac{z}{h})}{(1+4.7\frac{z}{L})^2 L} + \frac{44.18z(1-\frac{z}{h})^{3/2}}{(1+4.7\frac{z}{L})^3 L^2}\right] \tag{B.14}$$

and

$$\frac{\partial K_h}{\partial z} = 1.2\frac{\partial K_m}{\partial z} \tag{B.15}$$